Synthesis and Characterisation of Single Crystal Transparent Conducting Oxide – Gallium Doped Zinc Antimonate

Benjamin John Parrett

A dissertation submitted in partial fulfilment
of the requirements for the degree of
Doctor of Philosophy
of
University College London

Department of Physics and Astronomy
University College London

March 2021

Declaration

I declare that this thesis contains an account of my research carried out at the Rutherford - Appleton Laboratories (Oxfordshire) and the London Centre for Nanotechnology (Bloomsbury Campus, UCL) between February 2017 and January 2021. The research reported here has not been previously submitted, wholly or in part, at this or any other academic institution for admission to a higher degree.

UV - Vis spectroscopy measurements were carried out by Professor Tim Veal, in the Department of Physics at the University of Liverpool. Electronic transport measurements in Chapter 4 were assisted by Dr. Larissa Ishibe-Veiga in the London Centre for Nanotechnology. Laboratory based XPS measurements were carried out in the UCL Chemistry department by Yuhan Liu. Dr. Adam Jackson in the group of Professor David Scanlon (UCL Department of Chemistry) conducted the electron band structure calculations. All remaining data collection and analysis have been performed by the author.

Abstract

This thesis focuses on the synthesis and characterisation of a new transparent conducting oxide (TCO) – $Zn_{1-x}Ga_xSb_2O_6$ (ZGSO). Polycrystalline powders of ZGSO were obtained using a novel reaction technique, designed to minimise the evaporation of antimony. Powder x-ray diffraction confirmed the powders to be phase pure and with mass increases indicating nearly complete oxidation. Out of these powders, single crystals of ZGSO were synthesised *via* a refined chemical vapour transport (CVT) technique using Cl_2 as a transport agent.

Investigations into the electronic properties of undoped single crystals indicated n-type semiconducting behaviour. UV - Vis spectroscopy revealed a wide optical band gap (3.38 eV) allowing transparency throughout the visible region. Substituting small amounts of Ga^{+3} onto the Zn^{+2} lattice site increased the electron carrier density by three orders of magnitude, and created a degenerate semiconductor. Low resistivities $\sim 5 \times 10^{-4}$ Ω.cm were observed while retaining a wide enough band gap to prevent opacity of visible light, therefore, proving ZGSO behaves as a TCO.

Energy dispersive x-ray spectroscopy (EDS) was used to quantify the cation stoichiometry in the crystals. The gallium concentration was found to vary significantly between samples and even across an individual sample indicating an erratic nature to the doping process. X-ray diffraction revealed a reduction in lattice parameters and correspondingly unit cell volume upon doping.

Lab-based x-ray photoemission spectroscopy (XPS) and synchrotron-based hard x-ray photoemission spectroscopy (HAXPES) were used to measure the core levels and valence band in doped and undoped crystals. Analysis of the core peak position revealed a shift to higher binding energies under the influence of doping, a direct consequence of conduction band filling. Measurements of the valence band using HAXPES significantly enhanced the intensity of the conduction band. This

is explained by the changing photoionisation cross sections as a function of photon energy. Similarly, HAXPES revealed an in-gap state that was attributed to the 5s orbital of a fraction of Sb^{+3} existing in the crystals.

Data presented from an angle-resolved photoemission spectroscopy (ARPES) study on a (001) surface in highly doped ZGSO revealed an electron band dispersion in the valence band however displaying significant k broadening. The absence of obvious cleavage planes in the trirutile structure prevented a quality cleaved surface for measurement. Therefore, due to the poor quality of the data, quantification of the conduction band's effective mass could not be achieved.

Impact Statement

The rare combination of high electrical conductivity and low opacity of visible light exhibited by transparent conducting oxides (TCO's) make them a vital component in modern electronics; from smart windows to solar panels. However, increasing demand and fundamental performance limits in the current crop of TCO's restrict use in a broader range of applications, leading to additional research to find new candidates.

Recent computational calculations carried out by a collaborating group at UCL predicted a new TCO - $Zn_{1-x}Ga_xSb_2O_6$ (ZGSO) to exhibit these transparent conducting properties. This project proposes a single crystal growth method to synthesise this system for the first time. Research of single crystals is essential because it allows an understanding of the mechanisms involved in the rare combination of properties.

This work features a novel chemical vapour transport (CVT) technique, refined to allow growth of ZSO and ZGSO single crystals. Techniques described in this thesis have also synthesised polycrystalline samples with complete phase purity and nearly ideal stoichiometry, improving on the literature methods.

Characterisation techniques employed by this project successfully prove the ZGSO crystals are functioning TCO's. However, a complicated defect structure due to inconsistent doping leads to questions about the suitability of the chemical vapour transport method for carefully controlling the doping of wide band gap semiconductors. Nevertheless, undoped crystals were determined to be of high quality, enabling potential application as a substrate for thin-film growth, essential in the TCO industry.

This thesis uses various photoemission techniques to understand the electronic band structure of the valence band. Calculations of the valence band are an essential

tool used to predict many properties of a material. The data presented in this thesis provides an experimental reference that can be used to fit and refine calculation techniques.

Acknowledgements

There are many people I would like to thank who have contributed to the completion of this research.

Firstly I would like to thank my supervisor Dr. Robin Perry for the great many hours spent helping to grow, refine, polish and measured crystals. His guidance and suggestions kept this project on track. Secondly, I would like to thank Dr. Timur Kim at Diamond Light Source for helping me through many of the obstacles the four years presented, particularly for the time spent with me collecting ARPES data on stubborn crystals! I would also like to thank Dr. Moritz Hoesch who helped kick start this project without whom this would not have been possible.

There are many other people I would like to thanks who have made data collection in this project possible. Firstly to everyone at UCL: Yuhan Liu, Dr. Larrisa Ishibe-Veiga, Prof. Rob Palgrave, Prof. David Scanlon and Dr. Adam Jackson for their help collecting data and discussions and Joe Willis and Dr. Anna Regoutz for their help during my HAXPES beamtime at Diamond. I would also like thank Prof. Tim Veal at the University of Liverpool for the UV - Vis measurements as well as important discussions. Finally, Alex Tanner, for providing me with somewhere to stay and an office to work in during my rare visits to the university. Thank you all.

I would also like to thanks to everyone at I05: Dr. Cephise Cacho, Dr. Matthew Watson, Dr. Luke Rhodes, Dr. Pavel Dudin, Dr. Hideaki Iwasawa, Dr. Sungwon Jung, Zakariae El Youbi, Rowan Curtis, Dr. Saumya Mukherjee and everyone else involved with the group over the four years. Additional thanks to Dr. Tien - Lin Lee, whose office was always open for a discussion about the photoemission data. I also want to thank Kristina Penman and her student liaison team at Diamond for their excellent support through the many peaks and troughs over the four years. Finally, to Dr. Gavin Stenning and his team at ISIS Neutron and Muon source for

their training and supervision enabled a great deal of my data collection.

To all my friends, you have made this journey possible by providing me with many welcome distractions; I cannot thank you enough. To Mum, Dad, Emily, Mikey and Jo, for your continued encouragement throughout my studies, especially during lockdown one of the Covid pandemic. You allowed me to escape the confines of Didcot and made the summer of 2020 bearable with garden cricket and competitive quizzing. I am eternally grateful. Lastly, to Kelly, for your enduring support over the many years we have studied apart and the constant stream of coffee and chocolate digestives in the final few weeks! This thesis is for you.

Contents

List of Figures **12**

List of Tables **17**

1 Introduction **20**

1.1 Transparent Conducting Oxides 20

1.2 ZSO 22

1.3 Thesis Outline 23

2 Theory of Transparent Conducting Oxides **25**

2.1 Band Theory 25

2.2 Electronic Band Structure Characteristics for TCO's 28

2.3 Families of Transparent Semiconducting Oxides 33

2.4 Electrical Conductivity in Degenerate Semiconductors 36

2.5 Further Optical Properties 40

2.6 Determination of the Optical Band Gap 41

2.7 Figure of Merit 44

2.8 Electronic Band Structure of ZSO 45

3 Experimental Methods **48**

3.1 Measurements 48

3.1.1 Resistivity and Hall effect 48

3.1.2 UV-Vis Spectroscopy 51

3.2 Characterisation 52

3.2.1 Energy Dispersive X-ray Spectroscopy 52

3.2.2 X-ray Diffraction 54

3.3 Photoemission Spectroscopy . . . 58
3.3.1 Electron Analyser . . . 62
3.3.2 Ultra-High Vacuum . . . 63
3.3.3 XPS and HAXPES . . . 63
3.3.4 ARPES . . . 65

4 Synthesis of Single Crystal ZGSO 69
4.1 Precursor Powder Preparation . . . 69
4.1.1 Preparation Methods from Literature . . . 69
4.1.2 Preparation Using Argon Environment . . . 76
4.1.3 Lattice Parameters . . . 78
4.2 Single Crystal Growth . . . 80
4.2.1 Chemical Vapour Transport Theory . . . 80
4.2.2 Single Crystal Growth of ZSO and ZGSO . . . 82
4.3 Conclusions . . . 88

5 Measurements 90
5.1 Electronic Transport . . . 90
5.1.1 Undoped ZSO . . . 90
5.1.2 Doped ZGSO . . . 99
5.1.3 Nominal doping vs Measured Carrier Concentration . . . 101
5.1.4 Carrier Concentration vs Mobility/Resistivity . . . 103
5.2 Optical Properties . . . 105
5.2.1 Transmission and Absorption Coefficient . . . 105
5.2.2 Optical Band Gap . . . 109
5.3 Figure of Merit . . . 118
5.4 Crystal 70a . . . 119
5.5 Conclusions . . . 121

6 Characterisation of ZSO and ZGSO 123
6.1 Energy Dispersive X-ray Spectroscopy. . . . 123
6.1.1 Results . . . 126
6.1.2 Doping Inconsistency . . . 130
6.2 X-ray Diffraction . . . 133

6.3 Conclusions 139

7 Photoemission Studies 141

7.1 Core Level Spectroscopy 144

7.1.1 Ga $2p_{3/2}$ 144

7.1.2 Peak Line Shape 145

7.1.3 Peak Position 148

7.2 Valence Band Spectroscopy 149

7.2.1 Conventional XPS 149

7.2.2 HAXPES 150

7.2.3 Band Gap Renormalisation 152

7.2.4 Valence Band Maximum Discrepancy 153

7.2.5 Orbital Nature of the Valence Band Density of States 155

7.3 ARPES 160

7.3.1 Experiment Plan 160

7.3.2 Cleavage of $ZnSb_2O_6$ 161

7.3.3 Experimental Results 164

7.3.4 Experimental Failures 167

7.4 Conclusions 170

8 Conclusions 172

8.1 Summary and Conclusions 172

8.2 Future Work 175

Appendices 178

A Derivation of the Drude conductivity. 179

B Calculation of the Mass Loss of Sb_2O_3 181

C Crystal Growth using $TeCl_4$ as a Tranport Agent 183

Bibliography 185

List of Figures

1.1 Crystal structure of ZSO 22

2.1 Three-dimensional Brillouin zone for a simple cubic lattice 27

2.2 E v k band structure indicating second highest conduction band . . . 29

2.3 E v k band structure indicating conduction band filling effects 32

2.4 Band structure of n-type, p-type and bipolar TSO's plotted with energy scale aligned to the vacuum level. 33

2.5 Predicted temperature dependent electronic properties for a metal and a semiconductor 40

2.6 E vs k band structure indicating optical band gap 42

2.7 Band gap extrapolation *via* the traditional Tauc method and the Dolgonos method. 44

2.8 Calculated electronic band structure and density of states for ZSO . . 46

3.1 Schematic of the Hall effect 49

3.2 Schematic of the experimental geometry used in resistivity and Hall effect measurements. 50

3.3 3D printed sample holder for UV - Vis measurements 52

3.4 Principle of EDS spectroscopy 53

3.5 Example EDS spectrum for ZGSO 54

3.6 Cartoon of of Bragg diffraction in a periodic crystal lattice 55

3.7 Schematic of the PXD apparatus in a Bragg – Bentano arrangement . 56

3.8 Schematic of a backscattering Laue diffraction experiment 58

3.9 Schematic of a basic PES experiment 59

3.10 Inelastic mean free path of an electron as a function of kinetic energy 60

3.11 Photoionisation cross sections for Zn $3d$, Sb $5s$ and O $2p$ as function of photon energy 61
3.12 Schematic of a hemispherical electron analyser and detector system . 62
3.13 Schematic of the I09 beamline optics at the Diamond Light Source . . 64
3.14 Schematic of an ARPES experiment. 66
3.15 Schematic of the I05 beamline optics at the Diamond Light Source . . 67

4.1 PXD pattern for purchased Sb_2O_5 powder. 71
4.2 PXD patterns for bakes following the N-method 72
4.3 PXD patterns for bakes following the K-method 73
4.4 PXD patterns for bakes following the R-method 74
4.5 Temperature profile as a function of time for both reactions for precursor powder 76
4.6 Cartoon and photograph of the reaction ampoule for initial reaction of Sb_2O_3 and ZnO under argon pressure 77
4.7 Powder x-ray diffraction pattern for reacted $ZnSb_2O_4$ and $ZnSb_2O_6$ powders 78
4.8 Powder x-ray diffraction pattern for undoped and 6 % doped ZGSO precursor powders 79
4.9 Rietveld refinement of undoped precursor powder 80
4.10 Cartoon of the CVT growth of a closed system reaction using Cl_2 as a transport agent. 81
4.11 Schematic and photograph of the apparatus used to condense Cl_2 into the reaction ampoule 84
4.12 Temperature gradient across the two-zone furnace measured using a thermocouple. 85
4.13 Growth temperature profile versus time indicating the reverse gradient method. 86
4.14 Photograph and powder x-ray diffraction pattern of the SiO_2 powder formed during growth. 86
4.15 Photograph and cartoon of the polishing device and polishing method 88
4.16 Photographs of ZSO and ZGSO single crystals polished to thickness $\sim 150\ \mu m$ 89

5.1 Electrical transport data as a function of temperature for ZSO single crystals . . . 91
5.2 Schematic of the voltage contacts painted onto the side of a crystal . 92
5.3 Calculation of energy of donor state and density of acceptors for an undoped ZSO crystal. . . . 94
5.4 μ vs T for undoped ZSO with linear dependence traces displayed. . . 95
5.5 Electrical transport data as a function of temperature for ZGSO single crystals . . . 99
5.6 Room temperature carrier concentration versus nominal doping in ZGSO single crystals. . . . 102
5.7 Room temperature resistivity and mobility plotted versus carrier concentration of ZGSO single crystals . . . 104
5.8 Transmission data for grown single crystals between wavelength range 300 and 700 nm recorded using UV - Vis spectroscopy . . . 106
5.9 Transmission data for over photon wavelength range 380 - 700 nm recorded using UV- Vis spectroscopy and optical transmission microscopy. . . . 109
5.10 Absorption coefficient versus photon energy for single crystals 111
5.11 Tauc plot used to estimate the direct-forbidden band gap in undoped ZSO. . . . 112
5.12 Optical band gap shifts for ZGSO crystals compared to the band gap of undoped ZSO . . . 113
5.13 Cartoon of the effect of Urbach tailing on the electronic band structure in a simple one-dimensional band model. . . . 116
5.14 ln(α) vs $h\nu$ for crystal 99a plotted 100 meV below the band gap . . . 116
5.15 ln(α) vs $h\nu$ for crystal 67a plotted 100 meV below the band gap. . . . 118
5.16 Photograph of crystal 70a . . . 120
5.17 Tramsmittance and optical absorption data as a function of wavelength and energy for crystal 70a . . . 121

6.1 Schematic of how surface irregularity in a sample can affect the intensity of emitted x-rays . . . 124
6.2 SEM image of a representative crystal surface. . . . 125

6.3 EDS spectrum for undoped crystal 64a 126
6.4 EDS data for three undoped ZSO crystals 127
6.5 Carrier concentrations of ZGSO crystals plotted against the EDS obtained gallium doping 129
6.6 Measured doping versus nominal doping for a large set of ZGSO crystals 130
6.7 EDS spectrum for five crystals from growth 92 displayed over energy ranges 8 - 10 keV normalised to the intensity of Sb Lα 131
6.8 EDS spectrum for crystal 70 taken over both light and dark regions normalised to the Sb Lα intensity 132
6.9 Rietveld refinement for crystals from undoped growth batch 64. . . . 134
6.10 Rietveld refinement for crystals from doped growth batch 92. 135
6.11 X-ray diffraction patterns for the 110 and 103 peaks in a doped sample. 136
6.12 Lattice parameters for undoped and doped single crystals determined using Rietveld refinement. 137
6.13 Lattice parameters of ZSO and ZGSO as a function of gallium doping 138
6.14 Comparison of lattice parameters of ZSO obtained in this work and from the literature. 139

7.1 HAXPES spectra for Ga $2p_{3/2}$ peak in the undoped and doped crystal showing a non-negligable intensity in the doped sample. 145
7.2 HAXPES spectra for Zn $2p_{3/2}$ and Sb $3d$ core peaks 146
7.3 XPS and HAXPES spectra of the Sb $3d$/O $1s$ peaks for the doped crystal showing oxygen contamination peak. 147
7.4 XPS valence band spectra for the undoped and doped sample. 150
7.5 HAXPES spectra of the valence band for the undoped and doped crystal 151
7.6 HAXPES spectra of the valence band maximum and conduction band for the doped and undoped crystal. 152
7.7 HAXPES and XPS valence band spectra for doped and undoped sample. 154
7.8 HAXPES valence band spectra for three undoped and four doped samples 155
7.9 Calculated density of states for ZSO weighted for both XPS and HAXPES photon energies. 156

7.10 Photoionisation cross section versus photon energy for relevant atomic orbitals contributing to the valence band 157
7.11 Experimental and predicted valence band spectrum for XPS and HAXPES 159
7.12 Brillouin zone of the tetragonal lattice with the calculated electronic band structure for the Γ - X and Z - R lines of high symmetry. 161
7.13 Schematic of the lattice orientation of a crystal required to ensure a cleaved (001) surface. 162
7.14 Schematic of the method devised to induce a cleave in ZSO single crystals. 163
7.15 Laue diffraction pattern of the large face of crystal 79d indicating a (110) plane 164
7.16 Analysis of the k_z variation in ZSO (001) 165
7.17 ARPES valence band dispersion for the doped sample taken using photon energies, $h\nu = 121$ and 148 eV 166
7.18 Energy distribution curves for 121 and 148 eV photon energies integrated over ± 0.5 Å^{-1} from the centre of the dispersion ($k_{\|} = 0$) . . . 167
7.19 Ratio of the photoionisation cross section ratio of the Zn 3d and Sb 5s atomic orbitals as a function of photon energy. 168
7.20 ARPES valence band dispersion ($h\nu = 148$ eV) with Brillouin zone imposed highlighting the significant broadening. 169
7.21 Laue diffraction results for the cleaved surface used in ARPES 170

C.1 Photograph of ZSO and ZGSO crystals grown by the CVT method using $TeCl_4$ as a transport agent 184
C.2 HAXPES ($h\nu = 5.29$ keV) survey spectrum of $TeCl_4$ grown single crystal. 185

List of Tables

2.1 Carrier density and plasma frequencies for literature TCO's 41
2.2 Resistivity, absorption coefficient and FOM for thin-film TCO's taken from literature. 45

4.1 Mass increase for ZSO precursor following the N-method 72
4.2 Mass increase for ZSO precursor following the K-method 73
4.3 Mass increase for ZSO precursor following the R-method 73
4.4 Quantification of antimony lost through evaporation from the literature preparation methods. 75
4.5 Lattice parameters for undoped and 6 % Ga doped ZGSO precursor powders 79
4.6 Log of a selection of successful crystal growths indicating conditions of growth and observations. 87

5.1 Room temperature electronic transport data for two undoped ZSO crystals. 91
5.2 Temperature dependence of Hall mobility in undoped ZSO 95
5.3 Room temperature electronic transport data for ZGSO single crystals 100
5.4 Comparison of room temperature electronic data for a highly conducting ZGSO crystal with two literature values. 104
5.5 Transmission, thickness and absorption coefficient of ZSO and ZGSO samples at 550 nm 106
5.6 Calculated plasma frequencies for three doped ZGSO samples. 107
5.7 Optical band gap values of ZSO taken from the literature 110
5.8 Experimentally determined values for the optical band gap of ZSO and ZGSO 111

5.9 Calculated Urbach energies for ZSO and ZGSO single crystals. 117
5.10 Room temperature resistivity, absorption coefficient and figure of merit for selected ZGSO crystals 119

6.1 Cation occupation determined from EDS for three undoped crystals . 128
6.2 Calculated cation occupation for ZGSO single crystals determined using EDS 128
6.3 Cation occupation for five ZGSO samples from growth batch 92 . . . 131
6.4 Lattice parameters of single crystals obtained using Rietveld refinement 134
6.5 Literature values for the lattice parameters in undoped ZSO 138

7.1 Binding energies of the Zn $2p_{3/2}$ and Sb $3d_{3/2}$ peaks for undoped and doped sample measured using HAXPES 149
7.2 Binding energies for key features in XPS valence band spectrum. . . . 149
7.3 Valence band peak positions for the undoped and doped samples with calculated shifts. 151
7.4 Photoionisation cross section for the valence band contributing orbitals for three relevant photon energies. 157

C.1 Crystal growth log for several growths using $TeCl_4$ as a transport agent. 184

Chapter 1

Introduction

1.1 Transparent Conducting Oxides

Transparent conducting oxides (TCO) are a rare class of materials, engineered to combine high electrical conductivity with low absorption of visible light, generally considered to be mutually exclusive properties. To be an n-type conductor, electrons must occupy the conduction band however, the wide band gap E_g required for transparency ($>$ 3.0 eV) prevents a significant number of electrons attaining the energy to allow conductivity. This obstacle can be overcome with careful doping.

This combination of properties makes them hugely desirable for industry, particularly as n-doped thin-films and are a crucial component in a wide variety of applications. Such examples include transparent electrodes in photovoltaic cells [1, 2], as they allow light to pass through to the active region of the solar cell and dissipate current. Similarly, they are used as transparent electrodes in flat panel displays [3, 4]. The high concentration of carriers they possess means they are opaque to infrared light, making them attractive for energy-efficient window applications. [5]. Additionally, TCOs are used in smart windows whereby the optical properties can be altered by applying a potential difference to an electrochromatic layer [6]. Recently, research has also showed TCOs can be synthesised as flexible electrodes, paving the way for a range of future technologies [7].

The first TCO was reported in 1907 by Bädeker [8] whereby upon thermally oxidising cadmium metal, non-stoichiometric CdO was formed with n-type transparent conducting properties. Despite a great deal of research into CdO, cadmium's

toxicity means the industrial applications are limited. Instead, the TCO industry focuses heavily on a group of wide band gap oxides: In_2O_3, SnO_2, ZnO and Ga_2O_3. The largest share of the TCO market is held by Sn doped In_2O_3 (ITO) with an estimated market value in 2020 to be around $3.46B [9]. This is primarily due to its superior electrical resistivity $\sim 10^{-5}$ Ωcm and high transparency > 90 % in films with thicknesses < 200 nm [10, 11]. Unfortunately, indium is a rare element in huge demand, not just for ITO but its importance in the fiber optics industry (GaInAs) [12] and, therefore, under increasing cost. Research has focused on finding a cheaper and more sustainable alternative with comparable properties.

Furthermore, there is an additional desire to discover materials for use in a wider use range of applications. TCOs are commonly used as electrodes on semiconducting devices, and to function they must form an ohmic contact at the interface [13]. This requires band alignment between the layers which is dependent on the work function or the energy between the vacuum level and the Fermi level. Particularly with organic photovoltaic devices, the current crop of TCO's do not possess work functions great enough [14]. These additional requirements have led to an uptake in research into new potential TCO compounds. Examples being the perovskites $SrSnO_3$ [15], $BaSnO_3$ [16, 17] and $SrGeO_3$ [18] as well as other structures such as spinel Cd_2SnO_4 [19].

Given their application in devices, the TCO literature is dominated by thin-film studies. However, single crystals, are vital for research as they allow unambiguous, quantitative transport measurements enabling a clear comparison between materials, particularly when dealing with transport data. Several early single crystal studies proved key in understanding the mechanisms involved in electron transport [20]. Kanai *et al* [21] managed to grow bulk single crystals of ITO using the flux growth method. This study highlighted a discrepancy between theory and experimental data, particularly by showing the Hall mobility became independent of carrier concentration. This observation began a discussion into the mechanisms of degenerate ionised impurity scattering. Another transport study on single crystals of ITO by Wen *et al* [22], highlighted a requirement to rethink how the conduction band is affected by Sn doping. Their mobility data was explained under the requirement that a change in the conduction band's effective mass occurs upon doping, later

understood by Walsh *et al* [23].

1.2 ZSO

The project focuses on a new class of TCO the stibnate compound $ZnSb_2O_6$ (ZSO) doped with gallium (ZGSO). ZSO or Ordonezite, is a naturally occurring mineral first discovered in 1942 by Byström *et al* [24]. It has a trirutile structure with space group $D^{14}{}_{4h}$ ($P4_2/mnm$) (136) and unit cell parameters a = 4.666 Å, c = 9.263 Å[25]. It is composed of six-coordinated ZnO_6 octahedra bonded to eight six-coordinated SbO_6 octahedra. Figure 1.1 displays the unit cell of ZSO.

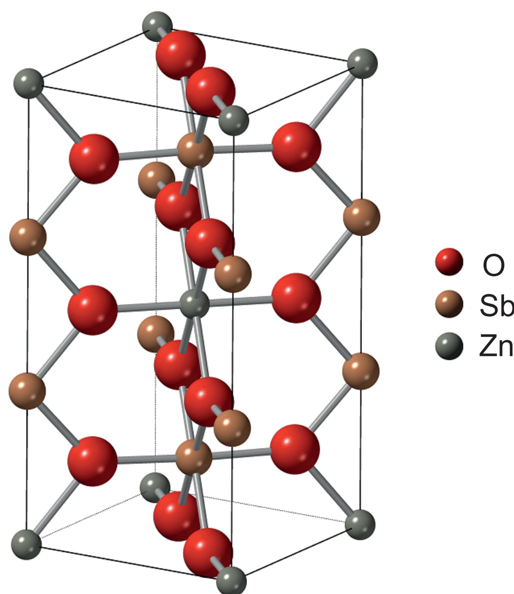

Figure 1.1: Crystal stucture for $ZnSb_2O_6$ obtained using structural data from Ercit *et al* [25]

Previous research into ZSO has shown it has many useful applications notably as a sensor. Several film studies have displayed its ability to detect NO_2 [26, 27], H_2S [28], CO_2, O_2, CO [29] as well as benzene, alcohol and acetone [30]. Nanoparticles of ZSO have also been shown to be useful as a photocatalyst in the degradation of rhodamine - B and methyl orange [31, 32].

Several UV - Vis diffuse reflectance studies have showed ZSO to have a wide optical band gap (3.0 - 3.5 eV) [31–35] allowing transparency in the visible light

range. The literature values are discussed further in section 5.2.2.

Electronic transport measurements of nominally undoped ZSO have been undertaken on polycrystalline samples. Kikuchi *et al* [36] indicated oxygen vacancies to be essential in creating carriers for metallic conductivity. Likewise, Nishiyama *et al* [37] and Katsui *et al* [38] conducted independent studies on the effect of cation substitution for Zn^{+2}. They measured electrical properties on powder pellets showing a decrease in the resistivity with Al^{+3} doping.

Recent theoretical research into cation doping in this material conducted by the Scanlon Materials Theory Group at UCL have predicted that doping of Ga^{+3} onto the Zn^{+2} lattice site should create n-type conductivity without significant detrimental impact to the wide band gap, therefore creating a TCO – $Zn_{1-x}Ga_xSb_2O_6$ (ZGSO).

1.3 Thesis Outline

This project focuses on the single crystal growth of ZSO and ZGSO. Chapter 2 examines the theory behind transparent conducting oxides and how the usually mutually exclusive properties of high conductivity and optical transparency can exist in a particular class of metal oxides. The calculated band structure for ZSO is presented at the end of the chapter, highlighting key features desirable for a potential TCO.

The growth of single crystal ZSO and ZGSO by the chemical vapour transport method is described in chapter 4. The refinement of the technique is discussed along with the preparation method for phase pure and nearly fully oxidised polycrystalline precursor powders. Electronic, optical, chemical and structural properties of the crystals were obtained using the experimental techniques reviewed in chapter 3. The majority of data collection was conducted at the Diamond Light Source and ISIS Neutron and Muon source located at the Rutherford Appleton Laboratory in Oxfordshire. Additional characterisation was carried out at the Department of Chemistry at University College London, and the Department of Physics at the University of Liverpool.

Doping of gallium into the ZSO lattice is expected to degenerately dope the

crystals without detrimental effects to the transparency. Chapter 5 presents the electronic transport and optical transmission results for both ZSO and ZGSO to determine the accuracy of the theoretical prediction.

An investigation into the consistency of gallium doping is discussed in chapter 6 by characterising the cation stoichiometry of grown single crystals using energy dispersive x-ray spectroscopy (EDS). This chapter also presents x-ray diffraction data, employed to determine how gallium doping affects the lattice parameters.

The last experimental chapter, chapter 7, discusses photoemission data taken during two synchrotron experiments at the Diamond Light Source, one on I09 (HAXPES) ($h\nu = 5.92$ keV) and the other on I05 (ARPES) ($h\nu = 120$ - 150 eV). Additional data taken using conventional lab based XPS ($h\nu = 1.48$ keV) is presented. Core level photoemission spectroscopy is used to determine binding energy shifts due to conduction band filling as a function of doping. Using both XPS and HAXPES, the density of states at the valence band was probed. By changing the photon energy, the photoionisation cross section of relevant atomic orbitals can be enhanced with respect to each other. The high photon energies used in HAXPES allowed the observation of the conduction band and similarly revealed an in-gap state sitting higher in energy than the valence band maximum. At the end of this chapter, ARPES data obtained from a (001) surface is presented and reviewed.

Finally, chapter 8 concludes the thesis, discussing the key points obtained during this work and explores the potential for future research on ZGSO.

Chapter 2

Theory of Transparent Conducting Oxides

To understand how TCO's can possess high levels of transparency while maintaining a low resistivity it is essential to understand the underlying physics of this class of compounds. This chapter discusses the origin of electron bands and the characteristic band properties that TCOs have. It also includes a discussion on other fundamental properties that TCO's possess. The chapter concludes by explaining why ZGSO should have the properties desired to be a transparent conducting oxide.

2.1 Band Theory

Individual atoms possess electron orbitals at well defined discrete energy levels. When these atoms move closer together, their outermost orbital wavefunctions begin to overlap. Due to Pauli's exclusion principle, the allowed energy levels split to accommodate these electrons; the more atoms, the more states. When dealing with materials with $\sim 10^{22}$ atoms, these tightly packed states appear continuous, forming what are known as bands. The characteristics of these bands are what provide materials with their vastly different properties.

To understand the behaviour of these electrons the time-independent Schrödinger equation for non-relativistic particles must be solved

$$\left[-\frac{\hbar^2}{2m}\nabla^2 + V(\mathbf{r})\right]\Psi(\mathbf{r}) = E\Psi(\mathbf{r}) \tag{2.1}$$

Where $\hbar$ is the reduced Planck's constant, m the mass of the electron, ∇^2 is the Laplacian, $V(\mathbf{r})$ is the potential as a function of position vector $\mathbf{r}$, $\Psi(\mathbf{r})$ is the wavefunction and E is the energy. In the free electron case i.e. in the absence of potential, the solutions to equation 2.1 are

$$\begin{aligned} E &= \frac{\hbar^2\mathbf{k}^2}{2m} \\ \Psi_{\mathbf{k}}(\mathbf{r}) &= e^{i\mathbf{k}.\mathbf{r}} \end{aligned} \tag{2.2}$$

Where $\mathbf{k}$ is the wavevector stemming from De Broglie's relation $\mathbf{p} = h/\lambda = h\mathbf{k}/2\pi = \hbar\mathbf{k}$ with $\mathbf{p}$ being the momentum, h is Planck's constant and λ is the wavelength.

In a crystalline system, the potential is a real function with the periodicity of the lattice. This potential originates from the Coulomb interaction between the electron and the positively charged ions and electron-electron interactions. Bloch's theorem states that eigenstates of the Schrödinger equation in a periodic potential can be written as the plane wave (equation 2.2) multiplied by a function with the periodicity of the lattice $u_{\mathbf{k}}(\mathbf{r})$.

$$\Psi_{\mathbf{k}}(r) = e^{i\mathbf{k}.\mathbf{r}}u_{\mathbf{k}}(\mathbf{r}) \tag{2.3}$$

The periodic potential becomes significant at $\mathbf{k}$ values of $\pm\frac{n\pi}{a}$ where n is an integer and a is the atomic separation. At this value, the wavefunction is made up equally of waves travelling in opposite directions π radian out of phase. The probability density of these wavefunctions places electrons either close to or in between the ions. This lowers or raises the potential energy of the electrons and opens up a band gap, an energy range that no possible states can exist. The Kronig–Penney model [39, 40] provides a mathematical derivation however it is outside the scope of this work.

Values of $k = \pm\frac{n\pi}{a}$ are known as the Brillouin zone boundary. Away from the Brillouin zone boundaries, the periodicity of the lattice has less effect on the energy of the electron. Because of the periodicity of k-space, Bloch's theorem states any electron with wavevector greater than $\pm\frac{n\pi}{a}$ can be translated into the 1st Brillouin zone using a reciprocal lattice vector. Furthermore, the symmetry of the recip-

rocal lattice implies all band information can be displayed in what is known in three-dimensional reciprocal space as the irreducible wedge. Figure 2.1 displays the Brillouin zone for a simple cubic (SC) lattice where the letters signify high symmetry points in k-space. The SC example is chosen because it has the highest symmetry and therefore simplest reciprocal structure. Typical band structures are plotted along these lines of high symmetry such as $\Gamma - X - M - \Gamma - R - X$ vs E with Γ by convention, to be the centre of the Brillouin zone.

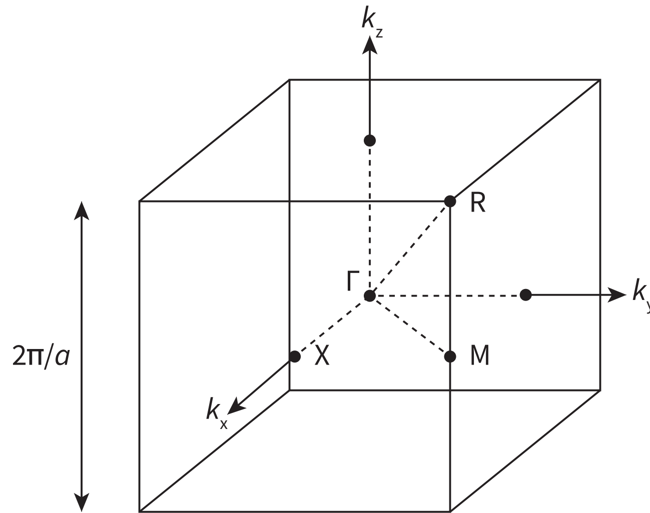

Figure 2.1: Three-dimensional Brillouin zone for a simple cubic lattice with atomic spacing a.

Electrons in a solid will naturally occupy the lowest energy state available. The electrons will fill corresponding to the density of states available, which considers Pauli's exclusion principle. Furthermore, their occupation is also determined by the Fermi - Dirac distribution, which provides a probability of the state being occupied due to thermal effects. The Fermi – Dirac function $f_0(\boldsymbol{k})$, is defined by

$$f_0(\boldsymbol{k}) = \frac{1}{\exp\left[\frac{E(\boldsymbol{k})-\mu}{k_B T}\right] + 1} \tag{2.4}$$

Where $E(\boldsymbol{k})$ is the energy of the state, μ is the chemical potential. k_B is Boltzmann constant and T is temperature. At $T = 0$ the chemical potential is equal to the Fermi energy E_F which is defined as the energy at which all states below are

filled.

The importance of the band gap becomes relevant when describing differences between metals, semiconductors and insulators. In metals, the Fermi level lies in the band, and therefore, even at absolute zero, electrons can create conduction under an applied electric field. In a semiconductor, at absolute zero, the Fermi level lies in the band gap with all filled states below known as the valence band. As the temperature is increased, the Fermi – Dirac function permits electrons to populate states above the Fermi level. If the band gap is small or the temperature is large enough, electrons can reside in the conduction band allowing conductivity. Insulators are defined by having band gaps too large for a significant density of electrons to be excited into the conduction band.

2.2 Electronic Band Structure Characteristics for TCO's

The search for a new TCO begins with finding a host oxide structure with a wide band gap, or the energy separating the highest occupied bands or valence band maximum (VBM) and the lowest unoccupied bands or conduction band minimum (CBM). Any photons impinging onto the material with energy greater than the magnitude of the band gap are absorbed by valence electrons, exciting them into unoccupied bands preventing transparency. For a TCO to be transparent throughout the visible light range, this band gap should be greater than the energy of blue light $\sim$3.0 eV. Furthermore, transparency can also be affected by the energy separation between the lowest conduction band and the second-highest conduction band (CBM+1) displayed in Figure 2.2. If the magnitude of this gap is not greater or equal to the band gap, electrons residing in the conduction band may be excited into the higher energy band in a process known as free carrier absorption [41].

For n-type TCOs, the conduction electrons must also be delocalised. Conduction bands are formed when the outer atomic orbitals between neighbouring atoms overlap. This conduction band's width is affected by the magnitude of overlap between the orbitals, a large overlap creating a broader band [42]. However, the overlap

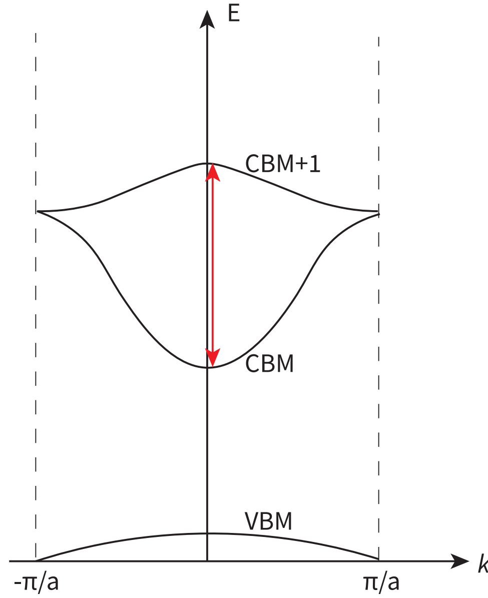

Figure 2.2: E v k band structure schematic indicating the energy separation between the conduction band minimum (CBM) and second highest conduction band (CBM + 1).

must not be so considerable as to inhibit the band gap. Therefore, oxide compounds where the atoms are close together or the outer orbitals are too spatially extended are unsuitable for transparency [43]. Furthermore, the conduction path should be isotropic in space created by the overlap of s orbitals. The energy E of the electrons residing in the conduction band close to the Brillouin zone centre is the same as equation 2.2 but with the electron mass m replaced by the band mass m^*.

$$E(\boldsymbol{k}) = \frac{\hbar^2 \boldsymbol{k}^2}{2m^*} \tag{2.5}$$

Electrons in a parabolic dispersion behave as though they are free but with a different mass, signifying how they respond to magnetic and electric fields. This parabolic approximation is suitable due to the weak interaction between electrons in the VBM and CBM in TCOs [44, 45]. The dispersion is directly related to the band mass by equation 2.6.

$$\frac{1}{m^*} = \frac{1}{\hbar^2} \frac{\partial E(\boldsymbol{k})^2}{\partial^2 \boldsymbol{k}} \tag{2.6}$$

A broad conduction band has a greater dispersion and therefore, lower effective mass.

The *d*-electrons also need to be fully occupied due to the colouration caused by partially filled orbitals [46]. Only a few cations are appropriate for creating TCO host lattices, elements with $d^{10}ns^0$ (n = 4,5) such as Zn, Sn, In and Sb [42]. Commonly used TCO host lattices such as ZnO and In_2O_3 have been shown to have valence bands that are predominantly O 2*p* in nature [47–51]. This O 2*p* valence band is highly localised and therefore weakly dispersing. In ITO, the effective mass for holes is as high as 38 m_e [52] which in part explains why hole acceptors for p-type TCOs are less common [53, 54] however this will be discussed further in section 2.3.

By nature, these host lattices are wide band gap insulators; however, to turn them into an n-type TCO, they must be doped with extra charge carriers. This is achieved in several ways, such as cation substitution or the introduction of cation interstitials and oxygen vacancies. Cation vacancies behave as acceptors and are therefore detrimental to n-type conductivity. King and Veal [55] provided a comprehensive analysis of the various mechanisms, however, as this thesis aims to create n-type conductivity using cation substitution, this will be the basis of the discussion.

N-doping by cation substitution is achieved by replacing a host cation for one with a similar size and higher valence creating a donor state that sits just below the conduction band minimum. The ground state of hydrogen can approximate the wavefunction of this donor state however the Bohr radius a_o is replaced by the effective Bohr radius a_o^*

$$a_o^* = \frac{\hbar \epsilon_r}{m^* e^2} \tag{2.7}$$

Where ϵ_r is the relative permittivity or dielectric constant of the material and e is the electron charge. For ITO, a_o^* is 13 Å[50], far more extensive than atomic spacing, causing them to overlap at moderate dopings. At low doping levels, this donor state sits close to the conduction band however if the donor concentration increases, this state overlaps with the conduction band shifting the Fermi level into the band creating a degenerate semiconductor. The critical carrier density n_c at which this transition occurs is governed by the Mott criterion [56].

$$n_c^{\frac{1}{3}} a_o^* \sim 0.25 \tag{2.8}$$

At the critical doping the conduction band is now populated allowing a conduc-

tivity but the material also largely retains the wide band gap. Shrinkage to the fundamental band gap has been observed in ITO due to the donor state sitting slightly lower in energy than the conduction band minimum [23].

E_g, the energy gap between the VBM and the CBM is known as the fundamental band gap. For TCOs however, the optical band gap, E_{opt}, is more relevant as this governs the transparency of the crystal. This is defined by the energy at which strong optical absorption occurs due to band transitions and can differ from the fundamental band gap. In_2O_3 provides a good example whereby the fundamental band gap was determined by photoemission spectroscopy to be 2.9 eV but possesses an optical band gap of 3.75 eV [57]. Walsh *et al* [58] determined that dipole selection rules forbade transitions from upper valence band to the conduction band and the onset of strong optical absorption would occur from states 0.8 eV below the VBM.

The optical band gap is also affected by electron population of the conduction band. If the lowest energy states in the conduction band are filled, electrons being excited out of the valence band *via* photon absorption cannot occupy these states. The nearest unoccupied states are higher in energy. The corresponding increase in the optical band gap is known as Burstein – Moss effect, ΔE_{BM} [59, 60] and is calculated using equation 2.9 and graphically represented in Figure 2.3.

$$\Delta E_{BM} = \left(\frac{h^2}{8m^*}\right)\left(\frac{3n}{\pi}\right)^{\frac{2}{3}} \tag{2.9}$$

Where n is the carrier density. Accompanying the Burstein– Moss shift is another effect known as band gap renormalisation ΔE_{RN}, which causes a reduction in the optical band gap as a function of doping occurring above the Mott criterion [61, 62]. The origin of this effect remains a controversial topic in the literature. A standard theory is this shrinkage of the band gap arises from Coulomb interactions between conduction electrons and impurity atoms as well as between valence and conduction electrons [63–65]. Jiang *et al* [66] successfully modelled the Burstein – Moss effect and the two electrostatic interactions [67, 68] to explain experimental band gaps in SnO_2. Despite literature suggesting this may occur in ITO [57], Walsh *et al* [23] conducted a density functional theory (DFT) study on the effect of dopants into the In_2O_3 lattice. They concluded the origin of the band gap shrinkage came primarily from hybridisation of the dopant s-orbitals with the In 5s conduction band

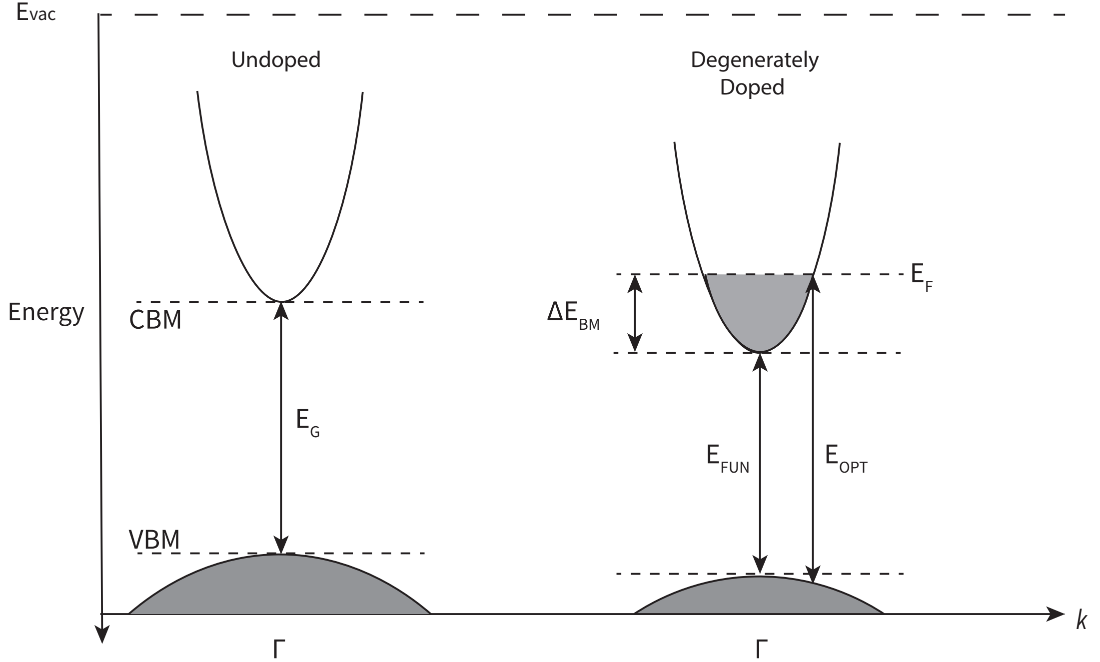

Figure 2.3: *Left* - Schematic of the $E(k)$ vs k dispersion for an undoped sample with fundamental band gap E_g highlighted, the shading indicates the states are occupied. *Right*- Band structure of a degenerately doped TCO with the bottom of the conduction band populated and Fermi energy E_F indicated. The Burstein – Moss shift, ΔE_{BM} and the optical band gap E$_{opt}$ is also highlighted. The effect of doping induces a drop in energy of both the conduction band and the valence band; however, the conduction band experiences a greater drop. Therefore, the fundamental band gap in a doped material $E_{FUN} < E_g$ in the undoped sample, a direct consequence of band gap renormalisation.

altering the dispersion. However, a recent study on La:$BaSnO_3$ [69] determined the renormalisation of the band gap was occurring solely due an electrostatic interaction similar to that throughout literature. Therefore, band gap renormalisation appears to be sensitive to the system under inspection. The effect ΔE_{BM} and electrostatically induced band gap renormalisation ΔE_{RN} have on the optical band gap E_g is shown in equation 2.10.

$$E_{opt} = E_g + \Delta E_{BM} - \Delta E_{RN} \tag{2.10}$$

2.3 Families of Transparent Semiconducting Oxides

Until now the discussion of TCO compounds has only been referring to the common n-type doping situation, however, a few other members of the TCO class of materials exists. For this section it is more precise to refer to these materials as transparent semiconducting oxides (TSO) because they have not been degenerately doped to become a *conductor*. Here the other members of this family are briefly discussed and also why certain materials such as ZnO will prefer to be doped n-type.

For this discussion, it is essential first to define a few parameters. The first is the electron affinity χ or the energy difference between the conduction band minimum and the vacuum level. The second is the energetic difference between the valence band maximum and the vacuum level known as the ionisation potential I_p. Using just these two properties, transparent semiconducting oxides can be grouped into three main classes: n-type, p-type and bipolar, with a representative simple band structure displayed in Figure 2.4.

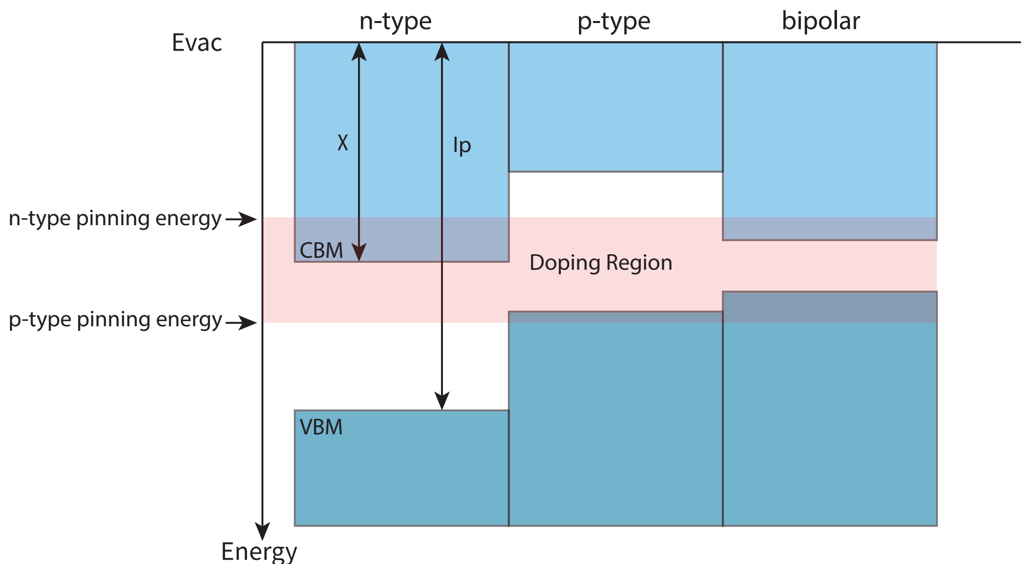

Figure 2.4: Representative band structure for three different classes of transparent semiconducting oxide materials. Displayed is the electron affinity χ and ionisation potential I_p. Additional labels are referred to in the text.

N-type TSO's have a large electron affinity formed by the dispersive *s*-type con-

duction band and a large ionisation potential owing to the localised states of the oxygen 2*p* previously discussed. This is the typical band structure of the vast majority of TSO's. Doping of these compounds usually occurs by substitution of a cation of higher valence such as Sn into In_2O_3 (ITO) donating a singular electron to the conduction band. In ITO, the tin dopant hybridises with the conduction band and therefore, the inclusion of tin creates scattering centres for the conduction electrons and lowers the mobility. This is often referred to as conventional cation substitution and is how the major TCO compounds such as F:SnO_2 and Al:ZnO function.

This reduction in mobility has been overcome by non-conventional cation substitution [70]. Doping of molybdenum into indium oxide creates two t_{2g} spin up states localised in the band gap and one spin down state high in the conduction band [71]. This down state provides the source of the single donor electrons but interestingly, because Mo doesn't hybridise with the conduction band, the conduction electrons are not affected by this Mo scattering centre. This is similar to the doping of La into $BaSnO_3$ resulting in the record high mobilities ∼320 cm^2/V.s [16].

P-type TSO's have both a small electron affinity and ionisation potential. The valence band maximum has been lifted in energy by an additional *d* or *p* state hybridising with the O 2*p* orbitals inducing an upwards dispersion. Perhaps the most famous p-type TCO is Cu_2O, where an overlap of the Cu 3*d* and O 2*p* states lifts the valence band and creates the reduction in ionisation potential and the weakly overlapping Cu 4*s* induces a low electron affinity [72, 73]. The dispersive valence band has been shown to have hole effective masses as low as 0.24 m_e [52]. However, it is unsuitable as a TCO with requirements for low opacity in the visible range due to a small optical band gap (2.17 eV), but it is the foundation compound for the entire copper based p-type TCO family. Figure 2.4 also displays a different class of materials, the bipolar transparent semiconducting oxides but a discussion on this class of materials will be reserved until the end of the section.

Certain wide band gap oxide materials will fall into one of these categories due to the relative band edge alignment with respect to the vacuum energy and the position of the Fermi level. Walukiewicz [74] successfully discusses why this is the case. When semiconducting materials are heavily irradiated with gamma radiation, a considerable amount of defect states are formed in the band gap which causes the

Fermi level to stabilise and tends to be ∼4.9 eV below the vacuum level regardless of material [75]. Around this exists a range of energies in which the Fermi level can shift comfortably with the inclusions of donors or acceptors and remain uncompensated. If the Fermi level moves towards the conduction band, as would be the case with intentional n-type doping with donors, an energy exists where compensating defects will be energetically favourable and spontaneously form. This Fermi level position is called the n-type pinning energy. Similarly, if the Fermi level is shifted towards the valence band by acceptor doping a p-type pinning energy exists where compensating donor defects will form. Therefore in a semiconducting material, a range of Fermi level positions exists where doping is possible without spontaneous compensation. Walukiewicz argues this range of doping is relatively consistent between samples with respect to the vacuum energy. In the case of n-type materials, this range extends into the conduction band but not into the valence band. Therefore it is very difficult to dope p-type without the formation of compensating defects. Similarly, in p-type TSO's the Fermi level region lies below the conduction band and into the valence band. This range is depicted in Figure 2.4.

When discussing this family of compounds and their practical use in devices, it is important to mention the transparent amorphous oxide semiconductor (TAOS) class of materials. The most famous of these is amorphous In-Ga-Zn-O (a-IGZO), a compound used as the backplane in thin-film transistors (TFT's) first developed in 2004 by the Hosono group in Japan [76]. To work in a transistor this material must be a semiconductor therefore, materials such as a-In_2O_3 were deemed unsuitable due to the difficulty in reducing carrier concentration from easily formed oxygen vacancies. Conventionally this backplane in flat panel displays has been amorphous silicon (a-Si); however, there is an increasing demand in technology for larger screens with better resolution requiring a material with superior electronic properties to a-Si [77]. This has pushed the research towards TAOS materials due to their superior and uniform electronic properties, the flexibility of the material, ease of production such as room temperature fabrication, and the possibility of working with TCO electrical contacts to create transparent electronics [78]. These materials work effectively because the isotropic nature of the overlapping cation *s*-orbital's creating the conduction band remains largely unperturbed by the structural disorder in the

amorphous state.

N-type TAOS materials are relatively well established, each with their own advantages however, for the next step in the advancement of transparent electronics, complementary metal oxide semiconductor (CMOS) devices are required forcing research into a similar p-type device [79]. This requirement has actually created a research market for bipolar transparent semiconducting oxide materials. Bipolar TSO's have both a relatively high electron affinity and low ionisation potential, creating a considerably reduced indirect fundamental band gap but with a large direct band gap enabling transparency. This bipolar behaviour has been observed in SnO with both a dispersive conduction band and valence band. The direct band gap is 2.7 eV [80] however a indirect band gap is observed to be 0.7 eV [81, 82]. Given this materials ability to be doped p-type and n-type [83, 84], it has been touted as a potential component in transparent thin film transistors (TTFT's).

2.4 Electrical Conductivity in Degenerate Semiconductors

Providing the TCO has been sufficiently doped, and the metal-insulator transition has occurred, the electronic properties will be analogous to conventional metal, albeit with a smaller carrier concentration. To understand how electron transport occurs, the semi-classical Boltzmann transport equation is used which treats electrons as particles obeying Fermi – Dirac statistics [85].

The probability of a state $\boldsymbol{k}$ being occupied at position $\boldsymbol{r}$ and time t is given by the probability distribution function $f(\boldsymbol{k},\boldsymbol{r},t)$. At thermal equilibrium, the Fermi – Dirac equation, $f_0(\boldsymbol{k})$, (equation 2.4) describes this occupation. To solve how the probability distribution function evolves over time and in a steady state, the partial differential is taken to be

$$\frac{df}{dt} = \frac{\partial f}{\partial t} + \frac{\partial f}{\partial \boldsymbol{r}}\frac{\partial \boldsymbol{r}}{\partial t} + \frac{\partial f}{\partial \boldsymbol{k}}\frac{\partial \boldsymbol{k}}{\partial t} = 0 \tag{2.11}$$

The probability distribution function changes due to scattering in and out of the final state given by $\left.\frac{\partial f}{\partial t}\right|_{scattering}$ which can be described by Fermi's golden rule [85] however in the relaxation time approximation is given by

$$\left.\frac{\partial f}{\partial t}\right|_{scattering} = \frac{f_0(\boldsymbol{k}) - f(\boldsymbol{k})}{\tau(\boldsymbol{k})} \tag{2.12}$$

Where $\tau(\boldsymbol{k})$ is the scattering rate. This states if an applied field is removed the system will tend back to its equilibrium state. The force on the electron is described by the Lorentz force $\boldsymbol{F} = \hbar\,\frac{d\boldsymbol{k}}{dt} = -e(\boldsymbol{E} + \boldsymbol{v} \times \boldsymbol{B})$ where $\boldsymbol{E}$ is the electric field and $\boldsymbol{B}$ is the magnetic field. The Boltzmann transport equation is given by

$$\frac{\partial f}{\partial t} = -\boldsymbol{v}.\nabla_r f + \frac{e(\boldsymbol{E} + \boldsymbol{v} \times \boldsymbol{B}).\nabla_k f}{\hbar} + \frac{f_0(\boldsymbol{k}) - f(\boldsymbol{k})}{\tau(\boldsymbol{k})} \tag{2.13}$$

Where $\boldsymbol{v} = \frac{\partial \boldsymbol{r}}{\partial t}$. Assuming a stationary state $\frac{\partial f}{\partial t} = 0$, and the system is close to equilibrium, $\Delta f \approx \Delta f_0$, yields the equation

$$f(\boldsymbol{k}) = f_0(\boldsymbol{k}) + \frac{\tau(\boldsymbol{k}) e(\boldsymbol{E} + \boldsymbol{v} \times \boldsymbol{B}).\nabla_k f_0}{\hbar} + \tau(\boldsymbol{k})\boldsymbol{v}.\nabla_r f_0 \tag{2.14}$$

The Fermi function derivatives are defined by

$$\nabla_{\boldsymbol{r}} f_0 = \frac{\partial f_0}{\partial T}\nabla_{\boldsymbol{r}} T + \frac{\partial f_0}{\partial \mu}\nabla_{\boldsymbol{r}}\mu \tag{2.15}$$

$$\nabla_{\boldsymbol{k}} f_0 = \frac{\partial f_0}{\partial E}\nabla_{\boldsymbol{k}} E(\boldsymbol{k}) \tag{2.16}$$

where only the temperature and chemical potential are dependent on position. The distribution function is now described by

$$f(\boldsymbol{k}) = f_0(\boldsymbol{k}) + \frac{\tau(\boldsymbol{k}) e(\boldsymbol{E} + \boldsymbol{v} \times \boldsymbol{B}).\frac{\partial f_0}{\partial E}\nabla_{\boldsymbol{k}} E(\boldsymbol{k})}{\hbar} + \tau(\boldsymbol{k})\boldsymbol{v}.\left[\frac{\partial f_0}{\partial T}\nabla_{\boldsymbol{r}} T + \frac{\partial f_0}{\partial \mu}\nabla_{\boldsymbol{r}}\mu\right] \tag{2.17}$$

that can be simplified using

$$\frac{\partial f_0}{\partial \mu} = -\frac{\partial f_0}{\partial E} = \frac{T}{E(\boldsymbol{k}) - \mu}\frac{\partial f_0}{\partial T} \tag{2.18}$$

leaving

$$f(\boldsymbol{k}) = f_0(\boldsymbol{k}) + \tau(\boldsymbol{k})\frac{\partial f_0}{\partial \mu}\left[-\frac{e}{\hbar}\left(\frac{\hbar \boldsymbol{k}}{m} \times \boldsymbol{B} + \boldsymbol{E}\right).\nabla_{\boldsymbol{k}} E(\boldsymbol{k}) + \frac{\hbar \boldsymbol{k}}{m}\left(\frac{E(\boldsymbol{k}) - \mu}{T}\nabla_{\boldsymbol{r}} T + \nabla_{\boldsymbol{r}}\mu\right)\right] \tag{2.19}$$

$\frac{\partial f_0}{\partial \mu}$ is zero except for close to the Fermi level, suggesting only electrons near the Fermi level participate in transport processes. The current density j_x in a conductor with an electric field applied in the x-direction is given by

$$j_x = -e \int v_x D(\boldsymbol{k}) f(\boldsymbol{k}) d^3k \tag{2.20}$$

Where $D(\boldsymbol{k})$ is the density of states which in three dimensions is given by $\frac{2}{(2\pi)^3}$. The numerator takes into account Pauli's exclusion principle. Applying the assumption that the conductor is uniform in space ($\nabla_{\boldsymbol{r}} T$ and $\nabla_{\boldsymbol{r}} \mu = 0$) and the magnetic field is zero the current density is shown to be equal to the Drude result (Appendix A) [86, 87].

$$\boldsymbol{j} = \frac{ne^2\tau}{m^*}\boldsymbol{E} = \sigma \boldsymbol{E} = \frac{\boldsymbol{E}}{\rho} \tag{2.21}$$

Where σ and ρ are the conductivity and resistivity respectively. To experimentally determine the resistivity, Ohms law is applied

$$V = IR \tag{2.22}$$

V being potential difference and R the resistance of the material. R is equal to

$$R = \frac{\rho L}{A} \tag{2.23}$$

With L being the length of the sample being measured and A is the cross-sectional area perpendicular to current flow. The mobility of a material is a common parameter used to characterise TCO's, it is defined by the velocity of an electron under an applied field.

$$\mu = \frac{\mathbf{v}}{\mathbf{E}} = \frac{e\tau}{m^*} \tag{2.24}$$

Therefore a highly dispersing conduction band provides a high electron mobility ($\mu \propto \frac{1}{m^*} \propto \frac{\partial E}{\partial k}$). Combining Equations 2.23 and 2.24 gives

$$\rho = \frac{1}{\mu n e} \tag{2.25}$$

In section 2.5 it is shown that an upper limit of carrier density exists in TCO compounds therefore it is important to maximise the mobility to minimise the resistivity. The mobility is a linear combination of the contributions from both impurities μ_i and phonons μ_t described by Matthiessen's rule.

$$\frac{1}{\mu_e} = \frac{1}{\mu_i} + \frac{1}{\mu_t} \tag{2.26}$$

Figure 2.5 provides a visual representation of how the properties vary as a function of temperature in metals and semiconductors. In high purity non-magnetic metals, where n is constant, the mobility is purely dependent on phonon scattering which is shown to be inversely proportional to temperature [87] therefore $\rho \propto T$ [88] This deviates at low temperatures due to lower phonon efficiency but this is less relevant to the TCO systems so will not be covered.

In semiconductors, the temperature dependence on mobility is more complicated. At low temperatures, ionised impurity scattering is prevalent due to an increased density of scattering centres. As the temperature increases, the carriers gain more energy, and the scattering cross section reduces. Carriers with more energy effectively spend less time near the ionised impurity. The low temperature dependence on mobility is proportional to $T^{3/2}$. At higher temperatures the phonon scattering takes precedent, and the mobility is proportional to $T^{-3/2}$ [89].

The carrier concentration is described in three regions. Electrons are frozen in their impurity bands at low temperatures without the energy available for activation into the conduction band. As the temperature increases the available thermal energy has activated all the donor state electrons. Finally at very high temperatures, electrons are able gain a large amount of thermal energy and valence band electrons can excite across the band gap, resulting in a steep rise in carrier density.

In the case of a degenerate semiconductor a combination of these properties is expected. The donor ionisation energy becomes zero and therefore the carrier concentration is constant throughout all temperatures, akin to a metal. For mobility, it becomes more complicated. A negative dependence is expected at high temperatures due to increased thermal lattice scattering. However, at the lower temperature region, the mobility becomes almost temperature independent. This is because of a screening effect between the conduction electrons and the ionised impurities [90, 91].

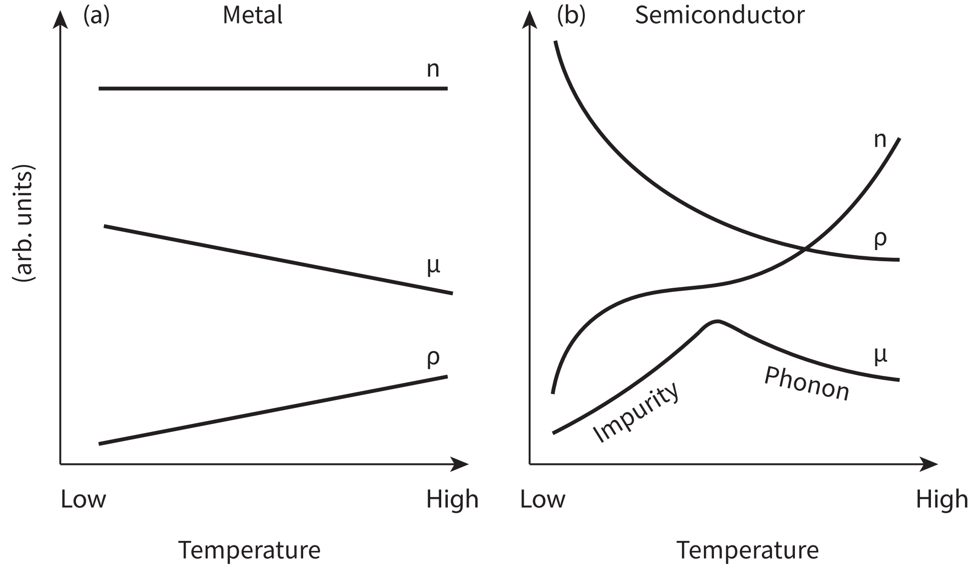

Figure 2.5: (a): Temperature dependence for the mobility, carrier density and resistivity for a typical metal. (b) Temperature dependence for properties in a typical semiconductor with impurity and phonon scattering contributions highlighted.

2.5 Further Optical Properties

By increasing the carrier density, the conductivity of a TCO will increase. However, a maximum carrier concentration exists at which a TCO will cease to be transparent, governed by the materials plasma frequency ω_p. The plasma frequency is a property of any metal under the influence of an electromagnetic field. The system can be considered as a liquid of charged particles (plasma) oscillating at a specific frequency with respect to a background of fixed ions. The dielectric constant or relative permittivity of the metal ϵ_r, is given by

$$\epsilon_r = 1 - \frac{ne^2}{\epsilon_0 m^* \omega^2} \tag{2.27}$$

Where ϵ_0 is the permittivity of free space, and ω is the frequency of the oscillating field. The plasma frequency ω_p is defined by

$$\omega_p^2 = \frac{ne^2}{\epsilon_0 m^*} \tag{2.28}$$

The refractive index of a material is proportional to the square root of the relative

permittivity and permeability. The permeability approaches unity in non-magnetic systems. The refractive index can be written as

$$\epsilon_r^{\frac{1}{2}} = \sqrt{1 - \frac{\omega_p^2}{\omega^2}} \tag{2.29}$$

If $\omega < \omega_p$ the refractive index becomes imaginary and the electric field cannot propagate through the material, i.e. is reflective. However, if $\omega > \omega_p$ the refractive index is real, the electric field can propagate through and the material becomes transparent. The high electron density in metals causes the plasma frequency to lie in the ultraviolet range, meaning that all visible light becomes reflective. This is not ideal for a TCO. The plasma frequency and carrier concentrations for some common TCOs are shown below in table 2.1. Conventionally, the plasma frequency is referred to in units cm^{-1} however, the values have been converted to energy to keep consistent with the units of the band gap.

Table 2.1: Carrier density and plasma frequency for several TCO compounds, La:$BaSnO_3$ (LBSO) [92], Sn:In_2O_3 (ITO) [93] and Al:ZnO (AZO) [94]

TCO	**n** ($x10^{20}cm^{-3}$)	ω_p (eV)	ω_p (cm^{-1})
LBSO	0.89	0.589	4750
ITO	9.30	1.862	15023
ITO	6.70	1.579	12734
ITO	3.30	1.106	8920
AZO	1.09	0.652	4529
AZO	1.98	0.797	6432

The plasma frequency in the highly doped ITO films is approaching the red portion of the visible spectrum ($\sim$ 1.8 eV) and is therefore at the upper limit for TCO carrier concentration.

2.6 Determination of the Optical Band Gap

Similar to that seen previously, Figure 2.6 displays a structure but with additional labels relevant to the discussion in this section. The optical band gap E_{opt} for the

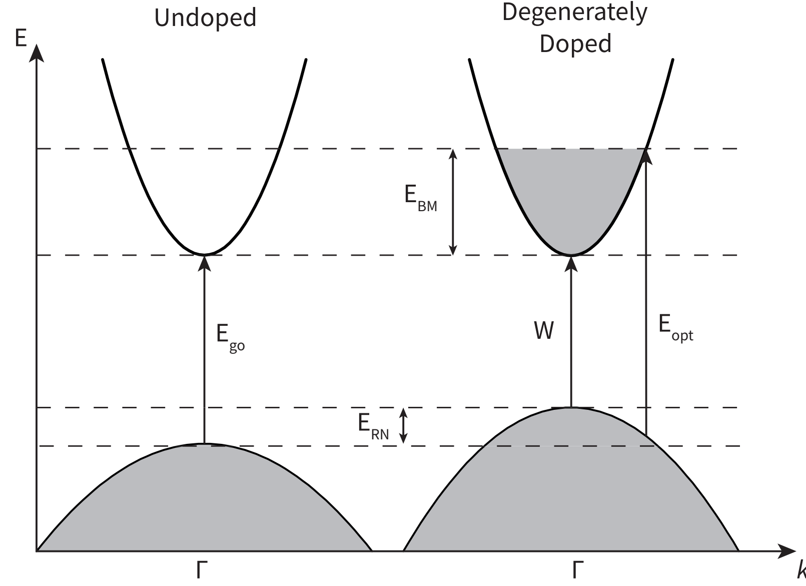

Figure 2.6: Band structure displaying the optical band gap E_{go} in an undoped sample and a degenerately doped sample with shading implying occupied states. Labels are discussed in the text. The energy scale is arbitrary.

materials can be obtained by first applying the Beer–Lambert law [95] to transmission data (T) to obtain the absorption coefficient α

$$T(\lambda) = e^{-\alpha d} \tag{2.30}$$

Where T is the transmission at a particular wavelength λ and d is the thickness of the material. The band gap of the material is determined by analysing the absorption coefficient as a function of the photon energy. It is commonly estimated using the Tauc method [96] given by

$$\alpha = \frac{A}{h\nu}(h\nu - E_g)^r \tag{2.31}$$

Where A is a scaling factor, $h\nu$ the photon energy and the exponent r is dependent on the nature of the transition [97].

- r = 1/2 for direct allowed transitions
- r = 3/2 for direct forbidden transitions
- r = 2 for indirect allowed transitions

- r = 3 for indirect forbidden transitions

A linear extrapolation of the $(\alpha h\nu)^{1/r}$ vs $h\nu$ at the onset of absorption to the intercept of the low energy background of the spectrum provides a value for E_g. This method is deemed adequate for a material with a Fermi level lower in energy than the conduction band as would be the case for an undoped sample.

However, this method is not applicable to degenerate semiconductors and is discussed in full by Dolgonos *et al* [98] following on from work undertaken by Hamberg *et al* [57]. It relies on the understanding that the transition rate R for optical absorption of a photon by an electron from an initial state $|i\rangle$ to final state $|f\rangle$ is governed by

$$R = \frac{2}{\hbar^2} \sum_{i,f} |\langle i| V |f\rangle|^2 \frac{\tau^{-1}}{(\omega - \omega_{if})^2 + \tau^{-2}} (P_i - P_f) \tag{2.32}$$

where P is the probability the inital and final states are occupied, $\omega_{if} = (E_i - E_f)/\hbar$ stating Heisenberg's uncertainty principle and τ is an time broadening constant and E_i and E_f are the energies of initial and final state respectively. If the transition is assumed to take place between a parabolic valence band and conduction band the transition rate can be expressed as [98]

$$R \propto \int_{x_o}^{\infty} (x + h\nu - W)^{1/2} \frac{\Gamma}{x^2 + \Gamma^2} (1 - P_c) dx \tag{2.33}$$

Where $x = \frac{\hbar^2 k^2}{2m_{vc}^*} + W - h\nu$, $x_o = \Delta E_g^{BM} + W - h\nu$, $\Gamma = \hbar/\tau$, P_c is the probability the conduction band states are occupied governed by the Fermi – Dirac equation and m_{vc}^* is the reduced effective mass. In the limit that the conduction band states are not occupied and $R \propto \alpha$ [57] it has been showed by Dolgonos *et al* [98]

$$\alpha^2 \propto (h\nu - W) \tag{2.34}$$

This is the classic Tauc equation where $W = E_g$, provides the optical band gap as displayed in Figure 2.6. In a scenario in which the conduction band is occupied, i.e. a degenerate semiconductor, these assumptions do not hold correct. Hamberg [57] showed equation 2.33, under the assumption that the Lorentzian is sharply peaked (Γ is small), can be expressed as

$$R \propto (\Delta E_g^{BM})^{1/2} \left[1 - \frac{2}{\pi} \tan^{-1} \left(\frac{W + \Delta E_g^{BM} - h\nu}{\Gamma} \right) \right] \tag{2.35}$$

Expanding α to first order terms yields the result [70]

$$\alpha \propto 1 - \frac{2}{\pi\Gamma}(E_g - h\nu) \tag{2.36}$$

giving the result of linear extrapolation of α to the abscissa intercept to be $E_g - \frac{\pi\Gamma}{2}$. Similarly, a series expansion on α^2 gives

$$\alpha^2 \propto 1 - \frac{4}{\pi\Gamma}(E_g - h\nu) \tag{2.37}$$

with a linear extrapolation of α^2 to $\hbar\nu$ to be $E_g - \frac{\pi\Gamma}{4}$. Combining these results provides a corrected optical band gap E_g for a degenerate semiconductor, highlighted by Figure 2.7. This method is not an exact determination of the actual optical band gap in the material due to the assumptions made in the derivation however, is an improvement on the Tauc method.

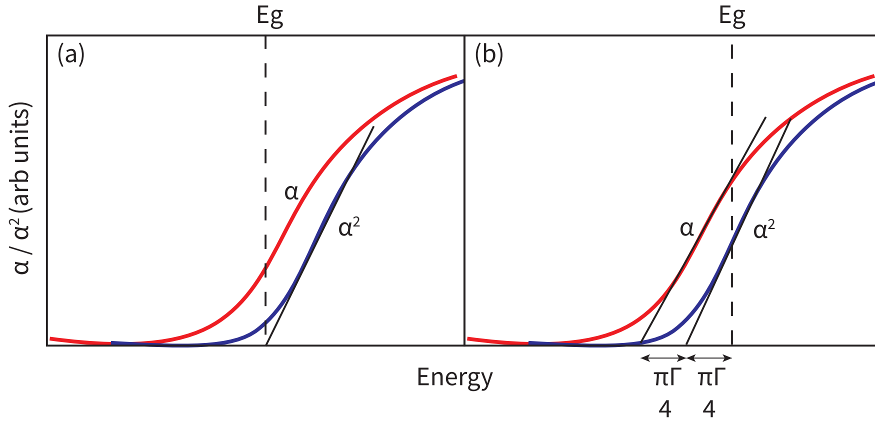

Figure 2.7: (a) Traditional Tauc plot extrapolation method for determining band gap in undoped material. (b) Visual representation of the Dolgonos method employed for this thesis in the degenerately doped samples. Figure adapted from Dolgonos *et al* [98]

2.7 Figure of Merit

There are two fundamental properties that can be used to judge a TCO's performance: the electrical resistivity and optical absorption. For comparison between

TCO compounds, figure of merits (FOM) are used that take into account these properties. There have several different formulations of what FOM to use [99–101] that has been reviewed comprehensively by Knickerbocker *et al* [102]. Almost all applications and studies on TCOs are carried out on thin-film specimens, therefore, if comparisons are to be made between single crystal and thin-film materials, a FOM must be used that is independent of thickness.

$$\text{FOM} = \frac{1}{\rho \times \alpha(550\text{nm})} \tag{2.38}$$

The absorption coefficient is a function dependent on wavelength, so 550nm, the wavelength that eyes are most sensitive to, is chosen by convention. Table 2.2 highlights a few example conventionally doped n-type TCO's from literature with an associated FOM.

Table 2.2: Resistivity, absorption coefficient and FOM for thin-film TCO's taken from literature.

TCO	ρ(300 K) (mΩ.cm)	α(550 nm) (cm^{-1})	FOM (Ω^{-1})
ITO [103]	0.253	4825	0.829
ITO [10]	0.458	4991	0.437
ITO [10]	0.219	4332	1.054
F:SnO_2 [104]	6.170	4326	0.039
Sn:$GaInO_3$[105]	3.500	560	0.519
Al:ZnO [106]	0.049	6927	2.887

Despite possessing the highest absorption coefficient, Al:ZnO (AZO) has the largest FOM due to its low resistivity property which heavily biases the result. The absorption coefficient in this material is high and therefore less transparent compared to films with a similar thickness. If TCOs are to be compared for a specific purpose, different factors in the FoM might be weighted; however, for this study, the above FoM definition will suffice.

2.8 Electronic Band Structure of ZSO

The electronic band structure of ZSO has previously been calculated by Matushima *et al* [34] and Mizoguchi *et al* [107] using conventional density functional theory

(DFT) techniques. Dr. Adam Jackson, working in the Scanlon Materials Theory Group, collaborating on this project has recently carried out electronic band structure calculations on ZSO using a hybrid quasi-particle self consistent GW (QSGW) method. Displayed in Figure 2.8 are the elemental projected band structure with the corresponding density of states calculations.

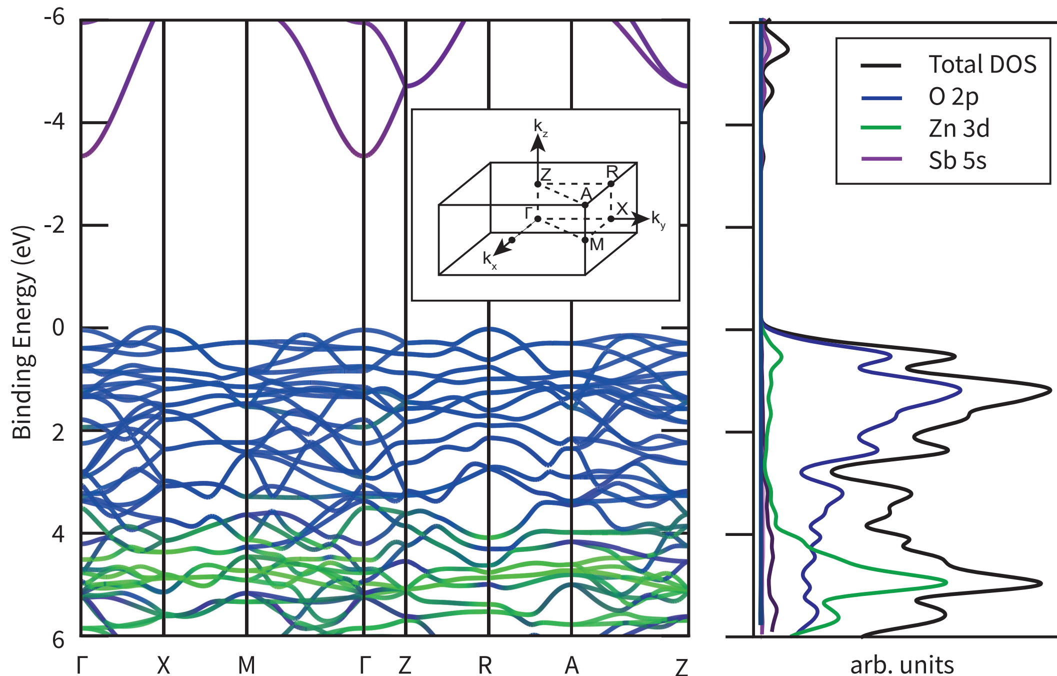

Figure 2.8: Calculated electronic band structure and corresponding density of states for ZSO. Orbital characteristics are highlighted by relevant the colours and Brillouin zone for the tetragonal structure is displayed in the inset. Both band structure and DOS were calculated by Dr. Adam Jackson using a hybrid QSGW method.

The upper valence band is primarily consisting of highly localised O 2p orbitals, common in the wide band gap oxides [108, 109]. The O 2p orbitals hybridise with the fully occupied Zn 3d orbitals $\sim$ 6 eV below the valence band maximum. The lower conduction band, centred at Γ, is formed due to the anti-bonding overlap of Sb 5s and O 2p orbitals. It is important to note that these orbitals are not the only contributors to the density of states at the valence band. This will be explored when the orbitals are weighted for photoionisation cross sections in chapter 7.

The effective mass of the conduction band is calculated to be 0.22 m_e in the Γ - Z direction and 0.27 m_e in the $\Gamma - X$ direction indicating a three-dimensional character to the electronic structure. Both DFT calculations predicted a band gap for ZSO

to range from 0.9 to 1.8 eV, however DFT calculations are known to underestimate calculated band gaps [110]. The QSGW method has provided a band gap ~ 3.3 eV, comparable with the optical band gaps in literature. These literature values are further discussed in section 5.2.2.

Additionally, by conducting defect calculations, it was predicted that substitutional doping of Ga^{+3} onto the Zn^{+2} site should provide enough free electrons to create n-type conductivity without detrimental effects to the wide band gap. Therefore, creating a transparent conducting oxide. This prediction provides the basis of this project.

Chapter 3

Experimental Methods

This chapter reviews the experimental techniques used to measure and characterise the many properties of grown single crystal ZGSO. Methods used to measure the electrical transport and optical properties are covered in section 3.1, with characterisation and photoemission methods discussed in sections 3.2 and 3.3, respectively.

3.1 Measurements

3.1.1 Resistivity and Hall effect

The Hall effect, discovered in 1879 [111], describes how electrons behave in a material under both electric and magnetic fields. If a current I_x flows through a material in the x-direction and a magnetic field is applied in the z-direction, a force and therefore electric field E_H is created in the y-direction because of the Lorentz force, highlighted by Figure 3.1. The equation of motion for the momentum of an electron undergoing collisions is displayed in equation 3.1.

$$\frac{d\mathbf{p}}{dt} = \mathbf{F} - \frac{\mathbf{p}(t)}{\tau} \tag{3.1}$$

Where $\mathbf{p}$ is the momentum, $\mathbf{F}$ is the force, and $1/\tau$ is the scattering rate. By introducing the Lorentz force as $\mathbf{F} = -e[\mathbf{E} + (\mathbf{v} \times \mathbf{B})]$

$$m\frac{d\mathbf{v}}{dt} = -e[\mathbf{E} + (\mathbf{v} \times \mathbf{B})] - m\frac{\mathbf{v}}{\tau} \tag{3.2}$$

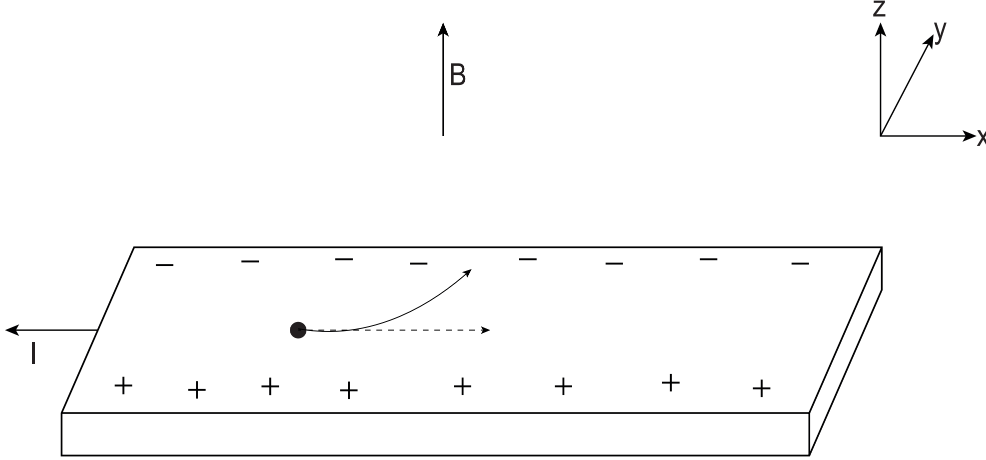

Figure 3.1: Schematic of the Hall effect through a bar shaped crystal. The black circle indicates the electron and its trajectory.

Where **E** is the electric field, **v** is the velocity and **B** is the magnetic field. When the current is constant, the solutions to equation 3.2 are

$$\begin{aligned} 0 &= -eE_x - eB_z v_y - m\frac{v_x}{\tau} \\ 0 &= -eE_y + eB_z v_x - m\frac{v_y}{\tau} \end{aligned} \tag{3.3}$$

By multiplying by $-ne/\tau$ and using the current density $j = -nev$ and the cyclotron angular frequency $\omega_c = \frac{eB}{m}$ it can be shown that in a steady-state, where no current is flowing perpendicular to the direction of applied current, the Hall electric field is

$$E_y = E_H = -\frac{\omega_c \tau j_x}{\sigma} = -\frac{1}{ne} j_x B_z \tag{3.4}$$

where $R_H = -\frac{1}{ne}$ is the Hall coefficient. In terms of measurable properties, R_H can be written as.

$$R_H = \frac{V_H t}{I_x B_z} \tag{3.5}$$

With knowledge of the applied current I, thickness t, and magnetic field B, the Hall coefficient is determined by measuring the potential difference V_H in the y-direction. The resistivity ρ_x of the material is measured by applying this same excitation current and measuring the voltage drop between the two contacts separated

by L shown in Figure 3.2. By using equation 2.23 the resistivity ρ_x is determined using

$$\rho_x = \frac{V_x A}{I_x L} \tag{3.6}$$

With A being the cross-sectional area. The measured values for the Hall coefficient and resistivity are used in equation 3.7 to give the Hall mobility μ_H.

$$\mu_H = \frac{R_H}{\rho_x} \tag{3.7}$$

Resistivity and Hall effect measurements were carried out using two Quantum Design PPMS-9 systems; one located at ISIS Neutron and Muon Source at Harwell and the other at the London Centre for Nanotechnology. For measurements, crystals were polished into a bar-like cuboid geometry, described in section 4.2. Figure 3.2 shows a schematic for the transport measurements.

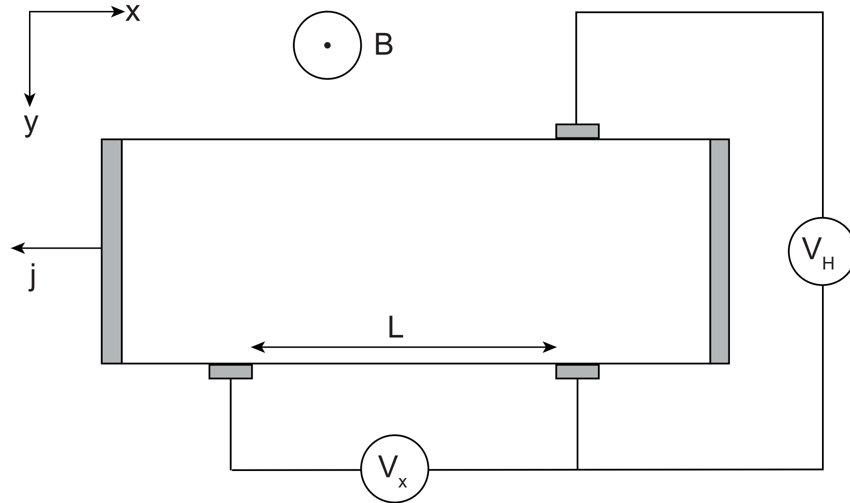

Figure 3.2: Schematic of the experimental geometry used in resistivity and Hall effect measurements. Silver shading indicates silver electronic contacts. Labels have been discussed in the text.

Resistivity measurements were carried out using the four - terminal method. Silver current contacts were annealed at 600 °C onto each end of the crystal and two

voltage contacts were annealed on the side separated by distance L. This method was employed to minimise the contact resistance between the silver contacts and the sample surface. By measuring the potential difference between the two voltage contacts, the voltmeter draws away very little current due to its high impedance and the resistance, therefore resistivity (equation 3.6) of the material is accurately determined. A fifth contact was attached opposite the current contacts to measure the transverse voltage V_H.

Samples were measured using an AC drive mode; this provided an AC square-wave excitation of 8.33 Hz synchronised to the 50 Hz power source to reject noise. The PPMS applied a DC current through the sample, records the voltage drop then reverses the polarity and measures again. An accurate resistance was determined using Ohm's law by averaging the magnitude of the positive and negative voltage drops. This method has an advantage over the DC mode, whereby it can remove offset voltages. Temperature-dependent data was collected between 50 - 350 K at 20 K steps. For Hall effect measurements, the magnetic field was varied $\pm$ 1 T at 0.25 T steps at every temperature interval, and the transverse Hall voltage was measured. Equation 3.5 states the Hall coefficient is obtained by measuring the Hall voltage at a particular magnetic field. In theory, at zero magnetic field, V_H should be equal to zero. Experimentally, this is not the case as there is a small V_x component originating from Hall contacts not being exactly orthogonal with B and I. Therefore, by measuring the magnetic field from -B to +B the Hall coefficient could be obtained neglecting this offset. A negative slope of the Hall coefficient indicated electrons were the dominant carrier type.

3.1.2 UV-Vis Spectroscopy

Ultraviolet-Visible Spectroscopy (UV - Vis) experiments were carried out using a Shimadzu Solid UV-VisIR 3700 spectrophotometer in the Department of Physics at the University of Liverpool. This setup comprises a light source, monochromator and detector. The sources were halogen and deuterium lamps that generate a white light into the monochromator. To choose a specific wavelength prisms and diffraction gratings were utilised. Initially, a baseline spectrum was measured without a sample in place and was set to 100 % transmission. The sample holder position had to be

carefully optimised to maximise the transmission signal due to the small size of the aperture to accommodate small crystals. A spectrum followed this with the sample placed in the path of the beam. The crystals were mounted in a bespoke 3D-printed holder (see Figure 3.3) to avoid any light being transmitted without passing through the sample. The ratio of the baseline spectrum and the spectrum for the crystal gives the sample's transmission spectrum at a percentage.

Figure 3.3: 3D printed sample holder for UV-Vis spectroscopy with crystal displayed at the centre.

3.2 Characterisation

Crystal characterisation is split into two sections: chemical composition of the samples was determined using energy dispersive x-ray spectroscopy (EDS) with the crystal structure for both powder, crystal, and orientation measured using various x-ray diffraction techniques. The theory of the method, as well as experimental arrangements, is discussed in this section.

3.2.1 Energy Dispersive X-ray Spectroscopy

Energy dispersive x-ray spectroscopy (EDS) is an experimental tool used for elemental analysis. The principle behind it relies on a two-step process; firstly, a high energy electron beam strikes the material. This beam imparts its energy onto the sample and excites core level electrons to either higher orbits or out of the sam-

ple leaving behind a positively charged hole. The second step is an electron from a higher orbital releases energy to fill this hole in the form of an x-ray. Figure 3.4 highlights this process. Moseleys law states that the energy E of the radiation emitted is proportional to the square of the atomic number

$$E = C_1.(Z - C_2)^2 \tag{3.8}$$

where C_1 and C_2 are constants that describe the orbital character. By detection of the x-rays, chemical information can be ascertained.

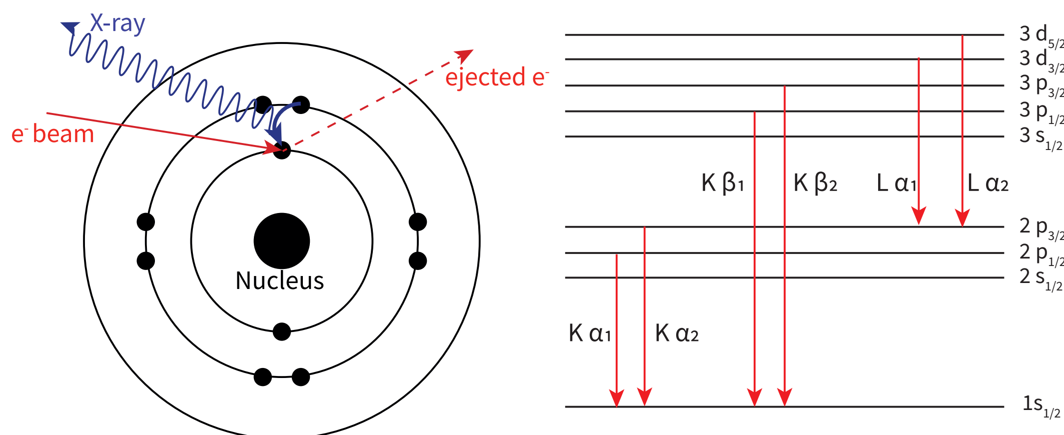

Figure 3.4: Principle of EDS spectroscopy. Transitions of electrons from higher orbitals into lower empty states produce x-rays. The labelling of the x-rays is highlighted on the right side with a few important transitions.

This project uses a Jeol JSM-66610LV scanning electron microscope (SEM) arrangement in the Research Complex at Harwell (RCaH), Oxfordshire. Thermionic heating of a tungsten filament creates electrons that electrostatic fields accelerate to high energies (20 kV). Condenser lenses narrow this electron beam to a spot size ~ 1 nm. Finally, deflecting coils allow x-y scanning of the beam on the sample. Emitted x-rays are detected using silicon drift detectors (SDD) built by Oxford Instruments, which count the radiation's intensity and energy. Energy resolutions achievable in EDS are ~130 eV [112]. Figure 3.5 displays a typical spectrum for ZGSO. The background of the spectrum originates from Bremsstrahlung radiation; the scattering of electrons by the electric field close to the nucleus emits x-rays. By convention, peaks are labelled in Siegbahn notation [113] described on the right-hand side of Figure

1.4. Obtained data was analysed using the Aztec software (Oxford instruments), which takes the relative peak intensity and applies x-ray absorption and matrix element corrections to obtain relative quantitative values for composition [114]. A concise discussion of the analysis technique is carried out in chapter 6.

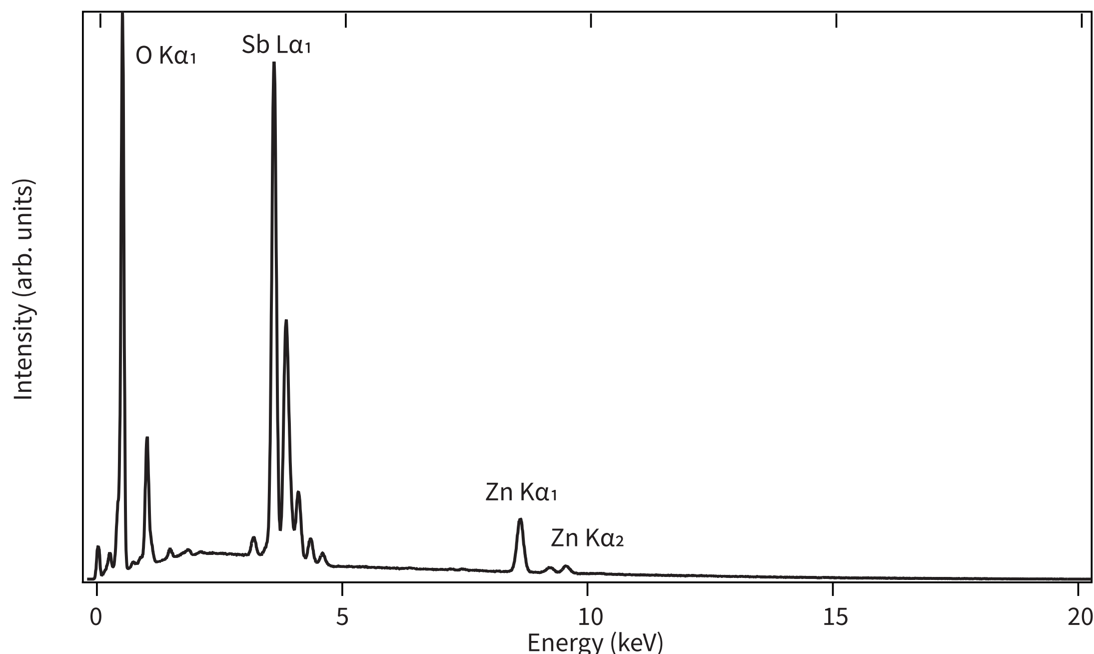

Figure 3.5: Example EDX spectrum for ZGSO with relevant highlighted spectroscopic peaks. The Bremsstrahlung radiation background has not been subtracted.

3.2.2 X-ray Diffraction

Max von Laue discovered that x-rays could be diffracted by periodic crystal lattices earning him the Nobel Prize in Physics in 1914 [115]. This thesis will utilise two different applications of this. Firstly, by using x-rays with a known wavelength, a materials crystal structure is determined. This technique is employed by powder x-ray diffraction. Secondly, using a white x-ray source (broad range of wavelengths), the crystallographic orientation of crystals can be determined using the Laue technique. This section covers the theory and experimental arrangements for the x-ray diffraction techniques used in this project.

X-ray diffraction is a technique utilising Bragg's law [116]

$$2d_{(hkl)}\sin(\theta) = n\lambda \tag{3.9}$$

Where d_{hkl} is the separation between lattice planes and n is a multiple of the wavelength λ and θ is the angle between beam and plane. If a monochromatic, collimated x-ray beam strikes a surface and diffracts, the beam will constructively interfere, providing the path length difference between the waves is $d\ \sin(\theta)$. Figure 3.6 highlights this process.

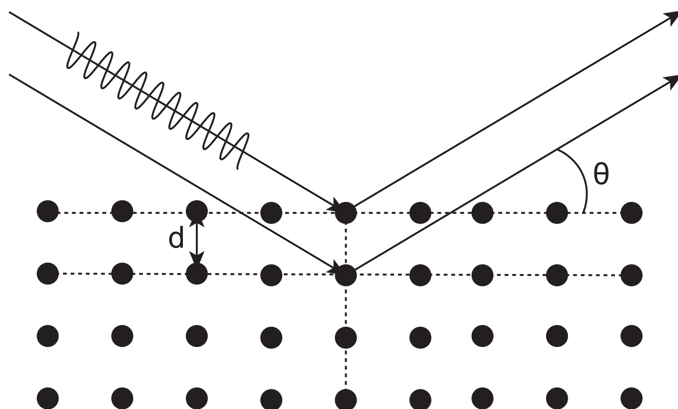

Figure 3.6: Bragg diffraction of a periodic crystal lattice with a plane separation highlighted by d.

The production of x-rays occurs following a similar method to EDS. By firing electrons at a target, emitted Kα and Kβ x-rays are collimated and directed towards the sample. The crystal structure will then either reflect, transmit or diffract the x-rays. A charge-coupled device (CCD) detects constructive interference patterns from diffracted x-rays at known angles, therefore, deducing the d parameter.

Powder X-ray Diffraction

In powder x-ray diffraction (PXD) it is assumed that a powder is made up of lots of microscopic crystallites ($\sim 1\ \mu$m) all randomly orientated. A monochromatic x-ray beam strikes the powder target; all planes orientated at the correct angle to satisfy the Bragg conditions will diffract the beam. The diffracted beam is in the shape of a cone known as a Debye - Scherrer cone, as seen in Figure 3.7. The cone occurs because crystallites are angled to satisfy the Bragg diffraction, however, rotated from each other by 2π with respect to the axis of the beam. The experimental

schematic in Figure 3.7b is known as the Bragg - Bentano arrangement. The sample is fixed in place at the centre of the apparatus. The source and detector rotate around this centre point to increase θ and therefore 2θ. By increasing the angle, different orientations will satisfy the Bragg conditions, and the detector will pick up the intensity as a function of 2θ. Each crystal structure has a unique diffraction pattern, and therefore, the powder's phase/structure can be determined.

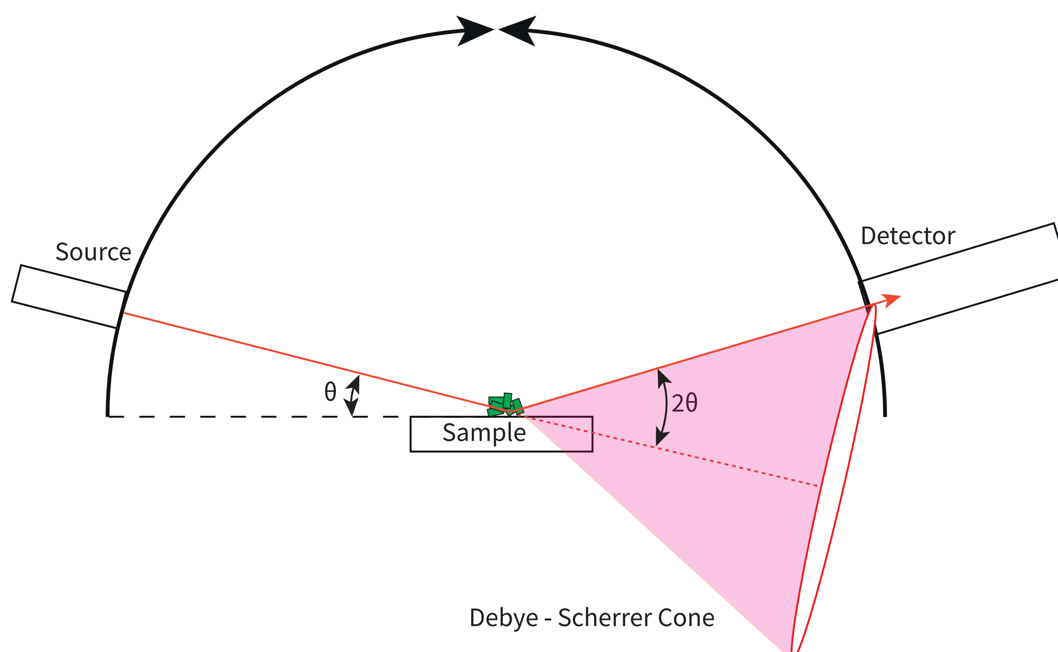

Figure 3.7: Schematic of the PXD experiment in Bragg-Bentano arrangement. A Debye–Scherrer cone is highlighted.

A Rigaku Miniflex diffractometer was used to determine the phase of powders. This employs a Cu Kα x-ray source (λ = 1.541 Å) with 2θ chosen to be from 10 - 80°. This diffractometer is based in the materials characterisation lab in ISIS Neutron and Muon source. Phase identification was carried out using the inbuilt PXRD software which has access to the Crystallographic Open Database (COD). Accurate refinement of powders to determine the percentage of phase and lattice parameters was not possible with this miniflex experimental set up as the zero-point angle is not accurately calibrated. However, for phase identification, the system is adequate.

Where accurate structural data is required, PXD measurements were conducted

using a Rigaku SmartLab diffractometer, located at ISIS. The Smartlab provided more accurate angular data at the cost of data acquisition speed. This arrangement uses a rotating anode Cu Kα source, which provides a higher intensity of x-rays because electron heating effects are minimised.

In theory, lattice parameters could be obtained by looking at a chosen peak and using the Bragg diffraction equation to solve for d. However, the data was processed using Rietveld refinement [117] employed by the GSAS-II software [118]. By applying a non-linear least-squares method, the technique fits a previously documented structure to the obtained data. From the fit, structural properties such as unit cell parameters and lattice occupancy are determined.

Laue Diffraction

Laue diffraction is a technique most commonly used when the crystallographic orientation of a single crystal is required. Similarly, it is a useful technique to determine twinning in a crystal. An x-ray beam with a broad range of wavelengths strikes a sample. Certain wavelengths will obey the Bragg conditions at different planes without the requirement for sample rotation. In back-reflection geometry, a CCD is placed between the x-ray source and sample to detect the diffracted beam. Similarly, the CCD could behind the sample in transmission geometry. The result is a diffraction pattern with a large number of spots corresponding to plane reflections. This method is also able to determine the rotation symmetry of chosen orientation. For example, if the beam propagation is perpendicular to the $ZnSb_2O_6$ (001) face, the resultant Laue pattern will also have a four-fold symmetry.

This thesis uses a Photonic Science Crystal Orientation system based in ISIS, which creates a beam spot on the sample of $\sim 200 \times 200\ \mu m^2$, and the high-resolution Photonic Science x-ray Laue back scattered camera allows an orientation accuracy $\sim 0.1\ ^{\circ}$. The orientations were determined by simulating the expected diffraction pattern using QLaue software and comparing to experimental data.

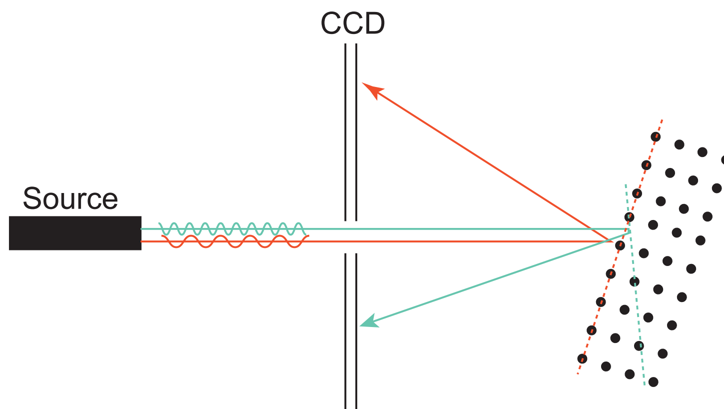

Figure 3.8: Schematic of the backscattering Laue process. Different wavelength photons will constructively interfere at different angles. The CCD detects the diffracted x-rays.

3.3 Photoemission Spectroscopy

Photoemission spectroscopy (PES) relies on the photoelectric effect principle, first discovered by Hertz in 1887 [119] when a change in voltage was observed when shining ultraviolet light across two metal electrodes. The photoelectric effect was later explained by Einstein, earning him the Nobel Prize in Physics in 1921 whereby he formulated that photons contained quantized amounts of energy, dependent on its frequency [120]. Upon measuring NaCl, Kai Siegbahn discovered the full potential of PES to characterise the chemical composition of materials [121].

The photoelectric effect states that a photon striking a material with energy ($h\nu$) can excite an electron out of the material, providing $h\nu$ is greater than the work function of the material ϕ. This electron is ejected with a kinetic energy E_{kin} highlighted by the energy conservation equation 3.10.

$$E_{kin} = h\nu - \phi - |E_B| \tag{3.10}$$

With E_B is the binding energy of the electron in the solid. The ejected electrons are emitted at all angles. By positioning an electron analyser, the kinetic energy is measured. The kinetic energies are converted into binding energy using equation 3.10. Binding energies are calibrated by measuring the Fermi level of polycrystalline gold in electrical contact with the sample. In XPS experiments, a

standard calibration method involves measuring the binding energy of adventitious carbon and setting C 1s to 284.8 eV [122], common in samples where charging may occur. When electrons are photoemitted, the surface becomes positively charged, conducting samples can gather electrons from the substrate. In contrast, insulating materials are unable to do this, and usually, an electron flood gun is required to provide a source of electrons. The corrected binding energies are a fingerprint to the sample's chemical makeup as each electron orbital has its own discrete binding energy values.

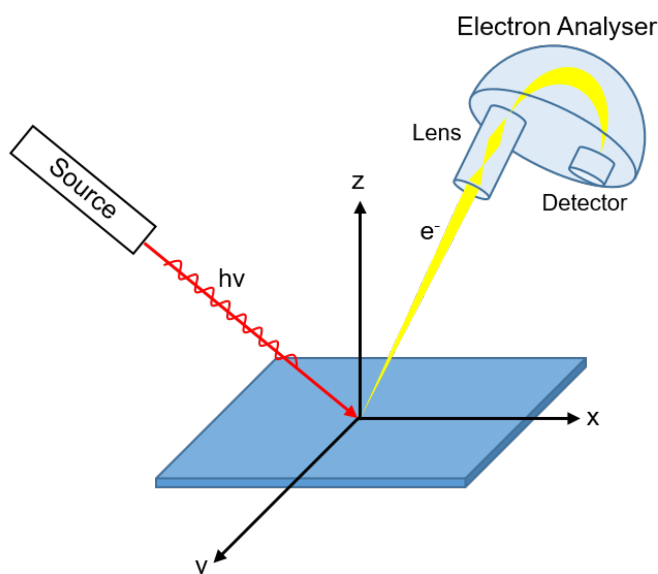

Figure 3.9: Basic schematic of a PES experiment. Photons with energy = hν impinge on a sample photoemitting electrons with kinetic energy E_{kin} and detected using analyser and detector system

Figure 3.9 is a highly simplified depiction of a PE experiment. Generally, the experiments most considerable variation originates in changing photon energy $h\nu$ or source.

- $h\nu$ < 1000 eV - Ultraviolet photoelectron spectroscopy (UPS) and vacuum - ultraviolet angle-resolved photoemission spectroscopy (VUV-ARPES). UPS is beneficial for measuring valence band states due to high resolutions $\sim$ 10 meV . For ARPES, low photon energies imply a better momentum resolutions however, this is discussed in section 3.3.4.

- $h\nu \sim$ 1000 - 2000 eV - Typical XPS photon energies, better suited to analysing

low energy core levels of the surface layers of materials.

- $h\nu > 2000$ eV - Hard x-ray photoemission spectroscopy (HAXPES). Similar to to XPS but the increased energy allows a greater probing depth.

This greater probing depth of HAXPES originates because of the increased photoelectron inelastic mean free path (IMFP) λ of the material. The IMFP is a measure of how far an electron can travel before being scattered in the material and is dependent on the electron's kinetic energy. Figure 3.10 shows the IMFP plotted as a function of kinetic energy of example metals with the theoretical curve shown in equation 3.11 [123].

$$\lambda = \frac{143}{E^2} + 0.054\sqrt{E} \tag{3.11}$$

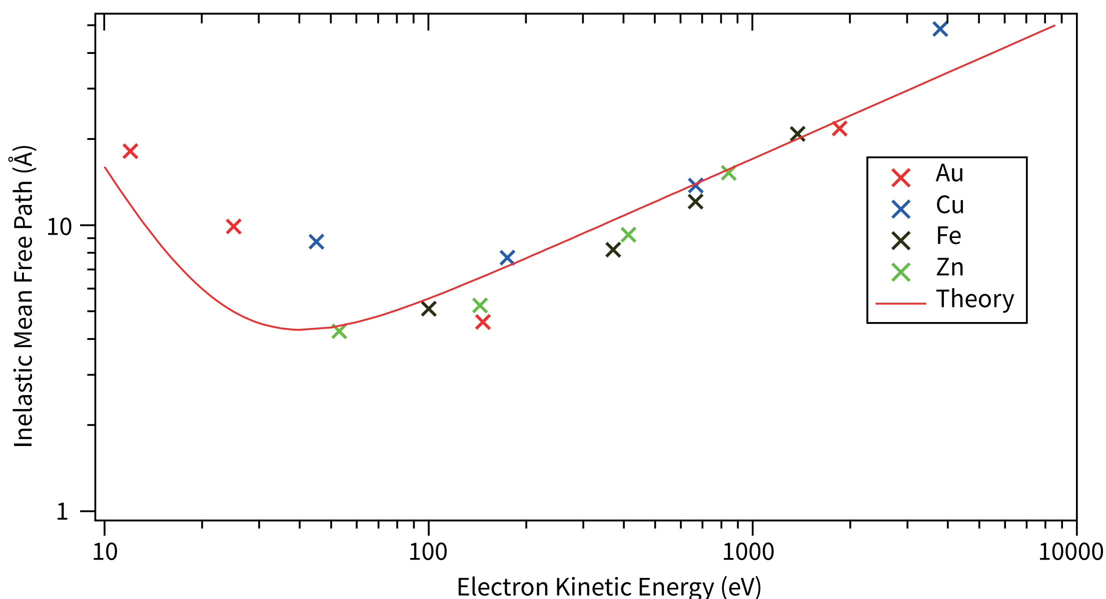

Figure 3.10: Inelastic mean free path versus electron kinetic energy for four elemental metals with theory line taken from Seah *et al* [123]. The IMFP data is taken from Powell and Jablonski [124].

At low energies, $h\nu \sim 100$ eV, electrons have a mean free path less than 10 Å implying experiments using low photon energies are extremely surface sensitive. Surface preparation in ARPES is essential and generally requires cleaving crystals

in vacuum. The increase probing depth for HAXPES experiments make them less susceptible to surface contamination.

Another difference in experiments is related to the photoionisation cross section σ of the atomic orbitals. This is a measure of how likely an electron in an orbital will interact with an incoming photon and is highly dependent on photon energy. Each electron orbital has a unique σ photon energy dependence and are widely tabulated by Yeh, Lindau, Scofield and Trzhaskovskaya [125–130]. Figure 3.11 displays three relevant σ values plotted as a function of photon energy.

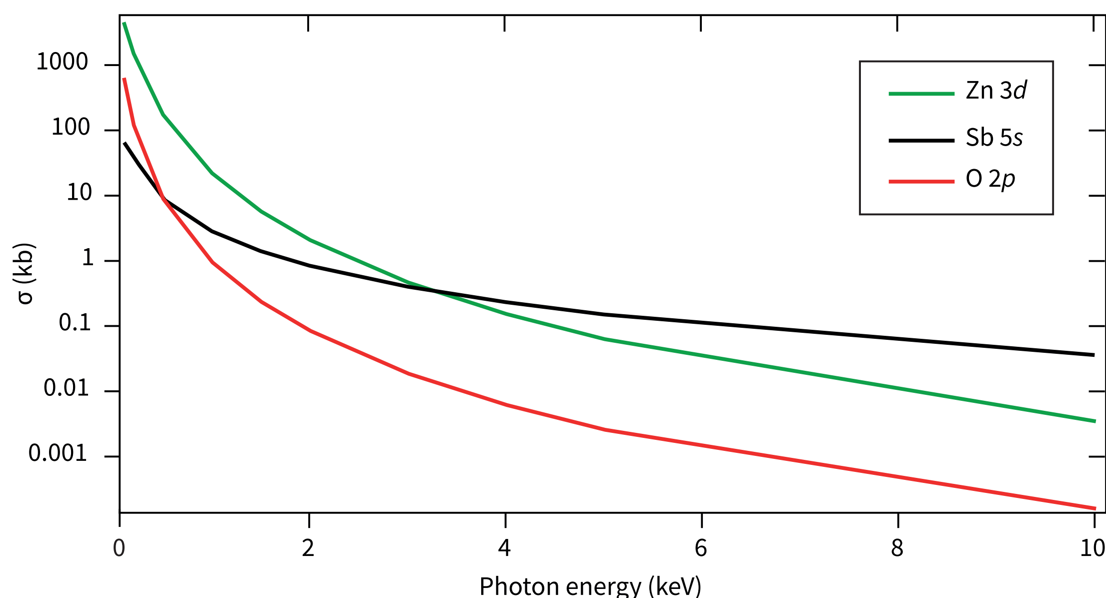

Figure 3.11: Example photoionisation cross sections for selected relevant orbitals as a function of photon energy ($h\nu$). Units are referred to in kilobarns (=10^{-21} cm^2)

There is an additional angular dependence of the photoionisation cross section, particularly relevant at high energy sources [125–128, 131, 132] however it is not explored for this project.

Finally, the kinetic energy and intensities of emitted electrons are affected by spin-orbit coupling where electrons with different spin have different binding energies. This appears as a peak doublet in the XPS spectrum, with each peak representing a j value where $j = l \pm s$ where j, l and s are total, orbital and spin quantum numbers respectively. Furthermore, the intensity of each peak is governed by

$$\text{relative intensity} = 2j + 1 \tag{3.12}$$

The magnitude of energy splitting between the two peaks increases as the atomic number does however, nuclear shielding for outer orbitals causes the splitting to decrease.

3.3.1 Electron Analyser

There are several types of electron detection systems however, all experiments used in this thesis use a hemispherical analyser. It contains three primary components highlighted in Figure 3.12. The electrostatic lens focuses and decelerates the electrons onto the hemispherical analyser entrance slit. By scanning the lens potential and choosing how much to decelerate electrons, the kinetic energy of the electrons is selected. The hemispherical analyser consists of two concentric hemispheres of radius R_1 and R_2 with potentials V_1 and V_2 applied respectively to create an electrostatic field in between. The potential difference is set in such a way as electrons will pass through the analysers central path, providing they have pass energy (E_{pass}). Electrons with energy ($E_{pass}\pm\ dE$) will also pass through to the detector with the lowest energy electrons being deflected most by the electrostatic field. This allows a narrow energy range snapshot without the need for adjusting the lens.

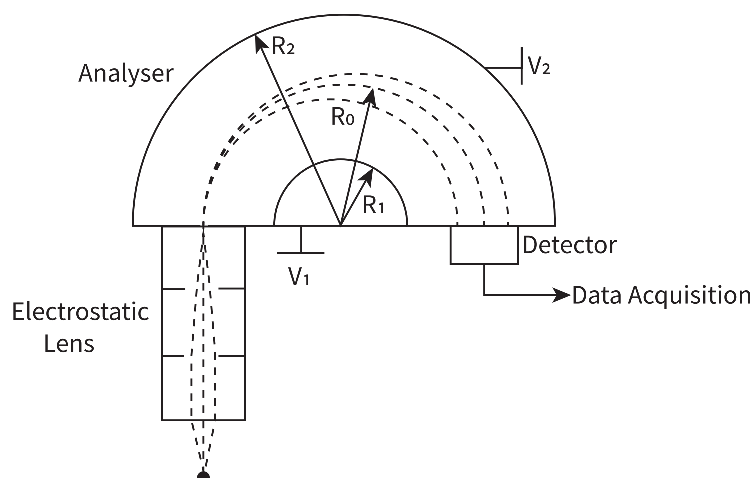

Figure 3.12: Schematic for a hemispherical electron analyser. The electrostatic lens focuses electrons onto the analyser where they are deflected by the electric field set by the potential difference between the two hemispheres. Electrons are detected at the detector.

$$R_o = \frac{R_1 + R_2}{2} \tag{3.13}$$

The energy resolution of the analyser ΔE_a is given by [133].

$$\Delta E_a = E_{pass}\left(\frac{w}{R_o} + \frac{\alpha^2}{4}\right) \tag{3.14}$$

where w is the width of the entrance slit and α is the acceptance angle. A lower pass energy corresponds to a better experimental energy resolution but at the cost of intensity. The total energy resolution ΔE_{tot} of an experiment is given by

$$\Delta E_{tot} = \sqrt{(\Delta E)^2 + (\Delta E_a)^2 + (\Delta E_{misc})^2} \tag{3.15}$$

ΔE is the photon beam spread and E_{misc} is the resolution contribution from other experimental effect [134].

Finally, the detector consists of a micro-channel plate (MCP), which amplifies the signal enough to react with a fluorescent phosphor screen with a charge-coupled device (CCD) camera used to record the signal.

3.3.2 Ultra-High Vacuum

The entire PE experiment, source to detection, occurs under a ultra-high vacuum (UHV) typically $< 10^{-9}$ mbar. This is required for several reasons: firstly, the electrons must travel from the sample surface to the detector without encountering scattering from residual gas molecules. Similarly, in certain materials, reactions with residual gases can decrease the sample lifetime if not kept under vacuum. Finally, the electron analyser must operate under vacuum due to the high voltage differences between the two hemispheres.

3.3.3 XPS and HAXPES

Lab based XPS

Lab-based XPS was carried out in the UCL Chemistry department using an XPS-Thermo K-alpha spectrometer equipped with a Al Kα x-ray source ($h\nu$ = 1486.6 eV). The x-ray beam spot diameter was set as 400 μm on the surface, and a dual-beam electron flood gun minimised charge compensation. Binding energies were

referenced to the adventitious C 1*s* peak (284.8 eV). The experimental resolution was determined to be 0.5 eV by fitting a room temperature Fermi function to the Fermi level of polycrystalline silver.

I09 Beamline at Diamond Light Source

Hard x-ray photoemission spectroscopy (HAXPES) measurements were conducted at the I09 beamline at Diamond Light Source, Oxfordshire. It is a third-generation synchrotron facility with the ability to accelerate and store electrons up to 3.0 GeV. Bending magnets or insertion devices, such as undulators, accelerate the electron beam creating electromagnetic radiation for practical use.

The I09 branch of the beamline allows the capability of measuring both soft (100 - 2100 eV) (XPS) and hard x-rays (2.1 - 20 keV) (HAXPES) by the use of two undulators and an optics system that directs both sources onto the sample. Figure 3.13 displays the optics arrangement for the I09 beamline.

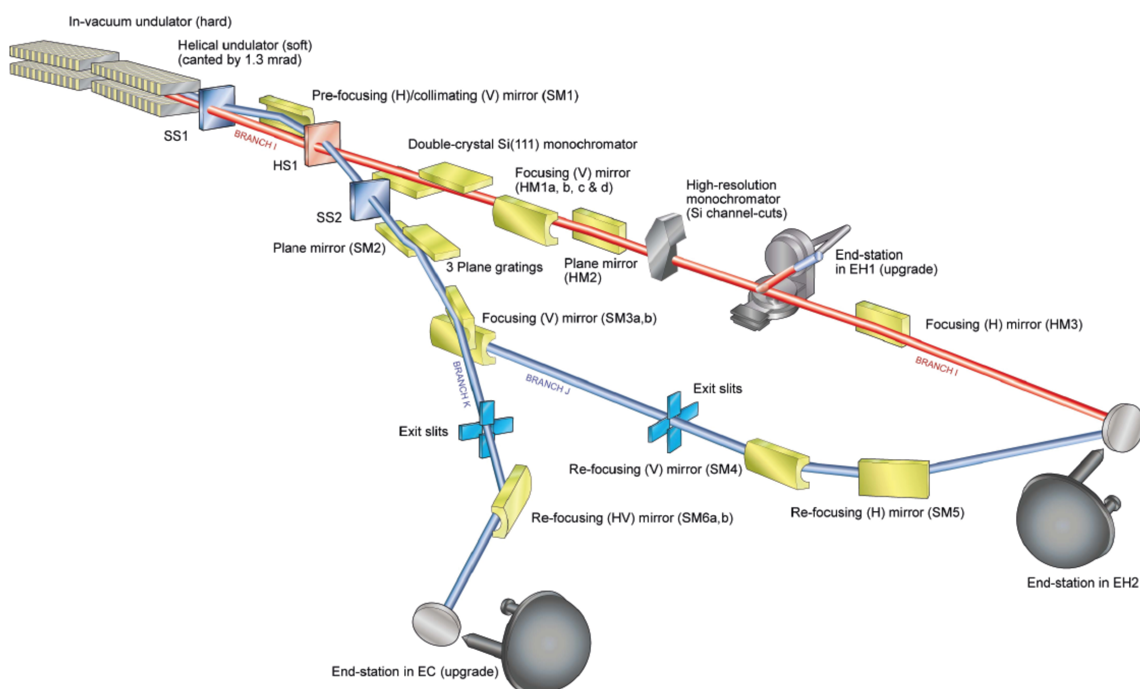

Figure 3.13: Schematic of the optics for the I09 beamline at the Diamond Light Source.

The hard x-ray branch features several focusing mirrors, a Si(111) double crystal monochromator and further high-resolution Si channel-cuts. The result is a highly focused and monochromated beam with beam spot 40 x 20 μm. The soft x-ray branch is not relevant for the project.

Turbomolecular and ion pumps on the end station maintain pressures below 10^{-9} mbar. A hemispherical electron analyser, VG Scienta EW4000, is placed at a 90° angle to the beam propagation and operated with a wide ± 30° analyser acceptance angle to improve electron capture rate.

Samples were irradiated at a semi-grazing geometry with 11° between the sample surface and the x-ray beam propagation. To obtain a binding energy reference, the Fermi edge of a polycrystalline gold sample in electrical contact with the system was measured. Additionally, by fitting a room temperature Fermi function to this edge, the experimental resolution was determined to be ∼ 340 meV.

All XPS and HAXPES data was analysed using the CASA-XPS software, with a Shirley background subtraction applied for all spectra.

3.3.4 ARPES

Theory

Angle-resolved photoemission spectroscopy is a technique able to probe the electronic band characteristics [133], a schematic is portrayed in Figure 3.14.

The theory relies on the same methodology as covered for PES. However, modern two-dimensional detectors can take a snapshot of kinetic energy versus angle along the direction of the entrance slit. By rotating the sample along 1 axis, it is possible to map the photoemission intensity in two angular dimensions. The kinetic energy and angle are converted into binding energy and momentum using equations 3.10 and 3.16. The electron momentum can be split into two components relative to the surface: the parallel component $\boldsymbol{k}_{\parallel}$ and the perpendicular component $\boldsymbol{k}_{\perp}$ indicated in Figure 3.14. The parallel momentum component is conserved because the crystal's surface does not disturb the translational symmetry in the x-y plane.

$$\boldsymbol{k}_{\parallel} = \frac{1}{\hbar}\sqrt{2mE_{kin}} \cdot \sin\theta \tag{3.16}$$

The $\boldsymbol{k}_{\perp}$ component is not conserved because there is a potential difference at the surface-vacuum interface. One can assume a nearly free electron description for the final state of the photoemitted electron and the perpendicular component can be approximated using equation 3.17.

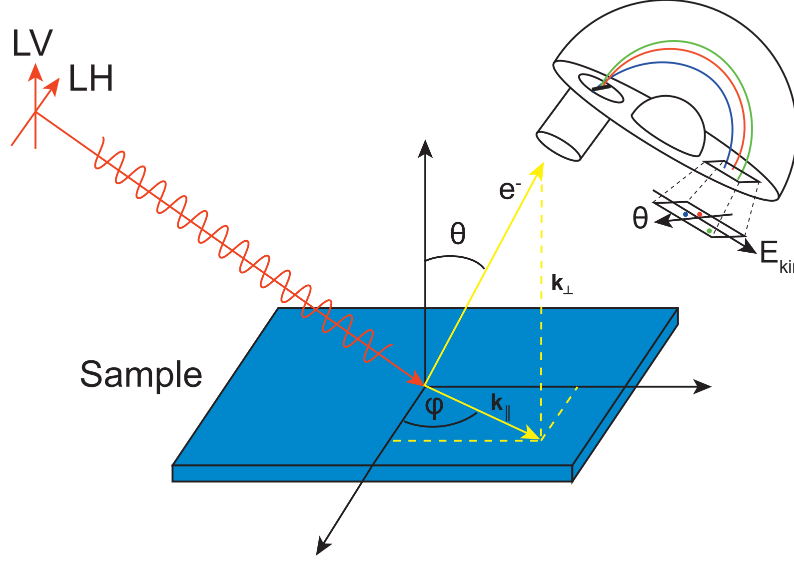

Figure 3.14: Schematic of ARPES principle. LV and LH correspond to linear vertical and linear horizontal polarisations respectively with θ being the polar angle and φ the azimuth.

$$\boldsymbol{k}_{\perp} = \frac{1}{\hbar}\sqrt{2m(E_{kin}\cos^2\theta + V_0)} \tag{3.17}$$

Where V_0, the inner potential, is defined as the energy gap between the vacuum energy and the valence band maximum (VBM). If the materials studied have a weak dispersion along the z-axis, the parallel component of the momentum almost wholly determines the electronic structure. One advantage of using a synchrotron photon source is the ability to tune the photon energy, allowing different k_z points of the Brillouin zone to be measured [135].

The energy resolution of an experiment is given in equation 3.15. The momentum resolution is given by

$$\Delta\boldsymbol{k}_{\parallel} \approx \sqrt{\frac{2mE_{kin}}{\hbar^2}}\cos\theta\Delta\theta \tag{3.18}$$

Where $\Delta\theta$ is the analyser's angular acceptance angle implying the momentum resolution is improved at lower energies (typically $h\nu < 150$ eV).

The inelastic mean free path in Figure 3.10 indicates VUV-ARPES is far more surface sensitive than XPS and HAXPES meaning the measured surface must be

free of contamination. The photoemission intensity is primarily characterized by the top few layers of the sample, which may not represent the bulk properties due to lower co-ordination of the surface atoms and possible surface states.

I05 Beamline at Diamond Light Source

ARPES data in this thesis was collected using the I05 beamline, another dual-purpose beamline at Diamond Light Source. One branch is for nano-ARPES, and the other for high-resolution ARPES (HR-ARPES). Figure 3.15 displays the schematic of the beamline [134].

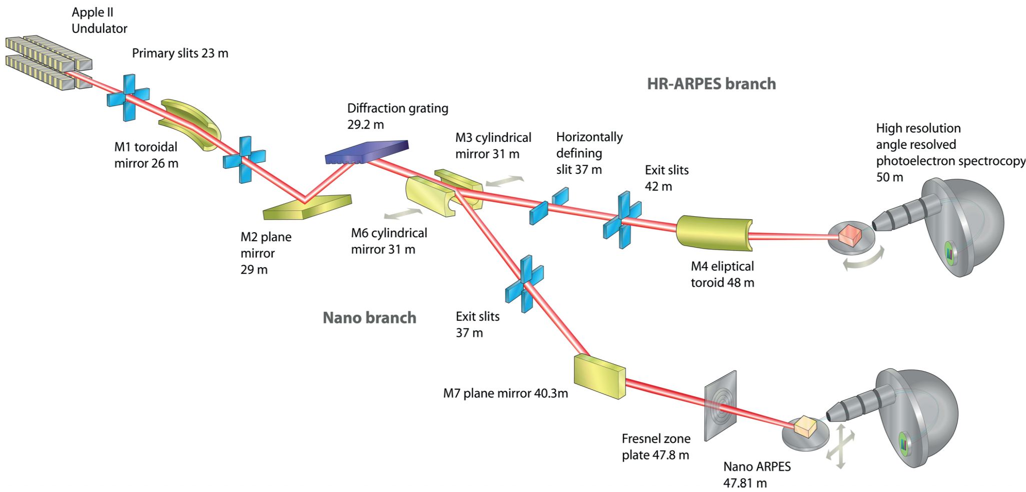

Figure 3.15: Schematic of the I05 beamline optics taken from Hoesch *et al* [134]

Photon beams are created using an APPLE-II undulator, able to deliver linear horizontal, linear vertical, and circularly polarised radiation at energies 18 - 240 eV. Therefore the experiments are performed in the vacuum-ultraviolet (VUV) range. The beam focused using a series of mirrors and slits to a sample spot size $\sim$ 50 x 50 μm^2. I05 uses a collimated plane grating monochromator (cPGM) yielding a photon beam energy resolving power ΔE/E = 20,000 below 100 eV (ΔE$\sim$ 2 meV) [134].

The end station is pumped using various turbomolecular and ion pumps, maintaining low pressures for measurements ($\sim 10^{-10}$ mbar). Samples are loaded onto a manipulator with the ability to cryogenically cool samples down to liquid helium temperatures ($<$ 6 K). Additionally, the cryomanipulator allows the samples to move with six-degrees of freedom. x, y and z axis controls the position with the polar

θ, azimuth φ and tilt ϕ angles allowing the sample to be aligned accurately with the beam and perform angular mapping. The end station is equipped with an VG Scienta R400 electron analyser with an acceptance angle of $\pm$ 14°.

The ARPES experiment in this thesis was conducted at a temperature of 160 K and photon energies, $h\nu$ = 120 - 150 eV. Similar to HAXPES, the energy resolution was measured using the Fermi edge of polycrystalline gold and was determined to be $\sim$ 55 meV. The obtained data was processed using the IgorPro software and analysis functions developed by T. Kim.

Chapter 4

Synthesis of Single Crystal ZGSO

Single crystals of $Zn_{1\text{-}x}Ga_xSb_2O_6$ (ZGSO) were grown using a multi-step process that produced millimetre-sized, transparent single crystals. First, a polycrystalline powder of the crystal was synthesised as a precursor to crystal growth. As this is a new novel material, ZSO powders were not available for purchase. When the precursor was obtained, it was used in a growth process known as chemical vapour transport (CVT) where it disassociates and vaporises in a reaction with a transport agent and recrystallises as a single crystal. This chapter explores how the CVT method was developed and refined to synthesise both ZSO and ZGSO. Early attempts at crystal growth produced small, disordered crystals so much effort was spent refining the synthesis parameters. After **one hundred** growth attempts pristine, millimetre-sized crystals were obtained, suitable for further measurements.

4.1 Precursor Powder Preparation

4.1.1 Preparation Methods from Literature

Before creating powders of ZGSO, a method for obtained undoped ZSO was devised. The literature for synthesising polycrystalline ZSO powders focused on two approaches: One used a reaction of Sb_2O_5 solution with $3ZnCO_3.4Zn(OH)_2$ [36] and another involved a solid-state reaction of ZnO and Sb_2O_3 at high temperatures [37, 38]. Rebello *et al* [136] followed a similar method but used ZnO_2 instead of ZnO. Kikuchi *et al* [36] reported that, depending on the preparation method, powders were

produced with significant variations in electronic properties. The solid-state reaction yielded a powder with a resistivity of 10^7 Ω.cm and the solution method, ∼10 Ω.cm. ZSO is predicted to be a wide band gap insulator, therefore the solid-state method, the technique with the fewest free carriers, was chosen to be the method for this project.

Purchased powders of ZnO and Sb_2O_3 were mixed in stoichiometric amounts with 3N (99.9 %) and 4N (99.99 %) purity, respectively. By choosing an initial mass, m, for Sb_2O_3 the corresponding mass of ZnO powders was obtained using equation 4.1.

$$m_{\mathrm{ZnO}} = \frac{m_{\mathrm{Sb_2O_3}}}{M_{\mathrm{Sb_2O_3}}} \times M_{\mathrm{ZnO}} \tag{4.1}$$

with M indicating the molar mass of each compound.

Grinding the powders with an agate pestle and mortar ensured they were mixed homogeneously and the crystallites were of similar size. To obtain the $ZnSb_2O_6$ (126) phase, the antimony must be oxidised from a +3 to +5 oxidation state using a high temperature reaction in an oxygen environment.

Two analysis methods were used to determine the success of the precursor preparation. Powder x-ray diffraction (PXD) was used to ascertain if the powder reacted into the 126 structure or if any additional phases were present. The other method was to establish if the mass has increased sufficiently. In an ideal reaction for undoped powder, ZnO and Sb_2O_3 provide four oxygen atoms per formula unit and therefore, it must oxidise to reach the required six. The two additional oxygen's account for this mass increase.

$$\%\text{Mass Increase} = \frac{M_{\mathrm{O_2}}}{M_{\mathrm{ZnSb_2O_4}}} \times 100 = 8.58\% \tag{4.2}$$

This equation can be generalised for powders doped with Ga_2O_3 dopant value x.

$$\%\text{Mass Increase} = \frac{M_{\mathrm{O_2}}}{M_{\mathrm{Zn_{1-x}Ga_xSb_2O_{4+\frac{x}{2}}}}} \times 100 \tag{4.3}$$

Initially, powders of Sb_2O_5 were purchased to omit the requirement of oxidation during reaction however, the quality of powders was poor. Figure 4.1 displays the powder x-ray diffraction pattern for the as-bought Sb_2O_5 powder. The powder

is predominantly Sb_2O_4 with low crystallinity. Similar irregularities in purchased Sb_2O_5 powders was investigated by E. Glover [137].

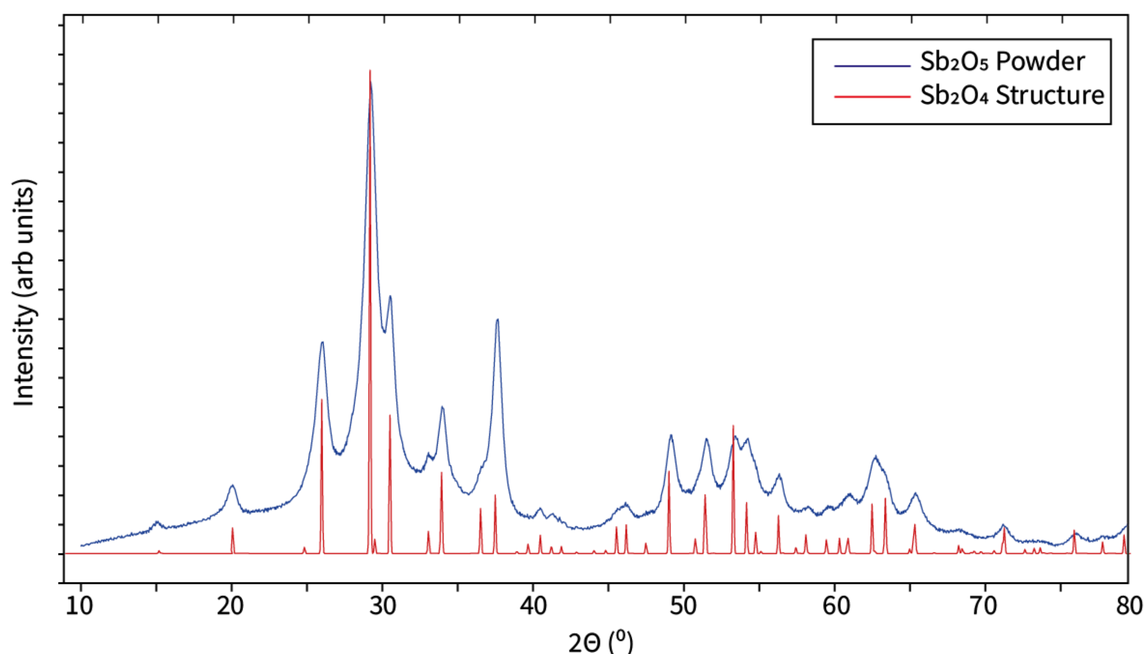

Figure 4.1: PXD pattern of purchased Sb_2O_5. The reference pattern included is the calculated diffraction pattern from cervantite (Sb_2O_4) [138].

Different powder preparation methods from the literature were recreated to determine if any were suitable for this project. The methods are labelled N for Nishiyama *et al* [37] and K for Katsui *et al* [38]. A variation of the Rebello *et al* [136] method (R-method) was examined but using ZnO instead of ZnO_2. The N-method baked premixed stoichiometric powders at 900 °C for four hours. An additional twelve hour bake was carried out to determine how duration affected the reaction. The K-method involved three bakes at 600 °C in air for two hours with intermittent grinding followed by a final bake at 800 °C for two hours. Finally the R-method was a two bake process where the initial powder was reacted in air at 600 °C for twelve hours, reground, pressed as a pellet, and baked for a further twelve hours at 800 °C.

Results

Powder x-ray diffraction patterns for the N-method are displayed in Figure 4.2 and table 4.1. Labels N1 and N2 represent a four and twelve hour bake, respectively.

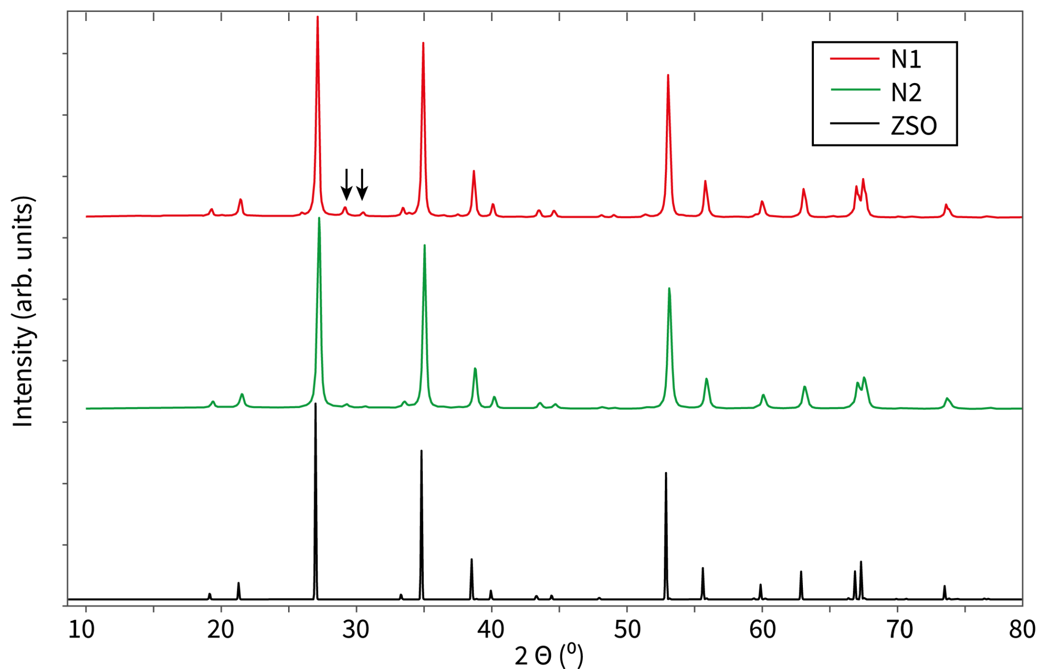

Figure 4.2: PXD diffraction patterns for both bakes following the N-method. The reference ZSO diffraction pattern is taken from Byström *et al* [24]. Black arrows indicate Sb_2O_4 peaks discussed in the text.

Table 4.1: Mass increase for ZSO precursor following the N-method

Method	T ($^\circ C$)	Duration (hr)	Mass Increase (%)	Expected increase (%)
N1	900	4	6.71	8.58
N2	900	12	6.48	8.58

The N method appears sufficient in partially reacting the powder into the 126 phase. However, the black arrows highlight peaks corresponding to the 112 and 004 planes of Sb_2O_4 at $2\theta = 29.1°$ and $30.3°$ respectively indicating partial non - reaction. These peaks are suppressed in the longer duration bake, suggesting a more completed reaction. However, the mass increase values imply less oxidation has occurred indicating potential evaporation of the Sb_2O_4 rather than reaction.

Figure 4.3 and table 4.2 displays the results for the K-method. The integer proceeding K indicates the bake number.

Despite the first bake, K1, reacting the powder predominantly into a 126 phase, closer inspection of this pattern suggests evidence for $ZnSb_2O_4$, not Sb_2O_4 peaks, as seen in the N-method. It is possible the bake was oxygen deficient. The powders have

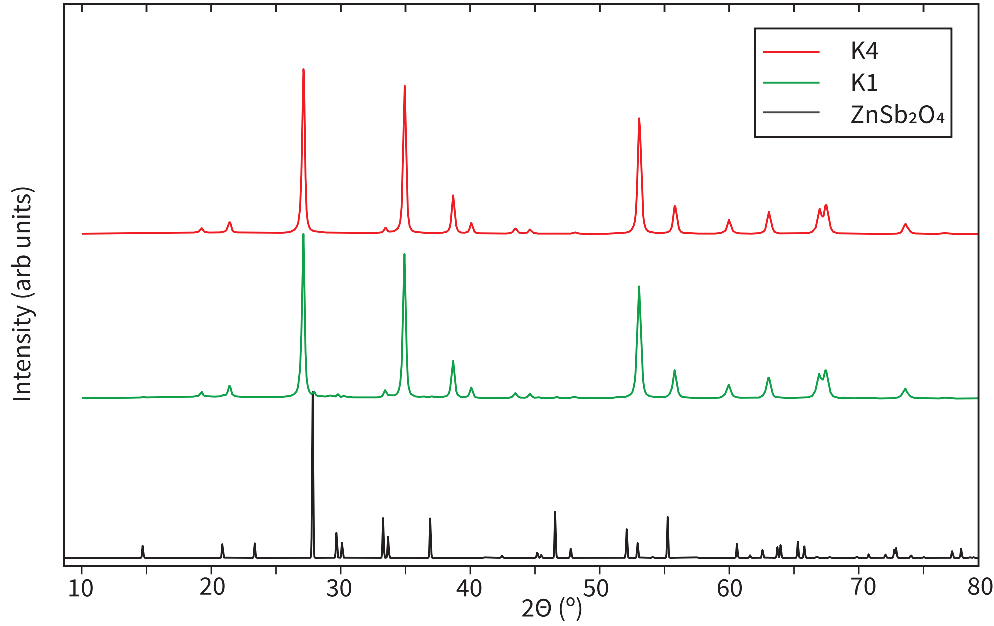

Figure 4.3: PXD patterns for the first bake K1 and final bake K2. The reference pattern is a $ZnSb_2O_4$ pattern simulated from Gavarri *et al* [139].

Table 4.2: Mass increase for ZSO precursor following the K-method

Method	T ($^\circ C$)	Duration (hr)	Mass Increase (%)	Expected increase (%)
K1	600	2	6.82	8.58
K2	600	2	6.96	8.58
K3	600	2	6.95	8.58
K4	800	2	7.06	8.58

reacted, however oxygen was not available to encourage reaction into the desired 126 phase. The final bake of K4 shows a loss of $ZnSb_2O_4$ peaks indicating the powder is entirely in the correct phase however, the mass increase test suggests it still has not reached the target of 8.58%.

Finally, Figure 4.4 and table 4.3 highlights the results for the R - method.

Table 4.3: Mass increase for ZSO precursor following the R-method

Method	T ($^\circ C$)	Duration (hr)	Mass Increase (%)	Expected increase (%)
R1	600	12	7.46	8.58
R2	800	12	7.49	8.58

The diffraction pattern of R1 signifies Sb_2O_4 peaks, similar to that seen in the

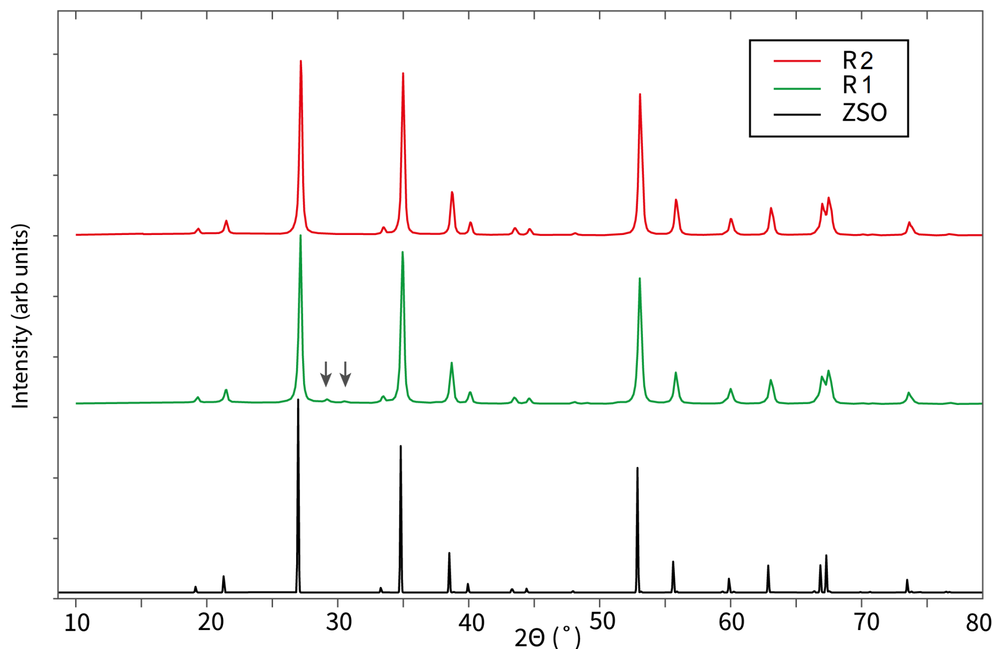

Figure 4.4: PXD patterns for both bakes described by the R-method with reference $ZnSb_2O_6$ pattern [24]. Highlighted arrows indicate of the presence of a Sb_2O_4 phase.

N-method. The antimony has not oxidised entirely into the +5 oxidation state and has also not reacted into the 126 structure. The absence of any additional phases in the second bake indicate the powder fully reacted into the 126 phase. The mass increase is in poor agreement with the expected value; however, improves on the previous two methods.

Analysis of the diffraction patterns for R and K-methods indicate both were able to provide a powder in the correct $ZnSb_2O_6$ phase. The two approaches were identical in terms of temperatures used but differ in duration, number of bakes and whether the final reaction was a pellet. The reason why $ZnSb_2O_4$ peaks appear in the K-method and Sb_2O_4 in the other two is unclear. $ZnSb_2O_4$ peaks indicate that zinc and antimony have reacted early but not oxidised whereas the presence of Sb_2O_4 infers Sb_2O_3 powder has oxidized slightly but not reacted into the 126 structure. It is possible the environment for second bake of the K-method was oxygen-deficient when compared to the other two methods. The N-method appears not to be appropriate as neither bake duration encouraged the powder to react into the correct phase fully. This indicates the importance of a lower temperature bake as demonstrated by both K and R-methods relative success.

The R-method managed to increase the powder's mass closer to the desired value. However, it still fell short of the expected value of 8.58 %. The longer duration of the initial bake encouraged a more significant amount of oxidation than the short bakes proposed by the K-method.

To explain why the powders were not achieving their required mass increase, the partial vapour pressures of the components was studied to determine if evaporation of any components was likely occurring. A powder with a higher vapour pressure at a particular temperature is more favourable to evaporate and, therefore, more likely to be the source of mass lost during the reaction. The melting point of ZnO is 1975 K at which point it disassociates and O_2 evaporates [140]. Below this, temperature the vapour pressure remains extremely low (log(p/atm) $<$ -13 at 1000 K) [141]. The vapour pressure of Sb_2O_3 suggests log(p/atm) values to be around -2 at 930 K [142, 143], eleven orders of magnitude greater than in ZnO. Therefore, it is concluded Sb_2O_3 is the evaporating constituent in the reaction process, a conclusion shared by Kikuchi et al [36]. For doped powders, it is also assumed little gallium is lost due to evaporation due to the high melting point of 2100 K. Exactly how much Sb_2O_3 is lost is quantified using the method from Appendix B and results shown in table 4.4. $\frac{\delta}{2}$ is the amount of Sb_2O_3 evaporated per formula unit.

Table 4.4: Quantification of Sb_2O_3 evaporating during the reaction of precursors from the recreated literature methods.

Method	δ	**Precursor Formula**
R2	0.025	$ZnSb_{1.97}O_{5.96}$
N1	0.035	$ZnSb_{1.96}O_{5.94}$
K4	0.043	$ZnSb_{1.96}O_{5.94}$

Although not perfect, the R-method appeared to be the most successful method to use as a starting point for precursor preparation. The method employed by this project used a lower first bake temperature that was slowly ramped up to 600 °C to achieve reaction whilst minimising the evaporation of antimony. The second bake also used a gradual ramping technique from 800°C to 900 °C as a pressed pellet. This ensured the powder reacts entirely into the correct phase. Attempts to carry out a final bake at 800 °C could not always guarantee a complete reaction. Figure

4.5 shows the temperature profile for both bakes.

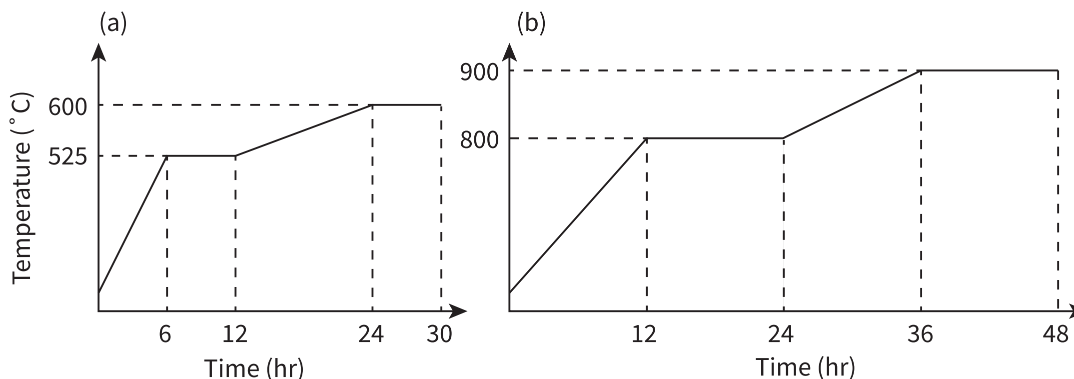

Figure 4.5: (a) Temperature profile as a function of time for initial bake as a loose powder. (b) Profile for the second bake as a pressed pellet.

Final powders were determined to be entirely in the 126 phase with a highest mass increase measured to be 7.89 %. Although an improvement on the R-method, the mass increase was still short of the desired target of 8.58 % indicating antimony was still evaporating. Baking in air is unlikely to overcome this problem as the high temperatures required to react the powder will always encourage antimony to evaporate. Adding an excess of Sb_2O_3 would likely overcome this however it was not explored in this project.

4.1.2 Preparation Using Argon Environment

To overcome the antimony evaporation a novel precursor preparation method was implemented. A stoichiometric well-mixed blend of ZnO - Sb_2O_3 was placed in a small Al_2O_3 crucible, $\varnothing \sim 10$ mm, with a lid and placed into a quartz ampoule with one end pre-sealed. The tube was evacuated to a pressure $< 10^3$ bar to remove any oxygen and other unwanted gases. The ampoule was subsequently filled with ~ 400 mbar of argon at room temperature, which, when heated to 600 °C, will create an internal pressure of ~ 1.15 bar. The tube was sealed using an acetylene/oxygen gas torch. Figure 4.6 shows a schematic for this arrangement.

The heating conditions used for all powders followed the improved ramping temperature method displayed in Figure 4.5. As it does not undergo oxidation, the resultant powder is $ZnSb_2O_4$ and zero change in the mass is expected which was

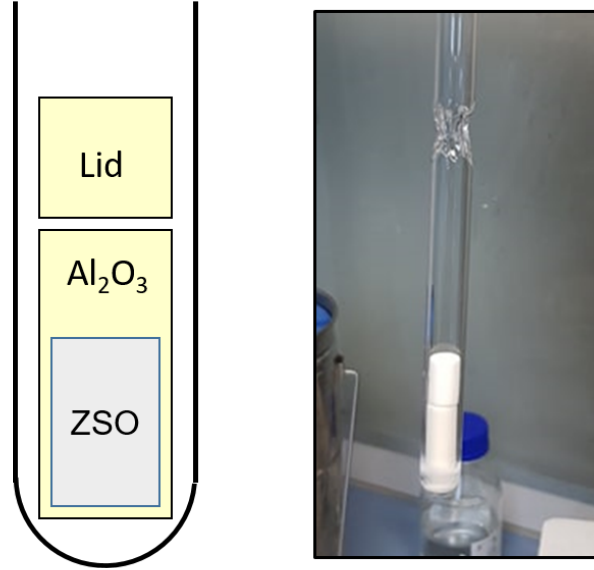

Figure 4.6: Cartoon and photograph of reaction ampoule used to react ZnO and Sb_2O_3 into $ZnSb_2O_4$ under argon pressure.

achieved to within 0.2 %. After the first bake the powder was extracted from the tube, ground using a pestle and mortar, then pressed into a pellet at 400 kg/cm^2, a value chosen arbitrarily. The pellet was placed onto a platinum lid, covered with an alumina crucible, and baked in air atmosphere following the second bake routine. This second bake oxidised the powder creating $ZnSb_2O_6$. Figure 4.7 displays both x-ray diffraction patterns with reference patterns taken from literature. The diffraction patterns indicate no additional phases present in both the $ZnSb_2O_4$ and $ZnSb_2O_6$ powders. Mass increase of the final powder was determined to lie consistently between 7.91 and 8.25 %. This provided a lower δ value of 0.01 and as a consequence, higher quality ZSO powders.

Following the success of the method, gallium doped powders were created by mixing to the correct molar stoichiometry using the following equations

$$m_{\mathrm{ZnO}} = \frac{m_{\mathrm{Sb_2O_3}}}{M_{\mathrm{Sb_2O_3}}} \times (1-x) M_{\mathrm{ZnO}} \tag{4.4}$$

$$m_{\mathrm{Ga_2O_3}} = \frac{m_{\mathrm{Sb_2O_3}}}{M_{\mathrm{Sb_2O_3}}} \times \left(\frac{x}{2}\right) M_{\mathrm{Ga_2O_3}} \tag{4.5}$$

with the mass of Sb_2O_3 was chosen arbitrarily and the gallium doping initially x = 0.00 - 0.10. Section 4.2 discusses a requirement for additional gallium in the growth process.

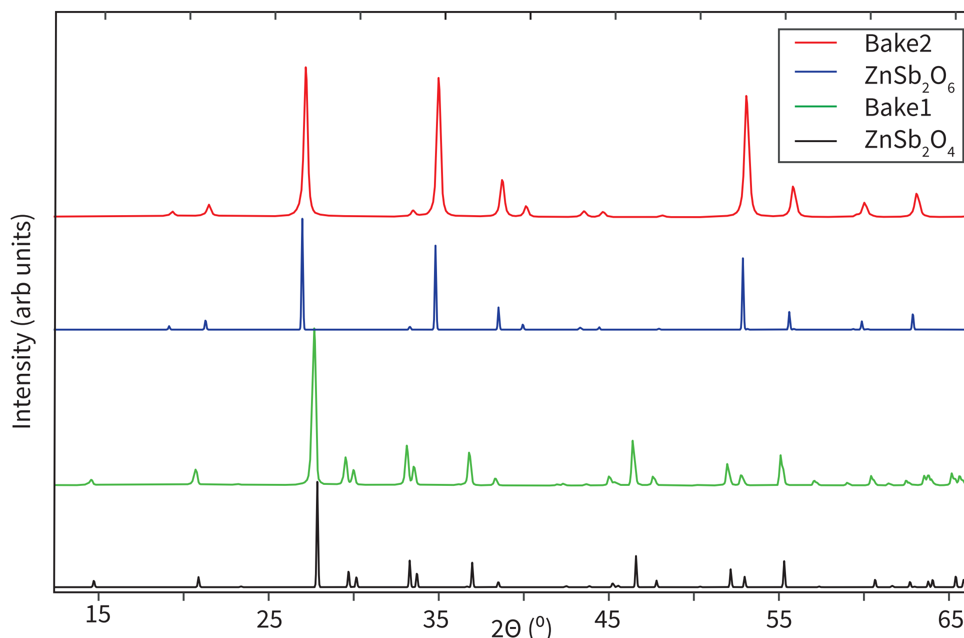

Figure 4.7: Powder x-ray diffraction patterns for an undoped powder reacted under the argon pressure method (bake 1) with secondary bake as a pellet (bake 2). The two reference patterns, $ZnSb_2O_6$ and $ZnSb_2O_4$ were taken from structural files [24, 139].

4.1.3 Lattice Parameters

The lattice parameters of the powders were determined using powder x-ray diffraction measurements. The diffraction patterns for powders with different Ga doping values (x = 0.00 and 0.06) are displayed in Figure 4.8(a) with (b) showing a zoom of the 110 peak.

The peak position of the 110 peak is shifted to higher 2θ for the doped sample. According to Bragg's law, a shift to higher 2θ values corresponds to a decrease in the d-spacing and shrinking in lattice parameters.

Slight asymmetry is observed in the 110 peak with tailing extending to lower 2θ values. The asymmetry is an artefact of removing the incident Soller slit prior to measurement to increase the photon flux. A Soller slit is conventionally installed after the source to diverge the photon beam in the direction perpendicular to the 2θ plane. Without this slit, reflections from the edge of the sample obey Bragg diffraction at what appears to be a lower 2θ creating peak broadening and asymmetry, particularly at low 2θ.

By employing GSAS-II [118] the lattice parameters were determined and are

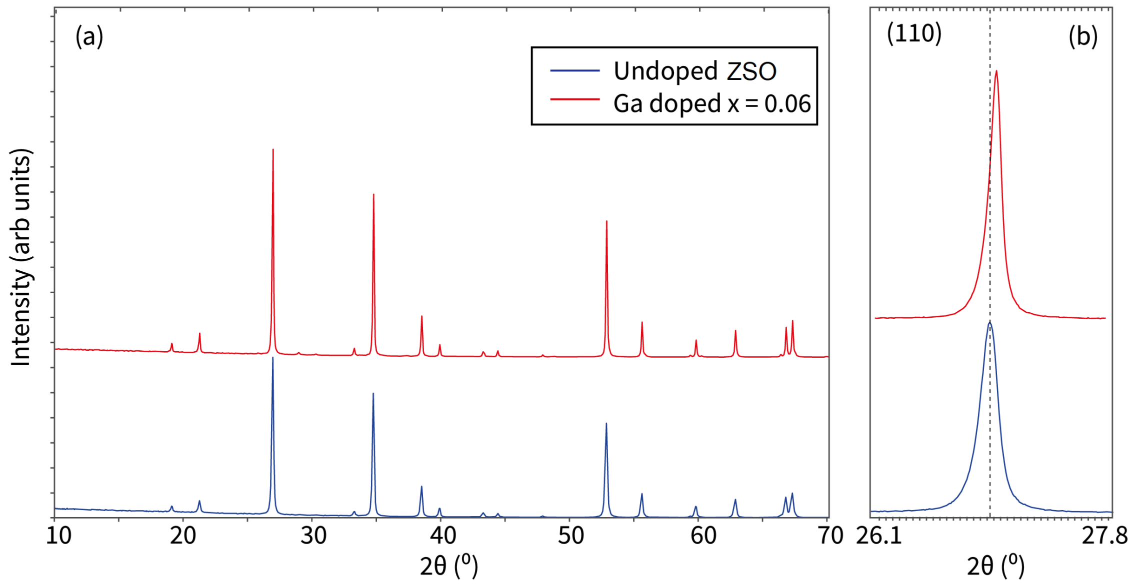

Figure 4.8: (a) Powder x-ray diffraction pattern for undoped and 6% doped ZGSO precursor powders (b) Zoom around 110 peak.

displayed in table 4.5. An example refinement shown in Figure 4.9.

Table 4.5: Lattice parameters for undoped and 6% doped obtained from Rietveld refinement with comparative literature values.

Powder	a,b (Å)	c (Å)	R_{wp}
Undoped	4.667	9.266	6.546%
6% Ga	4.663	9.264	7.730%
Byström [24]	4.67	9.26	-
Ercit [25]	4.66	9.26	-

The lattice parameters for the undoped powder are in excellent agreement with the literature values. Doping has reduced the lattice constants, therefore, reducing the unit cell of the crystal. This is further explored when the lattice parameters for single crystals are determined in section 6.2.

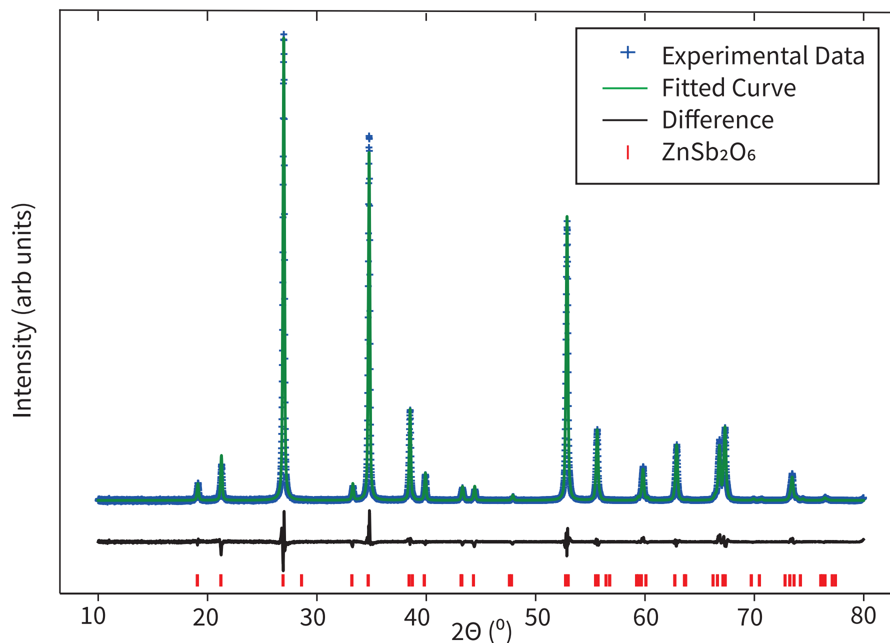

Figure 4.9: Example refinement of an undoped powder using GSAS-II software. The difference curve is the sum of the experimental curve minus the fitted curve.

4.2 Single Crystal Growth

4.2.1 Chemical Vapour Transport Theory

Chemical vapour transport (CVT) is a crystal growth method, first documented by Bunsen in 1852 [144]. He noticed Fe_2O_3 crystals were forming due to HCl gases near volcanoes.

Although a form of the CVT technique was utilised by van Arkle and de Boer [145] in the 1920s, it wasn't until Schäfer [146, 147] comprehensively studied chemical vapour transport systems in the 1950's that the technique became a popular tool for crystal growth.

Despite variations on the method, the general principles remain the same. An initial precursor is volatilised by a transport agent and enters into a vapour phase. The vapour transports to a place of deposition and recrystallizes. This zone in which crystallization occurs is generally a place with a temperature different to that of volatilisation. Experimentally this temperature gradient is usually created using multi-zone furnace. CVT can take place in both an open and a closed system. If the system is closed, as is common in most laboratory experiments, far less transport agent is required as it can be effectively recycled. It is an ideal crystal growth

method for systems where the crystal's melting point is too high or if one of the components has a high partial vapour pressure [148]. Figure 4.10 displays a cartoon depicting the CVT process for an endothermic reaction in a closed system.

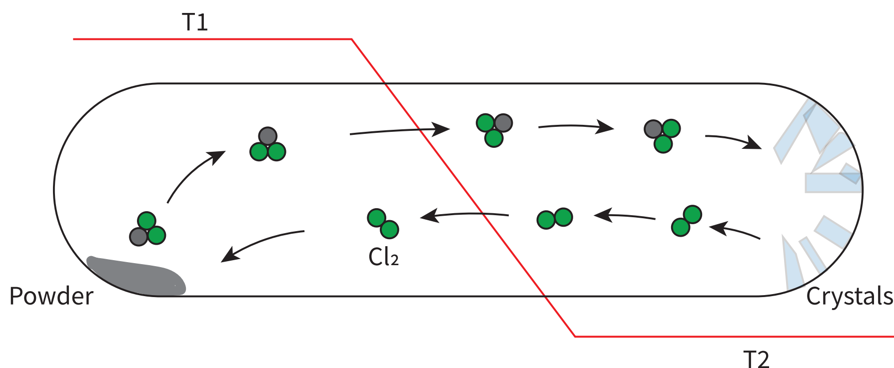

Figure 4.10: Cartoon of the CVT process for a closed system in an endothermic reaction and T1>T2, with T being temperature. Cl_2 transforms the powder into gaseous phases which is transported and deposited in the cold sink. The Cl_2 is recycled in a closed system.

Binnewies *et al* [149] provided a particularly relevant example of why a transport agent is required to grow ZnO crystals. As mentioned in the section 4.1, ZnO has a high melting point and its vapour partial pressure is minimal below 1000 °C. If Cl_2 is used as a transport agent, $ZnCl_2$ and O_2 gaseous phases form with high partial vapour pressures even at low temperatures.

To successfully grow single crystals by CVT, several important factors have first to be taken into consideration:

- Choice and quantity of transport agent
- Temperature for growth
- Duration of growth

Calculations can predict suitable transport agents for a particular system providing thermodynamic information of all phases is available. By choosing a transport agent, typically halogens such as Cl, I or Br, and simulating reactions, values of the equilibrium constants K_p can be obtained. It is shown that CVT reactions will only occur if $10^{-4} < K_p < 10^4$ [150]. As a general rule of thumb, the mass of transport

agent added should be enough to create an internal pressure of around 1 bar during the reaction. Furthermore, if thermodynamic data is available for the reaction, temperatures at which growth will occur can also be predicted. This occurs when the Gibbs free energy of the reaction $\Delta_r G^0_T = 0$.

$$\ln K_p = -\frac{\Delta_r H^0_T}{R.T} + \frac{\Delta_r S^0_T}{R} \tag{4.6}$$

$$\Delta_r G^0_T = \Delta_r H^0_T - T.\Delta_r S^0_T \tag{4.7}$$

$$T_{opt} = \frac{\Delta_r H^0_T}{\Delta_r S^0_T}$$

With T being the reaction, R the ideal gas constant and $\Delta_r H^0_T$ and $\Delta_r S^0_T$ being the enthalpy of reaction and change in entropy of the reaction respectively.

The duration of growth must also be sufficient to allow the precursor to be vaporised entirely, transported and deposited as a crystal. The rate of the growth is generally measured in mg.h^{-1}.

4.2.2 Single Crystal Growth of ZSO and ZGSO

Crystal growth of pentavalent antimonates (+5) is difficult to achieve using methods such as melt growth because the heavier pnictide elements (group 15) are more thermodynamically stable in a +3 oxidation state rather than +5 at higher temperatures [151]. This is due to the inert pair effect where s-orbitals with a higher total quantum number n, in the case of antimony, $5s^2$ are poorly shielded from the large nuclear charge's effects and therefore require more energy to ionise. There have been several reported successful CVT growths of +5 antimonates, such as rare earth compounds $RESbO_4$ [152, 153], $Ni_2InSb_2O_6$ [151] and the trirutile compound $CuSb_2O_6$ [154, 155] all grown using $TeCl_4$ or HCl as a transport agent.

In Appendix C, a study of ZSO growth carried out using $TeCl_4$ as a transport agent is discussed. Unfortunately, due to the inclusion of tellurium into the lattice during growth, this method was discounted.

Crystal Growth using Cl_2 as a Transport Agent

The initial study using $TeCl_4$ as a transport agent proved a success with regarding growing single crystals, albeit contaminated. Therefore, the method was refined to remove the tellurium out of the growth and use Cl_2 as a transport agent. Due to very little thermodynamic information available for the ZSO system, calculations to predict growth conditions were not possible. However, by looking at dominant vapour phases during CVT reactions for similar compounds [149, 156], a transport equation for undoped ZSO is assumed to be

$$2ZnSb_2O_6 + 6Cl_2 \leftrightharpoons 2ZnCl_2 + 2SbCl_3 + 2SbOCl + 5O_2 \tag{4.8}$$

The introduction of gallium significantly increases the uncertainty in the transport constituents. In CVT growths for Ga_2O_3 using Cl_2, $GaCl_3$ is a major vapour phase [157], therefore likely to exist in the transport process of growing doped crystals. From experience, the transport is known place from hot to cold (endothermic) and therefore the enthalpy of reaction $\Delta_r H_T^0 > 0$.

Cl_2 is a gas at room temperature, and is therefore difficult to place a quantifiable amount into ampoule without unwanted gases. To introduce Cl_2 as a transport agent, a method similar to that was discussed by Binneweis *et al* [149] was conceived. By heating $PtCl_2$ to temperatures > 500 °C, it decomposes into its constituents Pt(s) and Cl_2(g). The transfer of Cl_2 into the reaction ampoule was carried out by the following steps

- 1-3 grams of ZSO/ZGSO was placed into a quartz ampoule and a mass of $PtCl_2$ into another. The ampoules are connected to a vacuum system similar to that displayed in Figure 4.11.
- The system was evacuated down to an internal pressure $\sim 10^{-6}$ bar and, the valve subsequently closed.
- Using an acetylene/oxygen torch, the $PtCl_2$ was heated down to the point of decomposition.
- The bottom of the ZSO ampoule was placed in liquid nitrogen to encourage condensation of the gaseous Cl_2.

- Using the torch, the ZSO ampoule was sealed at a length of $\sim$ 15cm, achieved by carefully melting the quartz.

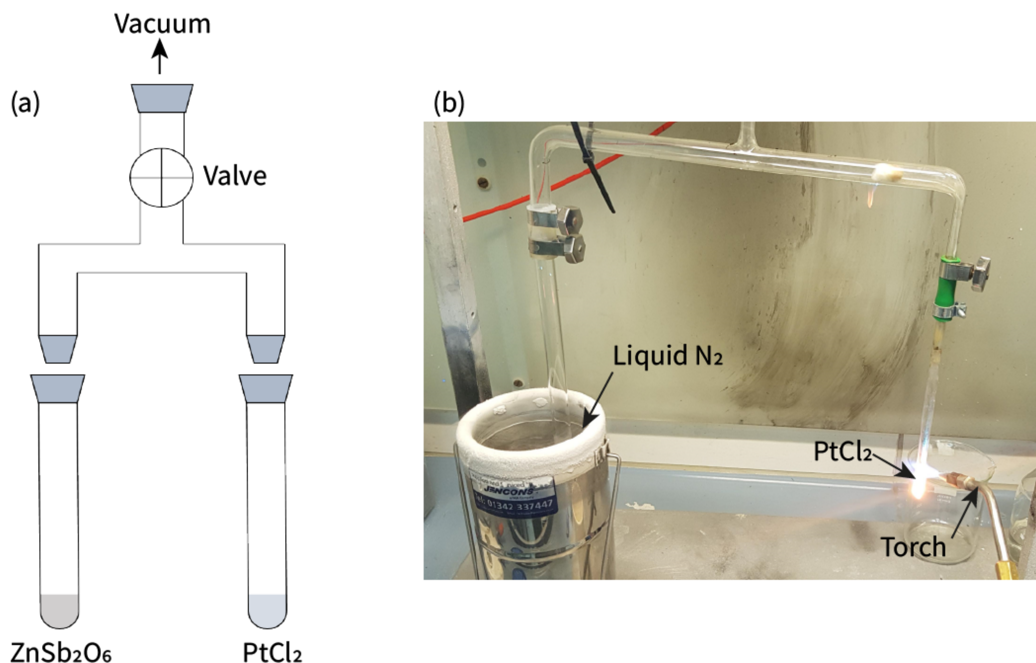

Figure 4.11: (a) Cartoon of the apparatus used to condense Cl_2 into the reaction ampoule. (b) Photograph of the arrangement displaying the decomposition of $PtCl_2$, and condensation of Cl_2 in to the ZSO ampoule by condensation using liquid N_2.

The mass of $PtCl_2$ was calculated to ensure an internal pressure of 1 bar of Cl_2 at 1000 °C is achieved. This temperature was chosen due to its success in the $TeCl_4$ growths. The volume of the ampoule was predetermined to be 26.5 cm^3.

$$m_{\mathrm{PtCl_2}} = \frac{1\mathrm{bar.}\ 26.5\ .\ 10^{-3}\mathrm{l}\ \ .\ 265.99\ \mathrm{g}\ .\ \mathrm{mol}^{-1}}{0.08314\ \mathrm{l}\ .\ \mathrm{bar}\ \mathrm{K}^{-1}\ .\ \mathrm{mol}^{-1}\ .1273\mathrm{K}} = 66\mathrm{mg} \tag{4.9}$$

This mass was open to change and continuously refined between growths on a trial and error basis. Similarly, the temperatures involved in the growths were also subject to change.

A two-zone furnace was used to create a temperature gradient across the ampoule with either side controlled by a thermostat. The tube was placed horizontally and centred between the two zones. The values set by the furnace thermostat and those measured using a thermocouple are not identical. The temperature profiles for two thermostat settings commonly used for this work are displayed in Figure 4.12. The

temperature across the cold zone is seen to be non-homogeneous and varied by 7 °C due to the position of the heaters in each zone.

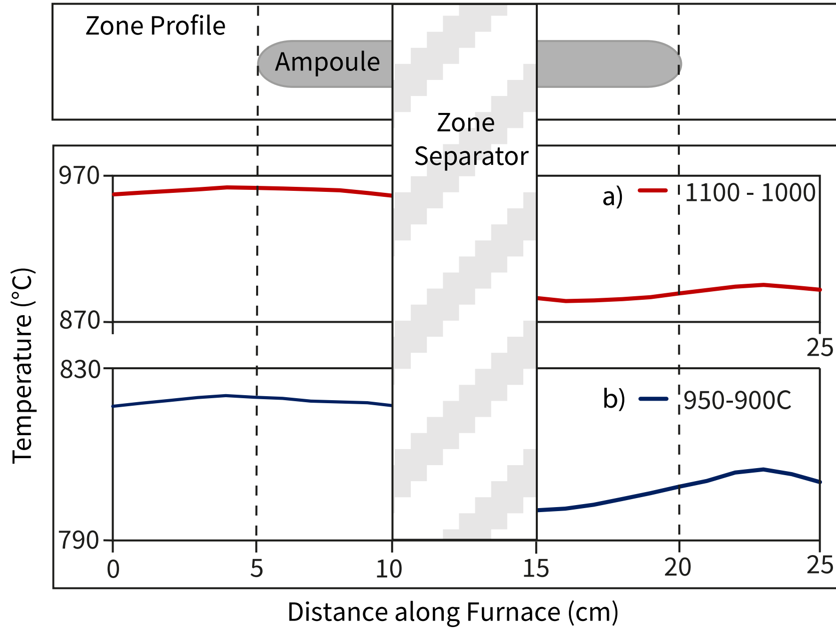

Figure 4.12: Temperature gradient across the two-zone furnace measured using a thermocouple for two furnace thermostat settings, (a) T_H = 1100 °C and T_C = 1000 °C. (b) T_H = 950 °C and T_C = 900 °C. T_H and T_C refer to hot and cold temperatures respectively.

A reverse temperature gradient was employed for the first sixteen hours. This reversal ensured the transport ampoule's sink side was cleaned of any small powder particles that can act as seeds for nucleation.

After the growth, a white layer of powder was found to be coating the ampoule's inner walls. By extracting the powder and conducting x-ray diffraction measurements, it was shown to be SiO_2 (Figure 4.14). This powder originated from an attack on the ampoule during the transport process. Legma *et al* [156] observed the same phenomena when growing WSe_2 using $TeCl_4$ and $SeCl_4$. This attack was determined to be strongest when the hygroscopic transport agent had been exposed to air and therefore adsorbed water. They concluded tungsten oxychlorides formed during transport due to water, reacted with the SiO_2. Thus one of the components during the transport of ZSO is likely to be a metal oxychloride. The attack occurred heavily in the doped transport and less so in undoped therefore it is likely to be pre-

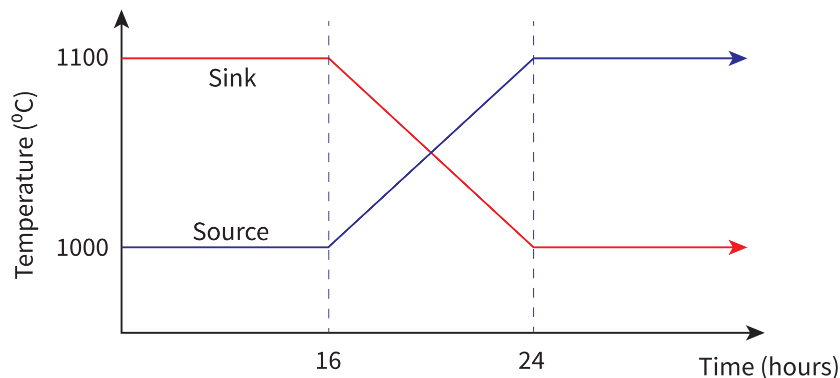

Figure 4.13: Growth temperature profile versus time indicating the reverse gradient method.

dominantly gallium oxychloride reacting with the ampoule [157]. To counteract this, an excess of 100% Ga_2O_3 was added to precursor powders.

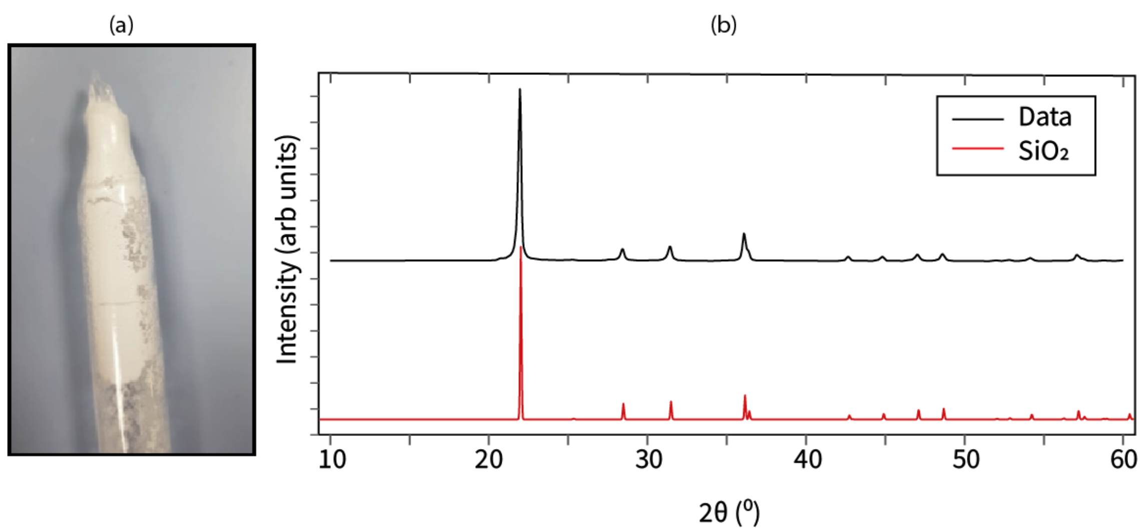

Figure 4.14: (a) Photograph of ampoule after crystal growth highlighting the attack on the ampoule (b) XRD pattern of the extracted powder, the bottom reference diffraction pattern is that of cristobalite (SiO_2) [158].

Results

Table 4.6 displays a log for growths of ZSO and ZGSO,

Table 4.6: Crystal growth log for several highlighted growths using Cl_2 as a transport agent. Displayed are conditions for growth and observations made. Three hundred thirty-six hours corresponds to two-week growths and charge is equivalent to precursor powder.

Growth Number	Duration (hr)	Mass of Charge (g)	Mass of $PtCl_2$ (mg)	Dopant Ga (x)	T_{hot} (°C)	T_{cold} (°C)	Comments
54	200	0.75	60	0	1050	1000	-Full Transport of powder >0.5mm transparent crystals.
61	200	1.0	25	0	1100	1000	Transparent crystals
62	200	1.0	50	0	1100	1000	-Much smaller crystals, too much $PtCl_2$
63	336	1.0	13	0	1100	1000	-Good sized crystals
64	336	2.0	20	0	1100	1000	-Well faceted transparent crystals ≈1mm 90% transport
67	336	2.0	30	0.01	1100	1000	-Blue/black large crystals
68	336	2.0	30	0.02	1100	1000	- ≈1mm black crystals, very cloudy tube
69	336	2.0	30	0.04	1100	1000	- ≈2mm black crystals
70	336	2.0	30	0.06	1100	1000	- ≈2mm black crystals
76	336	2.0	30	0.06	1100	1000	- >1mm black crystals, lots of dislocations
79	336	2.0	30	0.10	1100	1000	- Significant tube clouding, Large black crystals
80	336	2.0	40	0.10	1100	1000	- Very brittle crystals, high density of grain boundaries.
82	336	1.5	30	0.10	1100	1000	- Heavy ampoule attack, large black crystals.
91	336	2.0	30	0	1100	1000	- Complete transport, Transparent crystals
92	336	2.0	30	0.08	1100	1000	-Huge >3mm crystals
93	336	3.0	30	0.08	1100	1000	-Complete transport, large black crystals

One major issue with using $PtCl_2$ as a transport agent is accurately determining the amount of Cl_2 condensing into the reaction ampoule. The actual mass of Cl_2 is likely to be less than the amount calculated. This is significant, given most successful crystal growths occurred using an initial $PtCl_2$ mass of 30 mg, subsequently creating ampoule pressure of < 0.45 bar, far lower than the recommended value.

The transport rates using Cl_2 are challenging to determine accurately as every growth shows complete transport of the precursor. However, the lower limits for transport rate in growths 54 - 80 range from 3.33 - 6.41 mgh^{-1} due to the mass of charge changes. Growth 93 contained more charge, and because it fully transported, the transport rate is > 8.92 mgh^{-1}. These changes are likely to occur due to fluctuations in the quantity of Cl_2 in the transport ampoule.

To visually compare crystals, they were polished down to a constant thickness ($\sim$ 150 μm). A schematic in Figure 4.15 highlights how crystal polishing works. Figures 4.15(a) and (b) are photographs and schematics of the polishing device, respectively. A crystal is glued to a silver-coloured polishing disk with a large facet faced down displayed in 4.15(c). This disk is attached to the brass post and sits on the silver-coloured sleeve. The brass post provides weight, and by rubbing the polishing device

over 25 μm diamond slurry, the crystal surface was eroded away down to a crystal in 4.15(d). This was an efficient abrasion method allowing quick erosion but it creates a rough surface. To obtain a clear finish on the crystal, the same device was used on 1 μm Al_2O_3 abrasive paper, providing a well-polished surface but at the cost of abrasion speed. Eventually, the example crystals displayed in Figure 4.16 were obtained.

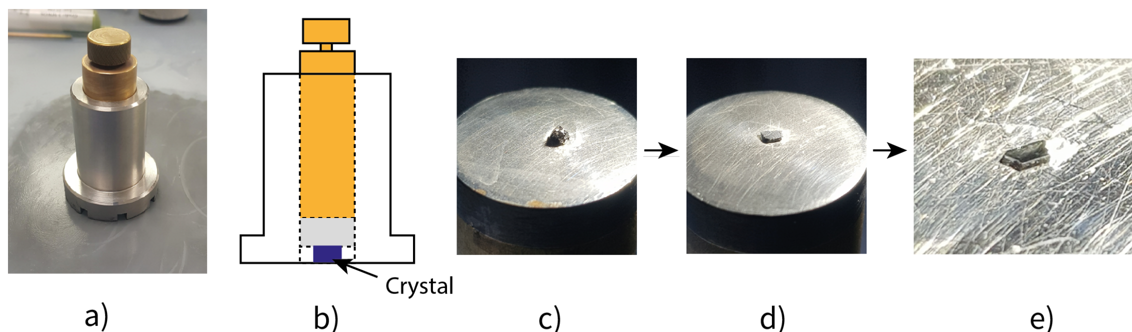

Figure 4.15: a) Photograph of polishing device. b) Schematic of the polishing device. c) As grown crystal glued onto disk. d) Crystal after rough abrasion. e) Crystal after fine abrasion.

Figure 4.16 highlights a few polished crystals from successful growths with different nominal Ga doping values. Undoped crystals are clear and transparent; however, gallium's inclusion provides the crystals a blue tint. Before polishing, the doped crystals have a dark, nearly opaque appearance similar to those seen in the Appendix C. Only when polished down to a thickness < 200 μm do they exhibit observable transparency. The blue tint caused by gallium's inclusion does not intensify upon increasing the nominal doping. By observation alone, a 1% doped crystal is indistinguishable from one of a higher dopant. 1% of doping refers to total percentage of gallium on the zinc site, equivalent to ($x = 0.01$).

4.3 Conclusions

The work in this chapter has discussed the methodology used to synthesise single crystal ZSO and ZGSO by the chemical vapour transport method. Polycrystalline powders of ZSO and ZGSO were synthesised and characterised by x-ray diffraction, to be entirely in the 126 phase. By calculating mass increases, the powders were

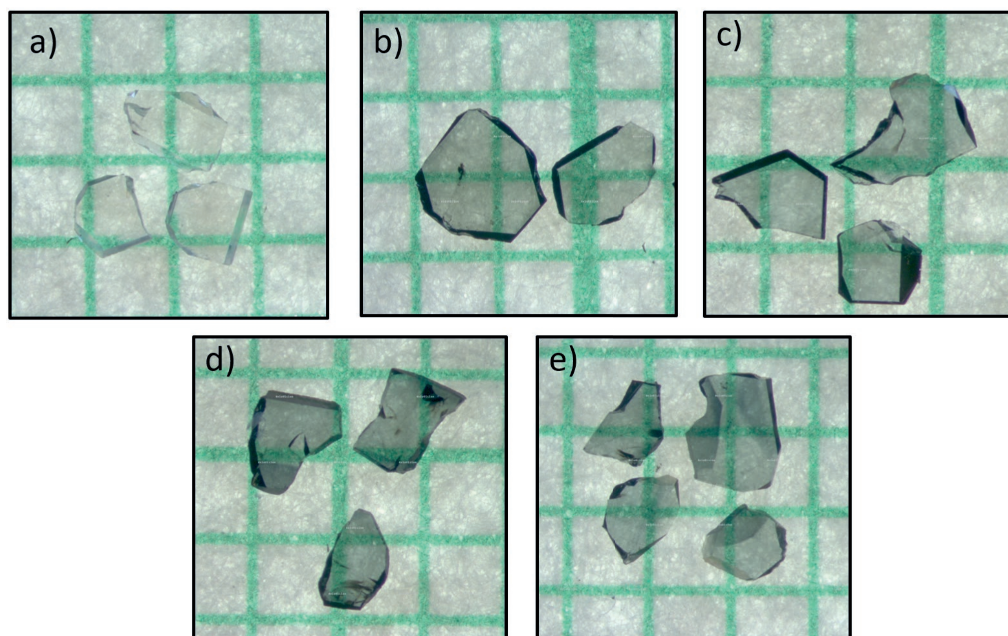

Figure 4.16: Crystals polished to thickness ∼ 150 μm **a)** 64 (0% Ga), **b)** 67 (1%), **c)** 68 (2%), **d)** 70 (6%), **e)** 69 (4%) (grid lines represent 1 mm).

shown to be almost completely oxidised with little evaporation of Sb_2O_3, improving on previously attempted methods in the literature.

For the first time, well faceted, transparent single crystals were synthesised using Cl_2 as a transport agent. Crystals grown nominally doped with gallium have a clear blue tint.

Chapter 5

Measurements

For a material to be considered a TCO, it must possess high electrical conductivity and low opacity over visible wavelengths. The work in this chapter focuses on determining these properties. Using a physical properties measurement system (PPMS), the resistivity, mobility, and Hall coefficients of undoped and doped samples were measured as a function of temperature and doping.

Furthermore, UV - Vis spectroscopy was used to understand the optical properties of the crystals. By determining the onset of absorption of the light, the optical band gap for the grown crystals is determined. Combining both the resistivity and the absorption coefficient at 550 nm, a figure of merit FOM was determined to quantify the performance of ZGSO in comparison to other commonly used TCOs.

5.1 Electronic Transport

5.1.1 Undoped ZSO

To understand the electronic properties of ZGSO, it is essential to first examine the transport properties of the undoped host lattice ZSO, predicted to be a wide band gap insulator. Figure 5.1 displays temperature dependent resistivity, Hall mobility, and Hall coefficient data for two undoped crystals from growth 64. Room temperature data is displayed in table 5.1.

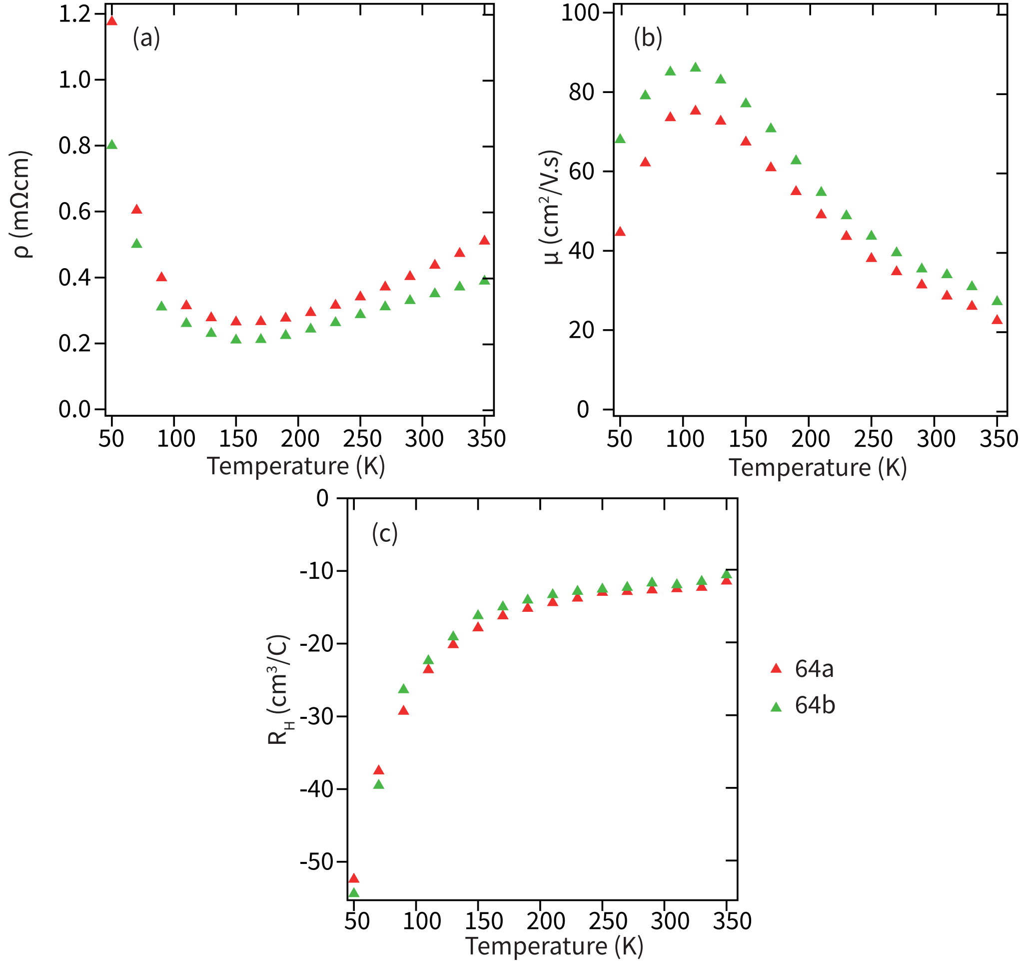

Figure 5.1: Electrical transport data for ZSO single crystals showing (a) resistivity ρ, (b) mobility μ and (c) Hall coefficient R_H as a function of temperature.

Table 5.1: Room temperature electronic transport data for two undoped ZSO crystals.

Crystal	ρ (mΩ.cm)	μ (cm^2/V.s)	n ($\times 10^{17}$cm^{-3})
64a	419.4 $\pm$ 83.9	30.0 $\pm$ 6.0	5.0 $\pm$ 1.4
64b	340.1 $\pm$ 68.0	34.7 $\pm$ 6.9	5.3 $\pm$ 1.5

The errors quoted in the table are primarily due to the large error in measuring length L in equation 5.1.

$$\rho = \frac{RA}{L} \tag{5.1}$$

Where R is the measured resistance and A is the cross section area perpendicular to the direction of current. To determine the distance between the two voltage

contacts, a grating built into a microscope was calibrated to measure lengths. The obtained L was $\sim$ 500 μm in size, however as the silver contacts are generally not painted perfectly straight, an error associated with this distance ($\sim$ 100 μm) carries through all obtained parameters. Figure 5.2 visualises this issue.

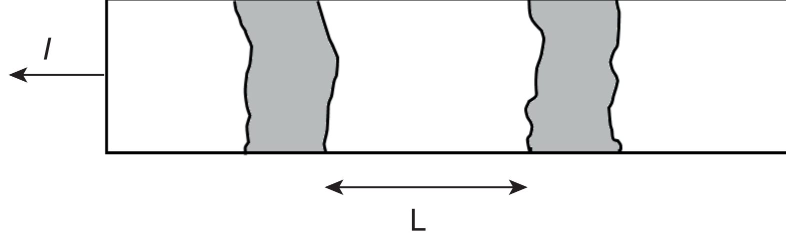

Figure 5.2: Schematic of the side view of a crystal showing the voltage contacts. The direction of current I and the distance between the voltage contacts L are labelled.

Both undoped crystals follow similar trends with regards to their properties as functions of temperature. A minima in resistivity is observed at $\sim$ 150 K with maxima in mobility at $\sim$ 110 K. Furthermore, the data suggests neither sample is an insulator. For wide band gaps (> 3.0 eV), concentrations due to intrinsic carriers (valence to conduction band thermal excitations) can be calculated [86]. The concentration of intrinsic electron carriers n_i is a function of both band gap E_g and temperature T and given by the equation

$$n_i = \sqrt{N_c N_v} e^{-\frac{E_g}{2kT}} \tag{5.2}$$

Where N_c and N_v are the density of states for the conduction band and valence band respectively given by,

$$N_c = 2\left[\frac{2\pi m_e^* k_B T}{h^2}\right]^{3/2} \tag{5.3}$$

$$N_v = 2\left[\frac{2\pi m_h^* k_B T}{h^2}\right]^{3/2} \tag{5.4}$$

m_e^* and m_h^* are the effective mass of the electron and hole band, and k_B is the Boltzmann constant. At room temperature and for band gaps $\sim$3.0 eV, the expected conduction band density is < 1 cm^{-3}!

To explain the carrier densities observed, an additional donor mechanism is explored.

Hall Coefficient

Firstly it is essential to identify the nature of the charge carrier. The negative Hall coefficient states this conductivity is dominantly n-type, confirmed with a copper test sample using identical wiring geometry as the crystals.

Given ZSO is predicted to be a wide band gap insulator, the n-type conductivity is presumed to originate from doping, whether extrinsically or intrinsically. At high temperatures, the Hall coefficient indicates the presence of conduction electrons. However, as the temperature drops, the carrier density also decreases, suggesting a freeze out of donor states – not enough thermal energy is available to excite electrons from a donor state into the conduction band. Using semiconductor calculations [89] and some prior knowledge about the material, the energy of the donor level with respect to the conduction band can be determined. Furthermore, these calculations can also provide an insight as to whether charge compensation is occurring. The values for n obtained from Hall effect measurements provide a net carrier concentration. Over the range of temperature measured, carrier density is dominated by the ionisation of donors and expressed by equation 5.5 with N_d and N_a being the number of electrons in donor and holes in acceptor states. This method is valid, providing intrinsic electrons are excluded.

$$\begin{aligned} n &= -\frac{(N^* + N_a)}{2} + \sqrt{\frac{(N^* + N_a)^2}{4} + (N^*(N_d + N_a))} \\ N^* &= \frac{N_c}{2}\exp\left(-\frac{-E_c - E_d}{k_B T}\right) \end{aligned} \tag{5.5}$$

Where N_c is given by equation 5.3, E_c is the energy of the conduction band minimum set to zero and E_d is how deep in energy the donor state sits below the conduction band. The conduction band effective mass is assumed to be 0.22 m_e from band structure calculations displayed in chapter 2. Figure 5.3 shows the results of fitting equation 5.5 to the data.

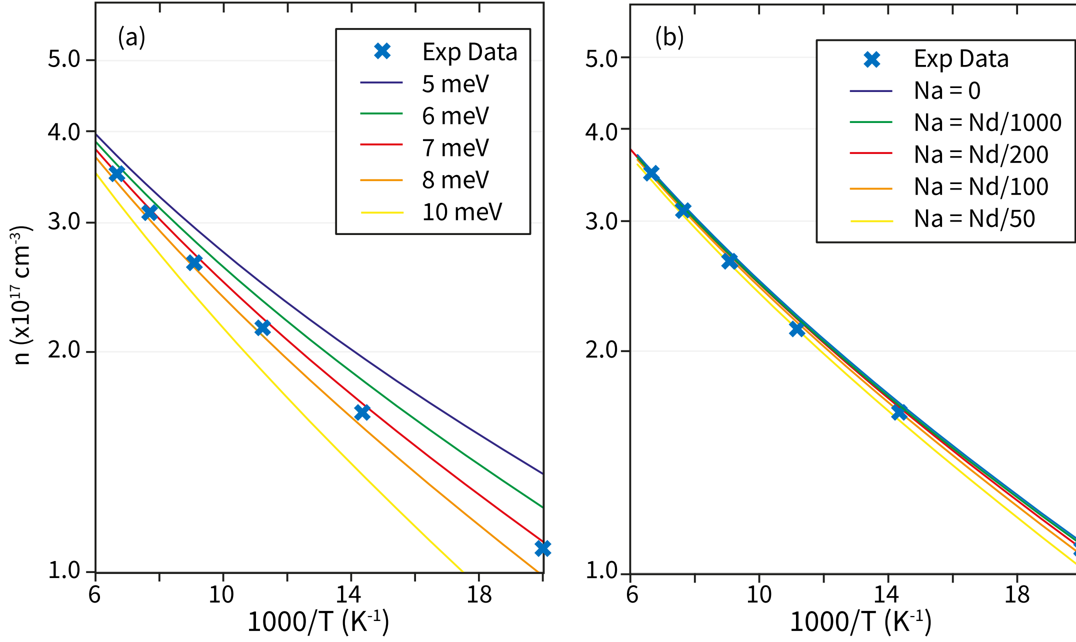

Figure 5.3: Fitting of equation 5.5 to experimental data for undoped ZSO. Fitting parameters $N_d = 8.2 \times 10^{17}$ cm^{-3}, $m^* = 0.22\ m_e$ (a) Assuming N_a is zero and adjusting the energy of the donor state E_d. (b) Setting the E_d to 7.0 meV and adjusting the number of acceptors.

Firstly it is apparent how significant, subtle variations in the value E_d makes to the fit. This obtained value of 7.0 $\pm$ 0.2 meV for crystal 64a signifies an extremely shallow donor level. The determination of the acceptor density is much less straightforward. Only when the acceptor density $N_a > N_d/100$ does it begin to impact the fitting, albeit detrimentally, contrasting with common semiconductor systems with deeper donor levels where slight changes in acceptor density profoundly affect the net carrier concentration [89]. Therefore the maximum acceptor density is assumed to be $N_a \sim N_d/100$. This calculation assumes a simple, one donor, one acceptor state system. It is possible a far more complicated situation occurs.

This study shows the donor level to be shallow; electrons can easily be thermally excited across the narrow gap even at low temperatures. However, it can not be ruled out that acceptor states are present in the ZSO system.

Mobility

The mobility plot in Figure 5.1 is indicative of semiconductor behaviour (Section 2.4). The two key influences on the mobility of a material are the thermal lattice vi-

brations (or phonons) and impurity scattering. At low temperatures, where phonons possess less energy, impurity scattering is the dominant process. Electrons interact with positively charged scattering centres due to the Coulomb interaction. It becomes less significant at high temperatures as the electrons possess more energy and interact with the scattering centre for a shorter period. As the temperature increases the mobility increases until the thermal lattice vibrations become the dominant scattering process and the mobility reduces. Theoretically, for semiconductors, the lower temperature dependence on mobility should be $\propto$ $T^{3/2}$ and at higher temperatures $\propto$ $T^{-3/2}$ [89]. The temperature dependence for mobility in ZSO is determined by fitting two linear traces to a log μ vs log T graph displayed in Figure 5.4.

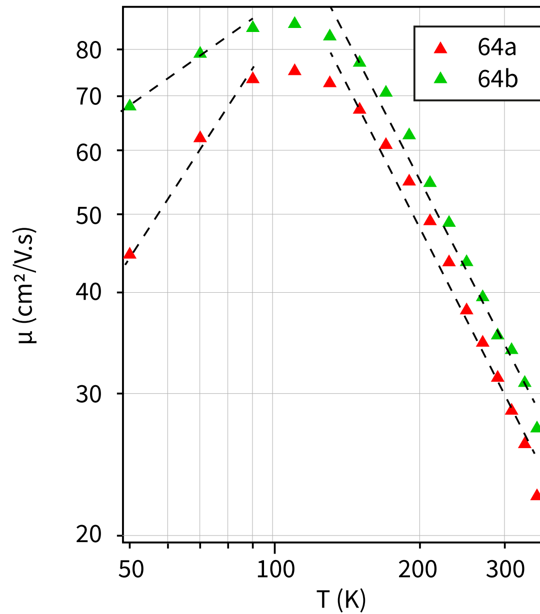

Figure 5.4: μ vs T for undoped ZSO with linear dependence traces displayed.

Table 5.2 displays the results obtained by a least-square fitting between 50 - 90 K and 130 - 350 K.

Table 5.2: Temperature dependence of Hall mobility in undoped ZSO crystals. ($\mu \propto T^{\alpha}$) for ZSO.

Crystal	α (low T)	α (high T)
64a	0.86 $\pm$ 0.09	-0.95 $\pm$ 0.01
64b	0.46 $\pm$ 0.10	-1.18 $\pm$ 0.01

Despite not agreeing with the expected dependence values, a positive and neg-

ative dependence is still observed at low and high temperature respectively. Below 110 K the phonon influence is overcome by the impurity scattering in a process explained above. At low temperatures there is a significant variation between the two data sets. Impurity scattering appears less dominant in crystal 64b suggesting less scattering centres. This would increase the relaxation time and create slightly higher mobility in this material ($\mu \propto \tau$).

The combination of mobility and the Hall coefficient contributes to the resistivity dependence ($1/\rho = \mu/R_H$). At higher temperatures, the constant carrier concentration and reduction in mobility induces a rise in resistivity. The minimum observed at $\sim$ 150 K originates from the donor electrons becoming saturated in the conduction band and a drop off in mobility as the temperature increases. At low temperatures ($<$ 100 K), both the carrier concentration and the mobility reduce and the resistivity spikes up to values exceeding 1 Ω.cm

Harrison [159] has previously measured the electronic properties of single crystal ZnO, with remarkably similar electronic properties to those presented in this study. In ZnO, temperature dependence for the resistivity exhibits a minima at a slightly higher temperature of $\sim$ 200 K. Hall measurements indicated a carrier density $\sim 10^{17}$ cm^3, again comparable to the data obtained for ZSO. The origin of this conductivity was determined to be due to both paired zinc and oxygen vacancies with additional oxygen vacancies.

Discussion

It is essential to understand the origin of the carriers in undoped ZSO. Intrinsic thermally excited electrons have been ruled out therefore, to be an n-type conductor, ZSO requires some form of donor. Electron doping can occur in several ways: an interstitial cation, oxygen vacancies, anion, or cation substitution. Nishiyama *et al* [37] conducted a study of three polycrystalline ZSO samples. The sample prepared in an oxygen-rich environment was determined to have the highest resistivity compared to a sample prepared in ambient and N_2 conditions, therefore concluding oxygen vacancies play a significant role. The following equation governs the proposed source of carriers.

$$O_o^\times \rightleftharpoons V\ddot{o} + \frac{1}{2}O_2 + 2e' \quad (5.6)$$

Which states oxygen vacancies ($V\ddot{o}$) and electrons (e') are formed as lattice oxygen ($O_o^\times$) becomes oxygen gas (O_2). Kikuchi *et al* [36] agreed with this conclusion and commented that these vacancies originated from poor crystallinity in powders therefore inducing cation disorder. Determining how this occurs in single crystal ZSO is not so simple, given crystallinity is presumed to be high. Kikuchi also suggested that cation disorder could be a direct provider for carriers with Sb^{+5} onto the Zn^{+2} site effectively providing three donor electrons. This disorder was attributed to creating lattice instability inducing oxygen vacancies therefore the actual mechanism remains undetermined.

An undoped single crystal was annealed in oxygen to investigate the relevance of oxygen vacancies in this system. Crystal 64b was annealed at 750 °C in flowing O_2 for twenty-four hours, and remeasured on the PPMS. The crystal showed no change in transport properties, indicating either the crystals are already fully oxidised, or the ionic mobility of oxygen through the ZSO lattice is low. This result is similar to that obtained by Galazka *et al* when measuring single crystals of In_2O_3 grown from the melt and by gas phase [160]. By measuring the electronic properties both before and after annealing in a non-reducing atmosphere, they found a significant difference in the melt-grown crystal's electronic properties. The gas-phase grown crystals were insensitive to heat treatment.

In contrast to this, Halliburton *et al* [161] conducted a similar study on CVT-grown ZnO single crystals and discovered that annealing in a Zn atmosphere could profoundly affect the electronic properties by inducing a ten-fold increase carrier concentration. They concluded that zinc interstitials or oxygen vacancies or a combination of the two formed due to the reducing atmosphere. Crystals grown by the CVT method may be sensitive to reducing under certain conditions however inert to oxidation. Future work on ZSO single crystals may help to understand this.

In chapter 4, the mass of precursor powders were recorded during the pre-reaction stage, and it was repeated shown the mass increase did not reach the ideal value. The starting powders entering the growth ampoule are possibly oxygen-deficient. Given the growth environment does not contain any extra oxygen, the deficiency in

powders would carry into the crystals.

If oxygen vacancies are assumed to be responsible for the electron donors and an oxygen vacancy provides two electrons, the stoichiometry of oxygen can be calculated. Figure 5.3 suggested a donor density N_d of $8.2 \times 10^{17}\text{cm}^{-3}$. Taking the volume of unit cell of ZSO V_{unit} to be 201.5 Å^3 [25] and each unit cell to contain two ZSO formulas the fraction of oxygen vacancies is calculated using

$$\frac{N_{V\ddot{o}}}{N_o} = \frac{N_d}{2}\frac{V_{unit}}{12} \approx \frac{1}{150,000} \tag{5.7}$$

where $N_{V\ddot{o}}$ is the density of oxygen vacancies and N_o is the density of oxygen sites in the lattice. Even very slight deviations from ideal stoichiometry would profoundly affect the conductivity in ZSO given how close in energy the donor state sits to the conduction band.

In a similar compound ZnO, the role of oxygen vacancies on the observed n-type conductivity has been debated a lot throughout the literature. Calculations have shown the defect state created by oxygen vacancies is deep in energy below the conduction band and therefore its role in the observed n-type conductivity was determined to be insignificant [48, 162]. However, more recent work has shown that despite sitting deep, doubly charged oxygen vacancies are crucial when discussing conductivity [163, 164]. Given it had taken over half a century of research and literature to arrive at this conclusion in a comparatively simple compound, it is likely that ZSO will not be solved soon. If applicable, however, shallow oxygen vacancies would explain the origin of n-type conductivity in ZSO.

There is also the possibility of an unintentional dopant entering the system such as hydrogen. King *et al* [165] determined hydrogen can exists as a shallow donor in In_2O_3 and SnO_2 and may be responsible for unintentional conductivity. Chemical analysis methods such as EDS employed by this project will not be able to detect light elements such as hydrogen. As the crystals are grown in a closed system without hydrogen it is hard to make the case that H doping is occurring. However, it cant be discounted entirely as water may have adsorbed into powders pre-growth.

5.1.2 Doped ZGSO

This section discusses the transport data collected for seven $Zn_{1\text{-}x}Ga_xSb_2O_6$ (ZGSO) crystals at a doping range (x = 0.01 - 0.10). Figure 5.5 displays the data with room temperature values listed in table 5.3.

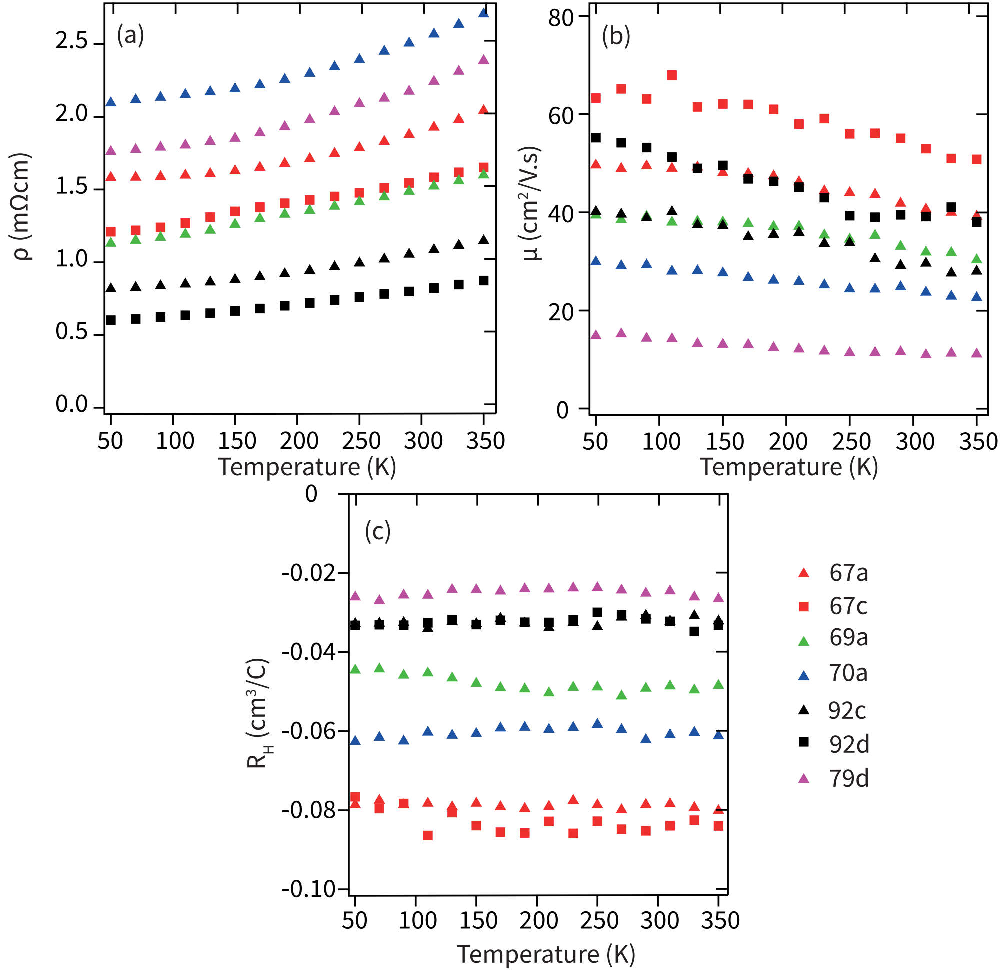

Figure 5.5: Electrical transport data for ZGSO crystals showing (a) resistivity ρ, (b) mobility μ and (c) Hall coefficient R_H plotted as a function of temperature.

Hall Coefficient

The temperature dependence of the Hall coefficients is in stark contrast to what was observed for the undoped crystals. Where previously a sharp drop in carrier concentration occurred, now almost no temperature dependence is seen. Within margins of the data fluctuations, the Hall coefficient remains constant because every ZGSO crystal is degenerately doped and the Mott criterion has been met. Even at low temperatures, the electrons are populating the conduction band. Due to a lack

Table 5.3: Room temperature electronic transport data for ZGSO crystals with varying x. * no temperature dependence of 99a is available however, the superior electronic transport properties are stated.

Crystal	Nominal doping (x)	ρ (mΩ.cm)	μ (cm^2/V.s)	n ($\times 10^{20}$cm^{-3})
67a	0.01	1.9 ± 0.4	41.2 ± 8.2	0.8 ± 0.2
67c	0.01	1.6 ± 0.3	54.1 ± 10.8	0.7 ± 0.2
69a	0.04	1.5 ± 0.3	32.5 ± 6.5	1.3 ± 0.4
70a	0.06	2.5 ± 0.5	24.3 ± 4.9	1.0 ± 0.3
92c	0.08	1.1 ± 0.2	29.4 ± 5.9	2.0 ± 0.6
92d	0.08	0.8 ± 0.2	39.3 ± 7.9	2.0 ± 0.6
79d	0.10	2.2 ± 0.4	11.2 ± 2.2	2.5 ± 0.7
99a*	0.08	0.5 ± 0.1	48.8 ± 9.8	2.4 ± 0.7

of prior research into the material, the relative permittivity is unknown therefore, an accurate critical carrier concentration at which the Mott transition occurs in ZSO is undetermined. An estimate is made by looking at values in other TCO compounds and applying the assumption that ZSO has a similar value. In ITO, Edwards *et al* determined $\epsilon_r = 4$ corresponding to a critical carrier concentration n_c to be approximately 8×10^{18} cm^{-3} [50]. Given this carrier concentration is an order of magnitude lower than those in ZGSO crystals, it can be reasonably assumed they are degenerate semiconductors.

The Hall coefficient's absolute values are smaller than in the undoped crystals and, consequently, the carrier concentrations are larger ($R_H \propto n^{-1}$). This assumes the only source of carriers in the Hall effect to be electrons. How the Hall coefficient varies as a function of doping is discussed in section 5.1.3.

Mobility

Like the Hall coefficient, the mobility temperature dependence differs when compared to the undoped samples. A slight reduction in the mobility at high temperatures occurs due to thermal lattice scattering, similarly to the undoped samples.

However, the low-temperature dependence does not carry the same negative trend; a direct consequence of being doped beyond the point of degeneracy. The conduction electrons are effectively electrostatically screened from the ionised impurities, and little temperature dependence is observed despite a higher density of scattering centres [90, 91]. Perkins *et al* [91] carried out a study on the gradient of the mobility versus temperature for In:ZnO thin-films with carrier concentrations spanning three orders of magnitude. They concluded there should be a negative temperature dependence for mobility as the concentration increases and became almost independent at carrier concentrations $n > 5 \times 10^{21}$ cm^{-3}. Ambrosini *et al* [166] reached the same conclusion measuring $In_2O_{3-\delta}$. For ZGSO, this effect is unclear due to the noise in the data and the comparatively small range in the crystal's carrier concentrations. The magnitude of the mobility is further explored in section 5.1.4.

The combined effect of a constant carrier concentration and a steady decrease in mobility upon elevating temperature creates a metallic-like resistivity dependence. At high temperatures, the resistivity follows a near-linear trend; however, the curve begins to flatten off at lower temperatures as the mobility also does. Although the limit of data collection is 50 K, a sharp increase in resistivity is not expected even at cryogenic temperatures. Once again, a consequence of the samples being electron doped beyond the Mott criterion.

The absolute value of resistivity has reduced nearly three orders of magnitude with gallium's inclusion as a dopant signifying the apparent success of the doping. Upon doping, the crystal has moved from a semiconductor with very shallow donor states to a degenerate semiconductor with metallic-like properties due to a significant electron population of the conduction band.

5.1.3 Nominal doping vs Measured Carrier Concentration

The nature of substitutional doping suggests a consistent increase in carrier density is expected as the doping is exaggerated. Displayed in Figure 5.6 is the room temperature carrier concentration n plotted against the nominal doping for ZGSO crystals.

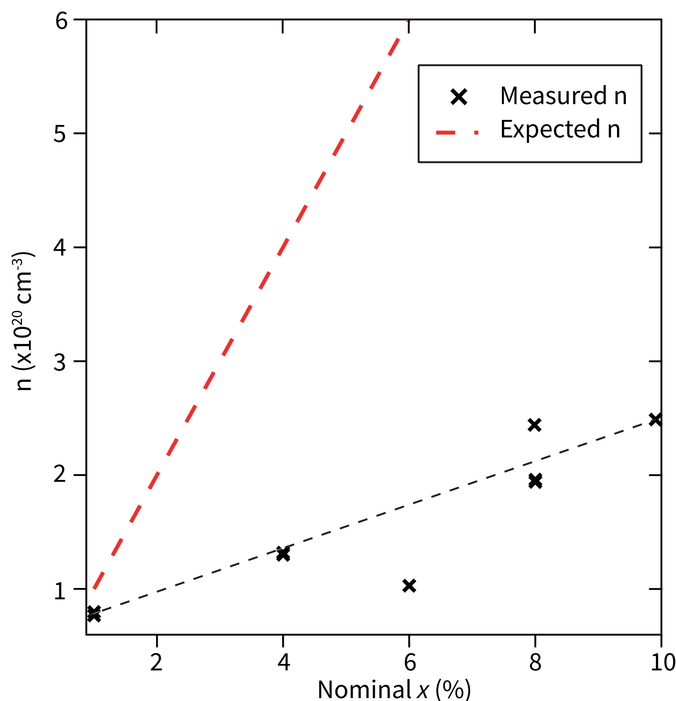

Figure 5.6: Room temperature carrier concentration n versus the nominal doping of the ZGSO crystals. A least-square fitting of the data is displayed ignoring the x = 0.06 value. Errors for n are included in table 5.3.

The expected n line comes from the idea that each Ga substituting with Zn should create an extra electron per formula unit. For crystal 70a (x = 0.06), the data included in the figures is omitted from the discussion until the end of the chapter as its behaviour is anomalous and provides an interesting case study.

The data suggests a positive trend concerning nominal doping is observed, albeit quite substantially less than expected. A least-squares fit to the data suggests ∼0.25 e^- / gallium. There are several possible explanations for this discrepancy. Firstly, the actual gallium content is less than the nominal doping suggests indicating not all of the gallium is successfully transporting into the crystals. Secondly, it can also imply the precursor powders are Ga deficient due to some evaporation loss in the powder preparation method. Given the high melting point of Ga_2O_3 and the excess added into the growth, it is considered unlikely.

Finally, this discrepancy can be explained if charge compensation occurs in the crystal. Carrier densities obtained from the Hall effect are a net value summed over negative electrons and positive holes. Cation vacancies would behave as acceptors increasing the hole concentration, although this scenario is less likely due to the

high density of single crystals. Excess oxygen of around 0.02 per formula could dope sufficient holes into the material; a distinct possibility given the flexibility of oxygen content in oxide materials [167]. Another scenario is cation disorder; Sb^{+3} has a similar ionic radius to that of Ga^{+3} [168], which could be substituted onto the Zn-site, forcing Ga^{+3} onto the Sb^{+5} site. Presuming an oxygen stoichiometry of 6.00, would increase the antimony's average charge, reducing the carrier density. Around 2% (atomic) of Ga^{+3} on the Sb site could account for the discrepancy.

Nonetheless, it has been shown that nominal doping values do not correctly portray the carrier concentration n. As the electronic properties are dependent on the latter property, n, it is more concise to use this in the analysis. A further discussion of this is carried out in section 6.1 when the samples' chemical composition is explored.

5.1.4 Carrier Concentration vs Mobility/Resistivity

Figure 5.7 shows the resistivity and Hall mobility for the ZGSO crystals plotted against n with the colour scale representing nominal doping. Most error bars are omitted but are found in table 5.3.

Initially the resistivity versus carrier concentration is reviewed. Providing the mobility μ is constant, as the carrier concentration n is increased, the resistivity ρ is expected to decrease with an inverse dependence ($\rho^{-1} = ne\mu$). The linear dotted lines highlight these fits for 50 and 30 $cm^2/V.s$. This linearity is not the case in degenerate semiconductors. Ellmer and Mientus [169, 170] conducted a study on the mobility dependence on carrier density for single crystal ZnO, In_2O_3, and SnO_2. Given the lack of data available for ZSO and the fact these three are all TCO's, it is reasonable to compare them. Over an extensive range of carrier densities (10^{15} - 10^{21} cm^{-3}), a step-like drop in mobility is expected as the carrier concentration increases. However, over the span of carrier concentrations that ZGSO crystals possess, only a small drop is expected. An approximate predicted drop for ZnO is highlighted in Figure 5.7 to provide perspective. This drop was attributed to increased ionized impurity scattering [88]. The increase in the number of carriers is accompanied by a rise in scattering centres and, therefore, scattering rate. As the scattering rate is inversely proportional to the mobility, a slight drop is expected

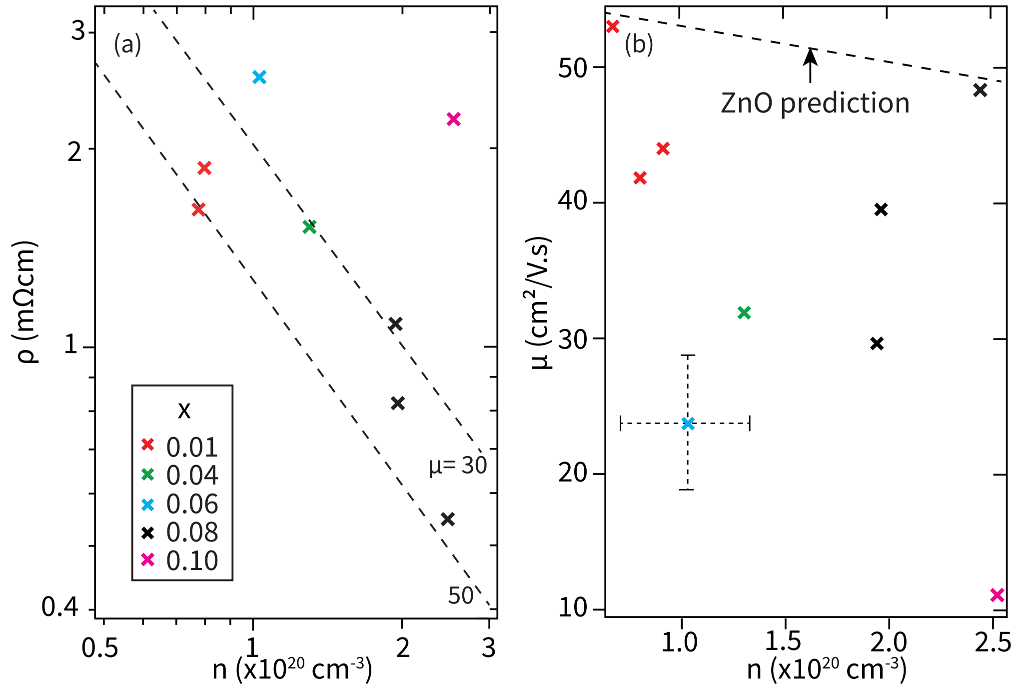

Figure 5.7: (a) Room temperature resistivity versus carrier concentration of ZGSO crystals. (b) Mobility versus carrier concentration. An example error bar is displayed. The ZnO prediction dotted line is taken from Ellmer and Mientus [169, 170].

even considering conduction electrons screening. The data for ZGSO suggests little correlation between the mobility and carrier density. The highly doped sample ($x = 0.10$) does exhibit a significant decrease in mobility however, this sample is assumed to have a high density of defects due to being over-doped, raising the scattering rate significantly while maintaining the high carrier density.

Table 5.4 displays the most conducting ZGSO crystal and two highly conducting TCOs from the literature (AZO = Al:ZnO).

Table 5.4: Room temperature resistivity, Mobility and carrier concentration data for a highly conducting ZGSO single crystal with literature values for two conducting TCO thin-films.

TCO	ρ (m.Ω.cm)	μ (cm^2/V.s)	n ($\times 10^{20} cm^{-3}$)
99a*	0.5 ± 0.1	48.8 ± 9.8	2.4 ± 0.7
ITO [171]	0.089	54.1	13
AZO [172]	0.085	47.6	15

Both TCO's used for comparison are thin-films created using the pulsed laser

deposition method. The ZGSO single crystal has a resistivity an order of magnitude larger than both thin films. Given the mobility is comparable for all three samples, the variation in resistivity stems from the carrier concentration. These values are far larger than any carrier concentration achieved in ZGSO. In an ideal scenario, with no charge compensation it would require doping of $x = 0.13$ and $x = 0.15$ to obtain these carrier concentrations. However, it has been shown in the $x = 0.10$ sample, that high levels of doping induces additional disorder.

The structure of the lattice is likely to prevent ZGSO attaining carrier concentrations comparable with those seen in ITO. The density of zinc sites in ZGSO is $\sim 10^{22}$ cm^{-3}. The density of indium in In_2O_3 is $\sim 6\times10^{22}$ cm^{-3} [173]. Assuming the same doping mechanism, the same carrier concentrations can be achieved in ITO with a fraction of the doping required for ZSO.

Galazka *et al* [174] reported melt grown single crystal La:$BaSnO_3$ with a similar resistivity to sample 92d but with a carrier concentration more than five times smaller (3.3×10^{19}cm^{-3}). This arises from an exceptionally high mobility $\sim$ 220 cm^2/V.s. They reported nearly complete electrical activation of La with almost no compensation. Improvements to the mobility in ZSO by refinement of the synthesis should further reduce the resistivity where the structure may be a limiting factor achieve higher carrier densities.

5.2 Optical Properties

5.2.1 Transmission and Absorption Coefficient

The optical properties, particularly the absorption coefficient in the visible range (550 nm) and the absorption edge/optical band gap were studied using UV-Vis spectroscopy. Two undoped (64a and 96a) and four doped crystals (67a, 92c, 92d and 99a) were measured. Figure 5.8 displays the obtained transmission data for the crystals. All transmission measurements were carried out at room temperature.

The literature of TCOs is significantly dominated by thin-films studies and often shows TCOs to have very high transparency $\sim$90 % [92, 93, 175], far higher than the ZGSO crystals displayed. Transmission alone is misleading as it is a function of the sample thickness (equation 2.30). Therefore, transparency must discussed in

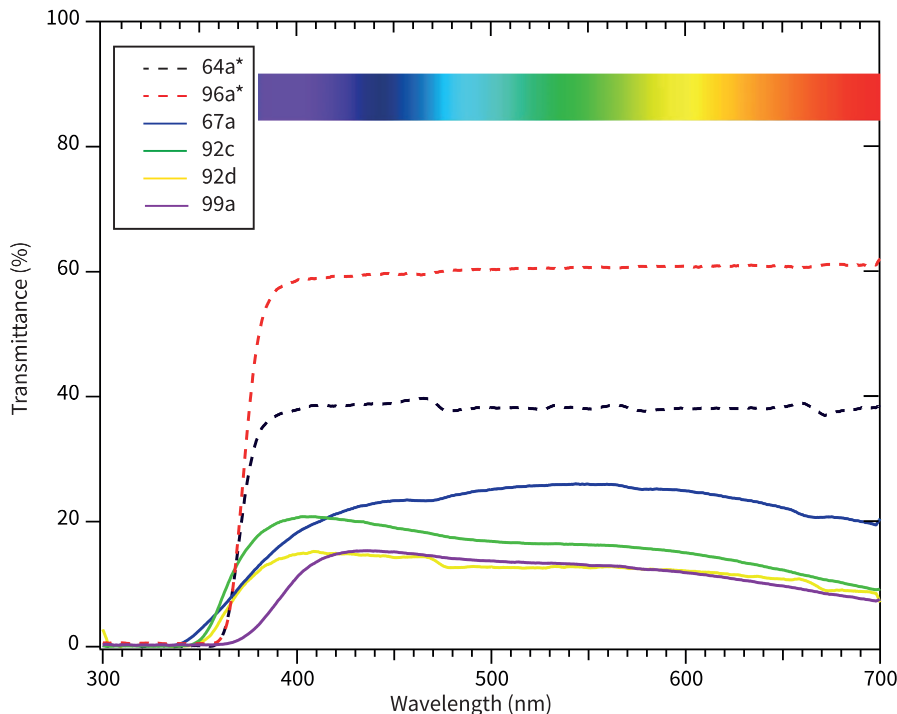

Figure 5.8: Transmission data for ZSO and ZGSO samples as a function of wavelength between 300 and 700 nm. * indicates an undoped sample.

absorption coefficient terms if optical properties are to be compared. Similarly, it is unfair to compare each crystal using transmission alone as the measured samples have slightly different thickness. Table 5.5 shows obtained transmission data at 550nm with corresponding absorption coefficients.

Table 5.5: Transmission T, thickness d and absorption coefficient α for ZGSO crystals at 550nm. * signifies undoped ZSO crystals.

Crystal	x	T (550nm) %	d μm	α (550nm) cm^{-1}
64a*	0.00	38.0	180	53.7
96a*	0.00	60.6	392	13.1
67a	0.01	26.0	202	66.7
92c	0.08	16.3	168	109.3
92d	0.08	12.8	120	171.2
99a	0.08	12.8	140	145.6

Figure 5.8 indicates the undoped samples have a higher transmittance in the visible range when compared to the doped counterparts further reinforced by the low absorption coefficients. It is therefore indisputable that doping is detrimental

to transparency. Another clear difference between doped and undoped samples manifests itself at the low energy end of the transmission data. Doped samples exhibit an increase in absorption at wavelengths approaching the infrared, which is potentially a problem as the crystals are coloured blue due to this. This trend is common in TCO compounds; however, the absorption onset occurs at shorter wavelengths in ZGSO than other compounds, usually $\sim$ 1000 nm [52, 176, 177].

Generally, two processes create low energy absorption: free carrier absorption, where conduction electrons are excited to higher unoccupied states [178, 179], or opacity of the material for low energy photons governed by the plasma frequency calculated in equation 5.8.

$$\omega_p = \sqrt{\frac{ne^2}{\epsilon_o m^*}}[\text{rad/s}] \tag{5.8}$$

Using an effective mass of 0.22 m_e, table 5.6 displays the three calculated plasma frequencies. The undoped samples are omitted due to having little physical relevance.

Table 5.6: Calculated plasma frequency for the three doped samples, $m^* = 0.22$ m$_e$.

Crystal	ω_p (eV)	ω_p (nm)
67a	0.71 ± 0.06	1758 ± 499
92c	1.10 ± 0.11	1126 ± 348
92d	1.11 ± 0.15	1118 ± 410

These calculated plasma wavelengths are longer than those measured in this experiment; therefore, the plasma frequency is assumed to be the cause of this absorption at visible light energies. The reduction in transmission towards the IR range is attributed to be almost solely due to free carrier absorption. Electrons residing in the conduction band are excited to higher energy unoccupied bands.

Peelaers *et al* [179], paying reference to SnO_2, discussed the origin of this free carrier absorption. The energy gap between the CBM and CBM + 1 is of the order of 4 eV and therefore, direct transitions ($\Delta k = 0$) were not considered significant. Instead, they examined indirect transitions where a scattering mechanism provided additional momenta, allowing lower energy photons to excite conduction electrons into higher unoccupied bands. These mechanisms are phonon scattering and im-

purity scattering. Because phonon scattering is intrinsic to the material, it would remain unaffected even if the crystal quality is improved [178]. At carrier densities comparable with those obtained for ZGSO crystals, impurity scattering becomes significant. A higher density of scattering centres generates a larger degree of free carrier absorption, enhanced significantly if charge compensation occurs.

Crystal 67a, where the free carrier absorption appears considerable, is likely to have a higher density of scattering centres than the other doped crystals purely due to low crystal quality. This is further clarified when the absorption edge is discussed in section 5.2.2.

An important point to note is there appears to be a difference between the absorption coefficients in table 5.5 for the two undoped crystals. The high α value is attributed to crystal 64a being unclean during measurement. Crystals were previously characterised using an optical transmission microscopy arrangement at UCL ChemEng department with the capability to measure transmission over the range of 380 - 700 nm. Figure 5.9 displays the transmittance data for three crystals measured using UV-Vis spectroscopy and optical transmission microscopy. Transmission data is in reasonable agreement for the two methods apart from sample 64a where transmission is over 50 % higher in the microscopy data than the UV-Vis spectroscopy data. The large mismatch in data for the two 64a measurements leads to the conclusion that this sample's UV-Vis data is unreliable, possibly due to surface contamination. Therefore, optical characterisation on this crystal is omitted for the remainder of the chapter.

Fluctuations in the transmission microscopy data occur due to multiple reflections at the front and back surface of the crystal interfering with each other when the sample thickness is uniform [180]. The microscopy beam spot size is 50 μm^2, compared to several millimetres for UV-Vis. During microscopy measurements, the small spot size impinges on a smaller region of crystal with uniform thickness. Over the large spot size used in UV-Vis, the sample thickness is likely to change slightly and dampen any interference effects.

The absolute value of the absorption coefficient at 550 nm for the undoped ZSO sample is compared to other TCO host lattices. Jain *et al* [101] reported In_2O_3 and SnO_2 thin films to have absorption coefficients of 5230 and 7410 cm^{-1}, respectively.

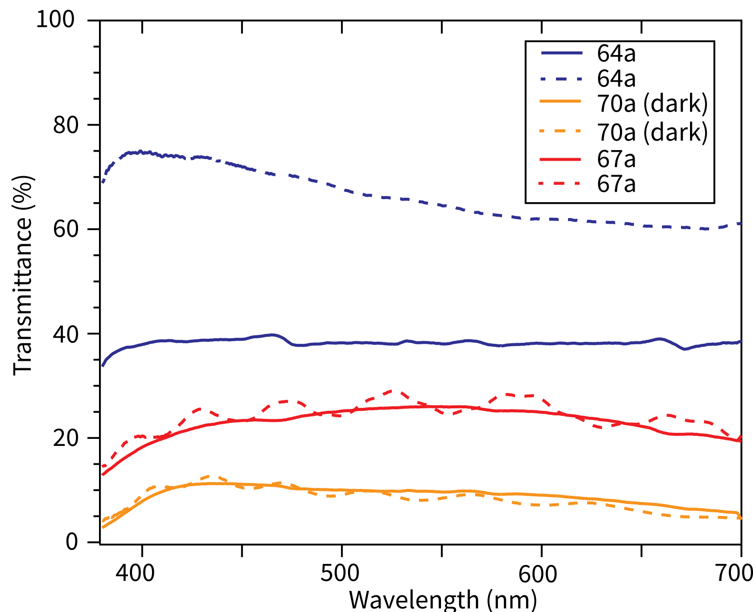

Figure 5.9: Transmission data using UV-Vis spectroscopy (solid line) and optical transmission microscopy (dashed line) for three single crystals. 70a (dark) refers to a region on the crystal covered at the end of the chapter.

Using this data it would appear the undoped ZSO is far more transparent than these other lattice counterparts; however, it may not be reasonable to compare single crystal and thin-film data.

Galazka *et al* produced melt grown single crystals of In_2O_3 [160] and $BaSnO_3$ [174] which exhibited very low absorption coefficients at 550 nm (< 5 cm^{-1}). The In_2O_3 was also grown under a gas phase and exhibited lower transmission than their melt grown counterparts ($\alpha \sim 11$ cm^{-1}). This has a possible implication that vapour grown ZSO are comparable with other TCO host lattices and, like In_2O_3, may be improved further by growing from techniques such as melt growth.

5.2.2 Optical Band Gap

Displayed in table 5.7 are values for the optical band gap of ZSO obtained from the literature. The variety suggests no agreed value for the optical band gap likely due to the varying morphologies of the samples measured. Calculation methods such as density functional theory (DFT) commonly underestimate the values for semiconductor band gaps.

Similarly, the effect of doping on the band gap is also unresolved. Arunkumar

Table 5.7: Optical band gaps of ZSO obtained from literature. * indicates the values were calculated computationally. Experimental band gaps were obtained using UV - Vis diffuse reflectance spectroscopy.

Literature	Morphology	Optical Band Gap eV
Dutta *et al* [33]	Nanoparticles	2.91
"	-	3.5 *
Liu *et al* [176]	Nanoparticles	3.3
"	-	0.84*
Matsushima *et al* [34]	Polycrystalline Powder	3.1
"	-	0.9*
Arunkumar *et al* [31]	Polycrystalline powder	3.35
Kikuchi *et al* [36]	Thin-film	3.0
Mizoguchi *et al* [107]	Polycrystalline Powder	3.5
"	-	1.8 *

et al [31] measured a reduction in band gap down to 2.82 eV upon doping with nitrogen. They attributed this reduction to N 2p states sitting higher in energy than the O 2p host lattice valence band. However, this doping mechanism is less relevant to that employed by this thesis.

The optical band gap for ZSO and ZGSO is determined using the appropriate methods described in section 2.6. However, the interpretation of Tauc plots can prove a challenge. This method has known difficulties with linear extrapolation, particularly between the points where extrapolation starts and ends. Weidner [181] covered this issue regarding SnO_2 and explained why ambiguity in the extrapolation point led to band gaps ranging from 3.6 - 4.4 eV in literature [175, 182]. A common practice in thin-film analysis is to fix a cut-off $(\alpha h\nu)^{1/r}$ value and extrapolate down to the intercept of zero intensity, the abscissa of this intercept providing the E_g values.

Figure 5.10 displays the absorption edge data for the five crystals displayed as α vs $h\nu$ and α^2 vs $h\nu$. A standard cut-off intensity for linear extrapolation was not possible in this case owing to the varying intensities between samples. Instead, a least-squares method was employed fitting a linear line with a maximum value chosen to be 90 % of the absorption edge maximum with errors assigned to be 1 % of the measured best fit.

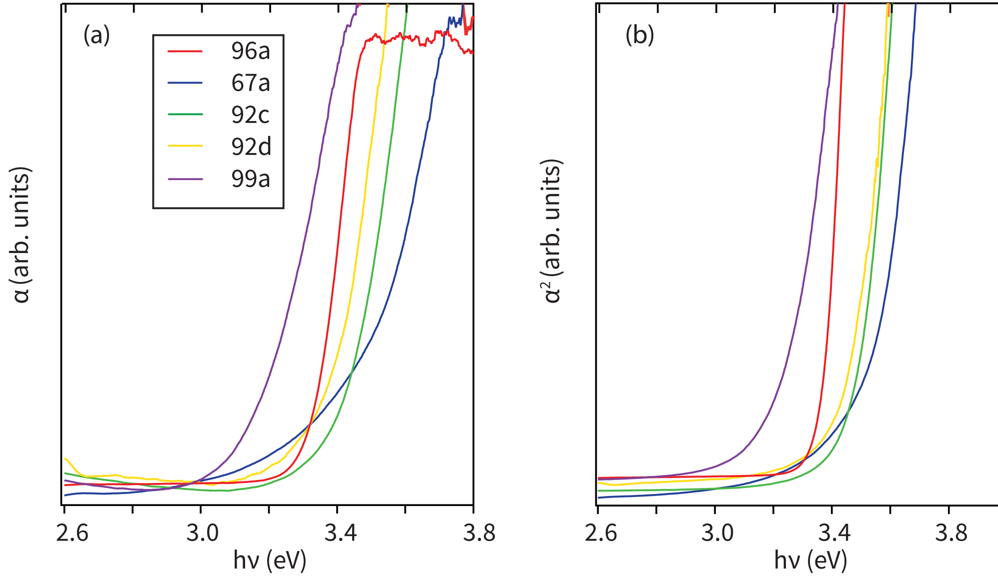

Figure 5.10: (a) absorption coefficient α versus $h\nu$ (b) α^2 versus $h\nu$.

Table 5.8 displays the extrapolated intercept values and optical band gaps calculated from the Dolgonos method (section 2.6). This method is not applied to the undoped sample 96a as it not a degenerate semiconductor. The optical band gap for this crystal is determined by conventional Tauc analysis.

Table 5.8: Experimentally determined optical band gap values obtained from α and α^2 vs $h\nu$ plots following the method described in the text.

Crystal	α (eV)	α^2 (eV)	Optical Band Gap (eV)
96a (x = 0.00)	3.32 ± 0.03	3.38 ± 0.04	3.38 ± 0.04
67a (x = 0.01)	3.42 ± 0.03	3.53 ± 0.04	3.64 ± 0.05
92c (x = 0.08)	3.43± 0.03	3.49 ± 0.03	3.55 ± 0.04
92d (x = 0.08)	3.38 ± 0.03	3.46 ± 0.03	3.54 ± 0.04
99a (x = 0.08)	3.15 ± 0.03	3.24 ± 0.03	3.33 ± 0.04

The most significant point to make here is the optical band gap for all samples lies comfortably in the UV - Vis region of the spectrum, one of the essential requirements for a transparent conducting oxide. The optical band gap in ZGSO single crystals have been experimentally proven to be wide enough to allow transparency through the visible light range.

The nature of the fundamental band gap in ZSO is also unclear in the literature. Matsushima *et al* [34] claimed ZSO may have a direct-forbidden band gap. Similarly Dr. Adam Jackson, the computational collaborator, indicated the strong onset of optical absorption may occur below the valence band maximum. This project is focused on the optical band gap and therefore, on the direct-allowed transition (r = 2) from section 2.6. However, a measurement of the direct-forbidden band gap (r = 2/3) for the undoped material is provided to suggest the fundamental band gap in ZSO is dipole-forbidden.

Figure 5.11 displays the absorption edge data for the undoped sample plotted to determine the direct-forbidden band gap. A linear extrapolation reveals a direct-forbidden band gap lying at 3.31 ± 0.02 eV, indicating the onset of strong optical transitions occurs ∼ 60 meV below the valence band maximum.

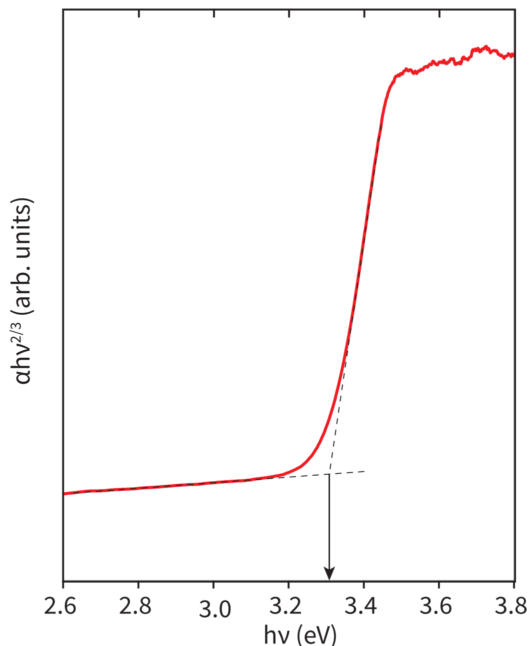

Figure 5.11: Tauc plot for undoped sample 96a used to estimate the direct-forbidden band gap indicated by the arrow.

The remainder of this discussion focuses on the values for direct - allowed transitions. Except for crystal 99a, it is clear the absorption edge, and therefore the optical band gaps have shifted to higher energies upon doping, caused by the Burstein – Moss effect. Figure 5.12 displays the energy shift of the absorption edge for the three doped crystals with respect to the fundamental absorption edge of undoped ZSO, plotted against their measured carrier concentrations n. The red dotted line

indicates the expected Burstein – Moss shift for a conduction band of 0.22 m_e.

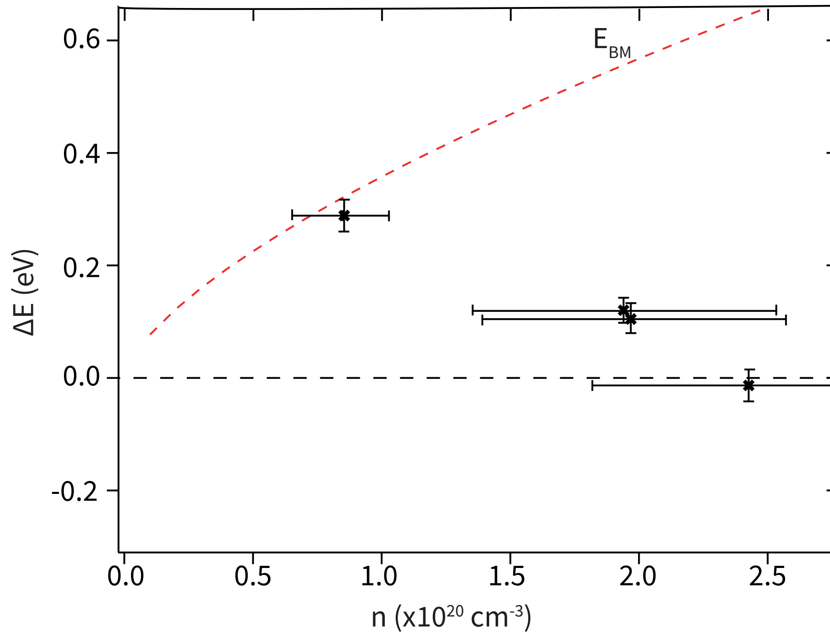

Figure 5.12: Optical band gap shifts versus carrier concentration with the undoped band gap set as 0.0 eV. Displayed also is the expected Burstein– Moss shift, E_{BM} for an effective mass of 0.22 m_e.

The weakly doped sample has an optical band gap shift close to what is expected due to the Burstein – Moss effect. However, in the higher doped samples, a significant suppression of this shift is observed and even a reduction in the highest doped sample. In part, this effect can be attributed to band gap renormalisation effects occurring in materials with a carrier density above the Mott criterion [58]. The crystals are degenerate, which implies this possibility should be considered.

However, the literature suggests that the origin of band gap renormalisation in oxide semiconductors is unresolved [55, 58, 61, 66, 69, 181]. Walsh *et al* [58] conducted a study on the effects of Sn and Ge doping into the In_2O_3 lattice. They determined both deviations from a parabolic band model and dopant choice have profound effects on the expected optical band gap shift. When the conduction bands effective mass is increased, the Fermi level is shifted higher in energy at a slower rate upon conduction band filling. This theory implies an increase in optical band gap upon doping, albeit slower than expected. Therefore, although this cannot be discounted at this stage, it does not explain why highly doped samples have a reduced shift compared to the weakly doped. Similar to the theory proposed by

Walsh, Lebens-Higgins *et al* [69] conducted a study on La:BaSnO3 (BLSO) and observed an increase in optical band gap, smaller than would be expected from the Burstein – Moss effect. However, DFT calculations and photoemission experiments showed this to originate from electrostatic interactions between the valence band and conduction electrons, not from a changing conduction band dispersion.

Two studies in the literature exhibit a similar optical band gap shift vs carrier density trend to ZGSO. Saw *et al* [61] conducted a study on In:ZnO and observed, at low carrier densities $\sim 10^{19}$ cm^{-3}, the absorption edge shift follows the Burstein Moss shift, however, as $n \rightarrow 10^{21}$ cm^{-3} the trend became negative as the effects of renormalisation increased. An increasing potential between the host lattice and donors effectively reduced the optical band gap. Similar to what was discussed by Lebens-Higgins [69].

The second study analysed is one carried out by Jiang *et al* on N:SnO_2 [66]. They observed a reduction of the band gap for increasing carrier concentrations, similar to this study. The change in the optical band gap was modelled using the Burstein – Moss effect and with the renormalisation calculated using an electron-electron exchange interaction E_g^{ee} determined by Camassel [67]

$$E_g^{ee} = \left(\frac{e^2}{2\pi\epsilon_r\epsilon_o}\right)\left(\frac{3}{\pi}\right)^{1/3} n_e^{1/3} \tag{5.9}$$

where ϵ_r is the material static dielectric constant, ϵ_o is the permittivity of free space and n_e is the electron density. The electron-impurity interaction E_g^{ei} was modelled using the expression from Hwang [68]

$$E_g^{ei} = \left(\frac{\pi^{4/3}\hbar^2}{3^{1/3}}\right)\left(\frac{1}{m_{vc}^*}\right) n_e^{2/3} \tag{5.10}$$

where m_{vc}^* is the effective carrier mass. These interactions combined have the effect of suppressing the optical band gap shift. Modelling using these three interactions only allows an increase in optical band gap with increasing carrier concentration albeit very small.

However, their negative trend was attributed to an additional interaction affecting the absorption edge position, the Urbach tailing [183], first described by Franz Urbach in 1953. A common problem in semiconductors, mainly oxides, is a high defect and grain boundary density, the latter being less relevant in this project as

these are not amorphous samples. The deviation from an ideal bulk crystal structure creates a decaying density of states extending into the band gap and causes absorption below the fundamental band gap [184–186]. Ionised impurities exhibit an attractive Coulomb force on conduction electrons and repulsive force on the valence electrons which perturb band edges. The Urbach tailing has been attributed to the apparent change in absorption edge position in SnO_2 [187] and In_2O_3 films, without any change in carrier concentration, in contrast to the band filling model.

The optical band gaps in samples with more disorder appear to shift to lower energies without necessarily a change in the fundamental band gap. Urbach tailing describes the absorption coefficient below the band gap and is given by

$$\alpha = \alpha_o \mathrm{exp}\left(\frac{h\nu}{E_u}\right) \tag{5.11}$$

where α_o is a characteristic material parameter and E_u is the Urbach energy, which describes the exponential band tail width. When plotted on a $\log(\alpha)$ vs $h\nu$ graph, this exponential tailing manifests as a linear region. Equation 5.11 indicates the inverse of the gradient for this linear region reveals the Urbach energy. Figure 5.13 displays a schematic of the Urbach effect in a simple band structure.

Upon measuring the Urbach energies E_u for various doping levels of N:SnO_2, the optical band gap shift ΔE was accurately modelled using equation 5.12

$$\Delta E = -E_u + E_g^{BM} - E_g^{ei} - E_g^{ee} \tag{5.12}$$

The absorption edge data for ZSO is plotted in logarithmic form to determine if Urbach tailing is occurring. Figure 5.14 displays an example of the linear trend below the optical band gap in crystal 99a. Values for the Urbach energy are displayed in table 5.9.

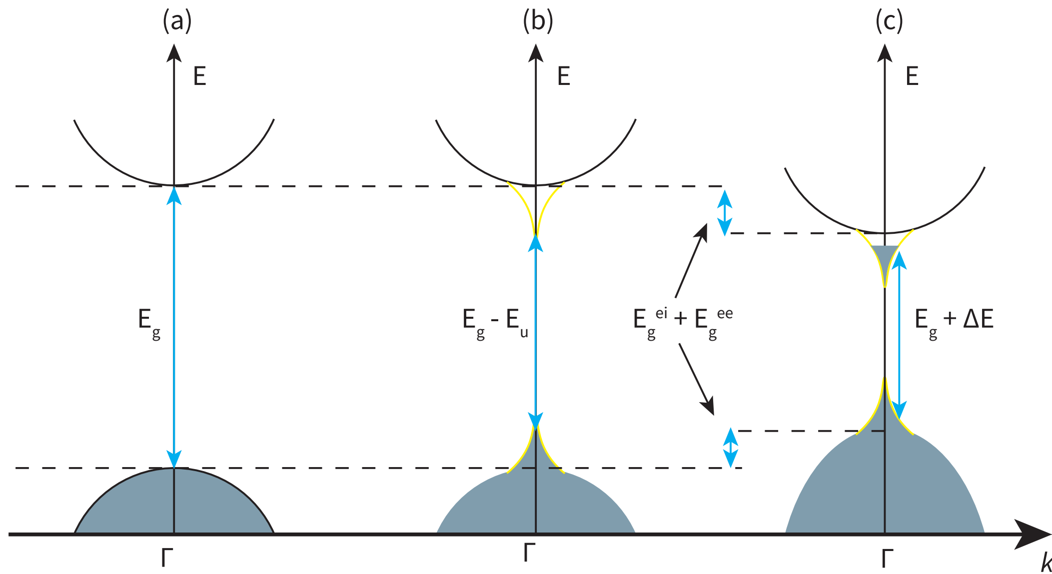

Figure 5.13: (a) Simple undoped band structure showing occupied (shaded) valence band and unoccupied conduction band. (b) Urbach tails highlighted in yellow showing a reduction in the band gap. (c) Adjusted band gap showing the effects of band gap renormalisation, Urbach tailing and conduction band filling. The figure is adapted from Jiang *et al* [66]

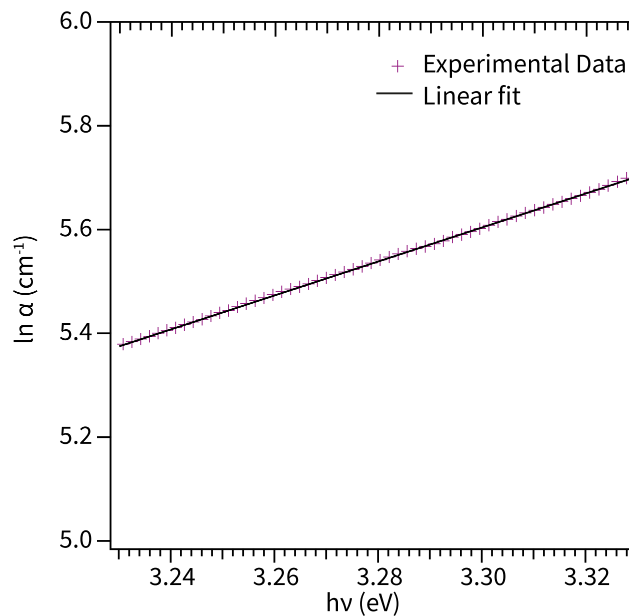

Figure 5.14: ln(α) vs $h\nu$ data for sample 99a plotted for 100 meV below the calculated optical band gap.

For consistency, the Urbach energies were extracted using a least-squares fit of

Table 5.9: Urbach Energy (E_u) for ZGSO crystals. (* indicates undoped ZSO)

Crystal	E_u (meV)
96a*	81
92c	181
92d	214
99a	305

the twenty-five data points below the band gap, the inverse of slope equal to E_u.

The doped samples have larger Urbach energy values when compared to the undoped sample. This is expected as doping inherently creates disorder. Furthermore, the sample with the largest Urbach energy, 99a, has the most significant optical band gap shift suppression. The rise in carrier density is accompanied by the increase in Urbach energy which can qualitatively explain the optical data observed. Additional analysis to compare theory and experimental data is hindered due to unknown material constants such as the static dielectric constant.

Crystal 67a, nominally doped $x = 0.01$, is not adequately described using the Urbach empirical formula. In a $\log(\alpha)$ vs $h\nu$ plot (Figure 5.15), no linear trend below the absorption edge is observed and therefore an Urbach energy is not obtained. The absorption edge for this sample is unique compared to the other measured samples (Figure 5.10). Despite the Dolgonos method revealing an optical band gap to be 3.55 eV, the onset of absorption occurs at a far lower energy ~ 3.0 eV creating a broader absorption edge. The transmittance spectrum in Figure 5.8 further reiterates this point where unlike the other doped samples, the peak transmission occurs in the green portion of the spectrum as absorption at blue wavelengths is enhanced.

In this crystal, the optical band gap is shifting due to the Burstein – Moss effect however an additional mechanism is causing absorption at lower energies creating a broad absorption edge.

Broadening of the absorption edge has been observed in other similar TCO compounds such as ITO and ZnO [160, 188–190]. There are many attempts in the literature trying to explain this effect's origin and paying particular reference to ZnO; the possible mechanisms are discussed. Wei *et al* [162] predicted native point defects such as oxygen vacancies (V_o) to be responsible for near-edge absorption

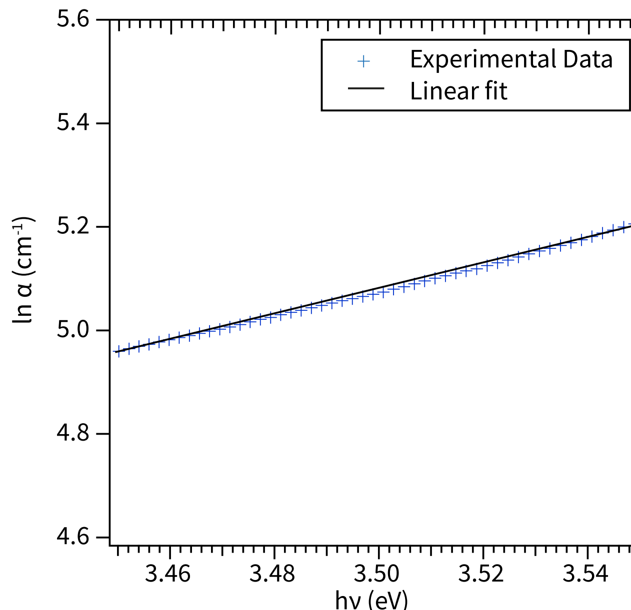

Figure 5.15: $\ln(\alpha)$ vs $h\nu$ data for 67a plotted for 100 meV below the calculated band-gap.

causing this apparent red-shift, a view shared by Mycielski *et al* [191]. More recently, Irmscher *et al* [188] observed this effect and attributed it to Mie scattering of light off spherical Zn nanoparticles formed during CVT growth, removed with a high-temperature anneal. Although this theory cannot be ruled out in the ZGSO crystal, the nanoparticles in ZnO created a significant larger degree of broadening to what is observed in this study and therefore is considered an unlikely mechanism. Most likely, a deep gap defect is prevalent in this crystal, causing the onset of absorption at lower energy [161]. This defect may also be responsible for the increased scattering creating the free carrier absorption.

5.3 Figure of Merit

Combining the electrical transport and absorption coefficient data, a figure of merit (FOM) is determined. Table 5.10 displays the resultant FOM for four ZGSO crystals calculated using the equation from section 2.7.

$$F = \frac{1}{\rho \times \alpha(550\text{nm})} \tag{5.13}$$

In table 2.2, the highest thin-film FOM was determined to be 2.89. Using this criterion every crystal is a better performing TCO. Given some of the films, particu-

Table 5.10: Room temperature resistivity, absorption coefficient and figure of merit for selected ZGSO crystals

Crystal	ρ (300K) $m\Omega$.cm	α (550nm) cm^{-1}	FOM Ω^{-1}
67a	1.9	66.7	7.9
92c	1.1	109.3	8.3
92d	0.8	171.2	7.3
99a	0.5	145.6	13.7

larly AZO (Al:ZnO) have resistivity an order of magnitude lower than ZGSO crystals this better FOM originates from the absorption coefficient. The single crystals have an absorption coefficient two orders of magnitude lower than the films implying the crystals are significantly more transparent than any thin-film TCO.

Absorption coefficient values for single crystals are routinely lower than thin-films and therefore carry a bias. For example, the literature shows ITO thin films to have an absorption coefficient at 550 nm to be $\sim$ 5000 cm^{-1} [10, 103, 104] whereas in single crystal In_2O_3, Galazka *et al* [160] measured absorption coefficients ranging 5 - 10 cm^{-1}. Additional absorption mechanisms are likely to be present in thin-films which create this apparent discrepancy. If a single crystal with absorption coefficient $\sim$ 10 cm^{-1} could feasibly be scaled down to a thickness comparable to a thin-film (150 nm), 99.99 % transparency would be expected.

Therefore, comparisons of TCO's using FOM's, is only justified when dealing with compounds with same morphology. The literature of single crystal TCO's is limited however Galazka *et al* [160] have reported electronic and optical properties of single crystal In_2O_3 and Ga_2O_3 [160, 192]. Extracted data yields FOMs ranging from 0.11 to 19.35. It is therefore concluded ZGSO should be a comparable TCO with the other industry standard compounds.

5.4 Crystal 70a

To highlight the difficulty in achieving the desired performance and to explain the high levels of disorder, 70a (x = 0.06), pictured in Figure 5.16 provides an interesting

study.

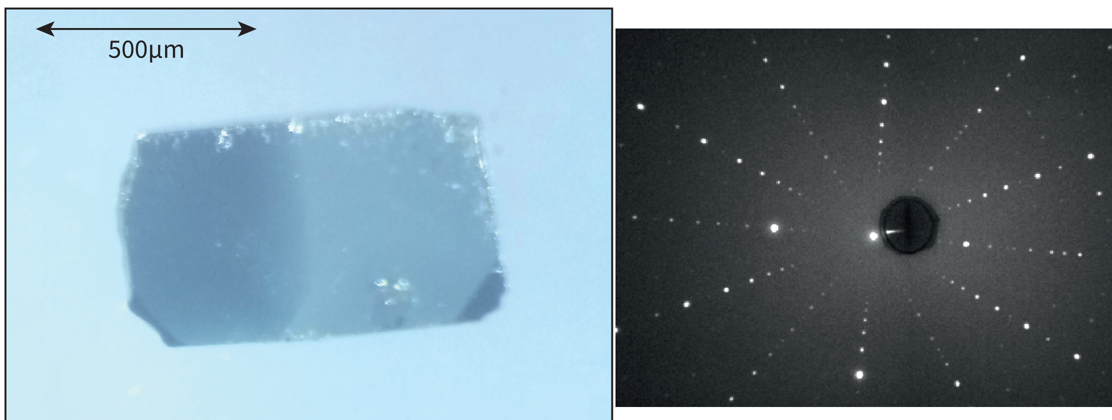

Figure 5.16: Photograph of crystal 70a. Two clear colours are evident with the left side being darker than the right. Laue diffraction pattern indicates a single crystal with no signs of twinning. The surface is (110) oriented.

This sample, a single crystal confirmed by Laue diffraction, displays two distinct areas with different colours. One a lighter blue and the other a deep dark, less visually transparent half. Optical data obtained for both halves of the crystal is displayed in Figure 5.17. The transmission data provides a fair assessment of the difference in transparency as both sides have the same thickness.

The transmittance in the light side of the crystal is higher than in the dark. The optical band gaps are 3.26 and 3.38 eV for the dark and light sides of the crystal, respectively, indicating an apparent disparity in the electronic structure between the two sides. Likewise, the Urbach energies for the dark and light side are 373 and 247 meV, respectively.

This observation in a single crystal highlights a problem with the doping technique; clearly, the two sides have different properties and therefore varying electronic structures. Unsurprisingly this crystal has a low measured Hall mobility (23.7 cm^2/V.s). This is further explained in chapter 6 when the gallium content is determined in this crystal.

If a single crystal can possess such variation in optical properties, then clearly accurate controlling of the doping becomes very difficult.

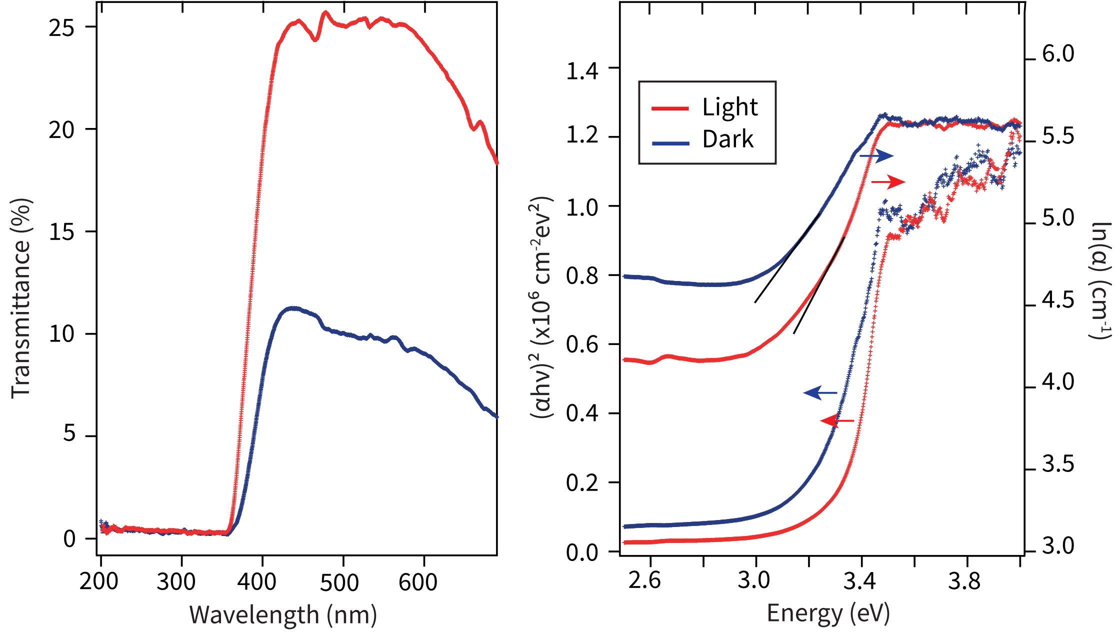

Figure 5.17: Transmittance and optical absorption data plotted as a function of wavelength/energy for two different sections of crystal 70a.

5.5 Conclusions

The work in this chapter has revealed undoped ZSO to exhibit n-type semiconducting electronic properties possibly originating from an undetermined shallow donor state. Using UV - Vis spectroscopy the optical band gap has been determined to be 3.38 eV.

The incorporation of gallium into the ZSO host lattice has created an n-type degenerate semiconductor with resistivity three orders of magnitude less than their undoped counterparts without significant detrimental effects to the optical properties. Therefore, proof has been provided that a new single crystal TCO, ZGSO, has been synthesised for the first time. The blue tint to the ZGSO has been attributed to free carrier absorption in the red/infrared region of the spectrum, making the transmission peak in the blue region ($\sim$ 400 nm).

Despite the overriding success of the crystal growth in achieving the goal of creating a new TCO, this chapter has also highlighted significant issues with doping. Anomalous behaviour, especially regarding band gap shifting has been observed and is attributed to large levels of disorder. This quaternary system has a very complicated defect structure which, in semiconductor physics where stoichiometry is

essential, has significant implications to the properties. Therefore, further improvements to the growing methods are needed to improve performance and FOM.

Chapter 6

Characterisation of ZSO and ZGSO

In this chapter, structural and chemical analysis on ZSO and ZGSO single crystals is carried out. The cation stoichiometry of the crystals were determined using energy dispersive x-ray spectroscopy (EDS) performed with a scanning electron microscope (SEM). Additionally, the EDS was employed to detect any unwanted contaminants in the crystal. Finally, powder x-ray diffraction experiments on powdered single crystals were performed to observe how the structure, in particular, the lattice parameters change under the influence of doping, similar to that carried out on the polycrystalline precursor powders.

6.1 Energy Dispersive X-ray Spectroscopy.

Before the results of EDS are examined, it is important to explain the sources of experimental error and how the data is analysed. One of the primary sources of errors in EDS originates from irregularities in the surface measured. The intensity of x-rays emitted from the medium or sample is dependent on the distance travelled, governed by equation 6.1 [193].

$$\frac{I}{I_o} = \exp\left[-\left(\frac{\mu}{\rho}\right)\rho d\right] \tag{6.1}$$

I_o is the starting intensity. I is the intensity after passing through a distance d of material with density ρ and μ being the material's mass absorption coefficient.

Surface irregularities can affect the intensity of emitted x-rays as highlighted in Figure 6.1.

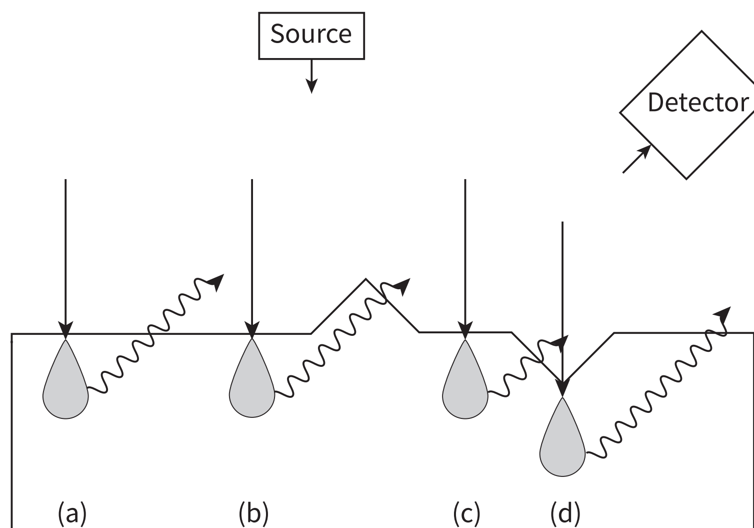

Figure 6.1: Schematic of how scratches and ridges affect the distance for x-rays to travel. (a) An ideal flat surface situation. (b) The emitted x-ray must travel through extra material/ridge before leaving the material, reducing intensity. (c) The emitted x-ray has less material to travel through as it escapes through the trough, increasing the intensity. (d) A reduction in intensity is caused by x-ray formation deeper into the material due to the trough. The grey *teardrop* represents the volume that the electrons interact with the atoms. Figure adapted Newbury *et al* [193].

Figure 6.2 displays a scanning electron microscope image of a representative ZSO crystal, indicating the high-quality surfaces measured throughout this chapter.

Depending on the method undertaken, composition data obtained through EDS carries an accuracy ranging from 2 - 25 %. The significant variation in these margins of error originates from analysis using standards or using standardless methods [194, 195]. Whilst standardless methods are acceptable for elemental detection, any further quantitative data such as formula determination is not possible. This project utilised a single standard quantitative analysis (SSQA) technique [196], which uses a library of remote standards. By calibration of a single element, in this case cobalt, reasonably high accuracy levels are obtained. This SSQA method employed by AZtec has been shown to carry a relative error of < 5 % for heavier elements and

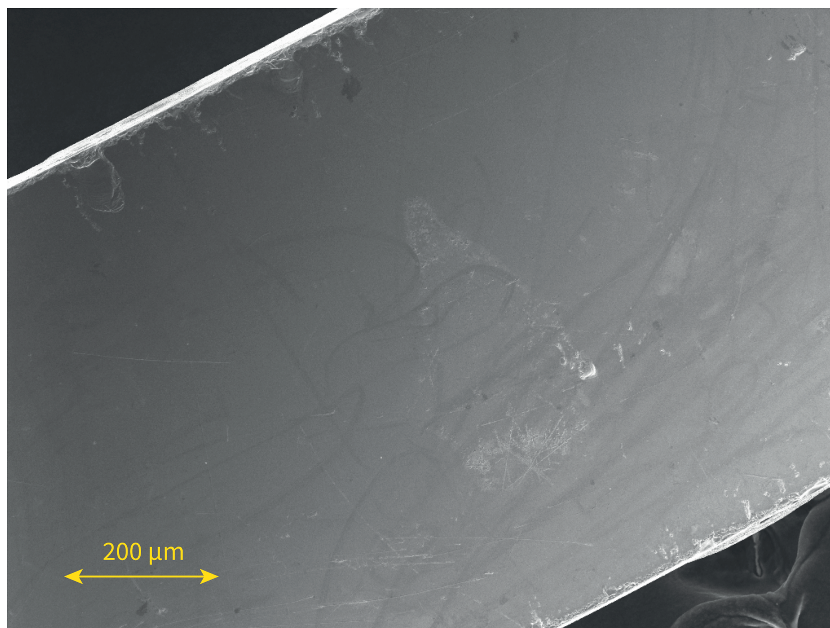

Figure 6.2: SEM image of a representative crystal surface.

∼ 2 % when lighter elements are excluded [197, 198].

Errors quoted in this chapter are a measure of the precision, that is the standard deviation divided by $\sqrt{N}$ with N being the number of times the measurement was taken. The high spatial resolution achievable in the SEM/EDS (∼ 50 nm) allows many measurements over different regions of the sample (N = 12).

For the undoped samples the SSQA method was used; however, the analysis technique was adapted for the doped samples by effectively creating a standard from an undoped crystal. The deviation from ideal stoichiometry across the undoped batch was found to be extremely low (see Section 6.1.1). Accordingly, one undoped crystal (64a) was chosen to be a standard to reference the doped crystals. By calculating the Sb:Zn intensity ratio of the standard, specifically of the Sb Lα and Zn Kα peaks and fixing this ratio to be 2:1 (ideal stoichiometry) the Sb:Zn ratio in all other crystals could be measured and the the occupancy of Zn (1-x) determined using

$$1 - x = \frac{I_{Zn,ZGSO}}{I_{Sb,ZGSO}} . \frac{I_{Sb,ZSO}}{I_{Zn,ZSO}} \tag{6.2}$$

This analysis required several constraints; the first being the stoichiometry of antimony was set to two. Therefore, it was not possible to determine if the value of antimony dropped, only how the value of zinc compared. The value of x obtained

from equation 6.2 was assigned to be the value for gallium because the concentrations of gallium are low and therefore, the peak intensity of Ga Kα is weak. This analysis assumes the cation's stoichiometry will equal three (Zn + Ga + Sb = 3) and therefore does not allow lattice vacancies or overfilling.

Additionally, the stoichiometry of oxygen was assumed to be six. EDS is a tool which can detect elements with atomic numbers down to boron. However, accurate quantification of light elements becomes tricky and fraught with error [194]. These assumptions may be limiting for accurately stating the chemical composition of ZGSO. However, it does enable accurate analysis of the ratios of the cations.

6.1.1 Results

ZSO Crystals

Displayed in Figure 6.3 is a background-subtracted EDS spectrum for undoped crystal 64a.

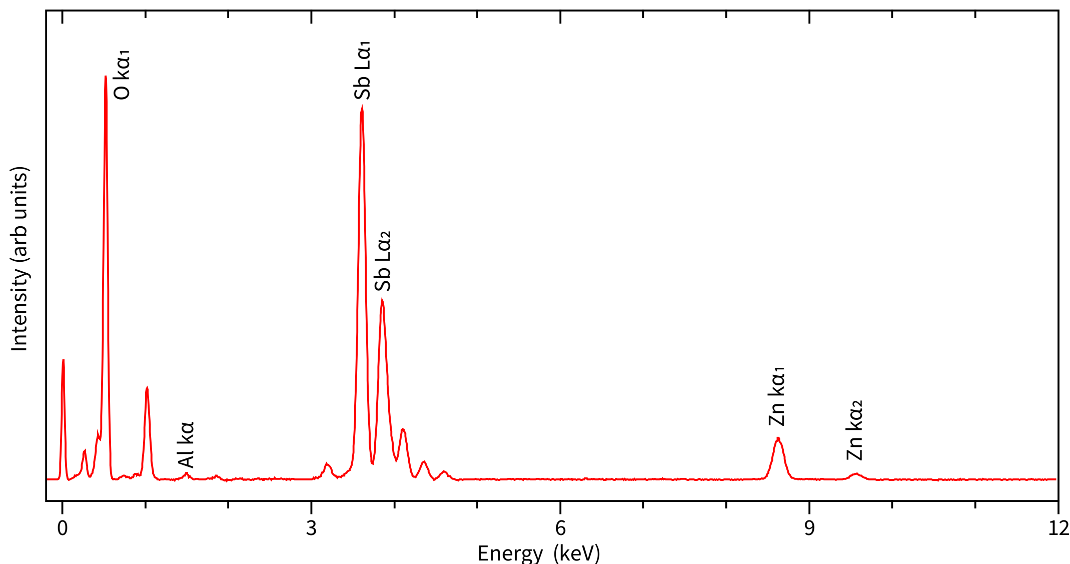

Figure 6.3: EDS spectrum from 0 - 12 keV for undoped crystal 64a with several important emission peaks highlighted.

The spectra indicates a clean crystal with little addition of unwanted elements, particularly chlorine, the transport agent involved in growth and silicon from the ampoule. In some samples, small carbon and sodium peaks are detected; however,

these are considered common surface contaminants and therefore discounted. One advantage with the closed system CVT method is that crystals are grown with high purity and with an absence of unwanted impurities. It is also worth noting Figure 6.3 indicates a small Al Kα peak at $h\nu = 1.48$ keV. Through a rigorous cleaning routine involving aqua regia, deionised water and acetone, aluminium is determined a surface contaminant, likely originating from the polishing process which used Al_2O_3 paper as an abrasive.

For the analysis of three undoped samples, the inbuilt SSQA technique employed by AZtec was used (see section 3.2.1). The technique totals the elements present to 100 % and assigns each component a percentage, unwanted elements such as aluminium are deconvoluted out of the results.

Figure 6.4 displays the atomic percentages of the two cations in the undoped sample - dashed lines indicate ideal stoichiometry. Crystals labelled by an integer were measured by EDS exclusively and characterised with no other technique.

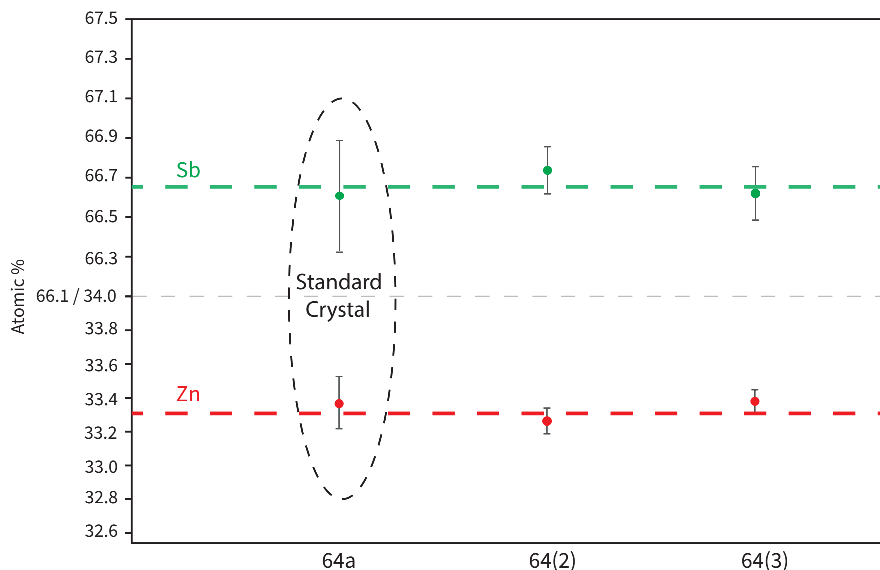

Figure 6.4: EDS obtained atomic percentages of Zn and Sb present in three undoped crystals where $Zn\%_{atm} + Sb\%_{atm} = 100$ %

The constraint, Zn + Sb = 3 is applied to convert from atomic percentage to formula unit. Table 6.1 displays the resulting values. This constraint indicates, in each compound, either some Zn^{+2} occupies the Sb^{+5} site or vice versa but cannot occupy the O^{-2} site. A reasonable assumption given the atomic radii of Zn^{+2}, Sb^{+5}

and O^{-2} with VI co-ordination are 0.74, 0.6 and 1.4 Å respectively [168].

Table 6.1: Cation occupation for undoped crystals obtained by applying the constraint Zn + Sb = 3.

Crystal	Zn	Sb
64a	1.002 ± 0.005	1.998 ± 0.005
64(2)	0.998 ± 0.002	2.002 ± 0.002
64(3)	1.001 ± 0.002	1.999 ± 0.002

Crystal 64a is taken to be the standard used to compare the Zn : Sb ratio in all other doped crystals. The electron density n due to the stoichiometry of the cations is determined by equation 6.3

$$n = (12 - 2\text{Zn} - 3\text{Ga} - 5\text{Sb})\,\frac{2}{V_{unit}} \tag{6.3}$$

The elemental symbols are their occupancy values respectively, i.e Zn = 1 Sb = 2 and V_{unit} is the unit cell volume. For 64a, the expected carrier density from equation 6.3 suggests a p - type conductivity with $n_{holes} \sim 9 \times 10^{19}$ cm^{-3}. However this technique does not take into account the oxygen vacancies. Given how sensitive the electronic properties are to crystal stoichiometry and the errors involved in EDS, attempts to predict electronic behaviour from the chemical analysis are not realistic.

ZGSO Crystals

Table 6.2 displays the obtained Zn values and, correspondingly, the calculated Ga values under the constraint of Sb = 2.

Table 6.2: EDS determined cation occupation for several ZGSO crystals under the constraints: Zn = 1-x, Ga = x, Sb = 2.

Crystal	Zn	Ga	Sb	x %	nominal doping (%)
67a	0.99 ± 0.01	0.01 ± 0.01	2	1	1
67c	0.96 ± 0.01	0.04 ± 0.01	2	4	1
69a	0.98 ± 0.01	0.02 ± 0.01	2	2	4
92c	0.95 ± 0.01	0.05 ± 0.01	2	5	8
92d	0.95 ± 0.01	0.05 ± 0.01	2	5	8
79d	0.96 ± 0.01	0.04 ± 0.01	2	4	10

Initial observations indicate that determined values for x, and the expected nominal values of x do not match, highlighting an issue with the doping; however, this is discussed in section 6.1.2.

In an ideal doping scenario, one gallium donor provides one single free electron. Figure 6.5 displays the carrier concentration versus measured gallium content, similar to what was carried out in chapter 5 but with measured gallium instead of nominal doping.

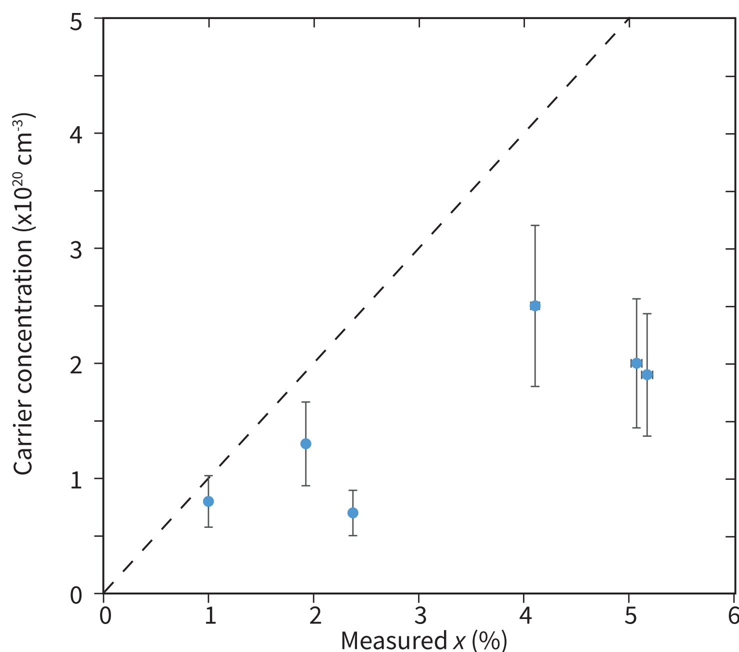

Figure 6.5: Values of the experimentally determined carrier concentrations plotted against the calculated values for gallium occupancy. The dotted line indicates one gallium provides one free electron.

The measured value of x and the carrier concentration do not follow the expected trend. In all crystals, the carrier concentration is less than what would be expected for the nominal doping. A deal of charge compensation is likely occurring in the crystals, and the number of conduction electrons is higher than values indicated from the Hall effect measurements.

The samples with a higher x value do tend to have higher carrier concentrations but a linear trend is not observed.

6.1.2 Doping Inconsistency

Throughout this project, a great deal of inconsistency between crystal properties has been observed. Whether between different growths, across the same growth or even in the same crystal, highlighted by the UV - Vis data for 70a. In this section, EDS is employed to display how inconsistency in gallium concentrations is likely to be a vital cause of this.

Figure 6.6 displays the measured gallium versus nominal doping for a large sample set over many growth batches.

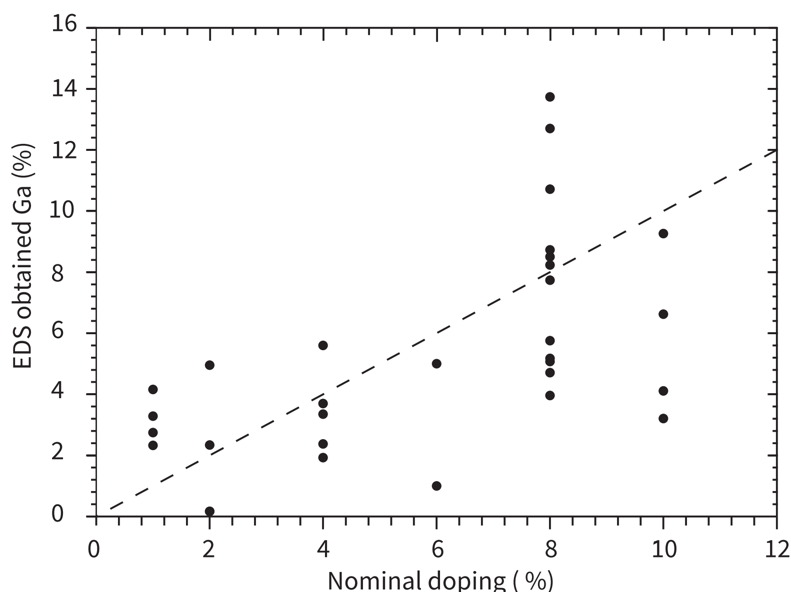

Figure 6.6: Values of gallium determined from EDS versus the expected nominal doping. Values are displayed as a percentage of doping. i.e Zn + Ga = 100%. The dashed line highlights expected values (nominal doping = measured value.)

Little correlation is observed between the measured and expected nominal doping values, further reiterating the difficulty in controlling the doping during growth. To understand this further, a single growth batch 92 is analysed.

Table 6.3 displays the obtained cation stoichiometry for five crystals from growth 92 (x = 0.08). Figure 6.7 shows the EDS spectrum over the x-ray energy range 8 - 10 keV covering the Ga Kα_1 and Zn Kα peaks.

The spectra is normalised to the intensity of Sb Lα peak, not shown as it lies at energy outside of this range (3.6 keV). Firstly, it may seem equivocal to suggest

Table 6.3: Cation occupation for batch 92 (x = 0.08) crystals under the constraints Zn = 1 - x, Ga = x and Sb = 2

Crystal	Zn	Ga	Sb	Ga %
92 (1)	0.96 ± 0.01	0.04 ± 0.01	2	4
92 (2)	0.86 ± 0.01	0.14 ± 0.01	2	14
92 c	0.95 ± 0.01	0.05 ± 0.01	2	5
92 d	0.95 ± 0.01	0.05 ± 0.01	2	5
92 (5)	0.91 ± 0.01	0.09 ± 0.01	2	9

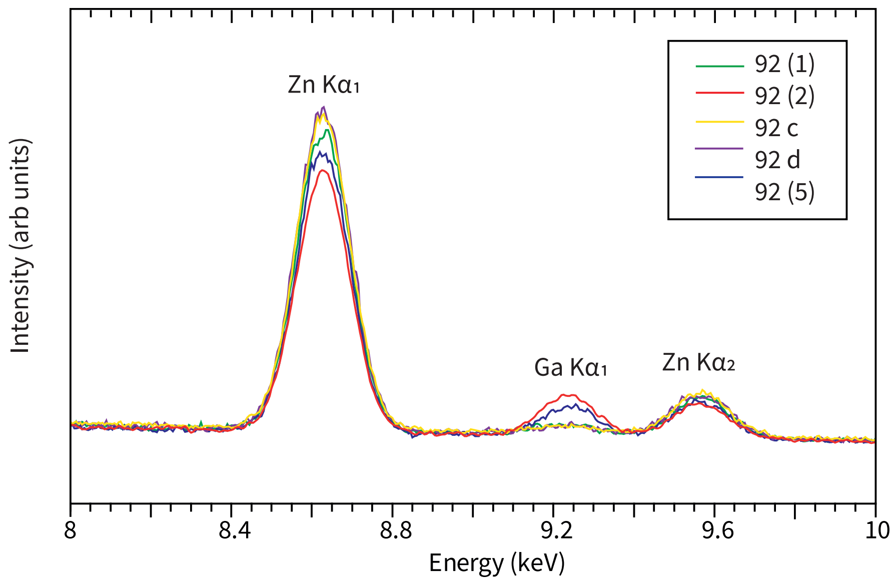

Figure 6.7: EDS spectrum for five crystals from growth 92 displayed over energy ranges 8 - 10 keV normalised to the intensity of Sb Lα with relevant peaks highlighted

gallium presides in the lower doped crystals given how weak the intensity of their peaks is. In chapter 7, HAXPES is used to prove that Ga does reside in the crystals. The variation in Ga content is particularly prominent in the spectra for crystal 92 (2) and 92 (5). A reduction in intensity for the Zn Kα_1 peak is complimented by an increase in Ga Kα_1, justifying the constraint where gallium is assigned to the absence of zinc.

The doping inconsistency is further reiterated in table 6.3 with measured gallium values ranging from 4 - 14%. From this alone, conclusive proof is provided that controlling doping in crystals grown by CVT is difficult. This observation reinforces the points made by Haseman *et al* [199] and Kumar *et al* [200]. They attributed

variations in doping to changing local conditions across a growth ampoule.

An additional source for this inconsistency is proposed by measuring the infamous crystal 70a. Twelve locations were measured on the light and dark side of the crystal with spectrum of the Zn Kα doublet displayed in Figure 6.8.

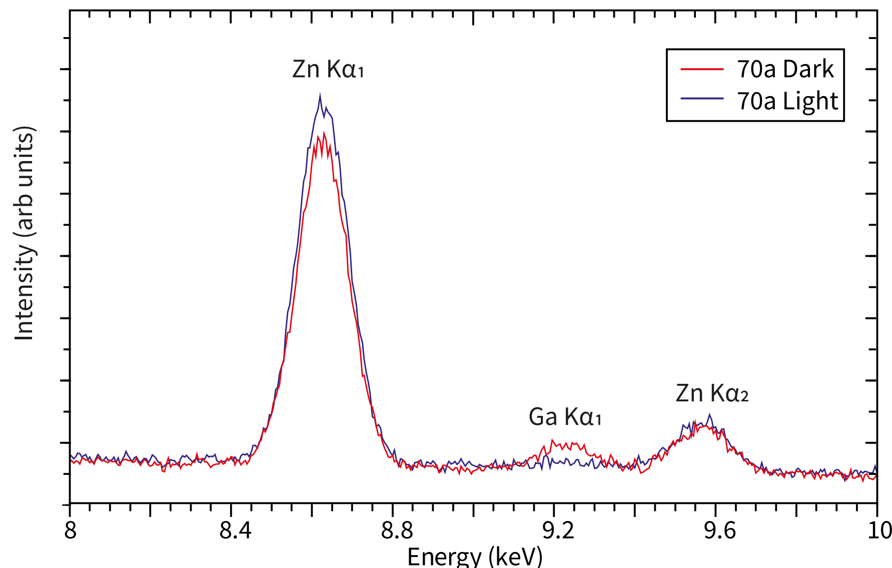

Figure 6.8: EDS spectra for crystal 70a taken from both light and dark regions on the crystal normalised to the Sb Lα peak not shown.

For the light and dark sides, x is determined to be 2 and 5 % respectively explaining the variation in optical properties across the two sides.

This variation suggests that the lighter side was grown under gallium deficient conditions when compared to the darker side. It is possible that gallium transports at a different rate during the growth. For instance, if the nucleation points in the crystals are gallium rich because the gallium transports early in the growth, as the crystals grow, less gallium is present in the vapour, and the remainder of the crystal is gallium deficient. Likewise, this could be occurring in reverse with gallium transporting late.

Doping ZSO crystals using the CVT method appears to be highly inconsistent. Crystals grown in the same batch can exhibit very different doping concentrations, likely due to local growth conditions. The variations of doping across a single crystal also indicate a potential for varying transport rates of the gaseous constituents during the growth process. This does not appear to be such an issue with the

undoped ZSO crystals due to the consistency in measured stoichiometry. This issue of controlling the dopant into single crystal TCO compounds is not unique to the CVT growth method. Zhang *et al* [201] determined the concentration of Sn into Ga_2O_3 single crystals grown from the melt was between 1 and 1.8 % of what was expected from nominal doping.

6.2 X-ray Diffraction

X-ray diffraction was carried out on ZSO and ZGSO powders obtained by grinding a number of crystals from a particular growth. Unfortunately not enough powder can be extracted from a single crystal for a reasonable measurement. For the undoped powder, the high degree of consistency between samples suggests the powder of many crystals should be a fair reflection of the structure in a single crystal. The data obtained from doped samples are be more prone to error given doping inconsistent throughout a growth, therefore a number of powders were created. Lattice parameters are determined using Rietveld refinement with the Byström [24] structure used as a model to fit the data against.

Figures 6.9 and 6.10 display the results for both the undoped and a representative doped refinement. Pictured are the difference (green) between the model (red) and experimental data (blue cross).

The difference between the model and the experimental data suggests the fitting was not an exact one. This can originate from a large variety of reasons and requires rigorous analysis of the individual peak fittings. Figure 6.11 focuses on the 110 and 103 peaks for the doped sample. The model underestimates the intensity from experimental data for the 110 peak and over estimates for the 103 peak, indicating a degree of preferential orientation in the powders. For the purpose of this project this is not an issue as the peak positions have been fitted at the correct 2θ values and therefore the d spacing and lattice parameters remain unaffected. If additional information such as site occupancy was to be determined, a better data set would be obtained using single crystal x-ray diffraction.

The obtained lattice parameters and corresponding weighted profile residual values R_{wp} are listed in table 6.4. These values are graphically displayed in Figure 6.12.

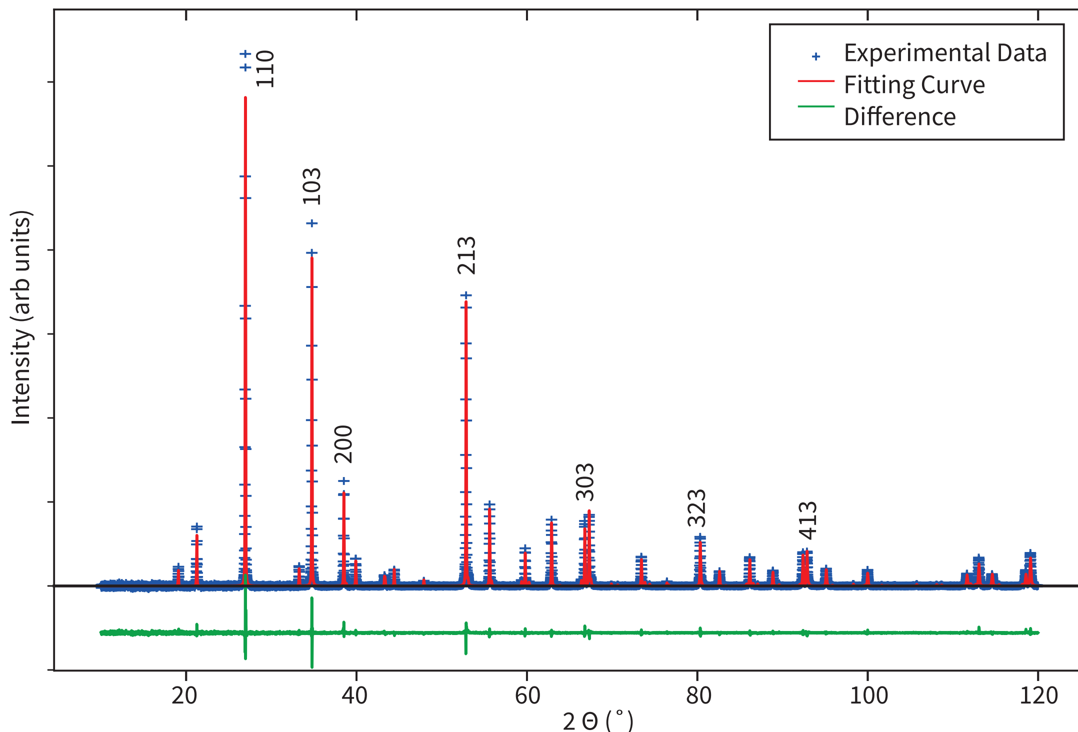

Figure 6.9: Rietveld refinement for powder x-ray diffraction pattern conducted on crystals from undoped growth batch 64. Certain crystallographic planes are highlighted.

Also displayed are values obtained from the precursor powders taken from section 4.1.3.

Table 6.4: lattice parameters from Rietveld refinement with corresponding parameter ratios and R_{wp} fitting values.

Powder	a (Å)	c (Å)	c/a	R_{wp} (%)
Undoped	4.667	9.266	1.985	7.401
Doped 1	4.663	9.265	1.987	7.914
Doped 2	4.663	9.264	1.987	8.126
Doped 3	4.664	9.265	1.986	9.215
Precursor Undoped Powder	4.667	9.266	1.985	6.546
Precursor 6% Ga Powder	4.663	9.264	1.987	7.730

The R_{wp} values or weighted profile residual factors are commonly used to determine the measure of agreement between the theoretical model and x-ray diffraction data [202].

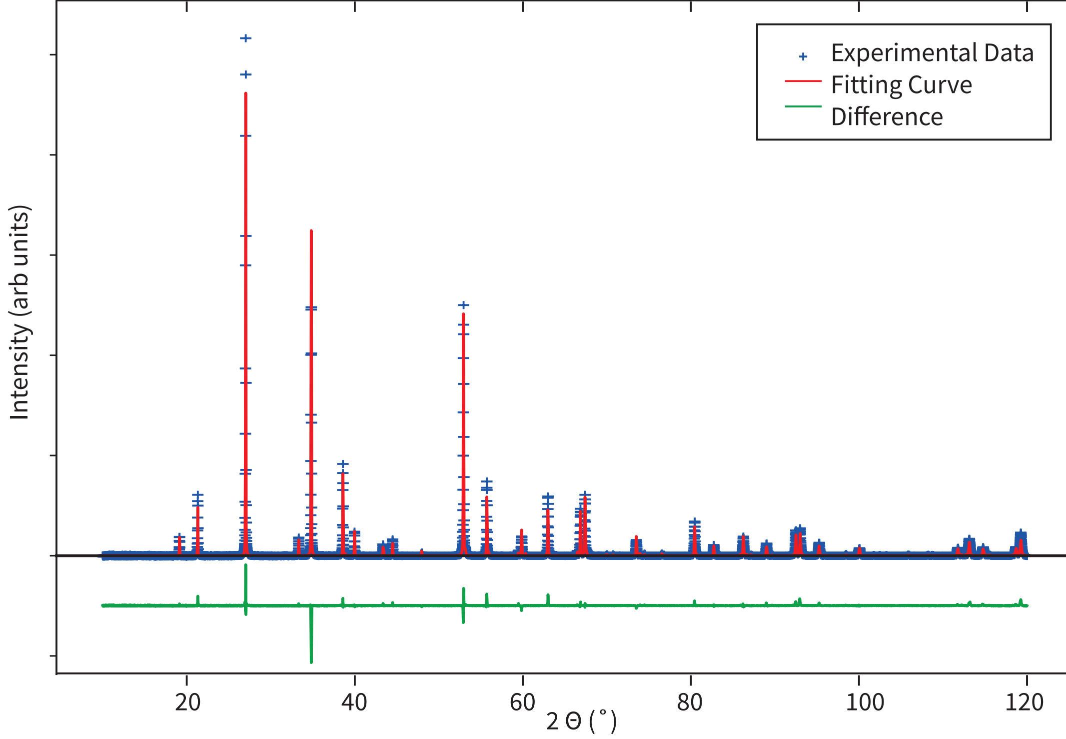

Figure 6.10: Rietveld refinement fit for powder x-ray diffraction conducted on crystals from doped growth batch 92.

$$R_{wp} = \sqrt{\frac{\sum_{i=1}^{N} \left[w_i \left(I_i^{exp} - I_i^{calc}\right)\right]^2}{\sum_{i=1}^{N} \left[w_i \left(I_i^{exp}\right)\right]^2}} \times 100\% \tag{6.4}$$

Where w_i is a weighting factor and I^{exp} and I^{calc} are the intensity of experimental and calculated point respectively. The most important way of assessing the quality of a Rietveld fit and the values obtained is by graphically viewing and analysing the patterns and deciding if the results obtained are physically believable [203].

The undoped precursor powder and single crystal have the same lattice parameter. Likewise, one of the doped samples is also in agreement with the initial precursor powder. The inclusion of gallium reduced the lattice parameters and therefore, the unit cell volume from 201.78 Å^3 to 201.48 Å^3.

The change in lattice parameters upon doping is common amongst semiconductors [204–206]. This effect is often described using Vegards Law [207] for the lattice parameter doping dependence. For a cubic lattice

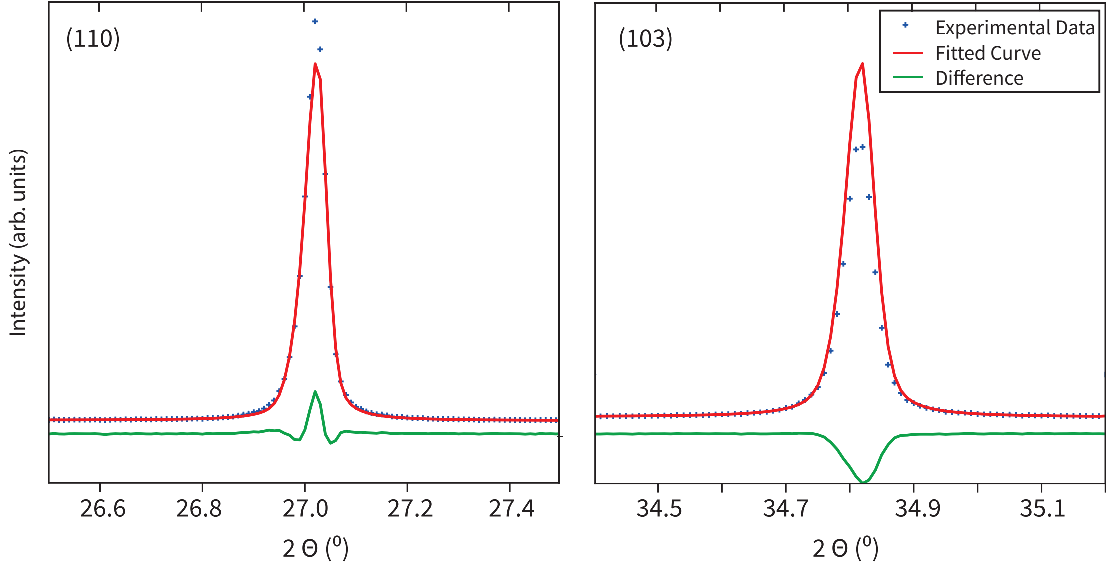

Figure 6.11: Enhancement of peaks 110 and 103 for the doped samples. The difference pattern indicated the model underestimated the 110 peak intensity and overestimated the 103 peak.

$$\frac{\Delta a}{a} = \beta_{size} N_I \tag{6.5}$$

where $\Delta a/a = ((a_{doped} - a_{undoped})/a_{doped})$ with a being the lattice parameter, N_I is the dopant concentration and β_{size} is a coefficient defined by

$$\beta_{size} = \frac{((r_i/r_H) - 1)}{N_H} \tag{6.6}$$

Where r_i and r_H are the atomic radii of the impurity and host respectively. N_H is the host atomic density. Given there are two Zn atoms per unit cell and assuming substitution only occurs by the mechanism of Ga^{+3} onto Zn^{+2} with ionic radii of 0.62 and 0.74 Å respectively, β_{size} is calculated to be -1.64 × 10^{-25} cm^{-3}. The negative sign indicates a reduction in lattice parameters is expected. Applying β_{size} to equation 6.5, the predicted lattice parameters are displayed in Figure 6.13 with experimental data included.

The experimental lattice parameters appear to decrease at a greater rate than is expected for a gallium onto zinc substitution especially with regards to the a parameter, this is highlighted by the increased c/a ratio in table 6.4. Vegard's law is sometimes accompanied by an additional electronic term, originating from electrons

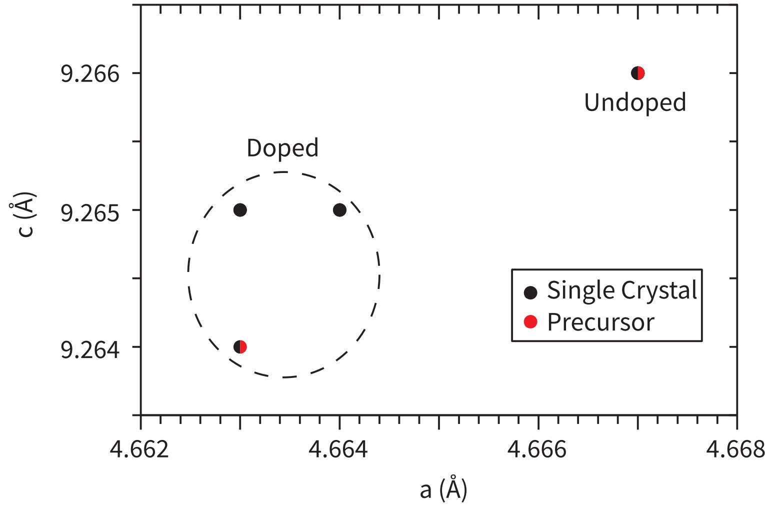

Figure 6.12: Lattice parameters for undoped and doped single crystals determined using Rietveld refinement.

being doped into the conduction band [208–211]. The energy of the system can be lowered if the conduction band minimum is also lowered in absolute energy [212]. This is possible by a hydrostatic deformation of the lattice. How the conduction band shifts in energy under volume deformations is described using deformation potentials [213]. This shift is also linear as a function of strain ϵ. There is an additional elastic energy cost due to this deformation given by

$$E_{elastic} = \frac{9}{2}B\epsilon^2 \tag{6.7}$$

Where B is the bulk modulus. By minimising the total energy with respect to strain, a minimum is found to occur at non-zero deformation.

When taken into account, this additional term has been shown, in As doped Si, to decrease the lattice volume despite it being predicted that β_{size} should be positive [214], similarly used to explain the lattice parameter increase in La:$SrTiO_3$ [215].

Currently determination of this effect is not possible in ZSO as the deformation potential and the bulk modulus is unknown. Further computational calculations would be essential to understand the lattice parameter variation in ZGSO. Furthermore, more data points are required to confirm the validity of Vegard's law as a linear trend can not be inferred from two data points.

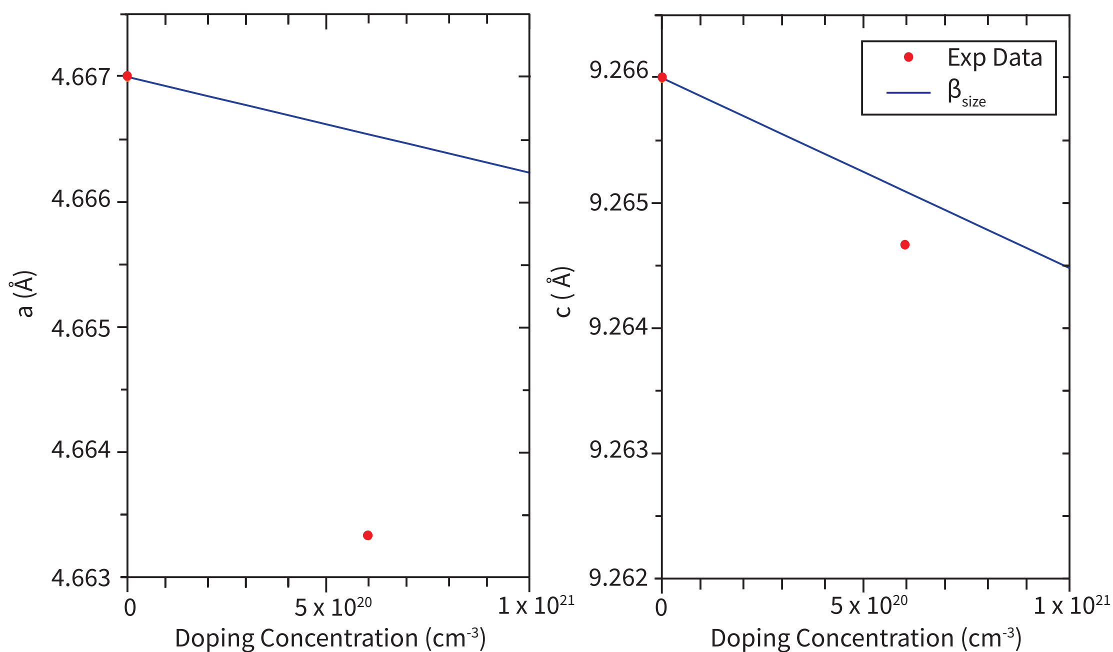

Figure 6.13: Lattice parameters of ZSO and ZGSO as a function of gallium doping lattice with a predicted line due to ionic size mismatch.

Comparison with Literature

The lattice parameters for the undoped single crystal are compared with values in literature displayed in table 6.5 and plotted in Figure 6.14. Only literature data quoted to three decimal points are displayed to avoid rounding errors.

Table 6.5: Literature values for the lattice parameters in undoped ZSO.* = assumed morphology given the preparation technique.

Study	a (Å)	c (Å)	Morphology
This work	4.667	9.266	Polycrystalline/Single Crystal
Rebello *et al* [136]	4.66	9.24	Single Crystal
Balasubramaniam *et al* [35]	4.666	9.265	Nanoparticles
Dutta *et al* [33]	4.660	9.249	Nanoparticles
Arunkumar *et al* [31]	4.672	9.265	Micro-crystalline Powder
Filipek *et al* [216]	4.665	9.270	Polycrystalline Powder*
Ercit *et al* [25]	4.664	9.263	Single Crystal
Bystrom *et al* [24]	4.67	9.26	Single Crystal
Nishiyama *et al* [37]	4.667	9.260	Polycrystalline powder
Guillen-Bonilla *et al* [217]	4.66	9.26	Microwires/Microrods
Kikuchi *et al* [36]	4.68	9.29	Polycrystalline Powder

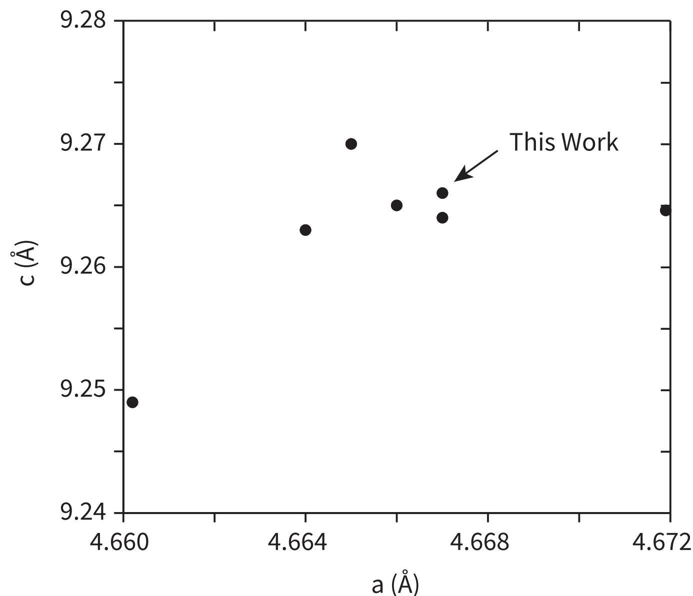

Figure 6.14: Comparison of lattice parameters of ZSO obtained in this work and from the literature.

The lattice parameters obtained for the undoped crystals are in reasonable agreement with many of the literature values. The significant outlier is from data obtained by Dutta *et al* [33] on nanoparticles of ZSO grown by the sonochemical method. Given this is the only reported literature for synthesis of ZSO by this method, it is likely to be the key factor behind this discrepancy. Additional strain may have been induced during the growth.

6.3 Conclusions

In this chapter, additional characterisation measurements were carried out for grown single crystal ZSO and ZGSO. Using the x-ray microprobe analysis method of EDS, undoped crystals of ZSO were determined to be highly stoichiometric and free of unwanted impurities. Taking one of the ZSO samples to be a standard for cation ratios allows the determination of the gallium concentrations in the ZGSO crystals.

Comparing the gallium doping values to the measured carrier concentrations suggests that more gallium is present in the samples than would be predicted if each gallium atom donated a single free electron. This leads to the conclusion that charge compensation is significant in ZGSO.

Additionally the measured gallium concentrations across crystals indicates that the CVT method is unreliable in controlling the quantity of dopant entering the lattice. Crystals grown out of the same precursor powder were found to vary in doping from 4-14 % doping, reiterating the points made previously in the literature. This was further explored by studying the gallium concentration across an individual crystal. The variations in gallium doping across both sides of the crystal indicated that rates of transport of gaseous constituents may be significant to describe the discrepancies observed.

Finally, in this chapter, structural measurements using powder x-ray diffraction revealed the lattice parameters for ZSO and ZGSO. A reduction in lattice parameter was observed upon doping as expected by ionic size mismatch between Ga^{+3} and Zn^{+2}. deviations from the expected values were discussed however additional material research is required.

Chapter 7

Photoemission Studies

Photoemission spectroscopy (PES) is a vital tool for understanding electronic properties of TCOs. This chapter uses three different methods; x-ray photoemission spectroscopy (XPS), hard x-ray photoemission spectroscopy (HAXPES) and angle-resolved photoemission spectroscopy (ARPES) to gain a better understanding of the nature of the valence band in ZSO and ZGSO. Furthermore, photoemission techniques were used to probe the density of states of the conduction band in the degenerately doped samples. An initial discussion about the literature of PES experiments on TCO's is presented before explaining how they are used throughout this study.

Core orbital peaks measured in CdO and SnO_2 have often been shown to exhibit an asymmetric line shape [44, 218–220]. This asymmetry has been attributed to an additional satellite peak at a slightly higher binding believed to originate from a screening effect caused by the conduction electrons reducing the kinetic energy of the emitted photoelectrons.

The binding energies of these peaks can also vary as a function of doping. When electrons are doped into the conduction band, the Fermi levels shifts in energy. Binding energies in PES experiments are referenced to the Fermi level and therefore band filling shifts core peaks to higher binding energies [44].

Some of the main results of this study were obtained using HAXPES. One of the advantages of HAXPES compared to lower energy photoemission techniques is the ability to probe the sample's bulk due to the increased electron mean free path (Figure 3.10). Swallow *et al* [220] successfully utilised the increased probing depth to

determine fluorine interstitials existed a few atomic layers deep in F:SnO_2, not just at the surface. This highlights another motivation for using photoemission techniques; the ability to determine the chemical state of the elements and not just the presence. The binding energies of electrons in a given orbital are dependent on the chemical state the atom resides in. If electrons are added to an atom, the interaction between each electron and the positively charged nucleus is reduced due to the increased screening. This effectively lowers the energy required to escape and therefore reduces the binding energy. This is experimentally observed in Appendix C where tellurium was observed in both a Te^{+4} oxidation states and another undetermined state.

One of the most common uses for core-level spectroscopy is determining chemical composition [221, 222]. Intensity ratios of different peaks are directly proportional to the chemical abundance. However, especially with regards to HAXPES, composition calculations can be laborious as they require knowledge of many factors such as the inelastic mean free path of the material and differential photoionisation cross-sections. Modern XPS analysis takes these factors into account using relative sensitivity factors.

Conventional PES experiments are often used to probed the density of states of the valence band. HAXPES has an advantage over conventional XPS when measuring the conduction band in TCOs due to their typical s orbital character. The intensity recorded by the detector is dependent on the photoionisation cross section of the atomic orbital the electrons have been emitted from and is a function of the photon energy. Changing the photon energy allows the intensity of peaks to be enhanced with respect to each other. This was demonstrated by Sallis *et al* [223] studying La:$BaSnO_3$. Using conventional XPS photon energies ($h\nu = 1.48$ keV), the conduction band ($5s$) could not be observed when compared to a valence band with dominantly O $2p$ character. Increasing the photon energy to 4 keV enhanced this feature and allowed observation of the conduction band. By measuring the width of the conduction band, the magnitude of band gap renormalisation effects have been determined by comparing with peak shift values [44, 69, 218].

Photoemission studies on the valence band have also revealed states that lie within the material's bulk band gap. Egdell *et al* [218, 224] observed a band gap state in undoped SnO_2 which was suppressed when doped with antimony. They

attributed the in-gap state to the reduction of surface Sn ions (+4 → +2) due to an absence of bridging oxygen. A hybrid 5*p* - 5*s* state was observed in the band gap. These reduced surface Sn^{+2} ions were replaced by Sb^{+3} upon doping which sits lower in energy and overlaps with the valence band.

Finally, HAXPES was used as a tool to experimentally prove the fundamental band gap of ITO was 0.81 eV smaller than the previously measured optical band gap [57] leading to the determination of the dipole-forbidden band gap [58].

The literature of ARPES measurements on TCOs is not so extensive, however, the technique's ability to probe the electronic structure in k - space has allowed several interesting studies. By measuring the (100) surface of CdO, Piper *et al* [225] observed quantised electron subbands just below the Fermi level in a surface electron accumulation layer [226]. Similar quantised electron subbands were observed by Zhang *et al* [227] in undoped (111) In_2O_3. Furthermore, ARPES provides the ability to resolve the nature of the band gap. For example, Joo *et al* experimentally determined the indirect nature of the band gap in $BaSnO_3$ [228] for the first time. By measuring ARPES along several different cuts, they determined the CBM was centred around Γ but the VBM located at the R point. Similar studies by Janowitz *et al* [229] confirmed the direct nature of In_2O_3 and indirect nature of Ga_2O_3 band gaps, all of which corroborate theoretical predictions. Finally, because of the capability to measure both energy and momentum simultaneously, ARPES has proved an invaluable tool for experimentally determining the conduction band mass [227, 230, 231].

This chapter will focus on looking at HAXPES data for the core peaks in several well characterised samples, and where necessary, provide conventional XPS data. The Zn $2p_{3/2}$, Sb 3*d* doublet and O 1*s* core levels were measured and analysed, focusing primarily on the binding energy positions, line shapes and peak shift as a function of doping. In chapter 6, the EDS signal for the Ga Kα peak in a number of ZGSO samples appeared very weak due to low concentrations of doping and therefore it was hard to convince that gallium resided in the crystals. Using HAXPES, the intensity of the Ga $2p_{3/2}$ peak is shown to be non-negligible.

The valence band of ZSO and ZGSO was measured using both XPS ($h\nu$ = 1.48 keV) and HAXPES ($h\nu$ = 5.92 keV). By changing the photon energy and therefore

the photoionisation cross sections, key atomic orbitals are enhanced with respect to each other. An estimate for the magnitude of band gap renormalisation occurring in a doped sample is obtained from comparing both conduction band width and core peak shifting.

Finally, the results of an ARPES experiment carried out on the (001) surface of a highly doped ZGSO sample is presented. For reasons that will become apparent, analysis of this data set is hindered.

7.1 Core Level Spectroscopy

This section focuses primarily on photoemission data for two crystals; one undoped (64a) and one with nominal doping, $x = 0.08$ (92c).

The core level peaks measured in both conventional XPS and HAXPES techniques are the Zn $2p_{3/2}$, Sb $3d$ doublet, O $1s$, and C $1s$. Binding energies are referenced to the Fermi level of polycrystalline Au sample. Surface charging effects were compensated using the C $1s$ (284.8 eV) peaks originating from residual contaminant carbon present on surfaces. In some highly doped samples, the conduction band and therefore a Fermi edge was observed using HAXPES, enabling clarification of the binding energy referencing technique.

7.1.1 Ga $2p_{3/2}$

The analysis method in the EDS section relied on the assumption that, when the Sb:Zn ratio was more than two, gallium made up the remainder of the absent zinc (Sb/(Zn + Ga) = 2). Although prominent for the highly doped samples (x > 0.10), the Ga Kα peak in some doped samples appeared negligible. Here, HAXPES was used as an additional technique to detect gallium and further prove that, although not exact, the EDS analysis method is reasonable to assume gallium presides in the bulk of ZGSO.

Figure 7.1 displays the photoemission data over the binding energy range covering the Ga $2p_{2/3}$ peak for both the undoped and doped sample. The signal to noise ratio is large due to the small concentration of Ga. This could be improved significantly by increasing the counting time, and would have been necessary if a

rigorous analysis was required. For this project the presence of gallium has been proved without the requirement for additional measurements.

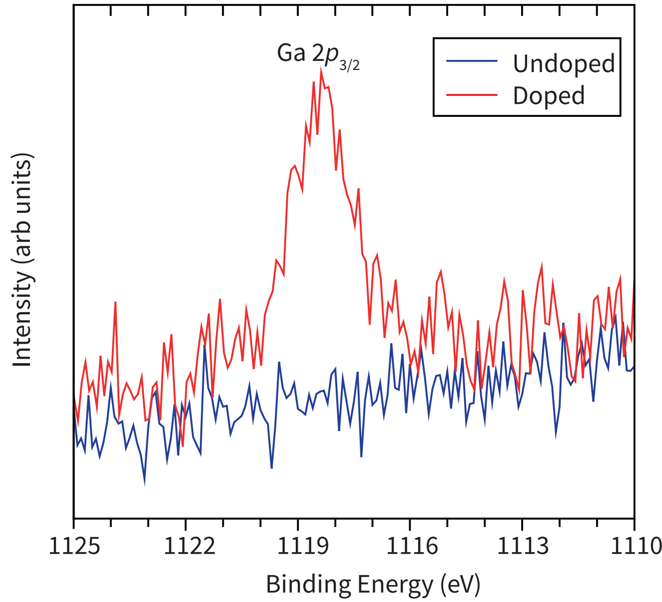

Figure 7.1: HAXPES spectra ($h\nu$ = 5.92 keV) for Ga $2p_{3/2}$ peak in the undoped and doped crystal showing a non-negligable intensity in the doped sample.

7.1.2 Peak Line Shape

Core peak spectrum data are analysed using the CasaXPS software, employing a Shirley background substitution [232]. The Zn $2p_{3/2}$ peaks are fitted using a symmetrical pseudo-Voigt curve, a Lorentzian that describes the emission broadened by a Gaussian which accounts for experimental resolution. Analysis of the Sb $3d$ doublet is slightly more involved because the Sb $3d_{5/2}$ and the O $1s$ overlap in binding energy. The higher binding energy Sb $3d_{3/2}$ peak is fitted using a similar pseudo-Voigt curve and the Sb $3d_{5/2}$ peak is fitted using the following constraints:

- The spin-orbit splitting of Sb $3d$ is 9.41 eV [233].
- The area ratio of the two components is known. The degeneracy of one state is given by $(2j + 1)$ therefore the intensity ratio I of a doublet is defined by

$$I = \frac{2j_{-} + 1}{2j_{+} + 1} \tag{7.1}$$

implying the $d_{3/2}$:$d_{5/2}$ ratio is 2:3.

- Finally, the full width at half maximum (FWHM) of the peak is the same between the two components.

After applying these constraints, the remainder of the peak is assigned to O 1s and fitted with another symmetrical pseudo-Voigt function. Displayed in Figure 7.2 is the peak fitting for the doped and undoped Sb 3d doublet.

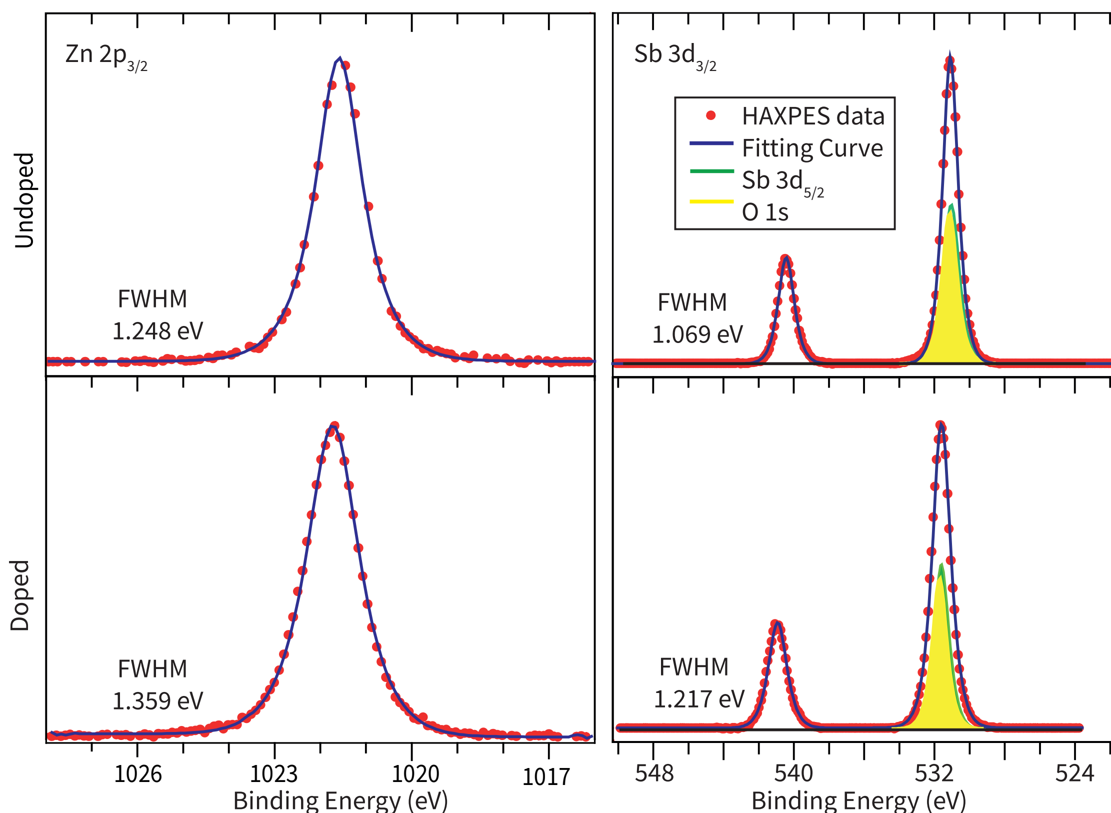

Figure 7.2: Zn 2$p_{3/2}$ and Sb 3d doublet taken using photon ($h\nu = 5.92$ keV) for undoped (top) and doped (bottom) samples. The Sb 3d peaks display the peak fitting of the Sb 3$d_{5/2}$ and O 1s components, displayed as green and yellow curves respectively.

All peaks measured using HAXPES are fitted using symmetrical, pseudo-Voigt line shapes, with the absence of any other components. Using conventional XPS, an extra component at higher binding energy in the Sb 3$d_{5/2}$/O 1s peak is observed and displayed in Figure 7.3(a). Given the enhanced surface sensitivity of XPS and the absence of this component in the Sb 3$d_{3/2}$ peak, this is attributed to a surface oxygen contaminant. Figure 7.3(b) displays the peak fitting of the lower binding

energy peak into three components: Sb $3d_{5/2}$, O $1s_{bulk}$ and O $1s_{surface}$. The O $1s_{surface}$ sits ~ 1.7 eV higher in binding energy than the bulk oxygen, consistent with oxygen in an organic compound [234].

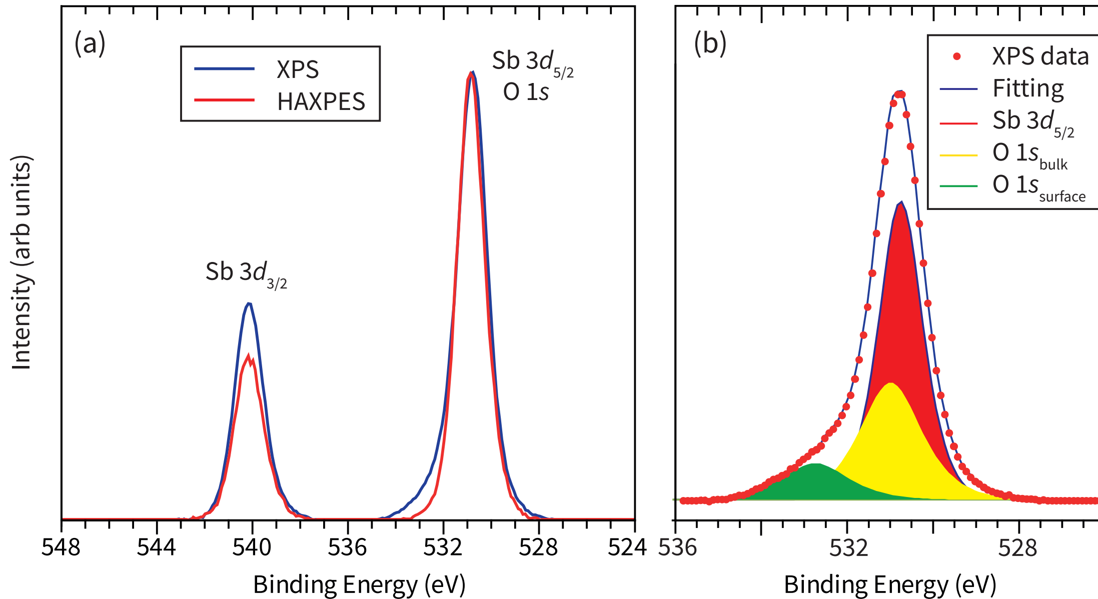

Figure 7.3: (a) Sb $3d$ doublet for the doped crystal recorded using conventional XPS ($h\nu = 1.48$ keV) and HAXPES photon energies ($h\nu = 5.92$ keV). The binding energies for both peak positions are determined to be equivalent. (b) Peak fitting of the Sb $3d_{5/2}$/O $1s$ peak measured using XPS indicating the presence of a higher binding energy O $1s$ component attributed to an oxygen surface contaminant.

Figure 7.3(a) also indicates that regardless of photon energy, peaks occur at the same binding energy. In thin-film TCO compounds such as SnO_2 and CdO, peaks obtained using XPS have been measured at higher binding energies than those obtained from HAXPES [44, 235]. In these compounds, a surface electron accumulation layer occurs [55, 165, 225], which the lower photon energy sources probe. This accumulation layer creates a band bending effect that rigidly shifts the binding energy. This is not observed in this study and therefore a surface electron accumulation or depletion layer [70], responsible for this effect, is assumed not to occur in single crystal ZGSO.

Throughout TCO literature, and extending into the broad class of metal oxides, the presence of conduction electrons induces an asymmetry to the core line shape [44, 218–220, 236–240]. This was first explained by Kotani [241], and the idea is

that when a core electron is photoemitted it leaves behind a hole. The unscreened Coulomb attraction of this photohole forces a localised state below the conduction band. Two different energetic final states are now available [181]:

1. The localised state remains unfilled, and a two-hole system forms. Conduction electrons react to screen this doubly ionised state in the form of a plasmon excitation. This state is referred to as *unscreened.*

2. A conduction electron fills this localised state, this electron can now effectively screen the photohole and referred to as a *screened* final state. The photoemitted electron carries more kinetic energy and therefore appears at lower binding energy.

$$E_k = h\nu - \phi - E_B \tag{7.2}$$

The difference in energy of these two final states manifests as a double peak conventionally in the XPS spectrum. These two peaks can also be considered as a main peak and one at higher binding energy separated by $\sim \hbar\omega_p$, where ω_p is the plasma frequency [236, 242]. Given the small plasma frequencies in TCO's, the separation is of the order $\sim$1 eV, resulting in peak asymmetry.

Such examples are given by $Sn_{1-x}Sb_xO_2$ [218, 237] and thin-film samples of In_2O_3 [238, 239], SnO_2 [220, 240] and CdO [44]. This effect can be enhanced by a surface electron accumulation layer [243], that has already been dismissed in the ZGSO crystals. However, the reason peak asymmetry is not observed in these samples is not determined. Future experiments, such as electron energy loss spectroscopy (EELS) [65, 224], could determine the plasma frequency's magnitude and help understand these spectra.

7.1.3 Peak Position

The binding energy of the core peaks for the undoped and doped samples measured using HAXPES are displayed in table 7.1. Only the Sb $3d_{3/2}$ component is discussed for the Sb $3d$ doublet as the information transfers to the lower binding energy peak *via* the fitting constraints previously mentioned.

Table 7.1: Binding energies of the Zn $2p_{3/2}$ and Sb $3d_{3/2}$ peaks for undoped and doped sample measured using HAXPES ($h\nu$ = 5.92 keV). $\Delta E = E_{doped}$ - $E_{undoped}$.

Peak	Undoped (± 0.01 eV)	Doped (± 0.01 eV)	ΔE (eV) (± 0.02 eV)
Zn $2p_{3/2}$	1021.44	1021.67	0.23
Sb $3d_{3/2}$	540.16	540.42	0.26

In the doped crystal, the peak position for both orbitals have shifted higher in energy. This is a direct consequence of conduction band filling. Upon doping, the Fermi level moves into the conduction band and correspondingly shifts the core peaks to a higher binding energy. The magnitude of the peak shift for both core orbitals is in reasonable agreement with the shift in optical band gap (0.17 ± 0.08 eV).

7.2 Valence Band Spectroscopy

7.2.1 Conventional XPS

Valence band spectra were recorded for the undoped and doped sample using conventional XPS and HAXPES. Where required, data from additional samples is presented. Figure 7.4(a) displays XPS obtained valence band spectra for the doped and undoped sample. An enhancement of the valence band maximum (VBM) up to the Fermi level is displayed in Figure 7.4(b).

The peak at ∼ 10 eV is predominantly Zn $3d$ in character. The shift of this peak is recorded in table 7.2. Additionally, the values of the VBM and its corresponding shift is also recorded. The VBM was determined by linear extrapolation of the band edge to zero intensity.

Table 7.2: Binding energies for key features in XPS valence band spectrum. ΔE = E_{doped} - $E_{undoped}$

Peak	Undoped	Doped	ΔE (eV)
Zn $3d$	10.18 ± 0.01	10.38 ± 0.01	0.21 ± 0.02
VBM	3.01 ± 0.03	3.07 ± 0.03	0.06 ± 0.06

The uncertainty in the position of the VBM is larger than that of the Zn $3d$

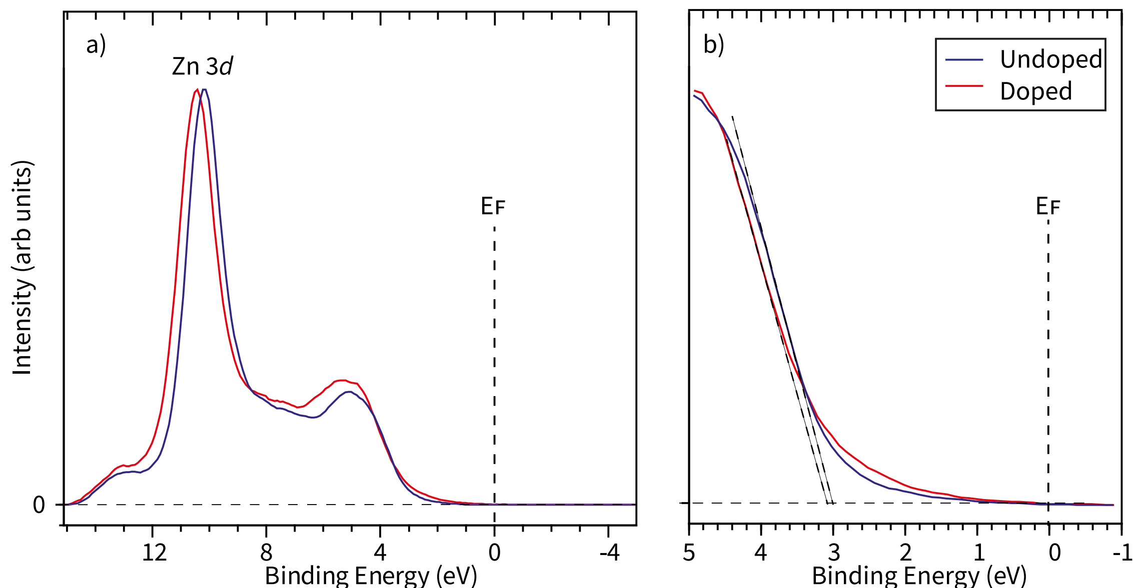

Figure 7.4: (a) XPS valence band spectra for doped and undoped crystal measured from BE = 15 → -5 eV using photons ($h\nu$ = 1.48 keV). Spectrum are normalised to the maximum intensity of the Zn 3*d* peak. (b) Zoom of the valence band maximum and Fermi level with band edge extrapolation lines displayed. No intensity is observed at the Fermi level for the doped samples.

because the peak position is well defined compared to extrapolating a linear fit onto the band edge.

The shift of the Zn 3*d* peak is consistent with the observed shifts in the core levels suggesting a rigid shift of the bands due to conduction band filling [44, 65, 218]. The VBM however, does not appear to experience the same rigid shift and instead a smaller shift is observed. The valence band changes shape highlighted by E_{Zn3d} - E_{VBM} increasing from 7.17 ± 0.04 to 7.31 ± 0.04 eV, however the reasons for this are undetermined.

7.2.2 HAXPES

Similar valence band spectrum were obtained using HAXPES ($h\nu$ = 5.92 keV) and are shown in Figure 7.5. Four prominent valence band features are labelled. The peak labelled C consists primarily of the Zn 3*d* orbitals. The binding energies of these features were calculated using the second derivative of the intensity curves and are displayed in table 7.3.

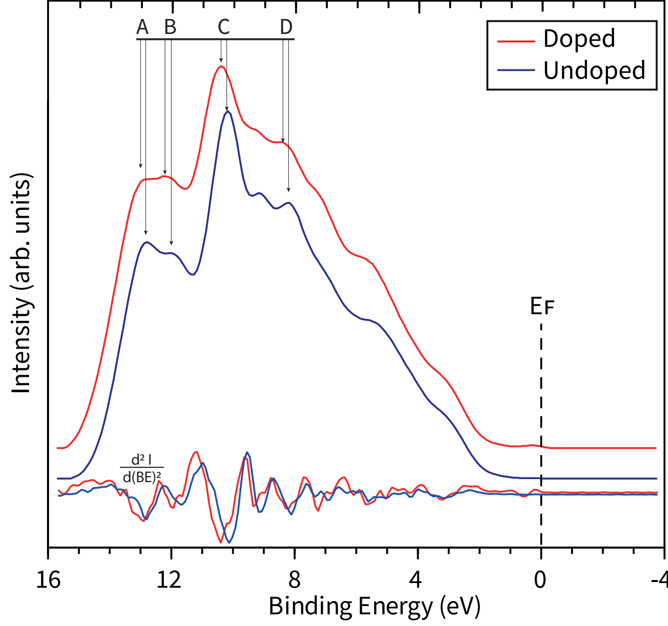

Figure 7.5: Valence band spectra for the undoped and doped crystal measured using HAXPES ($h\nu$ = 5.92 keV). The second derivative of the curves is displayed. Spectrum are offset in the intensity from each other and relevant peaks are highlighted.

Table 7.3: Valence band peak positions for the undoped and doped samples with calculated shifts.

Feature	Doped (± 0.05 eV)	Undoped (± 0.05 eV)	Shift (eV) (± 0.10 eV)
A	13.00	12.82	0.17
B	12.04	11.88	0.16
C	10.38	10.17	0.22
D	8.44	8.23	0.21

A persistent ∼ 200 meV shift to higher binding energies is seen for the doped samples features, similar to core lines and XPS valence band spectra. Figure 7.6 displays the valence band maximum and Fermi edge of both samples.

There are a few key comments to make about this zoomed spectrum. The first is related to the values for the valence band maximum. Linear extrapolation of both band edges reveals values to be 1.82 ± 0.05 and 1.87 ± 0.05 eV for undoped and doped respectively. Both values are ∼1.2 eV lower in energy than those recorded for the XPS spectrum. This discrepancy is discussed in section 7.2.4. The second comment relates to the conduction band in the doped spectrum, which was not

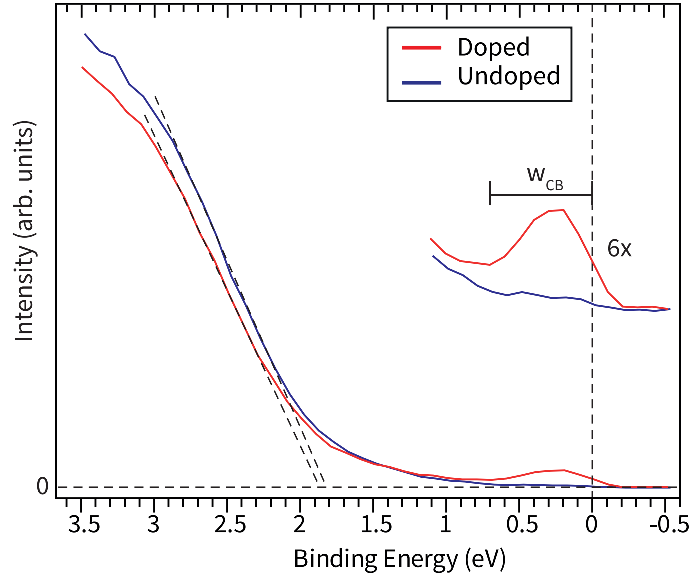

Figure 7.6: Valence band maximum and conduction band for doped and undoped crystal measured using HAXPES ($h\nu = 5.92$ keV). A 6 x intensity enhancement displayed around the Fermi level highlightnig the conduction band width w_{CB}.

observed in XPS measurements. The reasons for this are related to the photoionisation cross sections of the relevant atomic orbitals but is discussed in section 7.2.5. Instead the energy width of this conduction band feature w_{CB} is used to determine the magnitude of band gap renormalisation in the doped sample.

7.2.3 Band Gap Renormalisation

Following the method employed by Egdell *et al* [218], by measuring the conduction band width ΔE_{BM} and subtracting the energy of the peak shift $\Delta E_{peakshift}$, the magnitude of band gap renormalisation ΔE_{RN} is calculated.

$$\Delta E_{RN} = \Delta E_{BM} - \Delta E_{peakshift} \tag{7.3}$$

The width of the conduction band w_{CB} is determined from the high binding energy edge of the conduction band intensity measured to be 650 $\pm$ 50 meV. When combined with the peak shifting of 200 meV gives a renormalisation value of $\sim$ 450 meV for this doped crystal. This calculation carries the assumption that the Fermi level in the undoped sample sits just below the conduction band and the difference

in Fermi energies is taken to be the Burstein – Moss shift. This is reasonable given the determined shallow donor states in undoped ZSO.

The experimentally obtained conduction band width is compared with the predicted width due to the Burstein – Moss effect (Equation 7.4) with effective mass 0.22 m_e and carrier densities n taken from Hall effect measurements.

$$\Delta E_{BM} = \left(\frac{h^2}{8m^*}\right)\left(\frac{3n}{\pi}\right)^{\frac{2}{3}} \tag{7.4}$$

The expected conduction band width is be 561 ± 112 meV, ∼ 100 meV less than that observed. This is assuming a parabolic band model is acceptable in this system [23, 44, 90]. There are several reasons the conduction band is greater in width than expected: Firstly, the effective mass is smaller than expected and doping shifts the CBM at an exaggerated rate. This is considered unlikely because, in other TCO compounds, doping tends to flatten the conduction band [23]. Secondly, Mudd *et al* [44] reported this phenomenon in CdO however this increased width was attributed to a plasmon satellite of the conduction band, also considered unlikely in ZGSO due to the absence of plasmon satellites in core level spectroscopy.

Finally, charge compensation can provide net carrier density values lower than the conduction band's actual occupancy. n is solved using equation 7.4 and determined to be $2.62 \pm 0.05 \times 10^{20}$ cm^{-3} instead of the Hall value of 1.97×10^{20} cm^{-3}.

This evidence of charge compensation helps to explain the discrepancies between expected carrier densities from measured gallium concentration and Hall effect data.

7.2.4 Valence Band Maximum Discrepancy

This section discusses the difference between values obtained for the VBM from both conventional XPS and HAXPES spectra. Figure 7.7 overlays the hard and soft x-ray data for both undoped and doped samples to visualise this. The data is normalised to the peak intensity of the Zn 3*d* peak. This is not an ideal normalisation as this peak is not purely Zn 3*d* in nature with additional orbital components contributing to the intensity however, peak fitting is complicated especially with the degree of orbital hybridisation occurring in the valence band.

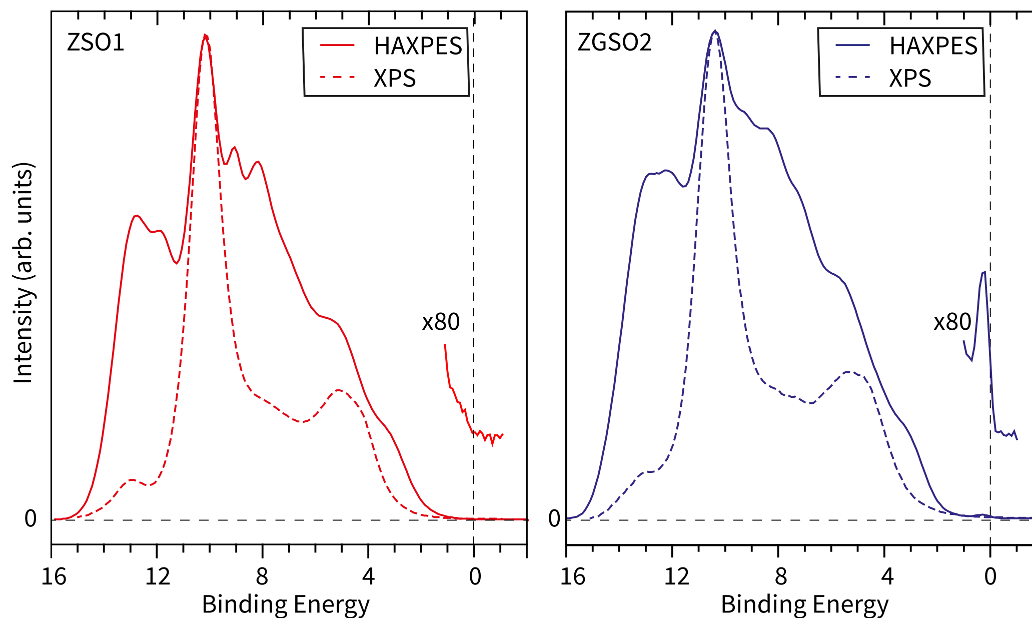

Figure 7.7: HAXPES ($h\nu$ = 5.92 keV) and conventional XPS spectra ($h\nu$ = 1.48 keV) for undoped and doped samples. For the doped sample the Fermi level is enhanced by 80x to visualise the conduction band for the HAXPES spectrum.

The discrepancy at the VBM is immediately apparent. To explain this an in-gap state is considered. Furthermore, given the wide optical band gap, this in-gap state plays no significant role in optical transitions. A similar peak was observed by Egdell *et al* [218] in Sb doped SnO_2 however they attributed it to the reduction of Sn^{+4} to Sn^{+2} on the surface due to an absence of bridging oxygen. The feature reduced upon doping with antimony as Sb^{+3} replaced Sn^{+2}. Gallium doping is assumed to play no role in this feature given its prominence in both doped and undoped spectra. Furthermore, the feature also appears to be sample dependent. Figure 7.8 displays the valence band spectrum of three undoped and three doped samples where a significant intensity variation of the in-gap state occurs.

Sample 64 (3) has a prominent peak at $\sim$ 2.5 eV, whereas it appears suppressed in 64 (2). Similarly, in the doped spectra, a sharp peak is observed at the VBM in two samples. EDS measurements suggest the cation stoichiometry to not vary significantly between the undoped samples therefore deviations in cation stoichiometry is not considered to be the cause of this.

It is proposed that this in-gap state is formed due to a reduction of Sb^{+5} to Sb^{+3}, shifting the energy of the 5s state. EDS measurements are insensitive to the chemi-

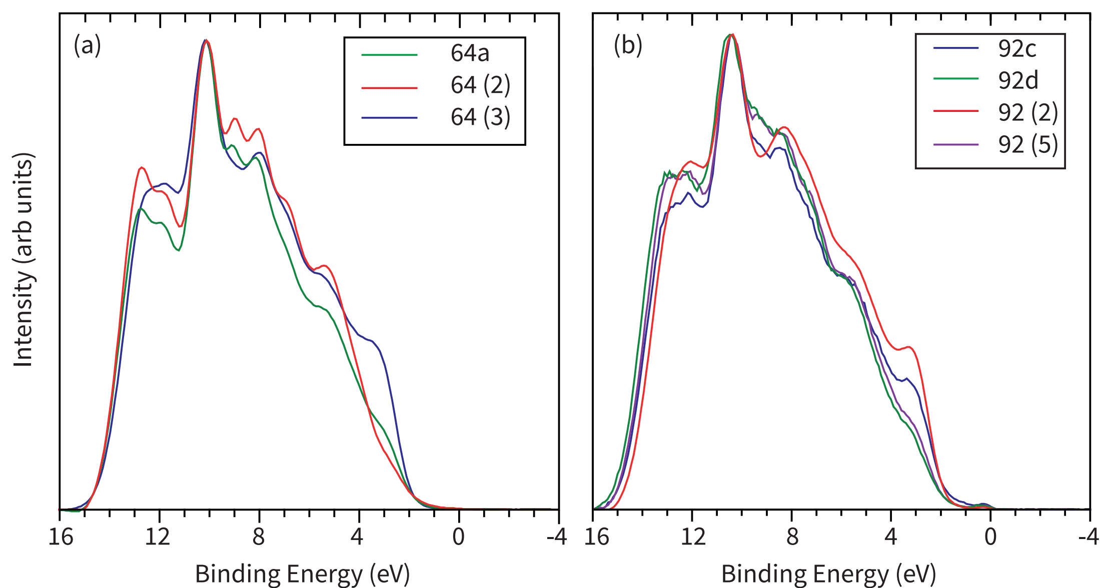

Figure 7.8: Valence band data obtained using high energy photons. (a) Three undoped samples normalised to the Zn 3*d* peak intensity. (b) Four doped samples. Clear variation at the VBM is observed between samples.

cal state of the ions so is unable to detect this effect. Similarly to Egdell, this could be a surface effect due to the absence of bridging oxygen. It could also be a more fundamentally bulk issue with oxygen vacancies prominent in these samples. Additional research into quantifying oxygen vacancies could be crucial to understanding this effect. Analysis of the O 1*s* peak measured in this experiment is unreliable due to the potential surface contaminants. It could also originate from bulk cation substitution with Sb^{+3} sitting on the Zn^{+2}, given they have similar ionic radii [168]. This would occur in small amounts, therefore not observable in the core level spectroscopy. This state being of *s*-character also explains why it does not inhibit the material's transparency as the dipole-selection rules forbid *s*-*s* transitions. The reason why this state is only observed using higher energy photons is discussed in the following section.

7.2.5 Orbital Nature of the Valence Band Density of States

The shape of the valence band is highly dependent on the photon energy used to measure. This section aims to explain why certain features such as the conduction band and in-gap state are observed using HAXPES but not in conventional XPS.

These changes originate primarily due to photon energy dependence of orbitals photoionisation cross section σ. This is a measure of a photons probability to photo-excite an electron out of the orbital and is strongly photon energy-dependent. In section 2.8, a calculated density of states for the valence band of ZSO is displayed indicating the top of the valence band to be heavily O $2p$ in nature with a strong Zn $3d$ peak (BE $\sim$ 10 eV) [34, 107]. To compare with experimental data, the calculated density of states needs to be modified. Photoelectron intensity is not directly related to the DOS but to the sum of the photoionisation cross section weighted partial density of states for each contributing atomic orbital [244, 245]. Dr. Adam Jackson, the computational collaborator on the project, has provided DOS calculations for ZSO with relevant atomic orbitals weighted for both Al Kα (1.48 keV) and HAXPES (5.92 keV) photon energies, broadened by a Gaussian to replicate experimental resolution. Figure 7.9 displays the density of states.

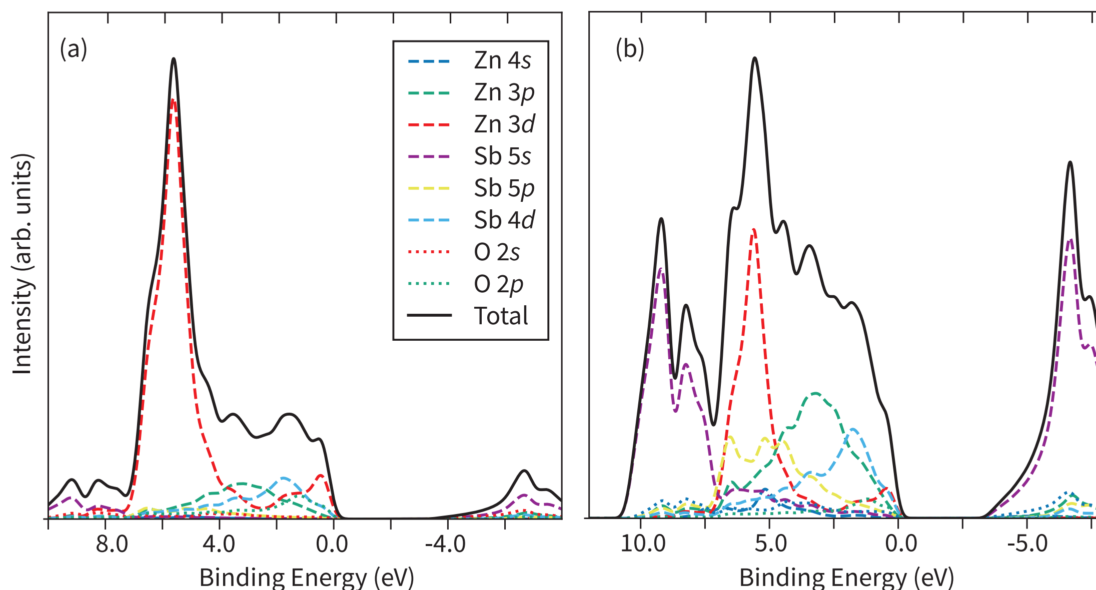

Figure 7.9: Photon energy weighted DOS determined using a hybrid QSGW calculation for (a) Al Kα photon energy ($h\nu$ = 1.48 keV) (b) HAXPES photon energy ($h\nu$ = 5.92 keV). The top of the valence band is set to a binding energy of zero by convention.

Figure 7.10 displays the photon energy dependence of the atomic orbital photoionisation cross section for all contributors to the valence band spectrum. Low photon energy data was calculated by Lindau and Yeh [130] and compiled by Kalha *et al* [246] with high energy data calculated by Trzhaskovskaya *et al* [126–128] and

collected by Willis *et al* [247, 248]. Table 7.4 highlights relevant photoionisation cross section values using in this research, ARPES experiments were carried out using photons $h\nu = 120$ and 148 eV so the cross section provided is that of Y Mζ (132.3 eV). Values for the HAXPES energies (5920 eV) were taken from the extrapolation of the data.

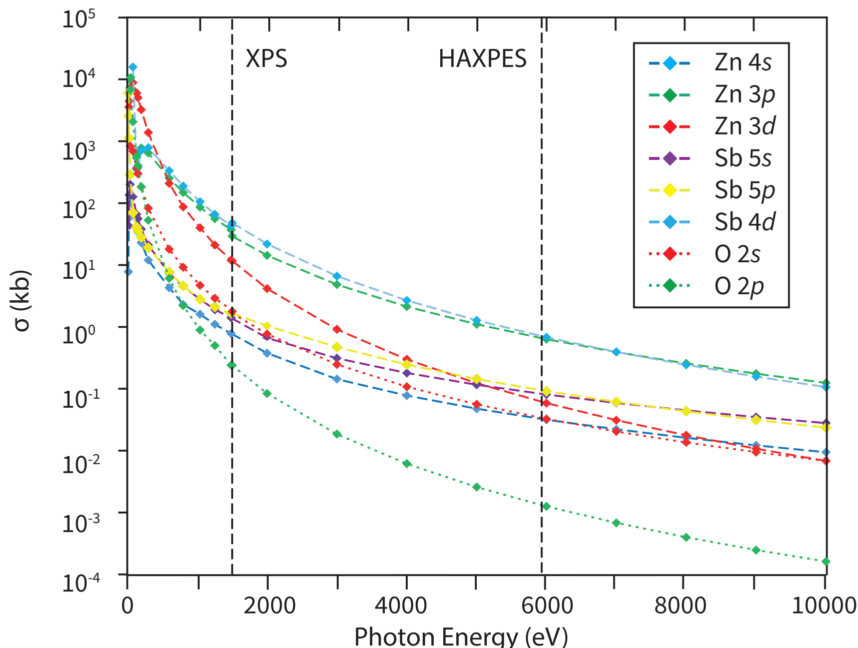

Figure 7.10: Photoionisation cross sections of relevant Zn, O and Sb atomic orbitals as a function of photon energy in units of kilobarns = 10^{-21}cm^2. Dotted lines highlight relevant photon energies. Data was taken from Lindau and Trzhaskovskaya [126–128, 130]

Table 7.4: Photoionisation cross sections for orbitals comprising the valence band in ZSO. Values are in kilobarns ($\times\ 10^{-21}$cm^{-2}). All data is displayed to as many significant figures as available in the literature.

Technique	Zn			Sb			O	
	4*s*	3*p*	3*d*	5*s*	5*p*	4*d*	2*s*	2*p*
ARPES (132.3 eV)	40	534.5	6052	66	41	352.3	367.7	577.2
XPS (1486 eV)	0.78	37	12	1.4	1.6	43	1.9	0.24
HAXPES (5920 eV)	0.032	0.634	0.0588	0.081	0.092	0.682	0.033	0.001

Interestingly, O 2*p* orbitals contribute little to the photointensity of the valence bands for both XPS and HAXPES. This is due to the comparatively low photoionisation cross section of the O 2*p* orbital. The significant change of the valence band shapes results from an enhancement of the Zn 3*p* and Sb 4*d* intensity relative to the

prominent Zn 3d peak. At XPS energies, the photoionisation cross sections of Zn 3p and Sb 4d are $\sim$ 3 and 4 times greater than Zn 3d, respectively. At HAXPES energies they are $\sim$ 10 and 11 times enhancing their contribution to the spectral intensity.

The contribution of Zn 3d to the spectral weight of the maximum peak also varies significantly between the two energies, making the spectrum normalisation used throughout this chapter purely a maximum peak intensity normalisation. However, the most important discussion relates to the change of photoionisation cross section of the Sb 5s conduction band. For this qualitative discussion, its change in cross section is referenced against the prominent Zn 3d orbital. At Al K-α energies the Sb 5s orbital is $\sim$ 8 times smaller than Zn 3d. However, at HAXPES energies, the Sb 5s is $\sim$ 1.4 times greater, significantly enhancing the conduction band's spectral weight. This directly demonstrates how useful higher energy sources can be in observing specific orbitals, particularly for s-orbitals [223]. This enhancement of the Sb 5s orbital explains why the in-gap state is only observed in HAXPES spectra.

Figure 7.10 demonstrates in all atomic orbitals, except at very low energies $h\nu$ $<$ 100 eV [130], the photoionisation cross sections decrease the photon energies increase. Development of bright synchrotron sources can overcome these small cross sections and have aided the development of hard x-ray photoemission experiments.

Figure 7.11 overlays the total DOS with the experimental data for the undoped crystal. DOS calculations are by convention, set to have the top of the valence band with zero binding energy therefore the binding energies must be rigidly shifted to line up with experimental data. However, this is not a trivial issue. In this instance, the VBM is set equal to the 3.01 eV value obtained from XPS. Under no rigid shift of binding energy does the experimental data and the total DOS align.

This chosen alignment does appear to provide reasonable agreement at the higher binding energy side of the spectrum however, significant discrepancies are noticed. Most notably, the Zn 3d peak observed $\sim$ 2.0 eV higher in energy than calculations suggest. This is not unique to this system as calculations on ZnO routinely underestimate the Zn 3d binding energies by values ranging 2.7 - 1.1 eV depending on the calculation method [249, 250].

To explain the further discrepancies between the experimental spectra and cal-

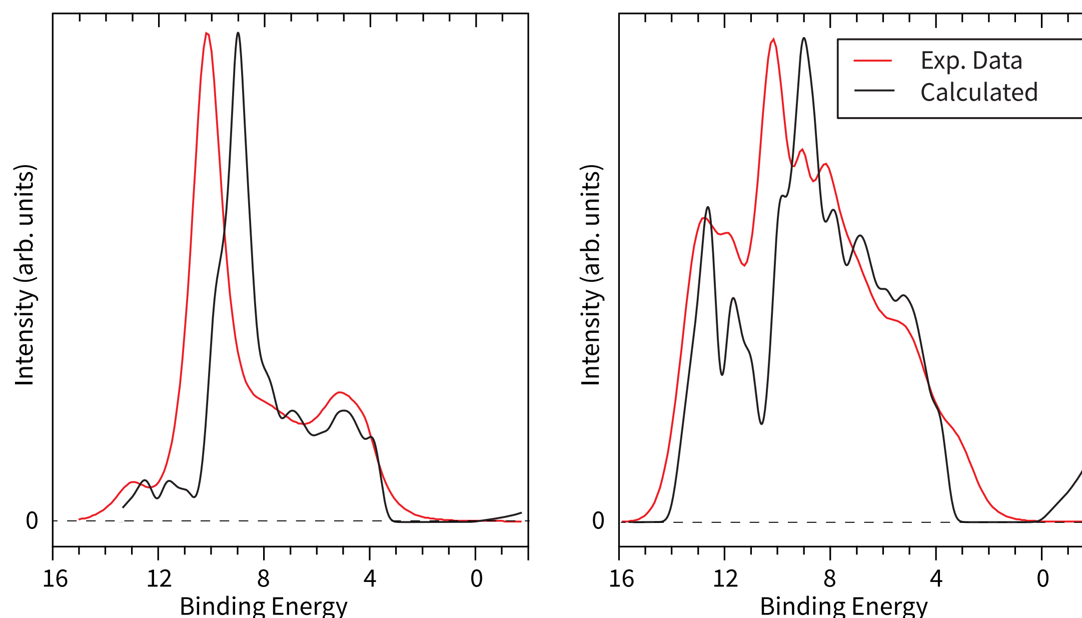

Figure 7.11: Comparison of experimental and calculated valence bands for undoped samples at XPS and HAXPES energies. The top of the valence band has been set to 3.01 eV.

culated DOS, additional factors need to be considered. Particularly at high photon energies, the experimental geometry becomes an important factor as the intensity of photoemitted electrons is not isotropic. Additional asymmetry parameters of the atomic orbitals must be considered by using the differential photoionisation cross section [126–128]. Correcting calculations for experimental geometry may go some way to reduce the differences between observed and calculated spectra [251]. However this is not explored for this project because the position of the Zn 3d band will remain unaffected. Shallow d orbitals have a profound effect on the rest of the valence band [165, 252]. The shallow d orbitals energetic positioning affects the hybridisation with the other valence band atomic orbital contributors and, therefore, the structure of the rest of the valence band. Improvements to the Zn 3d positioning could help negate discrepancies to experimental and theoretical data, similar to work carried out on ITO [253].

7.3 ARPES

This section discusses an experiment undertaken using an assigned in-house beam time on the I05 HR-ARPES branch at the Diamond Light Source. For reasons that will become apparent, analysis is not complete, however, obtained data is presented.

7.3.1 Experiment Plan

In ITO, Walsh *et al* [58] determined that doping of Sn into the In_2O_3 lattice tended to flatten the conduction band owing to the hybridisation of the donor s-state with the host conduction band. ARPES is an excellent tool to measure this effect due to its ability to map the electronic band structure in reciprocal space. The objective of the experiment was to measure the conduction band in highly doped ZGSO, in doing so, determine the effective mass which could be compared with the predicted value of 0.27 m_e along the Γ - X direction. The key experimental steps required to fulfil this objective are discussed.

The conduction band is known to be centred at the Γ point. To compare with band structure calculations, a surface must be chosen with a very well defined crystallographic orientation aligned with the reciprocal lattice vectors. This experiment aimed to measure the band dispersion along two cuts, Γ - X and Z - R as displayed in Figure 7.12.

Measurements of these cuts is possible if the measured surface has a (001) orientation. Due to the energies used in ARPES experiments, the photoelectron inelastic mean free path is small $\sim$ 1 nm. Therefore the requirement for a surface free of contamination becomes essential. Theoretically, ARPES can be carried out at higher energies to reduce the surface sensitivity but at the cost of energy and momentum resolution [254]. For the photon energies used in this experiment, $\sim$ 120 eV, a fresh surface needed to be created by cleaving the crystal in a vacuum, discussed in section 7.3.2.

Upon obtaining a clean (001) surface, the sample needs to be aligned with the beam by adjusting the tilt and azimuth angles to ensure that measurements occur at the high symmetry points. Furthermore, by adjusting the photon energy, different k_z points could be measured enabling the determination of Γ and Z points. Finally,

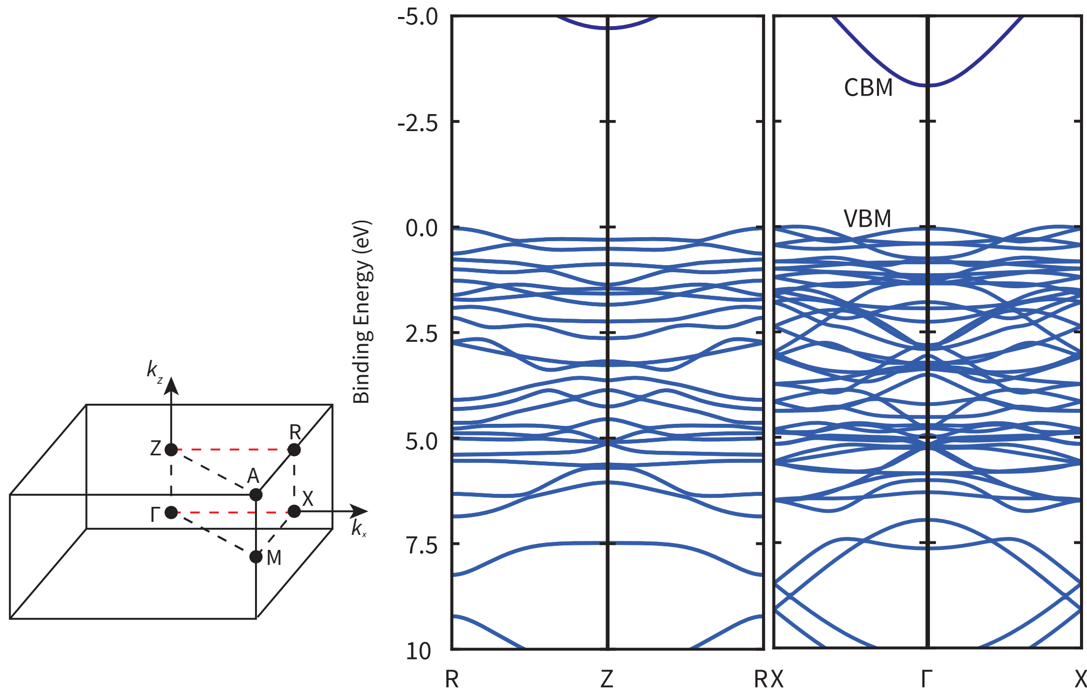

Figure 7.12: Brillouin zone of the tetragonal lattice with points of high symmetry indicated. The two cuts Γ - X and Z - R are highlighted as red dotted lines with DFT band structures for R - Z - R and X - Γ - X.

the Fermi level can be measured at the Γ point to measure the conduction band of ZGSO.

7.3.2 Cleavage of $ZnSb_2O_6$

The first and perhaps most significant problem with carrying out ARPES measurements on single crystal ZSO is their inability to cleave. The trirutile structure contains no obvious cleavage planes or planes bonded by Van der Waals forces that allow cleaving with minimal force. ZSO fractures conchoidally, common in brittle minerals and is characterised by curving rippled surface similar to a shell's surface. The fracturing also implies ZSO does not cleave along atomic planes with defined surface orientation making data analysis non-trivial. To overcome this, a method was devised to cleave the crystal effectively.

To maximise the possibility of a high quality surface, the (001) orientation was chosen. A Laue diffraction study on as-grown crystal facets revealed the (013) (110) or (001) surface to be the most common suggesting the creation of a (001) surface

may be possible. Furthermore, the (001) surface was determined to be ideal for measuring the conduction band dispersion along Γ - X.

The crystal was characterised first using the PPMS therefore the geometry was predetermined to be a cuboid. To ensure the smallest cross section of the crystal was the (001) plane, the crystal was prepared in the following steps:

1. A suitable crystal was chosen using Laue diffraction with a large facet, orthogonal to the (001) plane - (110)

2. The crystal was polished down to a thickness of $\sim 200\ \mu$m perpendicular to the (110) plane

3. The direction of the crystallographic c - axis was determined.

4. The longest sides of the cuboid were cut parallel to the c-axis.

Figure 7.13 displays a cartoon of a cuboid crystal with the orientation of the surfaces projected.

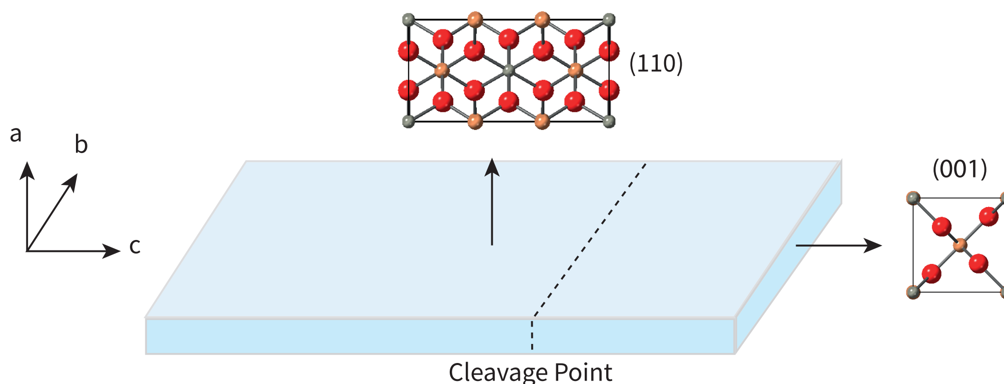

Figure 7.13: Schematic of the lattice orientation of a crystal required to ensure a cleaved (001) surface.

For typical experiments at I05-ARPES, samples are placed onto Cu/Be sample posts specifically designed for the six-axis cryo-manipulator and glued down with a conductive silver epoxy. Ceramic top posts glued onto the top of the sample act as levers and can cleave weakly bonded surfaces with little application of force. For ZSO crystals, this method does not work as the crystals do not have weakly bonded

planes therefore breaking the crystal requires more force than the ceramic top posts could apply.

Grooves were etched into the sample posts, slightly wider than the crystal's thickness and deep enough to allow the crystal to sit. Likewise a sturdier aluminium top post, $\varnothing \sim 5$ mm, also had a groove etched using a wire saw. The sample was glued in using a conductive silver epoxy as depicted by Figure 7.14. A notch was then cut into the crystal to induce a point of weakness. Upon applying force to the top post the sample could cleave at the point of weakness and a fresh (001) surface would be ready for measurement.

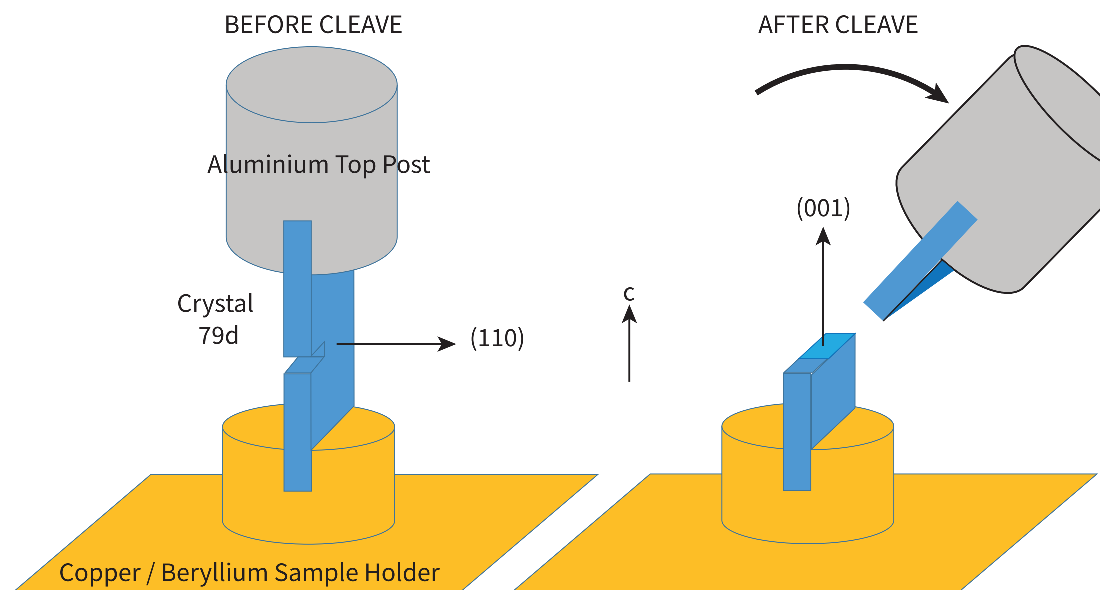

Figure 7.14: Schematic of the cleavage method before and after cleave with the crystal glued into the sample holder and top post. Applying force to the top post encourages the crystal to break at the induced point of weakness.

Crystal 79d ($x = 0.10$) was chosen as a suitable candidate for ARPES due to its high carrier density ($n = 2.54 \times 10^{20}$ cm^{-3}), therefore encouraging a greater conduction band intensity. It also had the desired facet orientation determined by Laue to be (110) as seen in Figure 7.15.

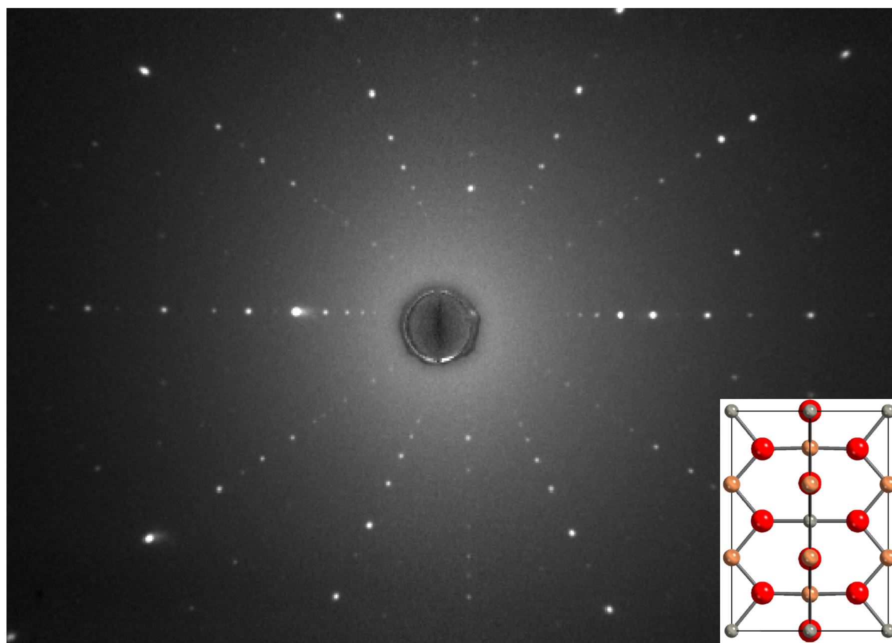

Figure 7.15: Laue diffraction pattern of the large face of the bar shape. The diffraction pattern indicates the surface normal to the x-ray beam is (110) oriented and the c-axis runs top to bottom.

The expected diffraction patterns were simulated using QLaue software, allowing comparison with experimental data. The orientation and direction of the c-axis were able to be confirmed. Figure 7.15 displays the two-fold symmetry expected by the (110) plane.

7.3.3 Experimental Results

The sample was cleaved at 160 K in a vacuum $< 10^{-9}$ mbar. The initial photon energy was chosen to be $h\nu = 120$ eV and of linear horizontal polarisation. Using the Fermi level of a sputtered polycrystalline Au sample, an energy resolution of $\sim$55 meV was calculated. The binding energies were also referenced to the Fermi edge of the gold sample.

Under these conditions, a dispersing electron band was observed at a binding energy of $\sim$ 8 eV. This dispersion was used to orientate and centre the sample. By adjusting the photon energy, different k_z points were probed, from which Γ and Z were determined to be 121 and 148 eV. However, for reasons that will be covered, the two high symmetry points were unable to be assigned a photon energy. Figure

7.16 displays the photoelectron intensity as a function of photon energy ($h\nu$ = 115 - 160 eV).

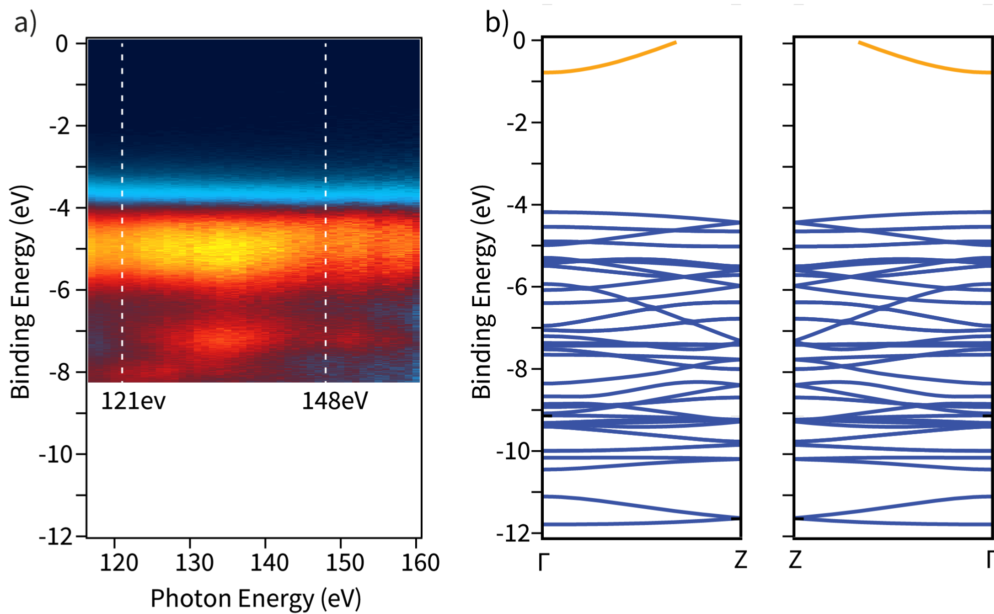

Figure 7.16: k_z variation of ZSO (001) (a) Energy distribution curve plot as a function of photon energy at normal emission. (b) Electron band structure calculations of Γ- Z and Z - Γ.

Figure 7.17 displays the dispersions recorded at both energies, with kinetic energy and polar angle converted into binding energy and momentum using equation 3.16.

Binding energies in ARPES are conventionally displayed as E - E_F and are therefore negative however they are equivalent to the binding energies used throughout this chapter. Intensities between E - E_F = -3 and -9.7 eV are enhanced by 10 x.

For both dispersions, an intense localised peak is observed at ∼ -10.6 eV, attributed to be of Zn 3d orbital character. This is a few hundred milli-electronvolts deeper in energy than the spectrum analysed in XPS and HAXPES. However, as this is a highly doped sample, this increased shift is likely due to the Burstein – Moss effect. The top of the valence band between -3.6 eV and -6.5 eV, is assumed to consist primarily of the localised O 2p states given the enhanced photoionisation cross section at 130 eV (table 7.4). The dispersing features between -6 to -9.5 eV distinguishes the two spectrum.

Displayed in Figure 7.18 are energy distribution curves (EDC) taken at both photon energies obtained by integrating the intensities over ± 0.5 Å^{-1} from the

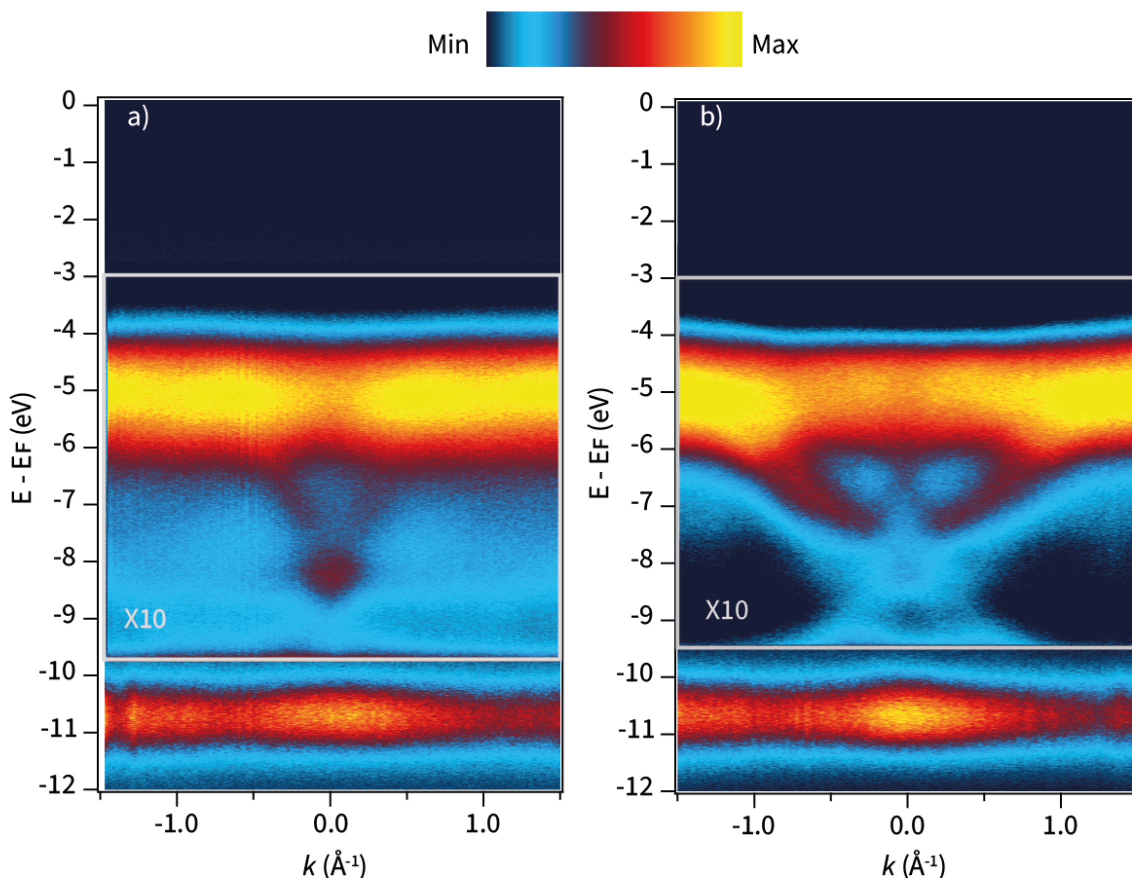

Figure 7.17: (a) Valence band dispersion for measured at 121 eV for the plane perpendicular to (001) surface (b) Dispersion at 148 eV. The intensity has been enhanced 10 x between BE = -3 and -9.7 eV.

centres of the dispersions. Both spectra are normalised to the maximum intensity of the peak with the majority Zn 3*d* character.

Linear extrapolation of the VBMs leading-edge provides values of 3.31 and 3.48 $\pm$ 0.05 eV for $h\nu$ = 121 and 148 eV respectively, indicating no intensity of the localised state in the band gap previously observed in several samples using HAXPES. Unfortunately, no intensity is observed at the Fermi level and therefore the conduction band is unable to be measured.

For now, this is where any meaningful ARPES data analysis ends, and the following section will focus on why this experiment did not meet its desired objectives.

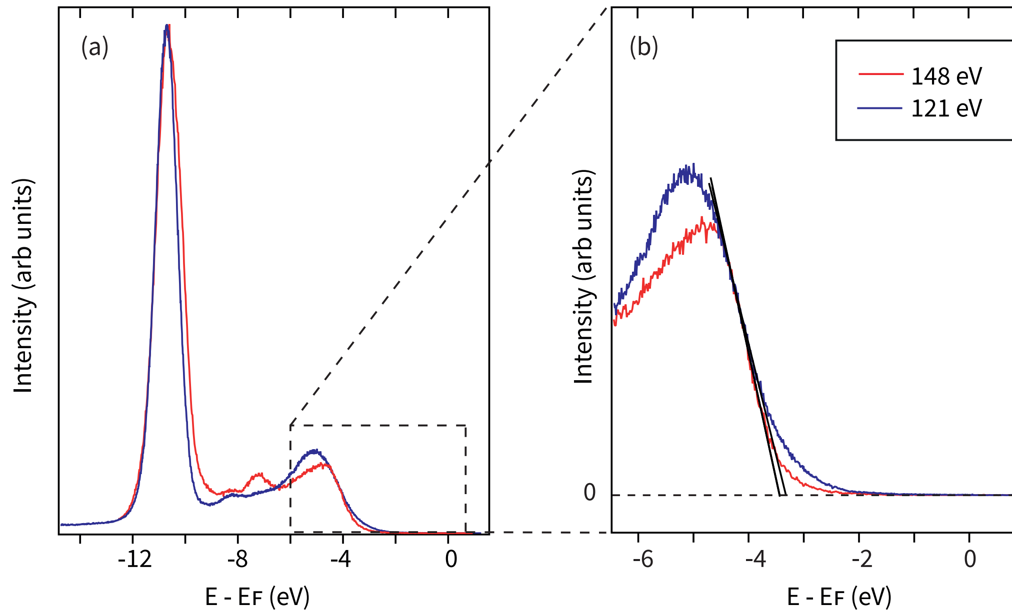

Figure 7.18: EDC's for both photon energies used obtained over an integration of ±0.5 Å^{-1}. (a) Energy scale of EDC taken to be -15 to 1 eV. (b) Zoom in at the valence band edge and Fermi level of (a). Both EDCs are normalised to the Zn 3d peak.

7.3.4 Experimental Failures

When analysing ARPES results, experimental data needs to be complemented by theoretical predictions such as electronic band structure. Figure 7.16 displayed a lack of strongly dispersing features as a function of photon energy. Therefore, it is not possible to determine, by comparison with band structure calculations, if 121 and 148 eV are energies corresponding to k_z points at the Brillouin zone's centre and edge.

Assuming one of the energies does correspond to the Γ point, the absence of photointensity at the Fermi level can be explained by a continuation of the discussion about photoionisation cross sections. Figure 7.19 displays the ratio of the photoionisation cross sections for Zn 3d and Sb 5s. Compared to the Zn 3d value, the conduction band intensity is most suppressed at the energies used for this experiment. To observe the conduction band at these energies would require a great deal of data collection around the Fermi level. By reducing the photon energy to $\sim$ 26 eV, the conduction band would be enhanced with the added bonus of improved energy and momentum resolution.

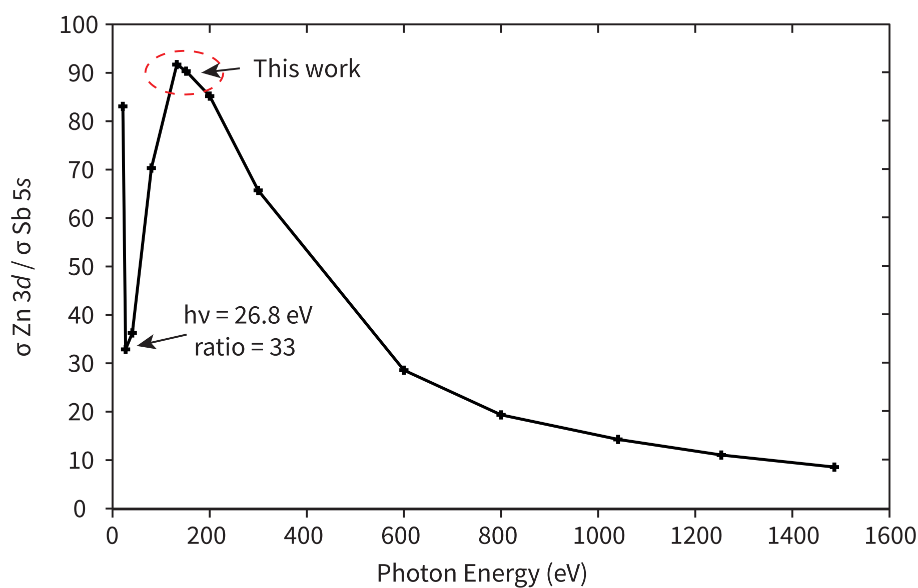

Figure 7.19: Ratio of the photoionisation cross section ratio of the Zn 3d and Sb 5s atomic orbitals as a function of photon energy.

The most significant discrepancy, however, is the k-space magnitude. Using the unit cell of ZSO, Γ - X and Z - R equates to 0.67 Å^{-1}, which looking particularly at the 148 eV band dispersion in Figure 7.20 does not correlate. Even a 45° rotation and assuming this is Γ - M / Z - A does not allow an accurate match.

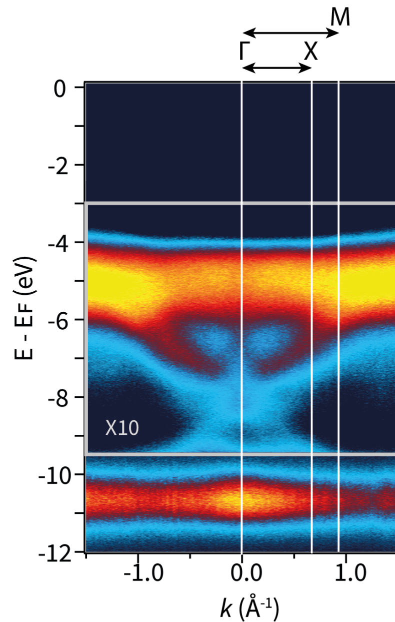

Figure 7.20: ARPES dispersion for photon energy = 148 eV. The lines imposed onto the dispersion indicate suggested Brillouin zone edges for the corresponding points of high symmetry.

Post experiment, LAUE diffraction was carried out on the surface to confirm this was indeed the (001) surface. Figure 7.21 displays a photograph of the cleaved surface as well as the LAUE diffraction.

The LAUE image confirms this is a (001) surface highlighted by the four-fold symmetry only observable in this plane for a trirutile structure. The Laue diffraction pattern's poor quality is due to a high noise intensity from back reflection of x-rays off the silver adhesive holding the crystal into the sample holder. The Laue diffraction pattern shows many peaks corresponding to one reflection indicating many surfaces with the same orientation, however, they are angled away slightly from each other. A similar pattern occurs in crystals that are twinned. The Laue diffraction, combined with the optical image indicates the fractured surface is uneven.

The large experimental beam spot used in ARPES covers many of these surfaces, with the average orientation (001). This creates a significant broadening in the data explaining the discrepancies in the k - space scaling. The spectra observed are the sum of many (001) dispersions tilted away from each other slightly. Unfortunately, this is likely always going to be an intrinsic property of ZSO due to the crystal structure. Possible improvements to the method that may allow reasonable ARPES

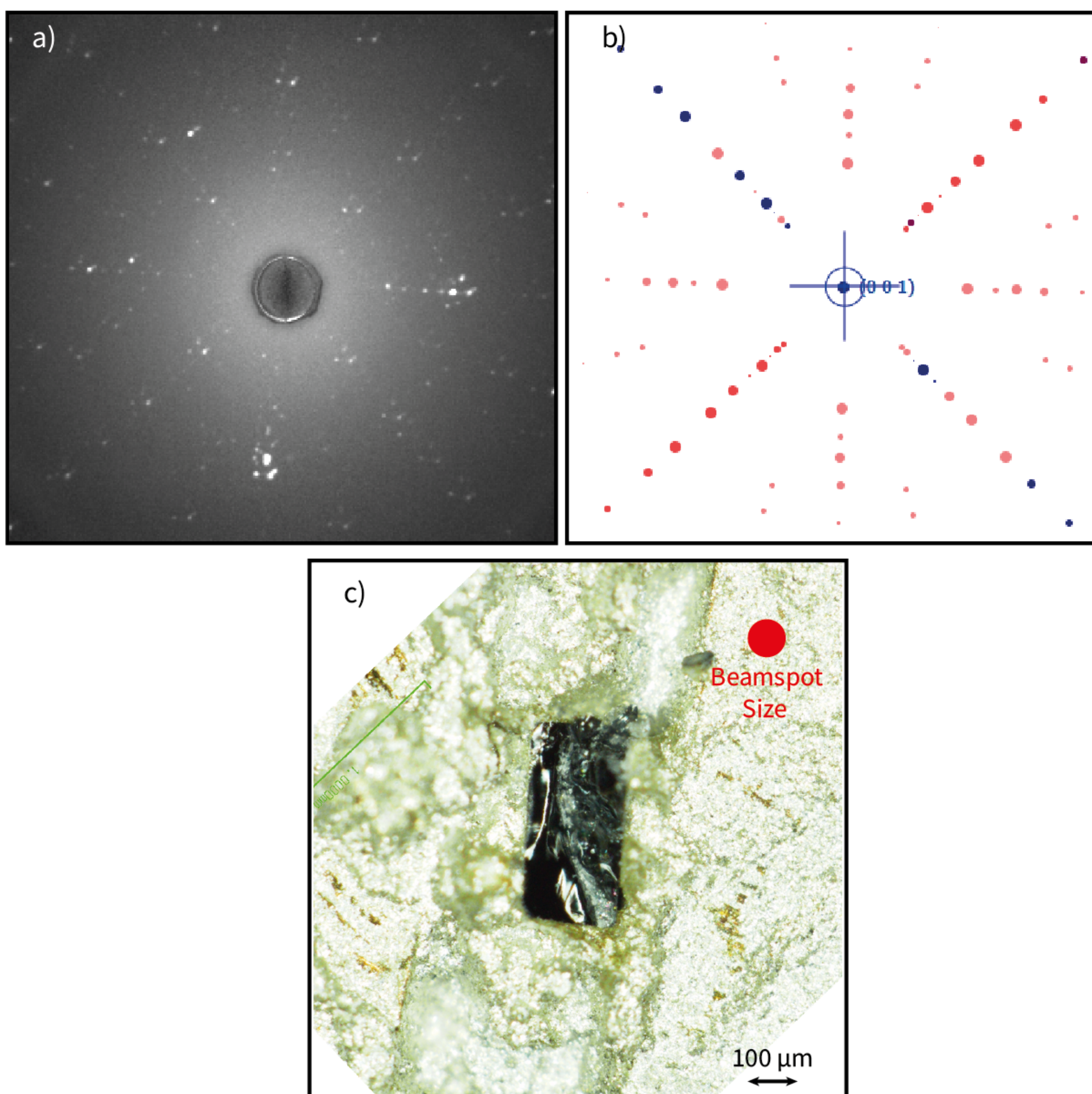

Figure 7.21: (a) Laue diffraction pattern of the cleaved surface of 79d (b) Simulated Laue diffraction of the (001) surface at a detector to sample distance of 35 mm. (c) Optical image of the cleaved crystal with ARPES beam spot size imposed.

measurements are discussed in the Future Work discussion at the end of this thesis.

7.4 Conclusions

This chapter has highlighted many successes of the photoemission experiments carried out. Initially, HAXPES was used as a complementary experimental technique to EDS to prove gallium's existence in bulk ZGSO, where the intensity of the Ga Kα peak in the EDS spectra was weak.

The peak shift of core levels under the influence of doping was determined using

HAXPES. The presence of an electron accumulation or depletion layer was ruled out by observation of HAXPES and XPS core lines occurring at the same binding energy. Detection of a plasmon satellite, expected in the core lines of doped samples was not possible because of the symmetric core line shapes. The reason why asymmetry is not detected remains unexplained. Further work into determining the plasma frequency in this material is required to explain the observations made in this chapter.

This chapter provided an excellent example as to why photon energy is an essential factor to consider when planning out a photoemission experiment. In ZGSO, conventional XPS measurements provided a probing of the valence band DOS. However, key features such as the conduction band and an in-gap state were not observed due to the small photoionisation cross section of the Sb 5*s* orbital. By increasing the photon energy to 5.92 keV, the photoionisation cross section of the conduction band was enhanced with respect to the Zn 3*d* orbitals and a clear conduction band (width ∼650 meV) was observed, from which a value for the band gap renormalisation was deduced.

The absence of a conduction band in ARPES experiments was also explained analysing the photoionisation cross section ratios of Zn 3*d* and Sb 5*s*. Unfortunately, the photon energies used in this study were highly detrimental to the observation of a conduction band. Additional research at lower photon energies (∼ 20 eV) would likely prove beneficial to measuring the conduction band.

Furthermore, ARPES analysis was hindered by the quality of the measured surface. The cleavage did not provide a single (001) surface but many small surfaces causing significant broadening to the valence band dispersions obtained.

Chapter 8

Conclusions

8.1 Summary and Conclusions

This thesis has presented the results for research carried out into synthesising and characterising single crystals of the new transparent conducting oxide - ZGSO.

Before crystals were obtained, a precursor powder was synthesised, determined by x-ray diffraction to be of the correct structure and with a powder mass increase indicating close to complete oxidation. This was achieved by conducting a review of methods in literature. A refined method was developed that minimised the evaporation of antimony by carrying out an initial reaction of ZnO and Sb_2O_3 into $ZnSb_2O_4$ under argon pressure. An additional higher temperature bake in an air atmosphere was shown to successfully react the powder into the $ZnSb_2O_6$ structure with mass increases approaching the expected values. Single crystal ZSO and ZGSO were grown out of the precursor powders by the chemical vapour transport method. The conditions of growth such as duration and temperature were refined using $TeCl_4$ as transport agent. As a HAXPES study showed this to be an unsuitable transport agent due to the inclusion of tellurium, a technique to use Cl_2 was devised. After nearly one hundred growth attempts millimetre-sized, transparent blue single crystals were synthesised.

Chapter 5 explored the key properties that ZSO and ZGSO required to be considered a transparent conducting oxide. Electronic measurements of undoped crystals suggested they possessed an n-type conductivity originating from a shallow donor state, the origin of which remains undetermined. However, it can be said that ZSO

falls into the transparent semiconducting oxide family of the n-type given that the unintentional defects formed created n-type conductivity, similar to ZnO, In_2O_3 and SnO_2.

By doping of Ga^{+3} onto the Zn^{+2} site, a drop in resistivity was observed and the temperature dependence of mobility and carrier concentrations indicated the samples were degenerate semiconductors. A systematic change in mobility upon doping was not observed however this is most likely an artefact of the varying crystal quality rather than a intrinsic situation occurring in the crystals. Given the nature of how the gallium defects are formed, we would expect to see a drop in mobility with doping due to the impurity scattering the conduction electrons. The results displayed here indicated that ZGSO has comparable electronic properties to well established n-type compounds with a similar mechanism of doping such as ITO and AZO. Only in n-type TCO compounds such as La:$BaSnO_3$ and Mo:In_2O_3 do we observe higher electron mobilities but as already mentioned in section 2.3, the mechanism of doping is dissimilar. Unfortunately, though likely originating from unpredictability of the CVT method, careful control of the electronic properties, in particular the electron density eludes us, a key requirement in the development of new TCO's and an issue that would need to be overcome to become a functioning material in industry.

UV - Vis spectroscopy measurements carried out on polished thin crystals revealed high optical transparency in all crystals across the visible light range with optical band gaps remaining > 3.3 eV even under the influence of doping. Variations of the band gaps were discussed using effects such as: the Burstein – Moss shift, band gap renormalisation, and band edge distortions described by Urbach tails. Significantly, the optical band gap in all ZGSO single crystals remains large enough for transparency for visible light. These results combined with the electronic measurements provides conclusive proof that ZGSO is a new transparent conducting oxide material. This discovery of the first trirutile TCO can be added into the *catalogue* of known TCO's that could potentially be applicable in technology, especially if the desired application requires a compound with similar lattice parameters, to prevent lattice mismatch at an interface.

To further understand the properties of the grown single crystals, the cation stoi-

chiometry and lattice structure was determined and results were discussed in chapter 6. EDS measurements showed grown crystals of undoped ZSO to be highly stoichiometric with little composition variation of between samples. Similar measurements of the doped samples indicated an erratic nature to doping of gallium into the ZSO structure. Across one growth batch, gallium doping was determined to range from 4 - 14 %, indicating growth conditions were non-homogeneous across the sink in the reaction ampoule. Furthermore, two sides of one single crystal was shown to have significantly different optical properties. Using EDS the variation in optical properties was explained by a change in gallium concentration across the sample. Given that local growth conditions would not vary significantly, it was determined that the rates of transport of the gaseous constituents should also be considered when discussing variations of doping across crystals grown by CVT. Powder x-ray diffraction and Rietveld refinement was used to determine the lattice parameters of undoped and 6% Ga doped crystals. An apparent reduction in lattice parameters was attributed, in part, to the size mismatch between the Ga^{+3} and Zn^{+2} ions.

Chapter 7 discusses photoemission spectroscopy experiments conducted on single crystals of ZSO and ZGSO. The binding energy and peak shapes of core orbitals were examined using conventional lab-based XPS ($h\nu$ = 1.48 keV) and hard x-ray spectroscopy HAXPES ($h\nu$ = 5.92 keV). The shift of peaks to higher binding energies in doped samples was attributed to band filling due to conduction band electrons. The absence of a higher binding energy component in the doped samples core lines remains an unanswered question. TCO compounds generally have asymmetric line shapes attributed to a plasmon loss feature however this was not observed in this project. This chapter has shown the importance of photon energy when carrying out photoemission spectroscopy experiments, especially when measuring the valence band. The higher energy photons used by HAXPES enhanced the photoionisation cross section of the Sb 5s conduction band with respect to the other valence band features, and clear photointensity was observed. Measurements of the conduction band's width combined with the core line shifts allowed determination of the magnitude of band gap renormalisation in a doped single crystal. Furthermore, this enhancement allowed observation of an in-gap state, observed in many samples, attributed to the Sb 5*s* orbital from a reduced Sb^{+3} ion, possibly at the surface due

to an absence of oxygen.

Finally this chapter discussed an ARPES experiment conducted on the (001) surface of highly-doped ($x = 0.10$) ZGSO single crystal. Two valence band dispersions were presented taken at photon energies 121 and 148 eV. Unfortunately, the trirutile structure of ZSO means no cleavage planes exist. Despite efforts to engineer a cleave of the (001) surface, the surface was deemed poor, creating a significant broadening of data preventing further analysis.

8.2 Future Work

The work described in this thesis has shown the overriding success of synthesising a new TCO. However, throughout this project, many problems have been discovered and discussed – the most significant being the inconsistency of doping.

The crystal growth method devised in this project allows very little control of the dopant into the system. Reducing any fluctuations in local growth conditions with a meticulous refinement of temperature gradients would likely still not alleviate this problem as rates of transport of the gaseous constituents is likely to be a significant factor. Therefore, the CVT method is probably not suitable for growing doped crystals when accurate control of dopant is required. However, this crystal growth method has achieved the main goal of proving this material behaves as a TCO. Future work may explore other growth techniques such as from the melt. With improvements to the method, the degree of charge compensation could be minimised, resulting in an increase in mobility and therefore, conductivity.

The origin of the shallow donor state in undoped ZSO remains undetermined. Defect calculations would prove vital in understanding the origin of this. Additionally, techniques such as secondary ion mass spectroscopy could help understand the role of oxygen vacancies in these samples [255]. However, this low electron density n-type semiconducting behaviour property of ZSO provides the potential basis for an exciting new project, that is to create a new transparent amorphous oxide semiconductor (TAOS). Similar compounds to ZSO such as In_2O_3 are unsuitable due to high native electron densities from oxygen vacancies.

To create a TAOS a high quality powder is required. The method used to

create the precursor powders prior to crystal growth was determined to produce ZSO powders with high phase purity and close to complete oxidation. By taking these precursor powders and sputtering *via* techniques such as pulsed laser deposition and attempting to make a thin film, there is a possibility that a new ZSO TAOS material could be created. Again, this would require an excellent understanding about the defects creating the semiconducting behaviour in order to control the carrier density.

There is always a desire for research into new TAOS materials. It is predicted that a mobility of 2 $cm^2/V.s$ [256] is more than sufficient for future large scale LCD applications. For a ZSO TAOS, it remains to be seen if the electron mobility is similar to its single crystal form. However, given IGZO's electronic properties are similar between crystalline and amorphous phases and the origin of the conduction band in both ZSO and IGZO is also similar, it can not be ruled out.

Additionally, future research on a ZSO TAOS material would likely focus on understanding other properties such as long term stability and how easily it can be produced on mass for industry. If a TAOS can be made from the ZSO precursor powders, then confirmation of these properties will determine where this material stands amongst the catalogue of other TAOS materials.

This thesis has determined many previously unknown properties of ZSO and ZGSO however, other unknown properties have often hindered additional analysis. Electron energy loss spectroscopy experiments could quantify the plasma frequency providing a lower energy photon limit for transparency and understand the core line spectra's shape. A single crystal diffraction study on a number of well-characterised crystals would allow clarification of Vegard's law. Additionally, computational calculations and determination of the bulk modulus of ZSO would allow an understanding of the lattice parameter variation due to electron doping.

The valence band measurements obtained using both XPS and HAXPES techniques highlight a discrepancy in the binding energy of the Zn 3*d* orbital in calculations and experiment. The work in this thesis has provided an experimental data set that future calculations can use to refine theoretical models, helping to understand the underlying theory in this class of materials.

Several methods can improve the outcome of any future ARPES experiments on single crystal ZGSO. Improvement to the surface quality would undoubtedly improve

the quality of data however, it has been suggested that a poor surface is likely intrinsic to the trirutile structure. A smaller beamspot size would allow measurement of one single (001) surface and remove the significant broadening observed in this project. The nano-ARPES branch on I05 at Diamond Light Source can achieve beamspots $\varnothing \sim 600$ - 700 nm with a zone plate and ~ 5 μm with a capillary mirror. Unfortunately, this beamline is unable to achieve the low photon energies (~ 26 eV) suggested to enhance the conduction band intensity. If broadening could be alleviated by a smaller beamspot size, the two k_z Brillouin zone points Γ and Z points could be accurately determined and a long exposure scan at Γ could increase the chance of a conduction band measurement regardless of photon energy.

Finally, another key property of TCOs particularly with regards to potential application as a component in semiconducting devices is the work function. This can be determined from the high binding energy cut off values of UPS spectra. A concise study on ZSO with different surface orientations would determine its viability for future use in industrial application.

Appendices

Appendix A

Derivation of the Drude conductivity.

The probability distribution function is given by (derived in chapter 2)

$$f(\boldsymbol{k}) = f_0(\boldsymbol{k}) + \tau(\boldsymbol{k}) \frac{\partial f_0}{\partial \mu} \left[-\frac{e}{\hbar} \left(\frac{\hbar \boldsymbol{k}}{m} \times \boldsymbol{B} + \boldsymbol{E} \right) . \nabla_{\boldsymbol{k}} E(\boldsymbol{k}) + \frac{\hbar \boldsymbol{k}}{m} \left(\frac{E(\boldsymbol{k}) - \mu}{T} \nabla_r T + \nabla_r \mu \right) \right] \tag{A.1}$$

and the equation for current density

$$j_{electric} = -e \int \boldsymbol{v}(\boldsymbol{k}) D(\boldsymbol{k}) f(\boldsymbol{k}) d^3k \tag{A.2}$$

$$= \frac{-e}{4\pi^3} \int \boldsymbol{v}(\boldsymbol{k}) f(\boldsymbol{k}) d^3k \tag{A.3}$$

Assuming the electric field is applied in the x-direction, no magnetic field and the conductor is uniform in space, the distribution function can be simplified to

$$f(k) = f_0 - eE_x v_x \tau \frac{\partial f}{\partial E} \tag{A.4}$$

therefore

$$j_{electric} = \frac{-e}{4\pi^3} \int v_x (f_0 - eE_x v_x \tau \frac{\partial f}{\partial E}) d^3k \tag{A.5}$$

The integral over the Fermi function can be omitted because at equilibrium their are as many electrons with velocity $-v$ as $+v$.

$$j_x = \frac{e^2 E_x \tau}{4\pi^3} \int v_x.v_x \frac{\partial f}{\partial E} d^3k \tag{A.6}$$

$$= \frac{e^2 E_x \tau}{4\pi^3} \int\int\int v_x.v_x \frac{\partial f}{\partial E} k^2 \sin\theta \, dk \, d\theta \, d\phi \tag{A.7}$$

$$= \frac{e^2 E_x \tau}{4\pi^3} \int_0^{2\pi} d\phi \int_0^{\pi} \sin\theta \cos^2\theta d\theta \int_0^{\infty} v_x^2 \frac{\partial f}{\partial E} k^2 \, dk \tag{A.8}$$

$$= \frac{e^2 E_x \tau}{4\pi^3} (2\pi)(2/3) \int_0^{\infty} \frac{\hbar^2 k^2}{m^2} \frac{\partial f}{\partial E} k^2 \, dk \tag{A.9}$$

$$\tag{A.10}$$

Converting to an integral over energy

$$dk = \frac{m}{\hbar^2 k_x} dE \tag{A.11}$$

$$j_x = \frac{e^2 E_x \tau}{4\pi^3} (2\pi)(2/3) \left(\frac{\hbar^2}{m^2}\right) \int_0^{\infty} \frac{\partial f}{\partial E} k^4 \frac{m}{\hbar^2 k} dE \tag{A.12}$$

The partial differential $\frac{\partial f}{\partial E}$ is approximated by a Dirac - delta function $\delta(E - \mu)$. The integral has the form

$$\int_0^{\infty} f(E)\delta(E - a) = f(a) \tag{A.13}$$

therefore

$$j_x = \frac{e^2 \tau}{m} E_x (\frac{k_F^3}{3\pi^2}) \tag{A.14}$$

Where $(\frac{k_F^3}{3\pi^2}) = n$

Appendix B

Calculation of the Mass Loss of Sb_2O_3

During reaction of precursor powders, if the only source of mass loss is assumed to from Sb_2O_3, the amount of evaporating is determined by measuring the mass of the powder before and after reaction. In the reaction, a single antimony gains a single oxygen to sufficiently oxidise from Sb^{+3} to Sb^{+5}. The equation of reaction can be written

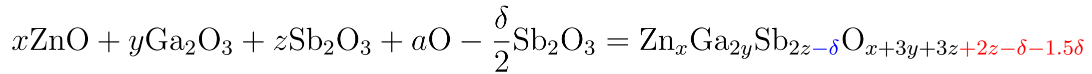

$$x\mathrm{ZnO} + y\mathrm{Ga_2O_3} + z\mathrm{Sb_2O_3} + a\mathrm{O} - \frac{\delta}{2}\mathrm{Sb_2O_3} = \mathrm{Zn}_x\mathrm{Ga}_{2y}\mathrm{Sb}_{2z-\delta}\mathrm{O}_{x+3y+3z+2z-\delta-1.5\delta}$$

Where the coefficients indicate a weighting of each compound. In ideal stoichiometric undoped ZSO, $x = 1$, $y = 0$, and $z = 1$. a indicates the amount of oxygen reacted into the system and is given by $2z$ - δ. The mass change is therefore given by

$$L = \frac{M_{O(2z-2.5\delta)} - M_{Sb(\delta)}}{M_i} \tag{B.1}$$

where M_O and M_{Sb} are the molar mass' of oxygen and antimony respectively and M_i is given by

$$M_i = M_{xZnO+yGa_2O_3+zSb_2O_3} = M_{Zn_xGa_{2y}Sb_{2z}O_{x+3y+3z}}$$

In a scenario with no mass loss due to evaporation ($\delta = 0$)

$$L = \frac{M_{O(2z)}}{M_i} = 8.58\%$$

Equation B.1 can be solved for δ

$$\delta = \frac{M_{O(2z)} - L.M_i}{M_{O(2.5)} + M_{Sb}}$$

Appendix C

Crystal Growth using $TeCl_4$ as a Tranport Agent

$TeCl_4$ has been shown to be a one of the more versatile transport agent in CVT of metal oxides [257] and was the initial choice of transport agent for growing single crystals. An assumed equation of reaction is given by equation C.1.

$$ZnSb_2O_6 + 4TeCl_4 \rightleftharpoons ZnCl_2 + 2SbCl_3 + 4TeOCl_2 + O_2 \quad \text{(C.1)}$$

The mass of $TeCl_4$ was calculated in the same way described in Chapter 3. The transport agent was added into the reaction ampoule in a argon filled glove box due to the hygroscopic nature of $TeCl_4$. The reaction ampoules were evacuated and sealed using the acetylene oxygen torch. The temperature of growth was optimised on a trial an error basis as there is no thermodynamic information available for ZSO. For the hot and cold side of the ampoule, $\sim$ 950 °C and 900 °C were determined to be suitable conditions. Table C.1 displays the log for a number of growths of ZSO and ZGSO using $TeCl_4$ as a transport agent with a photograph of two growth batches pictured in Figure C.1.

Table C.1: Crystal growth log for several growths using $TeCl_4$ as a transport agent.

Growth Number	Duration (hr)	Mass of Charge (g)	Mass of $TeCl_4$ (mg)	Dopant	T_{hot} (°C)	T_{cold} (°C)	Comments
15	200	1.0	30	0%	950	900	-40% powder transported, Small transparent crystals grown in cold end.
17	200	1.0	60	0%	950	900	-50% transported, Small blue crystals grown, 3.8mg largest crystal
20	200	0.5	30	0%	950	900	-high proportion transported ∼80-90%
29	200	0.5	40	2% Ga	960	900	-Complete transport, large black crystals.
30	200	0.5	40	2% Ga	960	900	- 50% transported, small transparent crystals, cloudy tube.

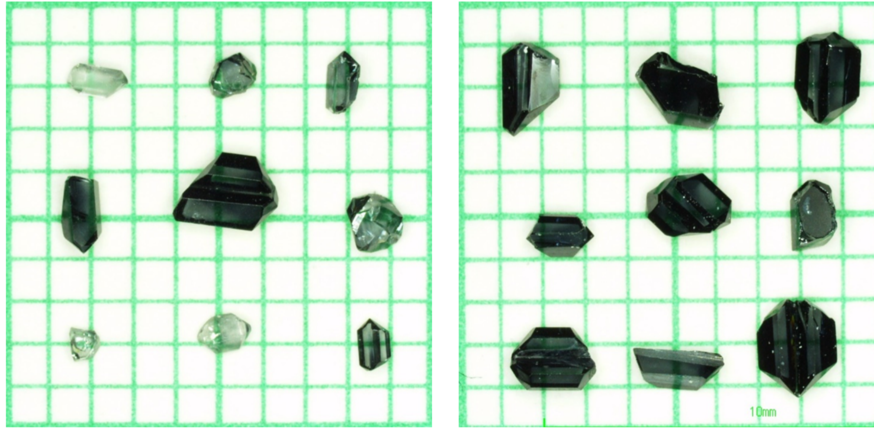

Figure C.1: Left- As grown crystals from batch 20 (undoped) **Right-** Crystals from batch 29 (2% Ga doping). Grid spacing is 1mm

Well faceted crystals with dimensions ∼ 2 mm were successfully grown for both undoped and 2% Ga doping levels. To check for any unwanted contaminants in the grown crystals, a HAXPES survey was carried out by Dr Tien-Lin Lee using the I09 beamline at Diamond Light Source using a 5.92 keV photon beam. The survey scan of binding energies ranging 1300 - 0 eV is shown in Figure C.2.

This survey highlighted a major issue in the crystals, Te 3*d* peaks observed at around a binding energy of 580 eV. The tellurium has been incorporated into the crystal during the vapour transport. Interestingly it is found in two oxidation states, +4 and a lower oxidation state indicated by the doublet at a lower binding energy, possibly metallic. How the Te^{+4} resides in the crystal is undetermined. There is a large mismatch in ionic radius for Te^{+4} (0.97 Å) with Sb^{+5} (0.60 Å) and Zn^{+2} (0.74 Å) all with a VI co-ordination [168]. Neither cation lattice sites provide a good match for a substitutional defect situation. The detection of tellurium impurities is

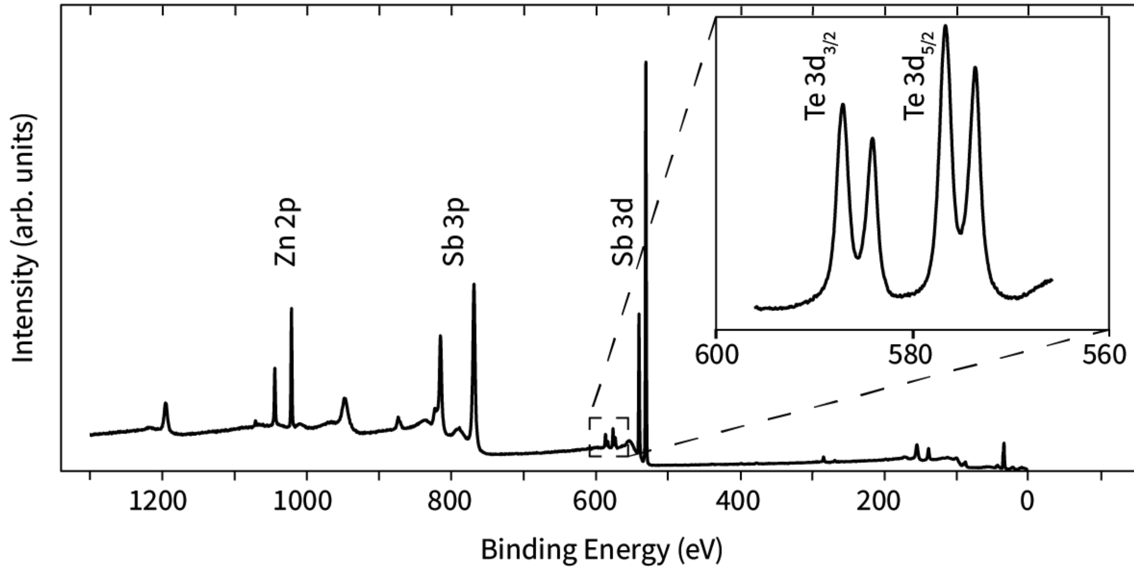

Figure C.2: HAXPES ($h\nu = 5.92$ keV) survey of undoped crystal from growth 37 with a highlighted core peaks. Inset: Spectrum of Te $3d$ peaks.

in contrast to conclusions made by Prokofiev *et al* whereby they confirmed tellurium was not detected in growths of $CuSb_2O_6$ [155]. The assigned tellurium doublet at lower binding energy is also undetermined, possibly originating from interstitial defects. It could also be a surface contamination of metallic tellurium however investigations into this were not continued. $TeCl_4$ is determined to not be a suitable transport agent for growths of uncontaminated single crystals of ZSO. The success of the growths indicated chlorine may be sufficient.

Bibliography

[1] A. N. Tiwari, G. Khrypunov, F. Kurdzesau, D. L. Bätzner, A. Romeo, and H. Zogg. *Prog. Photovolt: Res. Appl*, **12**:33–38, (2004).

[2] C. G. Granqvist. *Sol. Energy Mater Sol. Cells*, **91**:1529–1598, (2007).

[3] S. J. Laverty and P. D. Maguire. *J. Vac. Sci. Technol. B*, **19**:1–6, (2001).

[4] G. S. Chae. *Jpn. J. Appl. Phys*, **40**:1282–1286, (2001).

[5] I Hamberg and C.G Granqvist. *J. Appl. Phys*, **60**:123–159, (1986).

[6] A. Azens and C. G. Granqvist. *J Solid State Electrochem*, **7**:64–68, (2003).

[7] K. Sakamoto, H. Kuwae, N. Kobayashi, A. Nobori, S. Shoji, and J. Mizuno. *Sci. Rep*, **8**:3–4, (2018).

[8] K. Bädekar. *Ann. Phys*, **327**:749766, (1907).

[9] Global indium tin oxide market size. https://www.statista.com/statistics/1072926/global-indium-tin-oxide-market-size, 2020.

[10] N. M. Khusayfan and M. M. El-Nahass. *Adv. Condens. Matter Phys*, **2013**:1–8, (2013).

[11] I. A. Rauf. *J. Appl. Phys*, **79**:4057–4065, (1996).

[12] T. Pearsall. *IEEE J Quantum Electron*, **16**:709–720, (1980).

[13] A. M. Ganose and D. O. Scanlon. *J. Mater. Chem. C*, **4**:1467–1475, (2016).

[14] E. Fortunato, D. Ginley, H. Hosono, and D. C. Paine. *MRS Bull*, **32**:242–247, (2007).

[15] Q. Liu, J. Dai, X. Zhang, G. Zhu, Z. Liu, and G. Ding. *Thin Solid Films*, **519**:6059–6063, (2011).

[16] H. J. Kim, U. Kim, T. H. Kim, J. Kim, H. M. Kim, B. G. Jeon, W. J. Lee, H. S. Mun, K. T. Hong, J. Yu, K. Char, and K. H. Kim. *Phys. Rev. B*, **86**:061102, (2012).

[17] H Mizoguchi, P. M. Woodward, C Park, and D. A. Keszler. *J. Am. Chem.*

Soc, **126**:9796–9800, (2004).

[18] H. Mizoguchi, T. Kamiya, S. Matsuishi, and H. Hosono. *Nat. Commun.*, **2**:1 – 5, (2011).

[19] R. Mamazza, D. L. Morel, and C. S. Ferekides. *Thin Solid Films*, **484**:26–33, (2005).

[20] T. J. Coutts, J . D. Perkins, D. S. Ginley, and T. O. Mason. *Proceedings of the 195th Electrochemical Society*, page 127, (1999).

[21] Y. Kanai. *Jpn. J. Appl. Phys*, **23**, (1984).

[22] S. J. Wen, G. Couturier, J. P. Chaminade, E. Marquestaut, J. Claverie, and P. Hagenmuller. *J Solid State Chem*, **101**:203–210, (1992).

[23] A. Walsh, J. L. F. Da Silva, and S. H. Wei. *Phys. Rev. B*, **78**:075211, (2008).

[24] A. Byström, B. Hok, and B Mason. *Arkiv. Kemi. Mineral. Geol*, **15B**:7935–7941, (1941).

[25] T. S. Ercit, E. E. Foord, and J. J. Fitzpatrick. *Can. Mineral*, **40**:1207–1210, (2002).

[26] Y. Yamada and M. Ogita. *Sens. Actuators B Chem*, **93**:546–551, (2003).

[27] Y. Yamada, K. Yamashita, Y. Masuoka, and Y. Seno. *Sens. Actuators B Chem*, **77**:12–15, (2001).

[28] J. Tamaki, Y. Yamada, Y. Yamamoto, M. Matsuoka, and I. Ota. *Sens. Actuators B Chem*, **66**:70–73, (2000).

[29] C. R. Michel, N. L. López Contreras, M. A. López-Alvarez, and A. H. Martínez-Preciado. *Sens. Actuators B Chem*, **171-172**:686–690, (2012).

[30] B. L. Zhu, C. S. Xie, A. H. Wang, D. W. Zeng, M. L. Hu, and W. Y. Wang. *Mater. Res. Bull*, **39**:409–415, (2004).

[31] N. Arunkumar and R. Vijayaraghavan. *RSC Adv*, **4**:65223–65231, (2014).

[32] W. Liu, P. Lin, H. Jin, H. Xue, Y. Zhang, and Z. Li. *J Mol Catal A Chem*, **349**:80–85, (2011).

[33] D. P. Dutta, A. Ballal, A. Singh, M. H. Fulekar, and A. K. Tyagi. *Dalton Trans*, **42**:16887–16897, (2013).

[34] S. Matsushima, T. Tanizaki, H. Nakamura, M. Nonaka, and M. Arai. *Chem. Lett*, **30**:1010–1011, (2001).

[35] M. Balasubramaniam and S. Balakumar. *Nano Hybrids and Composites*,

17:18–23, (2017).

[36] N. Kikuchi, H. Hosono, H. Kawazoe, O. Tanegashima, I. Ota, and Y. Kimura. *J. Am. Ceram. Soc*, **88**:2793–2797, (2005).

[37] S. Nishiyama and T. Hattori. *J. Ceram. Soc. Japan*, **108**:435–438, (2000).

[38] A. Katsui and H. Matsushita. *Physica Status Solidi (A)*, **203**:2832–2835, (2006).

[39] R. Kronig and W. G. Penney. *Proc. R. Soc. Lond*, **130**:499–513, (1931).

[40] B. Kollmitzer and P. Hadley. *Physica B Condens. Matter*, **406**:4373–4380, (2011).

[41] S. C. Dixon, D. O. Scanlon, C. J. Carmalt, and I. P. Parkin. *J. Mater. Chem. C*, **4**:6946–6961, (2016).

[42] H. Hosono and K. Ueda. *Transparent Conductive Oxides.* Springer International Publishing, (2017).

[43] D. O. Scanlon, A. B. Kehoe, G. W. Watson, M. O. Jones, W. I. F. David, D.J. Payne, R. G. Egdell, P. P. Edwards, and A. Walsh. *Phys. Rev. Lett*, **107**:246402, (2011).

[44] J. J. Mudd, Tien-Lin. Lee, V. Muñoz-Sanjosé, J. Zúñiga-Pérez, D. Hesp, J. M. Kahk, D. J. Payne, R. G. Egdell, and C. F. McConville. *Phys. Rev. B*, **89**:035203, (2014).

[45] X. Chen, D. Parker, and D. J. Singh. *Sci. Rep*, **3**:2–7, (2013).

[46] K. Nassau. *Color Res Appl*, **12**:4–26, (1987).

[47] A. Janotti and C. G. Van De Walle. *Rep. Prog. Phys*, **72**:126501, (2009).

[48] A. Janotti and C. G. Van De Walle. *Appl. Phys. Lett*, **87**:122102, (2005).

[49] A. Mang, K. Reimann, and St Rübenacke. *Solid State Commun*, **94**:251–254, (1995).

[50] P. P. Edwards, A. Porch, M. O. Jones, D. V. Morgan, and R. M. Perks. *Dalton Trans*, **19**:2995–3002, (2004).

[51] O. Mryasov and A. Freeman. *Phys. Rev. B*, **64**:233111, (2001).

[52] K. H. L. Zhang, K. Xi, M. G. Blamire, and R. G. Egdell. *J. Phys. Condens. Matter*, **28**:383002, (2016).

[53] H. Kawazoe, M. Yasukawa, H. Hyodo, and M. Kurita. *Nature*, **389**:939–942, (1997).

[54] D. O. Scanlon and G. W. Watson. *J. Mater. Chem*, **22**:25236–25245, (2012).

[55] P. D.C. King and T. D. Veal. *J. Phys. Condens. Matter*, **23**:334214, (2011).

[56] *Rev. Mod. Phys*, **40**:677–683, (1968).

[57] I. Hamberg, C. G. Granqvist, K. F. Berggren, B. E. Sernelius, and L. Engström. *Phys. Rev. B*, **30**:3240–3249, (1984).

[58] A. Walsh, J. L. F. Da Silva, S. H. Wei, C. Körber, A. Klein, L. F J Piper, A. Demasi, K. E. Smith, G. Panaccione, P. Torelli, D. J. Payne, A. Bourlange, and R. G. Egdell. *Phys. Rev. Lett*, **100**:167402, (2008).

[59] E. Burstein. *Phys. Rev*, **93**:632–633, (1954).

[60] T. S. Moss. *Proc. Phys. Soc. B*, **67**:775–782, (1954).

[61] K. G. Saw, N. M. Aznan, F. K. Yam, S. S. Ng, and S. Y. Pung. *PLoS ONE*, **10**:1–17, (2015).

[62] J. W. Jeon, D. W. Jeon, T. Sahoo, M. Kim, J. H. Baek, J. L. Hoffman, N. S. Kim, and I. H. Lee. *J. Alloys Compd*, **509**:10062–10065, (2011).

[63] K. F. Berggren and B. E. Sernelius. *Phys. Rev. B*, **24**:1971–1986, (1981).

[64] B. E. Sernelius, K. F. Berggren, Z.C. Jin, I. Hamberg, and C. G. Granqvist. *Phys. Rev. B*, **37**:244–248, (1988).

[65] Y. Dou, T. Fishlock, and R. G. Egdell. *Phys. Rev. B*, **55**:381–384, (1997).

[66] J. Jiang, Y. Lu, B. K. Meyer, D. M. Hofmann, and M. Eickhoff. *J. Appl. Phys*, **119**:245703, (2016).

[67] J. Camassel, D. Auvergne, and H. Mathieu. *J. Appl. Phys*, **46**:2683–2689, (1975).

[68] C. J. Hwang. *Phys. Rev. B*, **2**:4117–4125, (1970).

[69] Z. Lebens-Higgins, D. O. Scanlon, H. Paik, S. Sallis, Y. Nie, M. Uchida, N. F. Quackenbush, M. J. Wahila, G. E. Sterbinsky, Dario A. Arena, J. C. Woicik, D. G. Schlom, and L. F. J. Piper. *Phys. Rev. Let.*, **116**:027602, (2016).

[70] J. E. N. Swallow. *Physics of Existing and Novel Transparent Conducting Oxide Semiconductors*. PhD thesis, University of Liverpool, (2019).

[71] D. S. Bhachu, D. O. Scanlon, G. Sankar, T. D. Veal, R. G. Egdell, G. Cibin, A. J. Dent, C. E. Knapp, C. J. Carmalt, and I. P. Parkin. *Chem. Mater.*, **27**:2788–2796, (2015).

[72] E. Ruiz, S. Alvarez, and P. Alemany. *Phys. Rev. B*, **56**:7189–7196, (1997).

[73] M. Heinemann, B. Eifert, and C. Heiliger. *Phys. Rev. B*, **87**:3–7, (2013).

[74] W. Walukiewicz. *Physica B Condens. Matter*, **302**:123–134, (2001).

[75] J. Robertson and S. J. Clark. *Phys. Rev. B*, **83**:1–7, (2011).

[76] K. Nomura, H. Ohta, A. Takagi, T. Kamiya, M. Hirano, and H Hosono. *Nature*, **432**:488, (2004).

[77] J. Y. Kwon, D. J. Lee, and K. B. Kim. *Electron. Mater. Lett.*, **7**:1–11, (2011).

[78] T. Kamiya, K. Nomura, and H. Hosono. *Journal of Display Technology*, **5**:468–483, (2009).

[79] Z. W. Shang, H. H. Hsu, Z. W. Zheng, and C. H. Cheng. *Nanotechnol. Rev.*, **8**:422–443, (2019).

[80] Y. Ogo, H. Hiramatsu, K. Nomura, H. Yanagi, T. Kamiya, M. Hirano, and H. Hosono. *Appl. Phys. Lett.*, **93**:3–5, (2008).

[81] H. J. Saji, Y. P. Venkata Subbaiah, K. Tian, and A. Tiwari. *Thin Solid Films*, **605**:193–201, (2016).

[82] N. F. Quackenbush, J. P. Allen, D. O. Scanlon, S. Sallis, J. A. Hewlett, A. S. Nandur, B. Chen, K. E. Smith, C. Weiland, D. A. Fischer, J. C. Woicik, B. E. White, G. W. Watson, and L. F.J. Piper. *Chem. Mater*, **25**:3114–3123, (2013).

[83] H. Hosono, Y. Ogo, H. Yanagi, and T. Kamiya. *Electrochem. Solid-State Lett.*, **14**, (2011).

[84] K. Nomura, T. Kamiya, and H. Hosono. *Adv Mater*, **23**:3431–3434, (2011).

[85] M. Lundstrom. *Fundamentals of Carrier Transport*. Cambridge University Press, (2000).

[86] N. W. Ashcroft and N. D. Mermin. *Solid State Physics*. Cengage Learning, (1976).

[87] C. Kittel. *Introduction to Solid State Physics, 8th edition*. Wiley, (2004).

[88] S. Kasap, C. Koughia, and H. E. Ruda. *Electrical Conduction in Metals and Semiconductors*. Springer International Publishing, (2017).

[89] B. van Zeghbroeck. *Principles of Semiconductor Devices*. Boulder, (2006).

[90] J. S. Cetnar and D. L. Rode. *J. Electron. Mater*, **48**:3399–3404, (2019).

[91] A. J. Leenheer, J. D. Perkins, M. F. A. M. van Hest, R. P. Berry, J. J. OHayre, and D. S Ginle. *Phys. Rev. B*, **77**:115215, (2008).

[92] D. Seo, K. Yu, Y. Jun Chang, E. Sohn, K. Hoon Kim, and E. J. Choi. *Appl.*

Phys. Lett, **104**:022102, (2014).

[93] A. Solieman and M. A. Aegerter. *Thin Solid Films*, **502**:205–211, (2006).

[94] V. Romanyuk, N. Dmitruk, V. Karpyna, G. Lashkarev, V. Popovych, M. Dranchuk, R. Pietruszka, M. Godlewski, G. Dovbeshko, I. Timofeeva, O. Kondratenko, M. Taborska, and A. Ievtushenko. *Acta Phys. Pol*, **129**:36–40, (2016).

[95] D. F. Swinehart. *J Chem Educ*, **39**:333–335, (1962).

[96] J. Tauc. *Mat. Res. Bull*, **3**:37–46, (1968).

[97] E. A. Davis and N. F. Mott. *Philos Mag (Abingdon)*, **22**:0903–0922, (1970).

[98] A. Dolgonos, T. O. Mason, and K. R. Poeppelmeier. *J Solid State Chem*, **240**:43–48, (2016).

[99] D. B. Fraser and H. D. Cook. *J. Electrochem. Soc*, **119**:1368–1374, (1972).

[100] G. Haacke. *J. Appl. Phys*, **47**:4086–4089, (1976).

[101] V. K. Jain and A. P. Kulshreshtha. *Sol. Energy Mater*, **4**:151–158, (1981).

[102] S. A. Knickerbocker and A. K. Kulkarni. *J. Vac. Sci. Technol. A*, **13**:1048–1052, (1995).

[103] H. Kim, C. M. Gilmore, A. Piqué, J. S. Horwitz, H. Mattoussi, H. Murata, Z. H. Kafafi, and D. B. Chrisey. *J. Appl. Phys*, **86**:6451–6461, (1999).

[104] Z. Y. Banyamin, P. J. Kelly, G. West, and J. Boardman. *Coatings*, **4**:732–746, (2014).

[105] R. J. Cava, Julia M. Phillips, J. Kwo, G. A. Thomas, R. B. Van Dover, S. A. Carter, J. J. Krajewski, W. F. Peck, J. H. Marshall, and D. H. Rapkine. *Appl. Phys. Lett*, **64**:2071–2072, (1994).

[106] K. N. Tonny, R. Rafique, A. Sharmin, M. S. Bashar, and Z. H. Mahmood. *AIP Adv*, **8**:065307, (2018).

[107] H. Mizoguchi and P. M. Woodward. *Chem. Mater*, **16**:5233–5248, (2004).

[108] M. Sasaki, R. Kiyoshima, S. Kohiki, S. Matsushima, M. Oku, and T. Shishido. *J. Alloys Compd*, **322**:220–225, (2001).

[109] S Matsushima. *Jpn. J. Appl. Phys*, **38**:4993 – 4996, (1999).

[110] J. P. Perdew. *Int. J. Quantum Chem*, **28**:497–523, (1985).

[111] E. H. Hall. *American Journal of Mathematics*, **2**:287–292, (1879).

[112] K. Thompson. *Microscopy Today*, **21**:30–34, (2013).

[113] M. Siegbahn. *Nature*, **96**, (1916).

[114] J. I. Goldstein, D. E. Newbury, P. Echlin, D. C. Joy, C. E. Lyman, E. Lifshin, L. Sawyer, and J. R. Michael. *Quantitative X-Ray Analysis: The Basics*, pages 391–451. Springer US, (2003).

[115] W. Friedrich, P. Knipping, and M. Laue. *Ann. Phys*, **346**:971 – 988, (1913).

[116] W. H Bragg and W. L Bragg. *Proc. R. Soc. Lond. A*, **88**:428 – 438, (1913).

[117] H. M. Rietveld. *J Appl Crystallogr*, **2**:65–71, (1969).

[118] B. H. Toby and R. B. Von Dreele. *J Appl Crystallogr*, **46**:544–549, (2013).

[119] H. Hertz. *Ann. Phys.*, **31**, (1887).

[120] A. Einstein. *Ann. Phys.*, **199**, (1906).

[121] K. Siegbahn and K. Edvarson. *Nuclear Phys*, **1**:137–159, (1956).

[122] D. Fang, F. He, J. Xie, and L. Xue. *J. Wuhan Univ. Technol. Mater. Sci. Ed*, **35**:711–718, (2020).

[123] M. P. Seah and W. A. Dench. *Surf Interface Anal*, **1**:2, (1979).

[124] A Powell, C.J. Jablonski. *Electron Inelastic-Mean-Free-Path Database.* NIST, (2010).

[125] M. B. Trzhaskovskaya, V. I. Nefedov, and V. G. Yarzhemsky. *At. Data Nucl. Data Tables*, **77**:97–159, (2001).

[126] M. B. Trzhaskovskaya, V. K. Nikulin, V. I. Nefedov, and V. G. Yarzhemsky. *At. Data Nucl. Data Tables*, **92**:245–304, (2006).

[127] M. B. Trzhaskovskaya, V. I. Nefedov, and V. G. Yarzhemsky. *At. Data Nucl. Data Tables*, **82**:257–311, (2002).

[128] M. B. Trzhaskovskaya and V. G. Yarzhemsky. *At. Data Nucl. Data Tables*, **119**:99–174, (2018).

[129] J. H. Scofield. *J Electron Spectros Relat Phenomena*, **8**:129–137, (1976).

[130] J. J. Yeh and I Lindau. *At. Data Nucl. Data Tables*, **32**:1–155, (1985).

[131] J. W. Cooper. *Phys. Rev. A*, **42**:6942–6945, (1990).

[132] O. Hemmers, P. Glans, D. L. Hansen, H. Wang, S. B. Whitfield, D. W. Lindle, R. Wehlitz, J. C. Levin, I. A. Sellin, and R. C. C. Perera. *Synchrotron Radiat News*, **9**:40–45, (1996).

[133] A. Damascelli. *Phys Scr*, **T109**:61–74, (2004).

[134] M. Hoesch, T. K. Kim, P. Dudin, H. Wang, S. Scott, P. Harris, S. Patel,

M. Matthews, D. Hawkins, S. G. Alcock, T. Richter, J. J. Mudd, M. Basham, L. Pratt, P. Leicester, E. C. Longhi, A. Tamai, and F. Baumberger. *Rev. Sci. Instrum*, **88**, (2017).

[135] M. D. Watson, S. Aswartham, L. C. Rhodes, B. Parrett, H. Iwasawa, M. Hoesch, I. Morozov, B. Büchner, and T. K. Kim. *Phys. Rev. B*, **97**:035134, (2017).

[136] A. Rebello, M. G. Smith, J. J. Neumeier, B. D. White, and Yi Kuo Yu. *Phys. Rev. B*, **87**:224427, (2013).

[137] E. Glover. *Design, Synthesis and Charactersation of Novel Materials for Photocatalytic Water Splitting*. PhD thesis, University College London, (2017).

[138] K. Von. Dihlstrom. *Z. Anorg. Allg. Chem*, **239**:57–64, (1938).

[139] J. R. Gavarri. *J Solid State Chem*, **43**:12–28, (1982).

[140] D. Klimm, S. Ganschow, D. Schulz, and R. Fornari. *J. Cryst. Growth*, **310**:3009–3013, (2008).

[141] R. Lamoreaux and D. Hildenbrand. **16**:419–443, (1986).

[142] W. B. Hincke. *J. Am. Chem. Soc*, **52**:3869–3877, (1930).

[143] R. G. Behrens and G. M. Rosenblatt. *J. Chem. Thermodyn*, **5**:173–188, (1973).

[144] R. Bunsen. *J Prakt. Chem*, **56**:53, (1852).

[145] J. H van Arkel, E. de Boer. *Z. Anorg. Allg. Chem*, **148**:345, (1925).

[146] H. Von Schäfer and J. Nickl. *Z. Anorg. Allg. Chem*, **274**:250–264, (1953).

[147] H. Von Schäfer, H. Jacob, and K. Etzel. *Z. Anorg. Allg. Chem*, **286**:27–41, (1956).

[148] K. Böttcher, H. Hartmann, and D. Siche. *J. Cryst. Growth*, **224**:195–203, (2001).

[149] M. Binnewies, R. Glaum, M. Schmidt, and P. Schmidt. *Chemical Vapor Transport Reactions*. De Gruyter, (2012).

[150] M. Schöneich, M. P. Schmidt, and P. Schmidt. *Z. Anorg. Allg. Chem*, **636**:1810–1816, (2010).

[151] M. Weil, R. Mathieu, P. Nordblad, and S. A. Ivanov. *Cryst. Res. Technol*, **49**:142–151, (2014).

[152] S. Golbs, F. M. Schappacher, R. Pöttgen, R. Cardoso-Gil, A. Ormeci, U. Schwarz, W. Schnelle, Y. Grin, and M. Schmidt. *Z. Anorg. Allg. Chem*,

639:2139–2148, (2013).

[153] S. Gerlach, R. Cardoso-Gil, E. Milke, and M. Schmidt. *Z. Anorg. Allg. Chem*, **633**:83–92, (2007).

[154] B. Gorshunov, M. Dressel, R. K. Kremer, A. V. Prokofiev, V. I. Torgashev, V. B. Shirokov, A. S. Prokhorov, P. Haas, B. J. Gibson, and W. Assmus. *Phys. Rev. B*, **67**:134433, (2003).

[155] A. V. Prokofiev, F. Ritter, W. Assmus, B. J. Gibson, and R. K. Kremer. *J. Cryst. Growth*, **247**:457–466, (2003).

[156] J. B. Legma, G. Vacquier, and A. Casalot. *J. Cryst. Growth*, **130**:253–258, (1993).

[157] H. Juskowiak and A. Pajaczkowska. *J. Mater. Sci*, **21**:3430–3434, (1986).

[158] W. Nieuwenkamp. *Z. Kristallogr. Krist*, **92**:454 – 548, (1935).

[159] S. E. Harrison. *Phys. Rev*, **93**:52–62, (1954).

[160] Z. Galazka, R. Uecker, K. Irmscher, D. Schulz, D. Klimm, M. Albrecht, M. Pietsch, S. Ganschow, A. Kwasniewski, and R. Fornari. *J. Cryst. Growth*, **362**:349–352, (2013).

[161] L. E. Halliburton, N. C. Giles, N. Y. Garces, Ming Luo, Chunchuan Xu, Lihai Bai, and L. A. Boatner. *Appl. Phys. Lett*, **87**:172108, (2005).

[162] X. Wei, Y. Zhao, Z. Dong, and J. Li. *J. Cryst. Growth*, **310**:639–645, (2008).

[163] L. Liu, Z. Mei, A. Tang, A. Azarov, A. Kuznetsov, Q. K. Xue, and X. Du. *Phys. Rev. B*, **93**:235305, (2016).

[164] J. Buckeridge, C. R. A. Catlow, M. R. Farrow, A. J. Logsdail, D. O. Scanlon, T. W. Keal, P. Sherwood, S. M. Woodley, A. A. Sokol, and A. Walsh. *Phys. Rev. Mater*, **2**:054604, (2018).

[165] P. D. C. King, R. L. Lichti, Y. G. Celebi, J. M. Gil, R. C. Vilão, H. V. Alberto, J. Piroto Duarte, D. J. Payne, R. G. Egdell, I. McKenzie, C. F. McConville, S. F.J. Cox, and T. D. Veal. *Phys. Rev. B*, **80**:1–4, (2009).

[166] A. Ambrosini, G. B. Palmer, A. Maignan, K. R. Poeppelmeier, M. A. Lane, P. Brazis, C. R. Kannewurf, T. Hogan, and T. O. Mason. *Chem. Mater.*, **14**:52–57, (2002).

[167] M. V. Ganduglia-Pirovano, A. Hofmann, and J. Sauer. *Surf. Sci. Rep*, **62**:219–270, (2007).

[168] R. D. Shannon. *Acta Cryst. A*, **32**:751–767, (1976).

[169] K. Ellmer and R. Mientus. *Thin Solid Films*, **516**:5829–5835, (2008).

[170] K. Ellmer and R. Mientus. *Thin Solid Films*, **516**:4620 – 4627, (2008).

[171] T. Minami. *Semicond Sci Technol*, **20**:S34 – S35, (2005).

[172] H. Agura, A. Suzuki, T. Matsushita, T. Aoki, and M. Okuda. *Thin Solid Films*, **445**:263–267, (2003).

[173] R. F. Minibaev, A. A. Bagaturyants, D. I. Bazhanov, A. A. Knizhnik, and M. V. Alfimov. *Nanotechnol Russ*, **5**:185–190, (2010).

[174] Z. Galazka, R. Uecker, K. Irmscher, D. Klimm, R. Bertram, A. Kwasniewski, M. Naumann, R. Schewski, M. Pietsch, U. Juda, A. Fiedler, M. Albrecht, S. Ganschow, T. Markurt, C. Guguschev, and M. Bickermann. *J. Phys. Condens. Matter*, **29**:075701, (2017).

[175] X. Feng, J. Ma, F. Yang, F. Ji, F. Zong, C. Luan, and H. Ma. *Mater. Lett*, **62**:1779–1781, (2008).

[176] Q. Liu, J. Liu, B. Li, H. Li, G. Zhu, K. Dai, Z. Liu, P. Zhang, and J. Dai. *Appl. Phys. Let.*, **101**:241901, (2012).

[177] G. Frank, E. Kauer, and H. Köstlin. *Thin Solid Films*, **77**:107–118, (1981).

[178] H. Peelaers, E. Kioupakis, and C. G. Van De Walle. *Appl. Phys. Lett.*, **100**:011914, (2012).

[179] H. Peelaers, E. Kioupakis, and C. G. Van De Walle. *Phys. Rev. B*, **92**:235201, (2015).

[180] R. Swanepoel. *J.Phys. E: Sci. Instrum*, **16**:1214, (1983).

[181] M. Weidner. *Fermi Level Determination in Tin Oxide by Photoelectron Spectroscopy.* PhD thesis, TU Darmstadt, (2015).

[182] G. Sanon, R. Rup, and A. Mansingh. *Phys. Rev. B*, **44**:5672–5680, (1991).

[183] F. Urbach. *Phys. Rev*, **92**:1324, (1953).

[184] V. R. Akshay, B. Arun, G. Mandal, and M. Vasundhara. *Phys. Chem. Chem. Phys*, **21**:12991–13004, (2019).

[185] J. M. Essick and R. T. Mather. *Am J Phys*, **61**:646–649, (1993).

[186] S. R. Unadkat. *Growth and characterization of Mixed Germanium Sulphoselenide (GeS_xSe_{1-x}) single crystals by Chemical Vapour Transport Technique.* PhD thesis, Sardar Patel University, (2012).

[187] I. H. Kim, J. H. Ko, D. Kim, K. S. Lee, T. S. Lee, J. h. Jeong, B. Cheong, Y. J. Baik, and W. M. Kim. *Thin Solid Films*, **515**:2475–2480, (2006).

[188] K. Irmscher, M. Albrecht, B. Heimbrodt, M. Naumann, T. Remmele, D. Schulz, T. Schulz, and R. Fornari. *Phys. Status Solidi C*, **6**:2658–2660, (2009).

[189] Z. Galazka. *Transparent Semiconducting Oxides: Bulk Crystal Growth and Fundamental Properties.* Jenny Stanford Publishing, (2020).

[190] P. Rudolph. *Handbook of Crystal Growth: Bulk Crystal Growth.* Elsevier Science, (2014).

[191] A. Mycielski, L. Kowalczyk, A. Szadkowski, B. Chwalisz, A. Wysmołek, R. Stepniewski, J. M. Baranowski, M. Potemski, A. Witowski, R. Jakieła, A. Barcz, B. Witkowska, W. Kaliszek, A. Jedrzejczak, A. Suchocki, E. Łusakowska, and E. Kamińska. *J. Alloys Compd*, **371**:150–152, (2004).

[192] Z. Galazka, R. Uecker, K. Irmscher, M. Albrecht, D. Klimm, M. Pietsch, M. Brützam, R. Bertram, S. Ganschow, and R. Fornari. *Cryst. Res. Technol*, **45**:1229–1236, (2010).

[193] D. E. Newbury and N. W. M. Ritchie. *Scanning*, **35**:141–168, (2013).

[194] D. E. Newbury and N. W. M. Ritchie. *J. Mater. Sci*, **40**:493–518, (2015).

[195] D. E. Newbury and N. W. M. Ritchie. *Microsc. Microanal.*, **25**:1075–1105, (2019).

[196] P. J. Statham. *Microsc. Microanal.*, **15**:528–529, (2009).

[197] P. T. Pinard, A. Protheroe, J. Holland, S. Burgess, and P. J. Statham. *IOP Conf. Ser.: Mater. Sci. Eng*, **891**:012020, (2020).

[198] S. Burgess. What is standardless quantitive analysis? https://nano.oxinst.com/library/blog/what-is-standardless-quantitative-analysis. Accessed: 2020-12-03.

[199] M. S. Haseman, P. Saadatkia, J. T. Warfield, J. Lawrence, A. Hernandez, G. E. Jellison, L. A. Boatner, and F. A. Selim. *J. Electron. Mater.*, **47**:1497–1504, (2018).

[200] E. S. Kumar, F. Mohammadbeigi, L. A. Boatner, and S. P. Watkins. *J. Lumin.*, **176**:47–51, (2016).

[201] J. Zhang, C. Xia, Q. Deng, W. Xu, H. Shi, F. Wu, and J. Xu. *Journal of*

Physics and Chemistry of Solids, **67**:1656–1659, (2006).

[202] W. I. F. David. *J Res Natl Inst Stand Technol*, **109**:107–123, (2004).

[203] B. H. Toby. *Powder Diffr*, **21**:67–70, (2006).

[204] K. Sharda and S. C Jayanthi. *Appl. Surf. Sci*, **256**:2630–2635, (2010).

[205] V. D. Mote, Y. Purushotham, and B. N. Dole. *Cryst. Res. Technol*, **46**:705–710, (2011).

[206] M. Zolfaghari and M. Chireh. *Adv Mat Res*, **829**:784–789, (2014).

[207] L. Vegard. *Z. Phys*, **5**:17–26, (1921).

[208] P. Huang, Y. He, C. Cao, and Z. Lu. *Sci. Rep*, **4**:1–7, (2014).

[209] G. S. Cargill, J. Angilello, and K. L. Kavanagh. *Phys. Rev. Lett*, **61**:1748–1751, (1988).

[210] F. Brunei, P. Germi, M. Pernet, A. Deneuville, E. Gheeraert, F. Laugier, M. Burdin, and G. Rolland. *Diam Relat Mater*, **7**:869–873, (1998).

[211] R. W. Keyes. *IBM J. Res. Dev*, **5**:266, (1961).

[212] I. Yokota. *J. Phys. Soc Japan*, **80**:71487, (1964).

[213] J. Bardeen and W. Shockley. *Phys. Rev.*, **80**:72–80, (1950).

[214] C. Xu, C. L. Senaratne, J. Kouvetakis, and J. Menéndez. *Phys. Rev. B*, **93**:041201(R), (2016).

[215] A. Janotti, B. Jalan, S. Stemmer, and C. G. Van De Walle. *Appl. Phys. Lett*, **100**:262104, (2012).

[216] E. Filipek and G. Dabrowska. *J. Therm. Anal. Calorim*, **94**:195–201, (2008).

[217] A. Guillén-Bonilla, V. M. Rodríguez-Betancourtt, M.n Flores-Martínez, O. Blanco-Alonso, J. Reyes-Gómez, L. Gildo-Ortiz, and H. Guillén-Bonilla. *Sensors*, **14**:15802–15814, (2014).

[218] R. G. Egdell, J. Rebane, and T. J. Walker. *Phys. Rev. B*, **59**:1792–1799, (1999).

[219] F. Borgatti, J. A. Berger, D. Céolin, J. S. Zhou, J. J. Kas, M. Guzzo, C. F. McConville, F. Offi, G. Panaccione, A. Regoutz, D. J. Payne, J. P. Rueff, O. Bierwagen, M. E. White, J. S. Speck, M. Gatti, and R. G. Egdell. *Phys. Rev. B*, **97**:155102, (2018).

[220] J. E. N. Swallow, B. A. D. Williamson, M. Birkett, A. Abbott, M. Farnworth, T. J. Featherstone, N. Peng, K. J Cheetham, P. Warren, A. Regoutz, D. A.

Duncan, Tien-lin Lee, D. O. Scanlon, V. R. Dhanak, and T. D. Veal. *IEEE 7th World Conference on Photovoltaic Energy Conversion (WCPEC*, pages 3052 – 3055, (2018).

[221] R. S. Swingle. *Anal. Chem*, **47**:21–24, (1975).

[222] M. Sachs, M. Gellert, M. Chen, H. Drescher, S. R. Kachel, H. Zhou, M. Zugermeier, M. Gorgoi, B. Roling, and J. M. Gottfried. *Phys. Chem. Chem. Phys*, **17**:31790–31800, (2015).

[223] S. Sallis, D. O. Scanlon, S. C. Chae, N. F. Quackenbush, D. A. Fischer, J. C. Woicik, J. H. Guo, S. W. Cheong, and L. F J Piper. *App. Phys. Lett*, **103**:042105, (2013).

[224] R. G. Egdell, S. Eriksen, and W. R. Flavell. *Solid State Commun*, **60**:835–838, (1986).

[225] L. F. J. Piper, L. Colakerol, P. D. C. King, A. Schleife, J. Zúñiga-Pérez, P. Glans, T. Learmonth, A. Federov, T. D. Veal, F. Fuchs, V. Muñoz-Sanjosé, F. Bechstedt, C. F. McConville, and K. E. Smith. *Phys. Rev. B*, **78**:165127, (2008).

[226] P. D. C. King, T. D. Veal, C. F. McConville, J. Zúñiga-Pérez, V. Muñoz-Sanjosé, M. Hopkinson, E. D. L. Rienks, M. F. Jensen, and P. Hofmann. *Phys. Rev. Lett*, **104**:256803, (2010).

[227] K. H. L. Zhang, R. G. Egdell, F. Offi, S. Iacobucci, L. Petaccia, S. Gorovikov, and P. D. C. King. *Phys. Rev. Lett*, **110**:056803, (2013).

[228] B. S. Joo, Y. J. Chang, L. Moreschini, A. Bostwick, E. Rotenberg, and M. Han. *Curr Appl Phys*, **17**:595–599, (2017).

[229] C. Janowitz, V. Scherer, M. Mohamed, A. Krapf, H. Dwelk, R. Manzke, Z. Galazka, R. Uecker, K. Irmscher, R. Fornari, M. Michling, D. Schmeißer, J. R. Weber, J. B. Varley, and C. G. Van De Walle. *New J. Phys*, **13**:085014, (2011).

[230] V. Scherer, C. Janowitz, A. Krapf, H. Dwelk, D. Braun, and R. Manzke. *Appl. Phys. Lett*, **100**:212108, (2012).

[231] K. Takahashi, M. Imamura, J. H. Chang, and T. Tanaka. *Sci. Rep.*, 9:1–10, (2019).

[232] D. A. Shirley. *Phys. Rev. B*, **5**:4709–4714, (1972).

[233] M. Pessa, A. Vuoristo, M. Vulli, S. Aksela, J. Väyrynen, T. Rantala, and H. Aksela. *Phys. Rev. B*, **20**:3115–3123, (1979).

[234] G. Beamson and D. Briggs. *High Resolution XPS of Organic Polymers: The Scienta ESCA300 Database*. Wiley, (1992).

[235] T. Nagata, O. Bierwagen, M. E. White, M. Y. Tsai, Y. Yamashita, H. Yoshikawa, N. Ohashi, K. Kobayashi, T. Chikyow, and J. S. Speck. *Appl. Phys. Lett*, **98**:232107, (2011).

[236] D. J. Payne, J. P. Hu, R. G. Egdell, V. R. Dhanak, and G. Miller. *Chem. Phys. Lett*, **443**:61–65, (2007).

[237] R. G. Egdell, T. J. Walker, and G. Beamson. *J Electron Spectros Relat Phenomena*, **128**:59–66, (2003).

[238] A. Bourlange, D. J. Payne, R. G. Palgrave, H. Zhang, J. S. Foord, R. G. Egdell, R. M.J. Jacobs, T. D. Veal, P. D.C. King, and C. F. McConville. *J. Appl. Phys*, **106**:013703, (2009).

[239] Y. Gassenbauer, R. Schafranek, A. Klein, S. Zafeiratos, M. Hävecker, A. Knop-Gericke, and R. Schlögl. *Phys. Rev. B*, **73**:245312, (2006).

[240] J. E. N. Swallow, B. A. D. Williamson, T. J. Whittles, M. Birkett, T. J. Featherstone, N. Peng, A. Abbott, M. Farnworth, K. J. Cheetham, P. Warren, D. O. Scanlon, V. R. Dhanak, and T. D. Veal. *Adv. Funct. Mater*, **28**:1–10, (2018).

[241] A. Kotani and Y. Toyozawa. *J. Phys. Soc. Japan*, **37**:912–919, (1974).

[242] J. E. Inglesfield. *J. Phys. C*, **16**:403–416, (1983).

[243] P. D. C. King, T. D. Veal, H. Lu, S. A. Hatfield, W. J. Schaff, and C. F. McConville. *Surface Science*, **602**:871–875, (2008).

[244] M. Gaowei, E. M. Muller, A. K. Rumaiz, C. Weiland, E. Cockayne, J. Jordan-Sweet, J. Smedley, and J. C. Woicik. *Appl. Phys. Lett*, **100**:201606, (2012).

[245] J. C. Woicik, E. J. Nelson, Leeor Kronik, Manish Jain, James R. Chelikowsky, D. Heskett, L. E. Berman, and G. S. Herman. *Phys. Rev. Lett*, **89**:077401, (2002).

[246] C. Kalha, N. Fernando, and A. Regoutz. *Digitisation of Scofield Photoionisation Cross Section Tabulated Data*. (2020).

[247] J. Willis, C. Kalha, M.B. Trzhaskovskaya, V.G. Yarzhemsky, D. O. Scanlon,

and A. Regoutz. *Digitisation of Trzhaskovskaya Dirac-Fock Photoionisation Parameters for HAXPES Applications*. (2020).

[248] J. Willis, C. Kalha, M.B. Trzhaskovskaya, V.G. Yarzhemsky, D. O. Scanlon, and A. Regoutz. *Digitisation of Trzhaskovskaya Dirac-Fock Photoionisation Parameters for HAXPES Applications, Part II*. (2020).

[249] F. Oba, A. Togo, I. Tanaka, J. Paier, and G. Kresse. *Phys. Rev. B*, **77**:245202, (2008).

[250] Y. Kang, G. Kang, H. H. Nahm, S. H. Cho, Y. S. Park, and S. Han. *Phys. Rev. B*, **89**:165130, (2014).

[251] J. J. Mudd. *Photoelectron Spectroscopy Investigation of CdO*. PhD thesis, University of Warwick, (2014).

[252] S. H. Wei and A. Zunger. *Phys. Rev. B*, **37**:8958–8981, (1988).

[253] P. Erhart, A. Klein, R. G. Egdell, and K. Albe. *Phys. Rev. B*, **75**:153205, (2007).

[254] A. Sekiyama and S. Suga. *J Electron Spectros Relat Phenomena*, **137-140**:681–685, (2004).

[255] J. Scola, A. Benamar, B. Berini, F. Jomard, and Y. Dumont. *J. Phys. D*, **50**:045302, (2017).

[256] T. Kamiya and H. Hosono. *NPG Asia Materials*, **2**:15–22, (2010).

[257] H. Oppermann, W. Reichelt, and E. Wolf. *J. Cryst. Growth*, **31**:49–55, (1975).